Development of the Contact Models to Determine Electrical Contact Resistance Including a Coupled Electro-thermo-mechanical Analysis Considering Temperature-Dependent Material Properties

by

Swarna Saha

A dissertation submitted to the Graduate Faculty of
Auburn University
in partial fulfillment of the
requirements for the Degree of
Doctor of Philosophy

Auburn, Alabama
August 08, 2020

Keywords: Axisymmetric sinusoidal asperity model, Asperity Interaction, Probability Density Function, Statistical Model Validation, Electro-thermo-mechanical Analysis, Temperature Dependent Material Modeling

Approved by

Robert L Jackson, Chair, Professor of Mechanical Engineering
Hareesh Tippur, Professor of Mechanical Engineering
George Flowers, Professor of Mechanical Engineering
Kyle Schulze, Assistant Professor of Mechanical Engineering
Hans Werner Van Wyk, Assistant Professor of Mathematics and Statistics

Abstract

Reliability of the electrical contact or interface is one of the major concerns in many applications such as batteries, solar cells, electrical connectors, MEMS based sensors for hybrid and electric vehicles, electronic devices, employment in mechatronics and so on. Different factors affect the reliability and efficiency of the electrical interface and also vary depending on the application. Electrical contact resistance is one of the most important factors. Electrical contact resistance value is affected by surface imperfection, cold welding or adhesion, vibration, hot-welding, material properties and contact behavior of the interface, organic contaminants, wear debris, various kinds of oxides or thin films and other features as well. Contact mechanics models are widely used to analyze the electrical contact behavior. This dissertation focuses on the development and validation of the contact models to determine the electrical contact resistance, which will be discussed subsequently in the next few paragraphs.

Closed-form finite-element empirical models are available for elastic and elastic-plastic cylindrical, spherical and sinusoidal shaped surfaces in contact. However, some of these models do not consider the effect of interaction with adjacent asperities or require extensive numerical resources because they employ a full 3-D model. Therefore, in this dissertation, a single asperity contact model has been developed, which is more realistic and computationally less expensive. To develop the asperity model, the behavior of an elastic and elastic- perfectly plastic axisymmetric sinusoidal surface in contact with a rigid flat has been analyzed and quantified for a wide range of material properties and asperity sharpness from initial to complete contact (high load). The numerical results agreed well with the Hertz model and the Jackson-Green elastic-plastic spherical contact model at low loads. Empirical equations for elastic and also elastic-

perfectly plastic cases are formulated for the contact pressure, contact area, and surface separation. From the current analysis, it is found that it is not any single parameter, but different combinations of material properties and surface geometry that govern the whole contact behavior. The critical value of the amplitude of the sinusoidal asperity below which it will deform completely elastically from initial to complete contact is established. At low values of amplitude normalized by the critical amplitude, it was found that the contact behaved similar to a spherical contact, with the average pressure (hardness) always remaining lower than three times the yield strength. However, at higher values the average pressure increased toward a value as high as six times the yield strength at complete contact. This is a very significant finding as it differs from the conventional theory of hardness. The developed empirical equations are a function of surface roughness and material properties. Therefore, if temperature and scale-dependent material properties are known, these equations should be able to predict temperature and scale-dependent contact behavior.

Greenwood and Williamson (GW model) first developed a rough surface contact model to solve the problem of electrical contact. The original GW model used the Hertz single asperity model and Gaussian distribution of the surface roughness. However, in many of the electrical contact cases, contact deformation surpasses the Hertz small deformation assumtion. For medium to complete contact cases, asperity lateral interactions become very important, and the Hertz model cannot predict this behavior. Besides asperity lateral interaction, the probability distribution function of the surface roughness is critical as not all the surfaces are Gaussian in nature. This work has shown the effect of asperity models to predict asperity interaction behavior. Then the asperity models are applied with different probability distributions of the surface roughness in the framework of the statistical rough surface model. For the elastic case, the newly proposed rough

surface models are compared with the Boundary Element Method (BEM) and Persson model that well predicted many of the practical applications. For the elastic-plastic case, electrical contact resistance has been measured between two rough surfaces using a four-wire resistance method. Then the newly proposed rough surface models are compared with the experimental results. Comparisons show that proper choice of the asperity model and the probability distribution function of the surface roughness can effectively model the contact behavior from the very small deformation region to the large deformation region.

Electrical contacts behave in a complicated way, and the effect of temperature makes the contact behavior more complicated. To analyze the temperature-dependent contact behavior, an axisymmetric sinusoidal asperity model of tin has been developed using Finite Element Method (FEM). The axisymmetric sinusoidal model reduces computational expenses and can effectively consider the asperity interaction, which is an important factor for large elastic-plastic deformation. The model considers the temperature-dependent yield strength, thermal conductivity, and resistivity. The effect of the thermal expansion coefficient is also included. For material modeling, the Johnson-Cook material model is employed, which can model the temperature-dependent material behavior from room temperature to melting temperature. Results show that temperature-dependent yield strength has a negligible effect on the electrical contact behavior for the cases analyzed. This work finds that temperature dependent resistivity and thermal conductivity are the key factors that govern the contact mechanism. The present work also confirmed the previous findings that Holm's electrical contact resistance equation does not work for high-temperature cases. The finite element results have been validated by comparing the results with the voltage-temperature relation provided by the Wiedemann-Franz law. Finally, an equation has been

suggested for the electrical contact resistance determination, modifying the equation derived by Greenwood. The equation should be able to predict the contact resistance from room temperature to high-temperature cases. This equation is a function of contact area. This contact area can be determined from the previously developed empirical equation for the contact area of an elastic-plastic axisymmetric wavy asperity.

Acknowledgement

I would like to express my heartfelt gratitude to my advisor, Prof. Robert L Jackson for his constant guidance and patience. When things were not going well he never lost trust on me and his positive attitude, knowledge and experience helped me to finish this dissertation. It is truly a privilege to work with such a knowledgeable Professor and an amazing human being. I was lucky to take excellent courses of Solid and Fracture Mechanics under Prof. Hareesh Tippur, which benefited me greatly during validation of the rough surface models and explaining some of the results in my dissertation. I am also grateful to Dr. Kyle Schulze for his assistance with the surface measurement, guidance and inspired discussions that helped me to improve my dissertation. I would also like to thank Dr. Hans Werner Van Wyk, for his Numerical Analysis course; the knowledge of this course later helped me in my other course works and also to finish my Dissertation. I am also very thankful to my committee member Prof. George Flowers for agreeing to be part of my committee and for assistance whenever I needed.

I want to thank my lab mate Dr. Yang Xu for his assistance since the beginning of my PhD life. He helped me to learn ANSYS APDL coding and his Fractal and Gaussian rough surafce generation code was a great assistance to validate the rough surface contact models. His research works have an immense impact on the rough surface contact models developed in this dissertation. I would also like to thank my other lab mates, Dr. Xianzhang Wang, Dr. Xiaohan Zhang, Dr. Hamid Ghaednia, Samuel Wynne, Geetanj Bhandari, Sanjeev KC, Nolan Chu, Alex Locker, Bowen An, Larkin Crilly, Sara Pope and Yang Zhao for their assistance and inspiring discussions. I am very grateful to my Auburn friends and seniors without whom life will not be easy far away from my family. I would also like to thank Dr. Sakib Hassan for his insightful discussion about

Fourier transform and signal processing which helped me to understand several concepts about rough surface analysis.

I am indebted to National Science Foundation and Auburn University Mechanical Engineering department for the funding support during my PhD life. I am very grateful for the support of the Auburn University Hopper Cluster and Auburn University Engineering Network Services.

At this point, I want to mention my fully supportive family member- my father, Sailesh Chandra Saha, mother, Moni Saha and elder brother, Shiba Prasad Saha, without whom none of the achievements would be possible. My family taught me to dream larger, work harder and they are the constant source of inspirations in my weal and woe. I am very grateful to God that I have found an amazing life partner, Arunodoy Saha. Although we have been living 2400 miles apart, he has always been a motivation to progress my career. I am also very thankful to my mother-in-law, Shibani Saha for her mental support and inspiration.

Table of Contents

List of Figures

List of Tables

Chapter 1

Introduction

Contact mechanics is an important factor in many applications, for example- electrical connectors, micro and nano electro-mechanical switches, bio-implants, mechanical seals, bearings, weapon systems and in many other cases. The analysis of the contact behavior has become more significant with the increasing importance of the energy industry. Due to the eventual shortage of fossil fuel and to reduce the greenhouse gas emissions, automobile industries are putting great efforts to shift towards hybrid and electrical vehicles. In the case of electric vehicles alone, there are many components such as, motor, transmission, steering system, tires, wheel bearings, constant-velocity joints, kinematic energy recovery system, comfort and safety devices, suspension and Micro-Electro-mechanical System (MEMS), which cause considerable amount of friction losses and wear, as a result decreases the overall efficiency of the EV [1]. With the increased research and usage of EV, the number of high-powered electrical connectors, connectors in printed circuit boards, integrated circuit packages have also increased. Besides EV, there are many applications of mechatronics and soldering in electronic devices where electrical connector can provide better solution and factors affecting the electrical contact are one of the major concerns there.

Battery is now at the core of many modern electronics applications, starting from hybrid/ EV to many other electronic applications. There are different agents that affect the reliability of a battery, two of the major agents are electrical contact resistance (ECR) and thermal contact resistance (TCR) generated due to the surface imperfection, and contact/interface behavior, which significantly affects the amount of heat generation and distribution, eventually controls the reliability of the battery [2]. The applications that require large collection of batteries, power loss

due to ECR and TCR can be significant. Literature shows that for a particular Li-ion battery, energy losses due to ECR can be as high as 20% of the total energy flow in and out of the battery under normal operating conditions. However, ECR losses can be reduced to 6%, applying proper contact pressure and surface treatment [3].

MEMS switches are popular in many of the electronics applications, including high frequency wireless communication systems, medical imaging, automotive, automated testing equipment, spectrum and signal analyzers and so on. They are getting more popular as they provide high isolation and figure of merit, low resistance and insertion loss compared to their competitors, i.e. PIN diodes and GaAs FET switches [4]. The power consumption in both electrostatic and piezoelectric MEMS switches is almost zero. Moreover, extremely high linearity of the RF MEMS switches separate it from the others [4]. Although these MEMS switches have immense advantages, the lower durability and reliability have limited its application and a better understanding of the surface science and contact mechanics of the electrical contact can play an important role in this case. Besides the above-mentioned applications, there are solar cell [5] and many other applications where the electrical contact plays a major role on the overall efficiency and reliability.

While studying electrical contact, electrical and thermal contact resistance (ECR and TCR) are two of the most important factors to consider. No matter how carefully the contacting metal surfaces are prepared they always have some irregularities. As a result, whenever the surfaces are brought into contact, their surfaces first touch at those points where the tips of the asperities on one surface meet the tips of the asperities on the opposing surface. If electric current passes through the metal-to-metal contact, current will pass through the asperities only. So only a very small fraction of the surfaces will be in electrical contact. This constriction in the current flow will create

additional resistance in the electric circuit and is known as electrical contact resistance. The phenomena of contact resistance is illustrated in Fig.1.1 [6]. Like electrical current, when the heat passes through the contact interface, heat also flows mostly through the asperities and the constriction induced on the heat flow can be defined as the thermal contact resistance. If the electrical contact resistance is high, then there could be lots of heat generation and due to high thermal contact resistance, if heat cannot flow through the contact, then the heat may get trapped locally at the contact and can cause thermal softening and even in some cases melting. In this dissertation, focus is given to electrical contact resistance and the factors that affect the electrical contact resistance will be discussed subsequently.

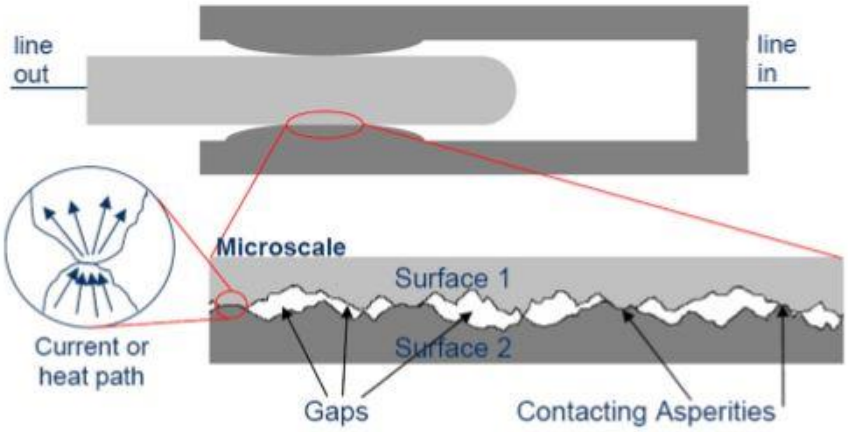

Fig. 1.1: Schematic representation of an electrical contact, Angadi, S. V., Wilson, W. E., Jackson, R. L., Flowers, G. T., & Rickett, B. I. (2008, October). A multi-physics finite element model of an electrical connector considering rough surface contact. In 2008 Proceedings of the 54th IEEE Holm Conference on Electrical Contacts (pp. 168-177), reprinted taking the permission from IEEE.

Cold-welding or adhesion is one of the key factors responsible for the degradation of the electrical contact in electrical connectors and MEMS switches [4]. In the case of electrical connectors, high contact normal forces between the connector pin and mated part autonomously generate cold welded interconnections, especially if the material used for the contacting parts have high adhesion energy between them. Due to the formation of this cold-welded intermetallic connection, the contact resistance value significantly reduces and in some cases also provides mechanical stability. This cold-welding is beneficial if the connection is permanent or does not require a large number of cycles to perform. However, in many cases where the connection is not permanent, sticking of one surface to the other causes failure to open and the system permanently stops working. Even if the system works, high adhesion may cause high surface wear.

Vibration induced fretting corrosion is another major concern for the surface degradation of the electrical connector [7]. The presence of organic contaminants during vibration can increase the abrasion and fretting degradation of the electrical connector interface, which may dramatically increase the ECR and cause surface failure. Besides organic contaminants and dirts, exposure of the electrical contact to vibration induced dynamic load for a long time, can cause higher electrical contact resistance [8]. The effect of the vibration direction on the electrical contact resistance is also investigated, and result shows that vibration direction has an important influence on the electrical contact resistance [8].

In many of the electrical contact applications, resistance generated due to organic contaminants is an important factor that affects the overall efficiency. Due to Au's low affinity to organic contaminants, it is popular as the electrical contact material. However, as Au is a very soft material and applications which need to withstand large number of cycles during their lifetime, for example- different MEMS switches, softness of Au leads to adhesion between the contacting surfaces [9-

11] and results in switches prone to failure by sticking. If we consider MEMS switch as an application, lots of research have been done using different alloys of Au, Pt, Ir, [12-14], oxygen plasma cleaned Ru [4] and different types of coatings [15] to improve the contact properties. One of the main reasons of using Au was it's high resistance to contamination. However, research shows that contamination in a MEMS switch can be reasonably prevented by hermetic packaging [4]. Ma et al. [16] showed that switch performance can be significantly affected by the package type and method. A comparison in their paper shows that while insertion loss of unpackaged switches tested in air typically increased after several million cycles, switches that were carefully packaged in an inert ambient like- clean and hermitic cavity reached several hundred million to billion cycles with little or no contact resistance change. These factors led researchers to concentrate more on adhesion and to design switches that do not fail by stiction. Although adhesion may cause surface wear, at the same time it helps to make good contact between the mating parts that decreases contact resistance. Therefore, an optimum value of adhesion is important for the efficient and reliable performance and the choice of material is very crucial for this.

In the electrical connector industry also, Au is widely used as the coating material. Extensive research projects are going on to replace Au, as it is a very expensive material. Sn is another popular coating material, however vibration induced fretting corrosion, oxidation and the Sn whisker, are major concerns when applied as a coated material. Sn whisker are electrically conductive and single crystal eruptions, grows very easily from surfaces where tin is deposited as a coating material. They may create short circuit that decreases the reliability of the connector significantly. Fig. 1.2 shows Sn whisker formations in different Sn plated applications. Different factors like- residual stress, externally-imposed stress, intermetallic formation, Sn diffusion, scratches, corrosion, coefficient of thermal expansion mismatches, etc. are responsible for whisker

growth; however, Crandall [17] specified intermetallic formation and diffusion as the main reasons. Crandall [17] also addressed that whisker growth can be prevented using topside metal films of Ni or Pt. When shorted current passes through the whisker, the temperature of the whisker increases due to heat generation and eventually the whisker melts. Jackson et al. [18] found the condition at which this melting happens in the whisker and provided an equation to predict the maximum current that the whisker can withstand before it melts.

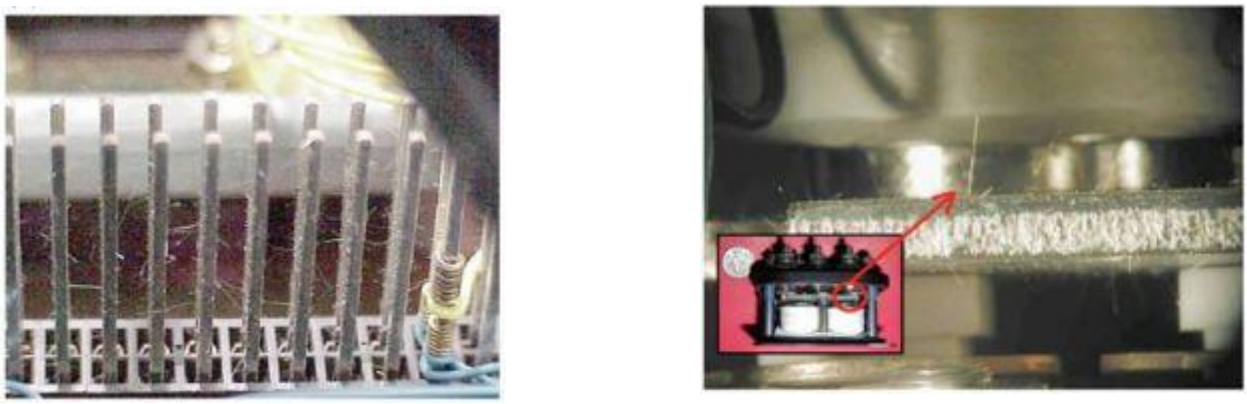

(a) (b)

Fig. 1.2 Sn whisker formations in different Sn plated applications (a) Sn-plated connector pins (b) Exterior surface of Sn-plated electromagnetic relays, Crandall, E. R. (2013). Introduction: Whiskers and Their Role in Component Reliability. In Factors Governing Tin Whisker Growth (pp. 1-24). Springer, Cham, reprinted taking the permission from Springer.

Hot welding is another major factor that affects and causes significant damage to the electrical contact. During the transition from off to on or on to off state of an electronic device, if the whole voltage applies across the electrical contact, the possibility of hot welding increases significantly. The gaps at the contact interface or improper contact is responsible for thermal arcing which causes local thermal run away or melting at the electrical contact. Bose et al. [4] studied a Ru-Ru micro

contact using AFM based test set up to understand the effect of hot-welding on the micro contact damage and failure. This AFM based test setup is basically a clamped-clamped beam structure with a contact bump at the center and a flat topped mating pillar formed the other end of the contact. The contact opening and closing replicated switching were controlled by mounting the pillar on a piezoactuator. Microcontacts were examined under a variety of hot switching conditions, ranging from different voltages, different polarities and different approach and separation rates. At the end, it was concluded that material transfer which leads to removal of contact material from one side of the contact to the other is the primary cause for contact failure in the DC hot switching condition as material transfer causes contact resistance to increase [4]. Small surface separation or improper contact (contact only via a molten metal bridge), field emission and evaporation, Thompson's effect and electromigration were specified as responsible for the material transfer. Bowden and Williamson [19] observed the response of an Au-Au cone shaped indenter against a rectangular block for different currents and found that the contact starts to collapse before it reaches the melting point of Au. Another later paper [20] explained this observation that for every material there is a critical or super temperature, when the surface reaches that temperature, thermal stability at that electrical contact is not possible anymore. Bansal et al. [21] investigates the behavior of electrical contact resistance for Cu-Cu and Al-Al sphere on flat contacts for a wide range of currents, loads and surface roughnesses. The analysis shows that the voltage drop across the contact initially increases with current until a certain voltage is reached. Beyond this critical point, any increase in the current causes essentially no change in voltage, which is known as saturation voltage and viscoplastic creep causes this voltage saturation. It is shown in the paper that, at high temperature a small increase in temperature causes a large increase in the strain rate. As a result, with the increase of voltage across the contact, current increases. Increase of current causes temperature

rise and with the temperature rise contact area increases and when the temperature at the contact gets high enough, a small increase in temperature causes high strain in the contact area. With the increase of the contact area, contact resistance continuously decreases and it would continue to decrease with increasing current only to the point where there is complete contact over the available area. Despite the rapid strain rate, contact resistance cannot decrease anymore at this point, and further increase in current would increase the voltage continuously upto the melting point. Besides viscoplastic creep, electroplasticity and electromigration have also held responsible for the electrical contact resistance behavior. Rezvanian et al. [22] used diffusion based creep equation in conjunction with an idealized single-asperity model to account for the reduction in the resistance of Au ohmic switches over time under the conditions of low voltage and current and the result shows that the increase in the contact radius is proportional to the strain rate. Bennett et al. developed a numerical simulation of the growth rate of a typical contact radius of the asperity as well as the rate of change of voltage based on the electromigration mechanism.

Gap or surface separation are the major source of electrical arcing. Electrical arcing occurs when an electric current flows through the air, from one conductive point to another. Arcing is associated with a flaw in an electrical circuit that causes the electrical current to cease travelling along its intended path and to instead jump across a shorter path, from one conductor to another. Electrical arcing causes the formation of oxides, nitrides, sulphides, carbonates and carbonaceous compounds [4] due to the high temperature generation at the contact. These formulated compounds at the electrical contact is another important factor that affects electrical contact behavior significantly. These compounds generally act as current insulators and are very thin. Tunneling current may pass through this thin film and oxides due to quantum electrical conduction. Formation of compounds at the contact increases the contact resistance, however due to tunneling contact

resistance may continuously decrease and makes it very difficult to get a consistent and reliable contact resistance measurement. Jackson et al. [23] modeled the electrical contact resistance between two surfaces separated by an anisotropic conductive film. The film consists of an epoxy with conductive spherical metallic particles dispersed within. This work shows that, without the consideration of the thin insulating film (in this case epoxy) between the metallic particles and the surfaces, theoretical results significantly underpredict the electrical contact resistance when compared with the experimental results. However, consideration of the thin insulating film using electron tunneling theory improves the electrical contact resistance value by a large extent.

The above discussion shows that different factors affect the electrical contact resistance. However, hot welding leads to more damage and reduced lifetime than cold-welding [4]. Surface oxides and contamination, improper contact or surface separation are the major source of hot welding and direct in-situ determination of the contact area due to thermal induced softening of the metal-metal contact is somewhat impossible. Besides that, during experiment, all the factors that affect the whole phenomenon act simultaneously which makes it difficult to understand which factor is affecting the most. Therefore, in this dissertation numerical technique has applied to analyze the contact behavior and determine the electrical contact resistance. Research has been done on electrical contact using numerical techniques [18, 20 and 24] considering temperature dependent properties of electrical resistivity and thermal conductivity. However, very few investigations have been done that also include temperature dependent yield strength properties of the material. Yield strength of any metal continuously decreases with temperature and at the melting temperature, the yield strength approaches zero. Therefore, the objective of this dissertation is to analyze the contact behavior such as-contact area, contact pressure, surface separation as a function of surface roughness and material properties. Therefore, if the temperature at the contact and the temperature

dependent material properties are known, the contact behavior can be predicted. There are different numerical techniques to model the contact behavior that will be discussed afterward.

All surfaces, whether natural or synthetic, have different degrees of roughness. Hertz probably first began the application of solid mechanics to contact problems by solving the problem of elastic deformation between two contacting parabolic asperities [25-26]. Since then, many researchers have applied this for modelling contact between elastic rough surfaces. Among them, the works of Archard [27] and Greenwood and Williamson [28] are noteworthy. The main idea of asperity based rough surface contact modeling is that depending on the application an asperity model can be developed for that particular application. The developed asperity model should be able to capture the contact behavior and parameters such as, contact area, contact pressure, contact gap, surface delamination etc. Then those asperity models are applied into different rough surface contact models. Surfaces are very random and multiscale in nature. Based on the Nayak's random process theory, Greenwood and Williamson [28] developed a rough surface contact model. Although the original Greenwood and Williamson model (GW model) was developed for an elastic and surface with asperities following a Gaussian distribution, this model has been expanded later [29-33] by developing more advanced asperity models and surface probability distribution functions. Another popular asperity based model is the multiscale model. Surface roughness varies over many scales, starting from the macroscale down to the atomic level and the multiscale model considers the multiscale nature of the surface during rough surface contact modeling. Archard [27] first developed a multiscale model based on the concept of "protuberance upon protuberance" where smaller spherical asperities protruded from the larger spherical asperities. However, real surfaces barely look like this. Later Majumdar and Bhushan [34] and Ciavarella [35] developed fractal surface based models to consider the multiscale nature of the surfaces. However, not all the

surfaces are fractal in nature. In 2006, Jackson and Streator [36] performed a Fast Fourier Transform on the surface profile to characterize the spectrum of the surface. Then based on the spectral analysis and single asperity model developed a multiscale model for contact between two rough surfaces.

Persson [37] developed a rough surface model that does not use the idea of the single asperity and relies on the relation between surface heights and contact pressure distributions. The developed model by Persson is extremely simple and predicts reasonably well the trend of contact behavior in many applications of tribology- viscoelastic rubber against a rigid flat [37], mechanical seals [38-41], lubricated rough surface contact [42-45], heat transfer between rough surfaces [43], adhesive contact [46-49], rubber friction [37, 50] and so on. However, the model assumes that the rough surfaces are perfectly fractal in nature, which is not true as showed in many later works [51-52].

There is another method called the deterministic model to analyze the rough surface contact behavior. In this method, the interface is designed as exactly as the surface is measured using the surface measuring instrument. The Finite Element Method (FEM) and Boundary Element Method (BEM) are generally used for the deterministic modeling. Deterministic models are generally used for the validation of the other rough surface contact models but are difficult to use for design problems, as they are computationally very expensive.

BEM is a numerical tool that solves the approximated solutions on the boundary of a specific problem. To solve the problem, BEM forms a boundary Integral equation (BIE) utilizing Betti's reciprocal theorem in conjunction with the Kelvin solution [53] or Boussinesq solution [54] or other solutions depending on the case. Then applying the Karush-Kuhn-Tucker condition as the

boundary condition, the problem is solved iteratively. To solve many of the tribological problems, the Boussinesq solution has been widely used with BEM. However, the Boussinesq solution provides a solution only for the cases where a flexible half-space is loaded with a point load. So for the rough surface contact problems, only the cases where contact area is several orders of magnitude less than the dimensions of the contact bodies, the Boussinesq solution can be applied. However, the Kelvin solution can be used with BEM to solve problems that involve complicated geometries. In Kelvin's problem, a concentrated force acts at an interior point of an infinite elastic body. The problem does not consider any length scale and the stress field is self-similar [55]. Xu [31] showed that BEM solved using the Boussinesq solution can be derived from the general purpose BEM that use the Kelvin solution. BEM in conjunction with the Kelvin solution is known as conventional or general purpose BEM, whereas BEM with all the other solutions is known as the special purpose BEM. If the problem involves contact, BEM generally uses the first Penalty method to solve the contact problem. The disadvantage of BEM is that, as BEM connects the surface displacement and traction at the boundary of the current problem to a special problem to form the BIE, the solution for stress and displacement must have to be known for the special problem. That's why in most of the cases it's application is limited to linear elastic problems.

FEM is a numerical method to solve boundary value problems using partial differential equations. FEM can solve most of the complicated problems that includes complicated material properties, contact, and complicated geometry. To solve the problem, FEM discretizes the whole computational domain into lots of small elements and develops a set of algebraic equations for each element depending on the application. Then combining the equations and boundary conditions for each element, equations for the whole geometry are developed. FEM uses variational principles or weighted integrals of partial differential equations to approximate a

solution by minimizing an associated error function. As a result, in many cases it generates impractical numbers of elements and sets of equations that make FEM computationally very expensive. However, with the development of computational methods and technologies, the ability of FEM is also increasing. Although FEM is a very computationally expensive method to solve, lots of research have been done on deterministic FEM to solve elastic [56] and elastic-plastic [57-62] rough surface contact problems as this can be used as the validation tool for the other rough surface models. However, surface resolution is a major hindrance in this case. As surface roughness varies over a wide range of scale, very fine mesh resolution can create millions of elements. Recently, Wang et al. [62] performed an analysis on the effect of resolution on the deterministic FE elastic-plastic rough surface contact under combined normal and tangential loading. The employed harmonic or spectral interpolation to refine the mesh resolution. The developed methodology for rough surface contact analysis in that paper may help to push the FE simulation results closer to reality.

Therefore, the objectives of this dissertation are the following:

1. To develop and validate rough surface contact models that can predict contact behavior from very small contact (Hertz contact region) to complete contact. Later these rough surface contact models will be used to predict the electrical contact resistance of the surface. For this purpose:
    - A Finite Element Models (FEM) of an elastic and elastic-perfectly plastic axisymmetric sinusoidal asperity have been developed for a wide range of material properties and surface sharpness. Analyzing the FE results, empirical equations have been formulated to predict the contact behavior as a function of geometrical parameters and material properties from the Hertz contact region to complete contact region. So if the temperature and scale

dependent material properties are known, then these equations should be used to predict the contact evolution with the change of temperature and scale.

- Statistical or multi-asperity models are developed for elastic and elastic-perfectly plastic cases based on Nayak's random process model. The rough surface contact methodology both for real and generated fractal surfaces are discussed.
- For the validation of the elastic rough surface contact model, the developed rough surface contact models are compared with the Boundary Element Method (BEM) and Persson's model.

2. Electrical contact resistance has been measured between two Aluminum surface using the four-wire resistance method and then the experimental results are compared with the electrical contact resistance determined using the rough surface contact models developed for the elastic-perfectly plastic rough surfaces.
3. A FE model of a coupled electro-thermo-mechanical axisymmetric sinusoidal asperity has been developed considering temperature dependent electrical, thermal and mechanical properties to observe the effect of the temperature dependent properties on the contact behavior. Both the frictionless and perfectly bonded contact cases are analyzed. Then an equation for the electrical contact resistance has been suggested by modifying the equation of Greenwood [63]. The suggested electrical contact resistance equation should be applicable for room to high temperature cases.

References

1. Farfan-Cabrera, L. I. (2019). Tribology of electric vehicles: A review of critical components, current state and future improvement trends. Tribology International, 138, 473-486.
2. Xia, G., Cao, L., & Bi, G. (2017). A review on battery thermal management in electric vehicle application. Journal of power sources, 367, 90-105.
3. Taheri, P., Hsieh, S., & Bahrami, M. (2011). Investigating electrical contact resistance losses in lithium-ion battery assemblies for hybrid and electric vehicles. Journal of Power Sources, 196(15), 6525-6533.
4. Basu, A. (2013). An experimental investigation of hot switching contact damage in RF MEMS switches. Doctoral dissertation, Northeastern University.
5. Römer, U., Peibst, R., Ohrdes, T., Lim, B., Krügener, J., Bugiel, E., ... & Brendel, R. (2014). Recombination behavior and contact resistance of n+ and p+ poly-crystalline Si/mono-crystalline Si junctions. Solar Energy Materials and Solar Cells, 131, 85-91.
6. Angadi, S. V., Wilson, W. E., Jackson, R. L., Flowers, G. T., & Rickett, B. I. (2008, October). A multi-physics finite element model of an electrical connector considering rough surface contact. In 2008 Proceedings of the 54th IEEE Holm Conference on Electrical Contacts (pp. 168-177). IEEE.
7. Gao, J., Chen, C., Flowers, G. T., Jackson, R. L., & Bozack, M. J. (2010). The influence of particulate contaminants on vibration-induced fretting degradation in electrical connectors. In 2010 Proceedings of the 56th IEEE Holm Conference on Electrical Contacts, 1-5. IEEE.

8. Joo, H. G., Jang, Y. H., & Choi, H. S. (2014). Electrical contact resistance for a conductive Velcro system. Tribology International, 80, 115-121.
9. Majumder, S., McGruer, N. E., & Adams, G. G. (2005). Adhesion and contact resistance in an electrostatic MEMS microswitch. In 18th IEEE International Conference on Micro Electro Mechanical Systems, 2005. MEMS 2005, 215-218. IEEE.
10. Eid, H., Chen, L., Joshi, N., McGruer, N. E., & Adams, G. G. (2010). Contact and Adhesion of Elastic-Plastic Layered microsphere. In STLE/ASME 2010 International Joint Tribology Conference, 341-343. American Society of Mechanical Engineers Digital Collection.
11. Arrazat, B., Mandrillon, V., Inal, K., Vincent, M., & Poulain, C. (2011). Microstructure evolution of gold thin films under spherical indentation for micro switch contact applications. Journal of materials science, 46(18), 6111-6117.
12. Chen, L., Guo, Z. J., Joshi, N., Eid, H., Adams, G. G., & McGruer, N. E. (2012). An improved SPM-based contact tester for the study of microcontacts. Journal of Micromechanics and Microengineering, 22(4), 045017.
13. Joshi, N. (2010). An SPM based tester for the study of micro-contacts. Doctoral dissertation, Northeastern University.
14. Coutu, R. A., Kladitis, P. E., Cortez, R., Strawser, R. E., & Crane, R. L. (2004). Micro-switches with sputtered Au, AuPd, Au-on-AuPt, and AuPtCu alloy electric contacts. In Proceedings of the 50th IEEE Holm Conference on Electrical Contacts and the 22nd International Conference on Electrical Contacts Electrical Contacts, 214-221. IEEE.

15. Liu, B., Lv, Z., He, X., Liu, M., Hao, Y., & Li, Z. (2011). Improving performance of the metal-to-metal contact RF MEMS switch with a Pt–Au microspring contact design. Journal of Micromechanics and Microengineering, 21(6), 065038.
16. Ma, Q., Tran, Q., Chou, T. K. A., Heck, J., Bar, H., Kant, R., & Rao, V. (2007). Metal contact reliability of RF MEMS switches. In Reliability, Packaging, Testing, and Characterization of MEMS/MOEMS VI, 6463, 646305. International Society for Optics and Photonics.
17. Crandall, E. R. (2013). Introduction: Whiskers and Their Role in Component Reliability. In Factors Governing Tin Whisker Growth (pp. 1-24). Springer, Cham.
18. Jackson, R. L., & Crandall, E. R. (2018). A Multiphysics Coupled Electro-thermo-mechanical Model of Whisker Shorting. In 2018 IEEE Holm Conference on Electrical Contacts, 48-55. IEEE.
19. Bowden, F. P., & Williamson, J. B. P. (1958). Electrical conduction in solids I. Influence of the passage of current on the contact between solids. Proceedings of the Royal Society of London. Series A. Mathematical and Physical Sciences, 246(1244), 1-12.
20. Greenwood, J. A., & Williamson, J. B. P. (1958). Electrical conduction in solids II. Theory of temperature-dependent conductors. Proceedings of the Royal Society of London. Series A. Mathematical and Physical Sciences, 246(1244), 13-31.
21. Bansal DG, Streator JL, Voltage saturation in electrical contacts via viscoplastic creep. Acta materialia, 2011, Vol. 59(2), 726-737.
22. Rezvanian, O., Brown, C., Zikry, M. A., Kingon, A. I., Krim, J., Irving, D. L., & Brenner, D. W. (2008). The role of creep in the time-dependent resistance of Ohmic gold contacts

in radio frequency microelectromechanical system devices. Journal of applied physics, 104(2), 024513.22.

23. Jackson, R. L., & Kogut, L. (2007). Electrical contact resistance theory for anisotropic conductive films considering electron tunneling and particle flattening. IEEE Transactions on Components and Packaging Technologies, 30(1), 59-66.
24. Ghaednia, H., Rostami, A., & Jackson, R. L. (2012). The influence of thermal expansion and plastic deformation on a thermo-electro mechanical spherical asperity contact. In 2012 IEEE 58th Holm Conference on Electrical Contacts (Holm), 1-7. IEEE.
25. Keer, L. M. (2013). History of contact mechanics. Encyclopedia Tribol., 1682–1684.
26. Jackson, R. L., Ghaednia, H., Lee, H., Rostami, A., & Wang, X. (2013). Contact mechanics. In Tribology for scientists and engineers, 93-140. Springer, New York, NY.
27. Archard, J. F. (1957). Elastic deformation and the laws of friction. Proceedings of the Royal Society of London. Series A. Mathematical and Physical Sciences, 243(1233), 190-205.
28. Greenwood, J. A., & Williamson, J. P. (1966). Contact of nominally flat surfaces. Proceedings of the royal society of London. Series A. Mathematical and physical sciences, 295(1442), 300-319.
29. Bush, A. W., Gibson, R. D., & Thomas, T. R. (1975). The elastic contact of a rough surface. Wear, 35(1), 87-111.
30. Greenwood, J. A. (2006). A simplified elliptic model of rough surface contact. Wear, 261(2), 191-200.
31. Xu, Y. (2017). Statistical Models of Nominally Flat Rough Surface Contact. Doctoral dissertation, Auburn University.

32. Jackson, R. L., & Green, I. (2006). A statistical model of elasto-plastic asperity contact between rough surfaces. Tribology International, 39(9), 906-914.
33. Jackson, R. L., & Green, I. (2011). On the Modeling of Elastic Contact between Rough Surfaces. Tribol. In Trans, 54, 300-314.
34. Majumdar, A., & Bhushan, B. (1990). Role of fractal geometry in roughness characterization and contact mechanics of surfaces. ASME Journal of Tribology, 112(2), 205-216.
35. Ciavarella, M., Demelio, G., Barber, J. R., & Jang, Y. H. (2000). Linear elastic contact of the Weierstrass profile. Proceedings of the Royal Society of London. Series A: Mathematical, Physical and Engineering Sciences, 456(1994), 387-405.
36. Jackson, R. L., & Streator, J. L. (2006). A multi-scale model for contact between rough surfaces. Wear, 261(11-12), 1337-1347.
37. Persson, B. N. (2001). Theory of rubber friction and contact mechanics. The Journal of Chemical Physics, 115(8), 3840-3861.
38. Lorenz, B., & Persson, B. N. J. (2009). Leak rate of seals: Comparison of theory with experiment. EPL (Europhysics Letters), 86(4), 44006.
39. Lorenz, B., & Persson, B. N. J. (2010). On the dependence of the leak rate of seals on the skewness of the surface height probability distribution. EPL (Europhysics Letters), 90(3), 38002.
40. Lorenz, B., & Persson, B. N. J. (2010). Leak rate of seals: Effective-medium theory and comparison with experiment. The European Physical Journal E, 31(2), 159-167.
41. Persson, B. N. J. (2008). Capillary adhesion between elastic solids with randomly rough surfaces. Journal of Physics: Condensed Matter, 20(31), 315007.

42. Persson, B. N. J., & Scaraggi, M. (2009). On the transition from boundary lubrication to hydrodynamic lubrication in soft contacts. Journal of Physics: Condensed Matter, 21(18), 185002.
43. Persson, B. N. (2010). Fluid dynamics at the interface between contacting elastic solids with randomly rough surfaces. Journal of Physics: Condensed Matter, 22(26), 265004.
44. Lorenz, B., & Persson, B. N. J. (2010). Time-dependent fluid squeeze-out between solids with rough surfaces. The European Physical Journal E, 32(3), 281-290.
45. Lorenz, B., & Persson, B. N. J. (2011). Fluid squeeze-out between rough surfaces: comparison of theory with experiment. Journal of Physics: Condensed Matter, 23(35), 355005.
46. Persson, B. N. J. (2007). Relation between interfacial separation and load: a general theory of contact mechanics. Physical review letters, 99(12), 125502.
47. Persson, B. N. J. (2003). On the mechanism of adhesion in biological systems. The Journal of chemical physics, 118(16), 7614-7621.
48. Carbone, G., Mangialardi, L., & Persson, B. N. J. (2004). Adhesion between a thin elastic plate and a hard randomly rough substrate. Physical Review B, 70(12), 125407.
49. Persson, B. N. J. (2008). Capillary adhesion between elastic solids with randomly rough surfaces. Journal of Physics: Condensed Matter, 20(31), 315007.
50. Selig, M., Lorenz, B., Henrichmöller, D., Schmidt, K., Ball, A., & Persson, B. (2014). Rubber friction and tire dynamics: A comparison of theory with experimental data. Tire Science and Technology, 42(4), 216-262.50.
51. Zhang, X., & Jackson, R. L. (2017). An analysis of the multiscale structure of surfaces with various finishes. Tribology Transactions, 60(1), 121-134.51.

52. Jackson, R. L., Xu, Y., Saha, S. & Schulze, K. (2020). Elastic Rough Surface Contact and Root Mean Square Slope of Measured Surfaces. 30th International Conference on Electrical Contacts, Switzerland, UK.
53. Brebbia, C. A., Telles, J. C. F., & Wrobel, L. C. (2012). Boundary element techniques: theory and applications in engineering. Springer Science & Business Media.
54. Boussinesq, J. (1885). Application des potentiels à l'étude de l'équilibre et du mouvement des solides élastiques: principalement au calcul des deformations et des pressions que produisent, dans ces solides, des efforts quelconques exercés sur une petite partie de leur surface ou de leur intérieur; mémoire suivi de notes étendues sur divers points de physique mathématique et d'analyse. Gauthier-Villars.
55. Barber, J. R. (2011). Linear elasto-statics. Continuum Mechanics, 1, 344.
56. Hyun, S., Pei, L., Molinari, J. F., & Robbins, M. O. (2004). Finite-element analysis of contact between elastic self-affine surfaces. Physical Review E, 70(2), 026117.
57. Pei, L., Hyun, S., Molinari, J. F., & Robbins, M. O. (2005). Finite element modeling of elasto-plastic contact between rough surfaces. Journal of the Mechanics and Physics of Solids, 53(11), 2385-2409.57.
58. Yastrebov, V. A., Durand, J., Proudhon, H., & Cailletaud, G. (2011). Rough surface contact analysis by means of the finite element method and of a new reduced model. Comptes Rendus Mécanique, 339(7-8), 473-490.58.
59. Song, H., Van der Giessen, E., & Liu, X. (2016). Strain gradient plasticity analysis of elasto-plastic contact between rough surfaces. Journal of the Mechanics and Physics of Solids, 96, 18-28.

60. An, B., Wang, X., Xu, Y., & Jackson, R. L. (2019). Deterministic elastic-plastic modelling of rough surface contact including spectral interpolation and comparison to theoretical models. Tribology International, 135, 246-258.60.
61. Wang, X., Xu, Y., & Jackson, R. L. (2018). Theoretical and finite element analysis of static friction between multi-scale rough surfaces. Tribology Letters, 66(4), 146.
62. Wang, X., An, B., Xu, Y., & Jackson, R. L. (2020). The effect of resolution on the deterministic finite element elastic-plastic rough surface contact under combined normal and tangential loading. Tribology International, 144, 106141.
63. Greenwood, J. A., & Williamson, J. B. P. (1958). Electrical conduction in solids II. Theory of temperature-dependent conductors. Proceedings of the Royal Society of London. Series A. Mathematical and Physical Sciences, 246(1244), 13-31.

Chapter 2

Literature Review on Elastic and Elastic-Plastic Asperity Models

2.1 Introduction

Contact behavior is a complicated phenomenon. Depending on the surface roughness, material and application, the contact response varies a lot. Hertz [1] first developed the solution of the contact between two elastic parabolic structures. The solution also provides a precise approximation of the elastic contact between spheres. The Hertz model assumes that the interference is small so that the geometry of the asperity does not change significantly; also, the surface interactions are frictionless and only repulsive. The model works well in early contact. Later other elastic asperity models [2-9] have been developed, which can predict contact behavior near complete contact or the entire range of contact from early contact to complete contact and will be discussed afterward. Before describing different asperity models, a few parameters are introduced that will be later used to describe the asperities. One way, an asperity can be described by three different parameters, asperity height, ξ^h, and principle curvatures $k_1^h$and k_2^h at a particular point. Superscript *h* denotes the asperity of a rough surface. The radius of curvature at a point on the curve is given by the following expression:

$$R = \frac{\left[1+(y'(x))^2\right]^{3/2}}{|y''(x)|} \tag{2.1}$$

In Eq. (2.1), the term $(y'(x))^2$ is very small compared to 1 for any value of *x* on the surface so that is often neglected. Therefore, the radius of curvature of an asperity along two principal directions can be expressed by the following two equations:

$$R_1 = \frac{1}{k_1} = \frac{1}{|y''(x)|} = \frac{1}{\left|\frac{d^2y}{dx^2}\right|}, R_2 = \frac{1}{k_2} = \frac{1}{|y''(x)|} = \frac{1}{\left|\frac{d^2x}{dy^2}\right|} \quad (2.2)$$

Instead of principle curvatures, asperities can also be described by mean, geometric, or semi-difference curvature of the summit of the asperity. Fig. 2.1 shows different ways of defining single asperity, and the definition of different asperity curvatures are given below [3, 10-11]:

1. Mean curvature, k_m^h [3,10]:

$$k_m^h = -\frac{\left(\frac{\partial^2 \xi^h}{\partial x^2} + \frac{\partial^2 \xi^h}{\partial y^2}\right)}{2} = -\left(\frac{k_1^h + k_2^h}{2}\right) \quad (2.3)$$

2. Geometric curvature, k_g^h [3,11]:

$$k_g^h = \left[\frac{\partial^2 \xi^h}{\partial x^2}\,\frac{\partial^2 \xi^h}{\partial y^2} - \left(\frac{\partial^2 \xi^h}{\partial x \partial y}\right)^2\right]^{1/2} = \sqrt{k_1^h\, k_2^h} \quad (2.4)$$

3. Semi-difference curvature of the summit, k_d^h [3, 11]:

$$k_d^h = \sqrt{\left(k_m^h\right)^2 - \left(k_g^h\right)^2} = \left[\frac{1}{4}\left(\frac{\partial^2 \xi^h}{\partial x^2} - \frac{\partial^2 \xi^h}{\partial y^2}\right)^2 + \left(\frac{\partial^2 \xi^h}{\partial x \partial y}\right)^2\right]^{1/2} = \left|k_1^h - k_2^h\right|/2 \quad (2.5)$$

The geometry of the contact pressure distribution, which is generally referred to as the "pressure surface," plays an important role to model the nearly complete contact. When a nominally flat rough surface, $h(x, y)$, is completely flattened by a rigid flat due to purely normal contact; the corresponding contact pressure can be determined using the following equation [3, 7 and 12]:

$$p_c(x, y) = \mathcal{F}^{-1}\left[\pi E' k \mathcal{F}[h](k_x k_y)\right] \quad (2.6)$$

where $k = \sqrt{k_x^2 + k_y^2}$, k_x and k_y are wave number in the *x* and *y* directions. $\mathcal{F}$ denotes the Fourier

transform of a function and $\mathcal{F}^{-1}$denotes the inverse Fourier transform of a function. There are various forms of Fourier transform pair. The following ones are adapted in this dissertation:

$$\mathcal{F}[f](k_x, k_y) = \int_{-\infty}^{\infty}\int_{-\infty}^{\infty} f(x,y)exp\left[-i2\pi(k_x x + k_y y)\right]dxdy, \tag{2.7}$$

$$f(x,y) = \mathcal{F}^{-1}\left[\mathcal{F}[f]\right](x,y) = \int_{-\infty}^{\infty}\int_{-\infty}^{\infty} \mathcal{F}[f](k_x, k_y)exp\left[i2\pi(k_x x + k_y y)\right]dk_x dk_y \tag{2.8}$$

E' is the equivalent elastic modulus which can be calculated using the following equation:

$$\frac{1}{E'} = \frac{1-\upsilon_1^2}{E_1} + \frac{1-\upsilon_2^2}{E_2} \tag{2.9}$$

In Eq. (2.9), E_i and v_i are Young's modulus and Poisson's ratio respectively of two contacting bodies and i=1, 2. For the "pressure surface" $\langle p_c \rangle = 0$ since $\langle h \rangle = 0$. $\langle \cdot \rangle$ denotes the ensemble average of the rough surfaces analyzed. "Pressure surface" can be analyzed in a very similar way as the rough surface, see Fig. 2.3(b). The statistical nature of a "pressure surface" is isotropic and Gaussian if the corresponding rough surface is an isotropic and Gaussian process. Xu [3] provided a proof to check the validity of this statement. Therefore, like the asperity of a rough surface, the asperity of a pressure surface can be expressed by asperity height, ξ^p, and the absolute maximum, k_1^p and minimum, k_2^p principal curvatures of the summit of the asperity. Superscript p denotes the asperity of a "pressure surface."

2.2 Elastic Asperity Models

2.2.1 Hertz Elliptical Contact Model

Hertz originally developed an elliptical contact model for linear elastic parabolic asperities [6, 7]. Now if a parabolic asperity is brought into contact with a flat surface or two parabolic asperities

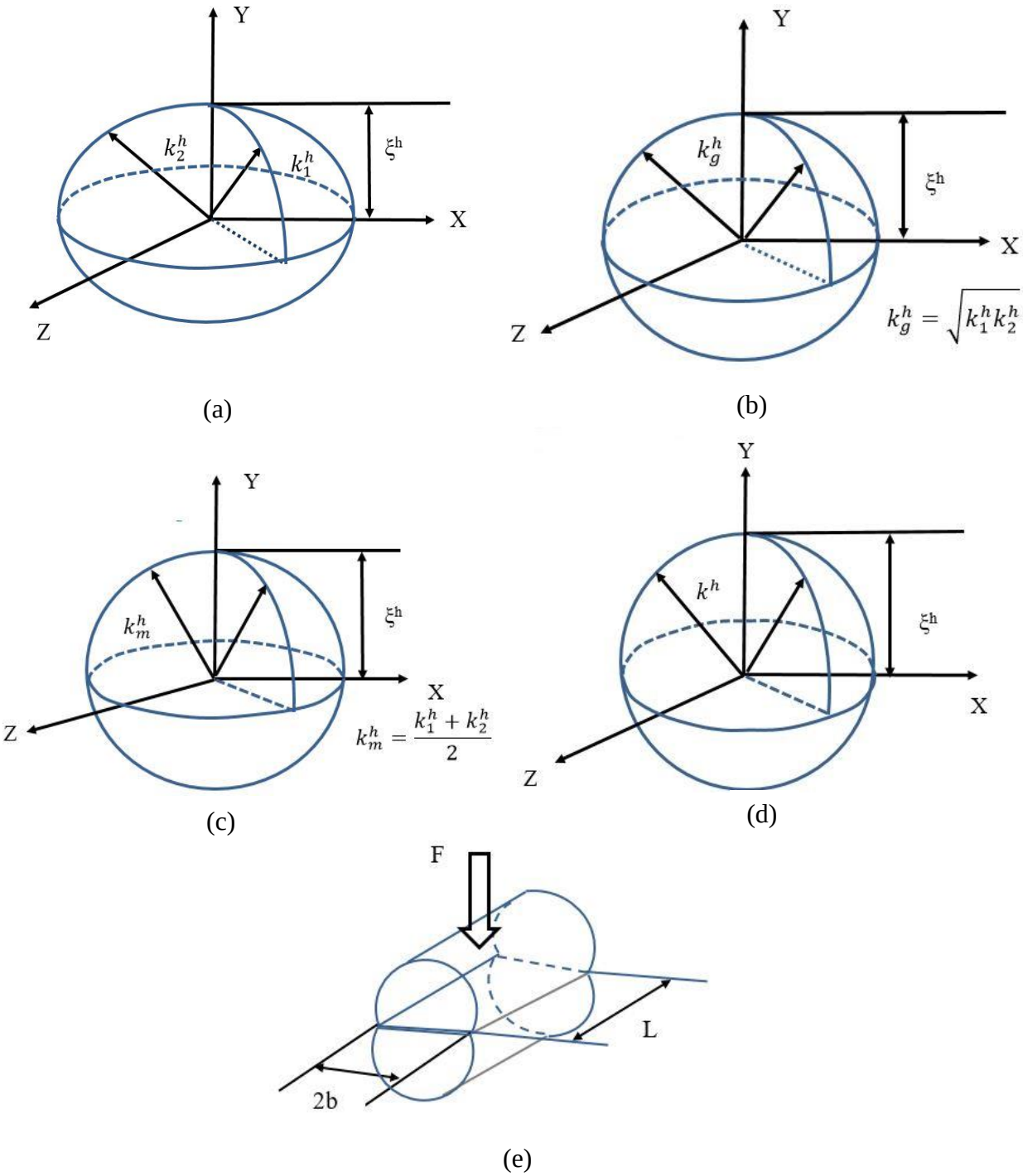

Fig. 2.1 Schematic representation of different single asperity, (a) Elliptical asperity (b) Mildly elliptical asperity with geometric curvature (c) Mildly elliptical asperity with mean curvature (d) Spherical asperity with circular contact (e) Cylindrical contact.

are brought into contact, and the geometry of the contact is elliptical, then the contact area and force can be expressed by the following two equations [6, 7]. Fig. 2.1 (a) is showing the schematic depiction of an elliptical asperity.

$$A_i\left(\delta, k_1^h, k_2^h\right) = \pi\left(k_g^h\right)^{-1}\delta F_1^2(e)/F_2(e) \tag{2.10}$$

$$F_i\left(\delta, k_1^h, k_2^h\right) = \frac{4}{3}E'\left(k_g^h\right)^{-1/2}\delta^{3/2}F_2(e)^{-3/2} \tag{2.11}$$

In Eq. (2.10) and (2.11), δ is the penetration depth that is the amount by which one surface is displaced to another surface, $F_1(e)$ and $F_2(e)$ are a function of the eccentricity of the ellipse, $e = \sqrt{1 - b^2/a^2}$, where *a*>*b* and can be expressed by the following formulas [6,7]:

$$F_1^3(e) = \frac{4}{\pi}e^{-2}(1-e^2)^{3/4}\left\{\left[\frac{E(e)}{(1-e^2)} - K(e)\right][K(e) - E(e)]\right\}^{1/2} \tag{2.12}$$

$$F_2(e) = \frac{2}{\pi}(1-e^2)^{1/4}[F_1(e)]^{-1}K(e) \tag{2.13}$$

where K(.) and E(.) are the complete elliptic integrals of the first and second kind respectively:

$$K(e) = \int_0^{\pi/2}\frac{d\theta}{\sqrt{1-e^2\sin(\theta)}}, \tag{2.14}$$

$$E(e) = \int_0^{\pi/2}\sqrt{1-e^2\sin(\theta)}d\theta \tag{2.15}$$

Curve fitting the plot of the closed-form solution provided by Johnson [7], Xu [3] obtained the following equation for *e*, which makes it more convenient to calculate contact area and force for the elliptical contact.

$$\sqrt{1-e^2} = exp\left[0.006709 \times log^2\left(k_1^h/k_2^h\right) + 0.6692 \times log\left(k_1^h/k_2^h\right)\right] \tag{2.16}$$

2.2.2 Hertzian Circular Contact Model

If the contacting parabolic asperities are axisymmetric, then $k_1^h = k_2^h = k^h$ and elliptical contact will turn into a circular contact. For circular contact, contact area and force can be expressed by the following two formulas [7]:

$$A_i(\delta, k^h) = \pi(k^h)^{-1}\delta \tag{2.17}$$

$$F_i(\delta, k^h) = \frac{4}{3}E'(k^h)^{-1/2}\delta^{3/2} \tag{2.18}$$

The equivalent radius of curvature, R=1/k^h and can be calculated from the following formula:

$$\frac{1}{R} = \frac{1}{R_1} + \frac{1}{R_2} \tag{2.19}$$

In Eq. (2.19), R_1 and R_2 are the radii of the curvature of the contacting bodies. If one of the contacting surfaces is concave and another one is convex in shape, for example, contact between a shaft and bearing bore in a journal bearing or contact between rolling elements and inner race in the rolling element bearing, for those cases, the equivalent radius of curvature can be calculated by making the sign of the curvature of the concave asperity negative. Fig. 2.1(d) is showing the diagrammatic representation of a spherical asperity with circular contact.

2.2.3 Hertzian Mildly Elliptical Contact Models with Geometric Curvature/ Mean Curvature

Hertzian mildly elliptical contact models with geometric curvature, k_g^h, and mean curvature, k_m^h, are equivalent to the Hertzian circular contact model if k^h in Eq. (2.17) and (2.18) are replaced by $k_g^h = \sqrt{k_1^h\, k_2^h}$ [3, 11] and $k_m^h = \left(k_1^h + k_2^h\right)/2$ [3, 10], respectively. Elliptical contact model, i.e., Eq. (2.10) and (2.11) are a function of $F_1(e)$ and $F_2(e)$. For Hertzian mildly elliptical contact

with geometric curvature, $F_1(e)$ and $F_2(e)$ in Eqs. (2.12) and (2.13) decay slowly from unity as $\sqrt{k_1^h / k_2^h}$ is increased (see Fig. 4.4 in [7]). For Hertzian mildly elliptical contact with mean curvature $\left(\frac{k_2^h}{k_1^h} \to 1^+\right)$, the model is expected to be valid when the principal curvatures are mildly different. Fig. 2.1(b) and 2.1(c) are showing a graphical rendition of a mildly elliptical asperity with geometric and mean curvature respectively.

2.2.4 Cylindrical Contact

Cylindrical contacts are not that commonly used to model rough surface contact; however, in some of the plane-strain and plane-stress applications, for instance-wheel contacts, gear teeth interaction, cylindrical roller bearings, and lubricated gear and cams, cylindrical contact models can predict the behavior well [13]. When a rigid flat is in contact with a cylinder, the contact area is initially a line. That is why cylindrical contact is often referred to as line contact. With the application of force, line contact gradually turns into a rectangle [8]. The same phenomena is observed when two cylinders come into contact, and their axis of symmetry is parallel. A schematic depiction of a cylindrical contact has shown in Fig. 2.1(e). Although the elastic solution of cylindrical contact is often attributed to Hertz, it is not clear who originally derived the solutions. However, Johnson [7] and Hamrock [14] provided explicit solutions for elastic cylindrical contact in their texts. Hamrock provided the following solution to calculate the deflection of an elastic cylindrical contact in his text:

$$\delta = \frac{F}{\pi E' L}\left[ln\left(\frac{4\pi E' RL}{F}\right) - 1\right] \tag{2.20}$$

In the above equation, F is the applied contact force, L is the length of the contact, $E'$is the equivalent elastic modulus, and R is the equivalent radius of curvature. For the plane-strain

condition, Eq. (2.9) can be used to determine the equivalent elastic modulus; however, for the plane-stress condition, Eq. (2.9) needs to be modified into the following form, setting $\upsilon_1 = \upsilon_2 = 0$ [15-16]:

$$\frac{1}{E'} = \frac{1}{E_1} + \frac{1}{E_2} \tag{2.21}$$

The cylindrical contact area can be calculated using the following formula:

$$A=2bL \tag{2.22}$$

According to Johnson [7], the following equation can be used to calculate the contact width:

$$b = \left(\frac{4FR}{\pi LE'}\right)^{1/2} \tag{2.23}$$

The contact pressure at the cylindrical contact is parabolic in shape, maximum at the center point of the contact, and zero at the edge of the contact. The maximum contact pressure at the cylindrical contact can be calculated using the following equation:

$$p_{max} = \frac{2F}{\pi bL} \tag{2.24}$$

2.2.5 Westergaard One-dimensional Wavy Surface Model:

In 1939, Westergaard [4] analyzed the contact of a one-dimensional wavy surface with an elastic half-space for the plane-strain condition. The geometry of the one-dimensional wavy surface is given by:

$$h(x) = \Delta\left(1 + \cos\left(\frac{2\pi x}{\lambda}\right)\right) \tag{2.25}$$

In the above equation, Δ is the amplitude, and λ is the wavelength of the sinusoidal surface. The one-dimensional wavy surface creates a line contact with the flat surface at the beginning of the contact, and with the increase of applied force gradually becomes a strip of width $2a$. The stress distribution within the elastic solids is two-dimensional. Fig. 2.2 is showing the schematic representation of the contact response of the problem analyzed by Westergaard. The contact pressure distribution for such contact can be expressed by the following equation [4]:

$$p(x) = \frac{2\bar{p}\cos(\frac{\pi x}{\lambda})}{sin^2(\frac{\pi a}{\lambda})}\left\{sin^2(\frac{\pi a}{\lambda}) - sin^2(\frac{\pi x}{\lambda})\right\}^{1/2} \tag{2.26}$$

In the above equation, a is the half of the contact width (see Fig. 2.2), $\bar{p}$ is the average nominal pressure and for $|x| \leq a$,

$$\bar{p} = (\pi E'\Delta/\lambda)sin^2(\frac{\pi a}{\lambda}) \tag{2.27}$$

The pressure required to flatten this elastic wavy surface completely is:

$$p^* = \pi E' \frac{\Delta}{\lambda} \tag{2.28}$$

When $\bar{p} \ll p^*$ that is $2a \ll \lambda$, the contact areas are very small and can be treated as isolated contact or asperities. Now if load F is applied on the summit of each asperity, then the average nominal pressure is, $\bar{p} = \frac{F}{\lambda}$. From Eq. (2.2), the radius of curvature of the sinusoidal asperity is:

$$R = \frac{\lambda^2}{4\pi^2\Delta} \tag{2.29}$$

Substituting the value of F and R into the Hertz equation for line contact the contact area is:

$$\frac{2a}{\lambda} = \left(\frac{2}{\pi}\right)\left(\frac{\bar{p}}{p^*}\right)^{1/2} \tag{2.30}$$

Similarly, near the complete contact that is, $\bar{p} \to p^*$ a small strip of width, $2b \ll \lambda$ remains out of contact and can be treated as isolated cracks, which do no interact with each other. The contact area of these non-contact regions can be determined by superimposing two contact problems using the superposition principle of fracture mechanics. One of the problems is if the surface reaches complete contact due to sufficient adhesion where tensile forces are acting at the non-contact region. Another problem is an equal and opposite value of tensile forces, the same as the first problem is acting on the crack surface. Fig. 2.3 shows the decomposition of the nearly complete contact problem into complete contact and pressurized cracks problem. For the Westergaard problem, it is assumed that the following equation of pressure is acting on the crack surface [4]:

$$p(x') \approx 2\pi^2 \left(\frac{x'}{\lambda}\right)^2 p^* - (p^* - \bar{p}) \tag{2.31}$$

where $x' = x - \lambda/2$ and $a \le x \le (\lambda - a)$ and the stress intensity factor at the end of the pressurized crack is [17]:

$$K_I = (\pi b)^{-1/2} \int_{-b}^{b} p(x')\{(b + x')/(b - x')\}^{1/2} dx' \tag{2.32}$$

As the cracks have no strength, the stress intensity factor at the end of the crack will be zero, $K_I = 0$. Using this boundary condition and substituting Eq. (2.31) into Eq. (2.32), the following equation for the non-contact area has been determined [4]:

$$\frac{2b}{\lambda} = \frac{2}{\pi}\left(1 - \frac{\bar{p}}{P^*}\right)^{1/2} \tag{2.33}$$

Subtracting the non-contact area from the contact area, the equation of contact area near complete contact can be determined. The contact area from initial to complete contact can be expressed by the following equation [4]:

$$\frac{2a}{\lambda} = \left(\frac{2}{\pi}\right) sin^{-1}\left(\frac{\bar{p}}{p^*}\right)^{1/2} \tag{2.34}$$

In Eq. (2.34), $2a$ is the real and λ is the apparent area of contact, $\bar{p}$ is the average nominal pressure and p^* is the average pressure at complete contact. Eq. (2.34), when compared with the early contact equation, Eq. (2.30), and near complete contact equation, Eq. (2.33), Eq. (2.34) matched well at the beginning and the end of the contact.

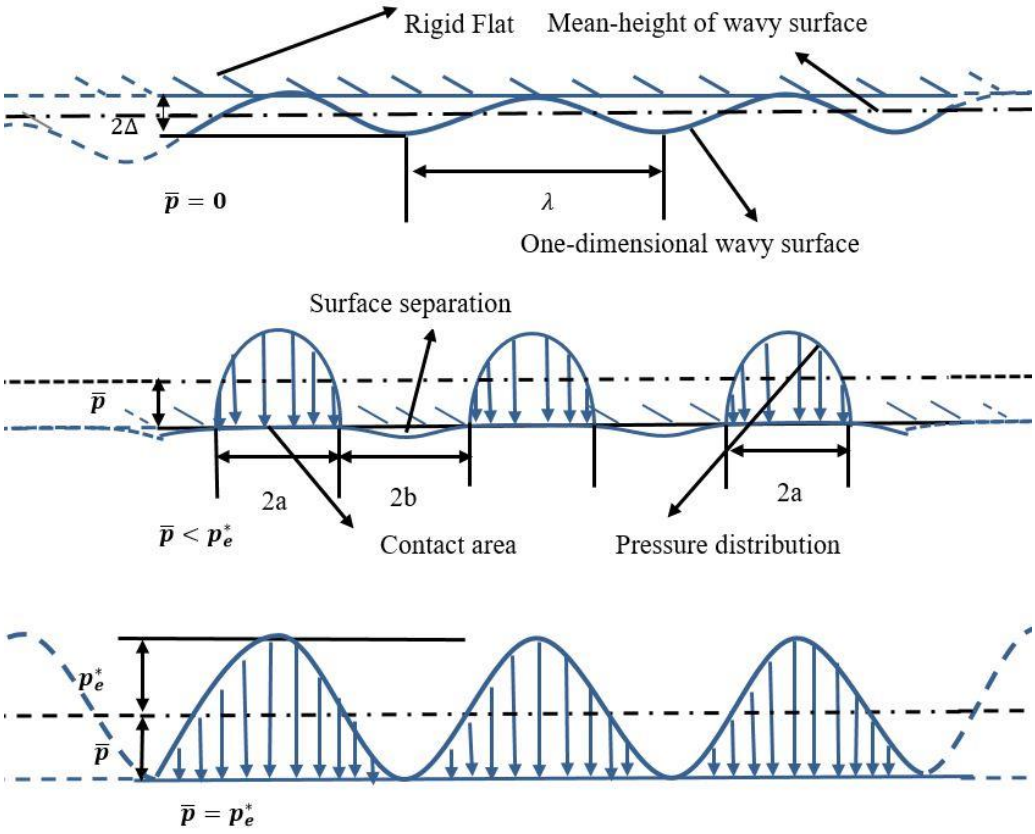

Fig. 2.2 Schematic representation of the contact of a one-dimensional wavy surface with a rigid flat at different contact conditions.

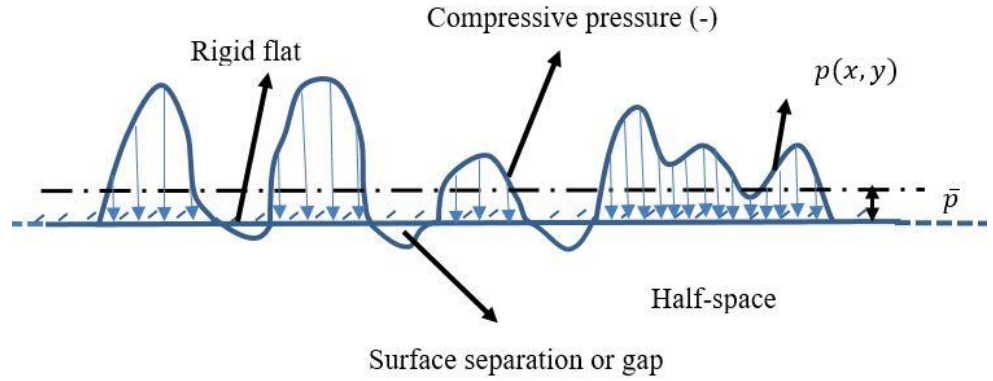

(a)

=

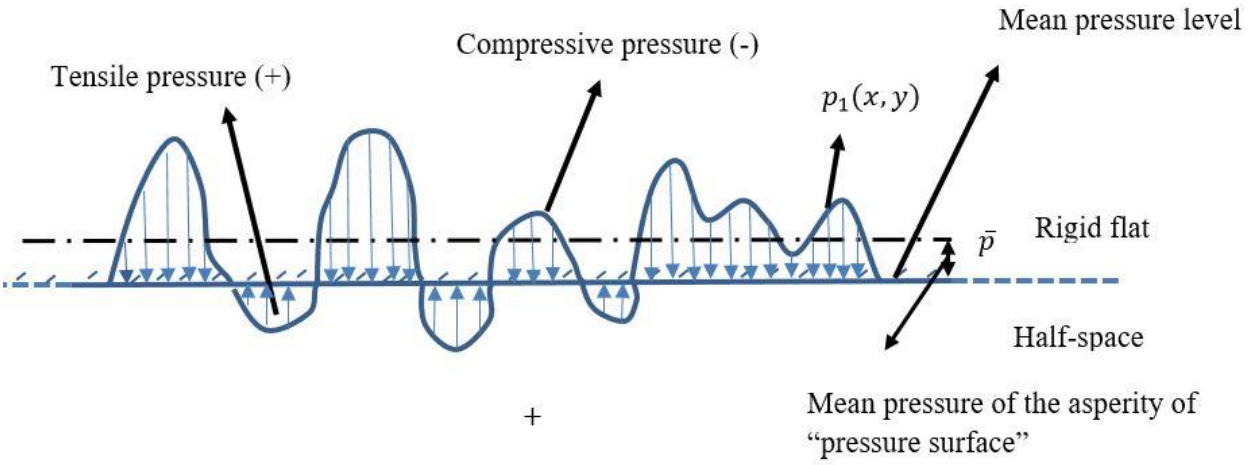

+

(b)

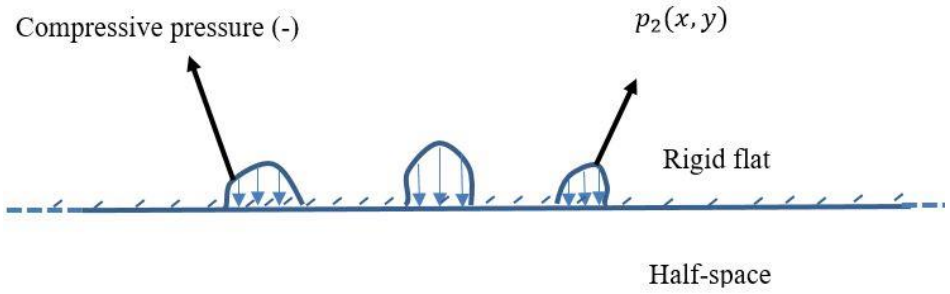

(c)

Fig. 2.3 Schematic representation of the decomposition of (a) partial contact problem into (b) complete contact and (c) pressurized crack problem.

Johnson et al. [5] derived an equation to calculate the change in surface separation for this problem from early contact to complete contact. According to Johnson et al., the change in surface separation can be expressed by the following equation:

$$G = \frac{\bar{g}}{\Delta} = 1 - \frac{\delta'}{\Delta} = 1 - \sum_{i=1}^{n}(A_i/i) \tag{2.35}$$

where, $\bar{g}$ is the current surface separation and Δ is the separation at the beginning of the contact. Johnson et al. used a quadratic programming method to determine A_i, minimizing the complementary energy function (Eq. (1) in [5]). For the same problem, Kuznetsov [18] gave the following expression to calculate the change in surface separation:

$$G = \frac{\bar{g}}{\Delta} = 1 - \left(\frac{\bar{p}}{p^*}\right)\left[1 - ln\left(\frac{\bar{p}}{p^*}\right)\right] \tag{2.36}$$

Johnson et al. [7] showed that Eq. (2.35) and (2.36) matched very well with each other.

2.2.6 Johnson, Greenwood, and Higginson (JGH) Two-dimensional Wavy Surface Problem

Johnson et al. [5, 7] analyzed the contact of a two-dimensional periodic elastic wavy surface in contact with a smooth flat surface. The waviness height is given by the following equation:

$$h(x,y) = \Delta\left(1 - cos\left(\frac{2\pi x}{\lambda}\right)cos\left(\frac{2\pi y}{\lambda}\right)\right) \tag{2.37}$$

The contact pressure distribution within elastic solids is three-dimensional. Change in the shape of contact with contact pressure is complicated (see Fig. 13.4 in [7]). At the beginning of the contact, the contact area is circular, and then gradually turns into the square shape of the contact area, $\frac{\lambda}{\sqrt{2}} \times \frac{\lambda}{\sqrt{2}}$ with the increase of force. That is why it is very difficult to obtain a continuous solution from the early contact to complete contact for this problem. If load *F* is applied on the crest of the wavy

surface, then the average nominal pressure is, $\bar{p} = \frac{2F}{\lambda^2}$ and the radius of curvature at the tip of the asperity is, $R = \frac{\lambda^2}{4\pi^2\Delta}$. Substituting the value of *F* and *R* into the Hertz equation of circular contact, Johnson gave the following asymptotic solution for the early contact of a wavy surface [5]:

$$\frac{A_r}{A_n} = \frac{2\pi a^2}{\lambda^2} = \pi \left\{\frac{3}{8\pi}\frac{\bar{p}}{p^*}\right\}^{2/3} \tag{2.38}$$

In the above equation, A_r is the real contact area, A_n is the nominal contact area and *a* is the contact radius of a single wave. Johnson gave another asymptotic solution for the near-complete contact region, assuming the non-contact region as the pressurized "Penny-shaped" cracks of radius *b*. Therefore, the contact area near the complete contact regime is [5]:

$$\frac{A_r}{A_n} = 1 - \frac{2\pi b^2}{\lambda^2} = 1 - \frac{3}{2\pi}\left\{1 - \frac{\bar{p}}{p^*}\right\} \tag{2.39}$$

For this contact problem, Johnson et al. [5] also gave two asymptotic equations for early contact and near the complete contact, to calculate the change in the surface separation. When $\overline{p} \to 0$, the normalized surface separation between two surfaces is [5]:

$$G = \frac{\bar{g}}{\Delta} = 1 - \frac{1}{2}\left(3\pi^2 \frac{\bar{p}}{p^*}\right)^{\frac{2}{3}} + \left[\left[4\ln\left(\sqrt{2}+1\right)\right]\left(\frac{\bar{p}}{p^*}\right)\right] \tag{2.40}$$

When $\overline{p} \to p^*$, the normalized surface separation is [5]:

$$G = \frac{16}{15\pi^2}\left(\frac{3}{2}\right)^{3/2}\left(1 - \frac{\bar{p}}{p^*}\right)^{5/2} \tag{2.41}$$

In Eq. (2.40) and (2.41), G is the normalized surface separation that is the ratio of current surface separation, $\bar{g}$, and initial surface separation, Δ. The change in surface separation from initial to complete contact can be determined using the following equation [5]:

$$G = 1 - \sqrt{2}\sum_{i=0}^{n}{}_{excluding}\sum_{j=0}^{n}{}_{excluding}\frac{A_{ij}}{(i^2+j^2)^{1/2}} \tag{2.42}$$

Like the one-dimensional wavy surface, for this case Johnson et al. also used a quadratic programming method to determine A_{ij} by minimizing the complementary energy function (Eq. (1) in [5]). Johnson et al. [5] also experimented with two two-dimensional wavy surfaces made of Perspex and Silicon rubber, and the experimental results showed excellent agreement with the numerical results.

2.2.7 Jackson and Streator Two-dimensional Wavy Surface Model

It has been discussed before that Johnson, Greenwood and Higginson (JGH model) [5] developed a model to predict the contact behavior of a two-dimensional wavy surface in contact with a flat surface. Johnson et al. [5] gave asymptotic solutions only for the early and nearly complete contact, although performed an experiment to observe the gradual change in contact behavior from early to the complete contact. Jackson and Streator provided a solution for the whole range by curve fitting to the experimental data collected by Johnson et al. and the solution matches well both with the experiment and asymptotic solutions derived by Johnson et al. The pressure required to completely flatten the two-dimensional wave can be calculated using the following equation [5]:

$$p_e^* = \sqrt{2}\pi E' \frac{\Delta}{\lambda} \tag{2.43}$$

When average contact pressure, $\bar{p} \ll p_e^*$ according to the JGH model,

$$(\bar{A}_{JGH})_1 = \pi\lambda^2 \left[\frac{3}{8\pi}\frac{\bar{p}}{p_e^*}\right]^{2/3} \tag{2.44}$$

when $\overline{p} \gg p_e^*$, according to the JGH model,

$$(\bar{A}_{JGH})_2 = \lambda^2 \left(1 - \frac{3}{2\pi}\left[1 - \frac{\bar{p}}{p_e^*}\right]\right) \tag{2.45}$$

Jackson and Streator [9] provided the following equation linking equation (2.44) and (2.45):

For $\frac{\bar{p}}{p_e^*} < 0.8$,

$$\bar{A} = \left(\bar{A}_{JGH}\right)_1 \left(1 - \left[\frac{\bar{p}}{p_e^*}\right]^{1.51}\right) + (\bar{A}_{JGH})_2 \left[\frac{\bar{p}}{p_e^*}\right]^{1.04} \tag{2.46}$$

For $\frac{\bar{p}}{p_e^*} \geq 0.8$,

$$\bar{A} = \left(\bar{A}_{JGH}\right)_2 \tag{2.47}$$

To observe the change in surface separation with the applied force, Johnson et al. [5] derived asymptotic solutions for this problem that is Eq. (2.40) for the early contact and (2.41) for the nearly complete contact. Rostami and Jackson [19] performed FEA and gave the following equation for the whole range of the contact, which also matches well with the asymptotic solutions derived by Johnson et al. [5] and FEM predictions:

$$G = \left(1 - \sqrt{P_e}\right)^{5/2} \tag{2.48}$$

In the above equation, $P_e = \frac{\bar{p}}{p_e^*}$ and $G = \frac{\bar{g}}{\Delta}$, where $\bar{g}$ is the current surface separation.

2.2.8 Xu Elliptical Crack Model for Nearly Complete Contact

At the beginning of this chapter, it has been discussed that when two surfaces reach complete contact, contact pressure distribution that is the "pressure surface" can be treated in a very similar way as the rough surface. Many researchers before [20-23] have solved the elliptical crack

problem. However, it is Xu et al. [2, 3] who gave an elliptical crack model suitable for the statistical model with different pressure distribution functions. If the asperity of the "pressure surface" can be described using asperity height, ξ^p and principle curvatures, k_1^p and k_2^p where $k_1^p < k_2^p$, then according to Xu [3], the contact area of the elliptical crack can be determined using the following equation:

$$A_i\left(p_0, k_1^p, k_2^p\right) = 3\pi\left(k_g^p\right)^{-1} p_0 F_1(e) \tag{2.49}$$

where

$e = \sqrt{1-\left(\frac{b}{a}\right)^2}$, where e is the eccentricity, b is the semi-minor and a is the semi-major radius of the elliptical crack

$$F_1(e) = 5\left[\frac{3}{2} + \frac{I_{00}^c(e) I_{22}^c(e)}{\Omega(e)} - I_{02}^c(e)\right]^{-1}\left[\sqrt{\frac{k_1^p}{k_2^p}} + \sqrt{\frac{k_2^p}{k_1^p}}(1-e^2)\right]^{-1}, \tag{2.50}$$

$$I_{00}^c(e) = 2\boldsymbol{E}(e),$$

$$I_{22}^c(e) = \begin{cases} \frac{1}{15e^4}\left[(14e^4 + 16e^2 - 16)\boldsymbol{E}(e) + 8(2-e^2)(1-e^2)\boldsymbol{K}(e)\right] & \text{where } e \in (0,1] \\ \frac{\pi}{2} & \text{where } e = 0 \end{cases},$$

$$I_{02}^c(e) = I_{20}^c(e) = \begin{cases} \frac{2}{3e^2}\left[(2-e^2)\boldsymbol{E}(e) - 2(1-e^2)\boldsymbol{K}(e)\right] & \text{where } e \in (0,1] \\ 0 & \text{where } e = 0 \end{cases},$$

$$\frac{k_1^p}{k_2^p} = (1-e^2)\left[(2e^2-1)\boldsymbol{E}(e) + (1-e^2)\boldsymbol{K}(e)\right] / \left[(1+e^2)\boldsymbol{E}(e) - (1-e^2)\boldsymbol{K}(e)\right], \tag{2.51}$$

$$\sqrt{1-e^2} = \exp\left[-0.00681 \times log^2\left(\frac{k_1^p}{k_2^p}\right) + 0.3953 \times \log\left(\frac{k_1^p}{k_2^p}\right)\right], \tag{2.52}$$

$$\Omega = I_{00}^c(e) I_{22}^c(e) - I_{02}^c(e) I_{20}^c(e),$$

$p_0 = \xi^p - \bar{p}$, $\bar{p}$ is the average of the "pressure surface" height

$\boldsymbol{K}(e)$ and $\boldsymbol{E}(e)$ can be determined from Eq. (2.14) and Eq. (2.15) respectively. The volume of the crack or non-contact region can be determined using the following equation:

$$V_i(p_0, k_1^p, k_2^p) = \frac{16\sqrt{3}}{5E'}\left(k_g^p\right)^{-3/2} {p_0}^{5/2} F_2(e) \tag{2.53}$$

where

$$F_2(e) = \frac{5}{2}(1-e^2)^{1/4} F_1(e)^{3/2}\left\{1 - \frac{3}{10}F_1(e)(1-e^2)^{-1/2}\left[\sqrt{\frac{k_1^p}{k_2^p}} + \sqrt{\frac{k_2^p}{k_1^p}}(1-e^2)\right]\right\} \tag{2.54}$$

In Eq. (2.49) and (2.53), k_g^p is the geometric curvature of the "pressure surface" and can be determined in a similar way as described in Eq. (2.4), only instead of superscript *h*, superscript *p* needs to be used that are parameters for the "pressure surface."

2.2.9 Xu "Penny-shaped" Crack for Near Complete Contact

When the semi-major and semi-minor radius of the elliptical crack is almost the same, that is $a \to b$ and $e \to 0$; the elliptical crack becomes like a "Penny-shaped" crack. Therefore, using $k_1^p = k_1^p = k^p$ and $e = 0$, Xu et al. [3] gave the following two equations for the contact area and volume of "Penny-shaped" crack:

$$A_i(p_0, k^p) = 3\pi(k^p)^{-1} p_0 \tag{2.55}$$

$$V_i(p_0, k^p) = \frac{16\sqrt{3}}{5E'}(k^p)^{-3/2} {p_0}^{5/2} \tag{2.56}$$

The curvature of the asperity, k^p of "pressure surface".

2.2.10 Xu Mildly Elliptical Crack with Geometric Curvature/ Mean curvature for Near Complete Contact

The main difference between the elliptical crack and "Penny-shaped" crack contact area and volume is the term $F_1(e)$ and $F_2(e)$. With the decrease of the ratio, $\frac{k_1^p}{k_2^p}$ from unity, values of $F_1(e)$ and $F_2(e)$ gradually deviate from unity. Using the same approximation as used for the Hertzian mildly elliptical contact with geometric curvature/ mean curvature, Xu et al. [3] gave equations for the contact area and volume of the mildly elliptical crack with geometric/ mean curvature. Therefore, the non-contact area and volume for the mildly elliptical crack with geometric/mean curvature can be easily determined by only replacing k^p in Eq. (2.55) and (2.56) by k_g^p from Eq. (2.4) for geometric curvature and k_m^p from Eq. (2.3) for mean curvature.

2.3 Elastic-plastic asperity models

One of the earliest contact mechanics models is the truncation model that has been widely used to predict the fully plastic behavior of the material. Literature traditionally attributes this full plastic truncation model to Abbott and Firestone [24], who never made any suggestions about load or mean pressure. The Abbott and Firestone model was originally developed to describe the wear process rather than the deformation process. Perhaps the truncation model has been extracted unsuitably from the work of Abbott and Firestone. According to the truncation model, the deformation of an asperity against a flat surface is equivalent to the geometrical truncation of the undeformed asperity at its intersection with the flat. So if the flat surface displaces to the asperity by an amount δ or ω, then the contact area of a spherical asperity can be calculated using the following equation:

$$A = 2\pi R\omega \tag{2.57}$$

R is the radius of the curvature of the asperity. Since the contact is assumed to be fully plastic in the truncation model, the contact force can be determined simply by multiplying the contact area by the average contact pressure, that is hardness. Thus the approximated fully plastic contact force is:

$$F = 2\pi R\omega H \tag{2.58}$$

Later experimental [25-27] and many numerical models [28-31] have been developed to improve the prediction of the contact for the elastic-perfectly plastic cases. One of them is the model developed by Chang, Etsion and Boggy (CEB model) which is worth mentioning. Chang et al. [32] approximated an elastic-perfectly plastic contact based on the volume conservation of a certain control volume of plastically deformed asperities. Elastic-perfectly plastic means no hardening is included in the model. In addition, the contact is considered frictionless. According to this model, hardness, $H = 2.8S_y$, suggested by Tabor [33]. However, later research [34-36] shows that the hardness and yield strength relation provided by Tabor is not always true. Besides that, the model cannot predict the elastic-plastic contact behavior as it assumes that the contact is either elastic or fully plastic. Zhao et al. [37] worked on the shortcomings of the CEB model and developed a semi-analytical model interpolating the elastic Hertz model and fully plastic truncation model but was later shown to contain significant pitfalls. Kogut and Etsion [38] developed a more realistic elastic-perfectly plastic model investigating the contact area, force, and average pressure in detail using the Finite Element Method (FEM) and also provided empirical equations for them. However, in their analysis also it was assumed that $H = 2.8S_y$, although the slope of $\frac{\bar{p}}{S_y}$ is not zero at the point where full plasticity is assumed, it was increasing monotonically.

Besides that, the empirical equations provided by Kogut and Etsion are not continuous throughout the contact region, which can cause problems while applying this model to the rough surface contact modeling. Jackson and Green [34] analyzed a similar elastic-perfectly plastic model using FEM. However, several improvements are included, which have made the model applicable for a wide range of elastic-perfectly plastic problems. Later, other elastic-perfectly plastic asperity models [13] have been developed, which will be discussed subsequently.

2.3.1 Jackson-Green (JG) Elastic-perfectly plastic Spherical Asperity Model

One of the important improvements made in the Jackson-Green model (JG model) [34] is that the work clearly showed that Tabor's relation for hardness is not true and provided semi-analytical equations for interference, contact area, and force at the initiation of yielding. Also, empirical equations for hardness to yield strength ratio, contact area, and contact force were developed. Several other improvements were made by Jackson-Green model. One of them is the mesh used in Jackson-Green model is at least an order of magnitude finer than that used by Kogut and Etsion model as necessitated by mesh convergence. JG model is continuous throughout the range of deformation and can predict more than twice deformation magnitude than that predicted by Kogut and Etsion model. Using the equations for stress within the deformed sphere provided by Johnson (resulted from the Hertz solution) [7,34] and von Mises yield criterion, Jackson et al. [34] showed that maximum contact pressure, p_{oc} at the initiation of yielding to the yield strength can be expressed using the following equation [34]:

$$\frac{p_{oc}}{S_y} = C = 1.295\exp(0.736\upsilon) \tag{2.59}$$

Using the Hertz elastic solution, Johnson [7] gave the following equation for interference, ω as a function of p_{oc}:

$$\omega = \left(\frac{\pi p_{oc}}{2E'}\right)^2 R \tag{2.60}$$

Now using Eq. (2.59) in Eq. (2.60), Jackson et al. obtained the following solution for critical interference:

$$\omega_c = \left(\frac{\pi C S_y}{2E'}\right)^2 R \tag{2.61}$$

Substituting Eq. (2.61), into the equation of Hertz circular contact area and force, the following equations for contact area and contact force at the initiation of yielding can be determined:

$$A_c = \pi^3 \left(\frac{C S_y R}{2E'}\right)^2 \tag{2.62}$$

$$F_c = \frac{4}{3}\left(\frac{R}{E'}\right)^2 \left(\frac{C}{2}\pi S_y\right)^3 \tag{2.63}$$

To make the solutions applicable for both macro and microcontact, Jackson et al. normalized all the parameters used for the analysis. Displacement, contact area, and contact force have been normalized by Eq. (2.61), (2.62) and (2.63) respectively as,

$$A^* = {A}/{A_c}, F^* = {F}/{F_c}, \omega^* = {\omega}/{\omega_c} \tag{2.64}$$

According to the Jackson-Green model, when the contact is effectively elastic ($0 \leq \omega^* \leq 1.9$) the normalized contact area and force from Hertz contact can be simplified to,

$$A^* = \omega^*, F^* = (\omega^*)^{3/2} \tag{2.65}$$

Eq. (2.65) is actually the Hertz model; the only change that is made is Eq. (2.65) has been expressed into normalized form. Once the initial yielding becomes significant ($1.9 \leq \omega^*$) the formula for normalized contact area and contact force can be expressed by the following equations:

$$A^* = \omega^* \left(\frac{\omega^*}{1.9}\right)^B \tag{2.66}$$

$$B = 0.14\exp\left(23.\frac{S_y}{E'}\right)$$

$$F^* = \left[exp\left(-\frac{1}{4}(\omega^*)^{\frac{5}{12}}\right)\right](\omega^*)^{3/2} + \frac{4H}{CSy}\left[1 - exp\left(-\frac{1}{25}(\omega^*)^{\frac{5}{9}}\right)\right]\omega^* \tag{2.67}$$

$\frac{H}{S_y}$ in the above equation can be expressed by the following equation,

$$\frac{H}{S_y} = 2.84 - \left(1 - exp\left(-0.82\left(\frac{a}{R}\right)^{-0.7}\right)\right) \tag{2.68}$$

In the above equation, *a* is the contact radius. This equation clearly shows that $\frac{H}{S_y}$ is not a constant ratio and changes continuously with $\frac{a}{R}$ which can be calculated using the following equation:

$$\frac{a}{R} = \frac{\pi C S_y}{2E'}\left[\omega^* \left(\frac{\omega^*}{1.9}\right)^B\right]^{1/2} \tag{2.69}$$

Eq. (2.69) is only applicable when $\omega^* \geq 1.9$ and Eq. (2.68) is valid only when $0 < \frac{a}{R} \leq 0.412$. However, during elastic-plastic rough surface modeling, the $\frac{a}{R}$ ratio for an asperity may exceed the value 0.412. For such cases, Jackson, Green and Marghitu [39] modified the Eq. (2.68) and provided the following equation which is valid from $0 < \frac{a}{R} < 1$:

$$\left(\frac{H_G}{S_y}\right) = 2.84 - 0.92\left(1 - cos\left(\pi\frac{a}{R}\right)\right) \tag{2.70}$$

Jackson-Green model was also compared with the test performed by Johnson [7] and Chaudhuri et al. [40], the predictions of the Jackson-Green model compared well with the experimental results. Quicksall et al. [41] performed a detail investigation for the same model for a wide range

of metallic materials by varying Young's modulus, E, yield strength, S_y and Poisson ratio, υ and concluded that the previously developed Jackson-Green and Kogut-Etsion model give fairly good prediction as the models compared well with the detail parametric study performed by them.

2.3.2 Wadwalkar, Jackson and Kogut Elastic-perfectly plastic Heavily Deformed Spherical Contact

Although Jackson, Green and Marghitu [39] provided an equation for large $\frac{a}{R}$ ratio value, JG model does not consider the change in the radius of curvature of the asperity with deformation. Therefore, for the heavily deformed spherical contact cases, JG spherical contact model [34] must needs to be modified. Wadwalkar et al. [42] improved this limitation, performing FEA, and developing analytical equations. To consider the change in radius of curvature due to geometry deformation, the volume conservation approach is adopted in their work for an elastic-perfectly plastic axisymmetric sphere in contact with a rigid flat. To develop a fully plastic spherical flattening model, two different boundary conditions have considered during the modeling, namely the deformable base case where the base of the sphere is allowed to move in the radial direction but is held stationary in the direction perpendicular to the base, and the rigid base case where the base of the sphere is fixed in all directions. Fig. 2.4 is showing the schematic representation of two such cases. The first case is equivalent to the case where a sphere is being compressed between two parallel surfaces and can be applied to the study of the flattening of wear debris, an anisotropic conductive film with metallic particles dispersed within, etc. [43-44] and the second case can be applied to model a stiffer rough surface [42]. There is not that much difference between these two cases at the beginning of the contact, that is $a \ll R$; however, with deformation, they gradually diverge from each other. Applying the conservation of volume, for the first boundary condition the following equation for radius of curvature is obtained [42]:

$$R_1 = \sqrt{\frac{2R^3}{3(R-\omega)} + \frac{(R-\omega)^2}{3}} \tag{2.71}$$

and for the second boundary condition, the radius of curvature is [42]:

$$R_2 = \sqrt{\frac{R^3}{\delta(R-\omega)} - \frac{a^2}{2}} \tag{2.72}$$

In Eq. (2.71) and (2.72), R is the initial radius of curvature, and δ is a constant that equals 0.76. Then using the radius of curvature equation, the following contact area equations for these two boundary conditions are formulated by Wadwalker et al. [42]:

For the deformable base,

$$\left(\frac{a}{R}\right)_{new} = \left(\frac{a}{R}\right)_{JG} + A_1\left(\frac{\omega}{\omega_c}\right)^2 - A_2\left(\frac{\omega}{\omega_c}\right) \tag{2.73}$$

In the above equation, $A_1 = 0.0826\left(\frac{S_y}{E'}\right)^{3.148}$ and $A_2 = 0.3805\left(\frac{S_y}{E'}\right)^{1.545}$

For the rigid base,

$$\left(\frac{a}{R}\right)_{new} = \left(\frac{a}{R}\right)_{JG} - A_3\left(\frac{\omega}{\omega_c}\right)^2 - A_4\left(\frac{\omega}{\omega_c}\right) \tag{2.74}$$

In the above equation, $A_3 = 158393\left(\frac{S_y}{E'}\right)^{5.605}$ and $A_2 = 0.0034\left(\frac{S_y}{E'}\right)^{0.8939}$

Contact pressure in the fully plastic regime or the hardness to yield strength ratio, $\frac{p}{S_y}$ or $\frac{H}{S_y}$ can be determined by substituting the R_1 and R_2 value from Eq. (2.71) and (2.72) to Eq. (2.70). For both boundary conditions, the following equation is developed for contact force [42]:

$$\frac{F}{F_c} = \left\{exp\left[-\frac{1}{4}\left(\frac{\omega}{\omega_c}\right)^{5/12}\right]\right\}\left(\frac{\omega}{\omega_c}\right)^{3/2} + \frac{p}{F_c}\pi R^2\left(\frac{a}{R}\right)^2_{new}\left\{1 - exp\left[-\frac{1}{25}\left(\frac{\omega}{\omega_c}\right)^{5/9}\right]\right\} \tag{2.75}$$

The analytical equations developed by Wadwalkar et al. [42] were also compared with the FEA result, and the experiment performed by Chaudhuri et al. [40]. Very good agreement is found with all the results.

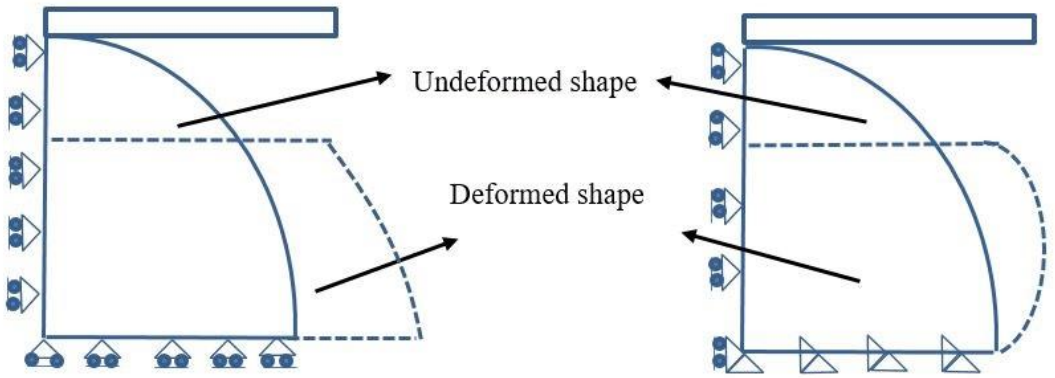

(a) (b)

Fig. 2.4 Schematic representation of spherical flattening (a) for the deformable base (b) for the rigid base.

2.3.3 Elastic-plastic Cylindrical Contact

Very few works have been done on the elastic-plastic cylindrical contact [15-16, 45-49]. Although some of them analyzed contact behavior using FEM, very few of them provided analytical or empirical equations to predict the behavior of elastic-plastic cylindrical contact. Using the equation of stress resulted from the Hertz equation and provided by Johnson [7] and using the von Mises yield criterion, Green [49] derived the following equations to predict the interference, contact area, and force for the cylindrical contact at the initiation of yielding:

$$\delta_c = R\left(\frac{C_1 S_y}{E'}\right)^2 \left[2ln\left(\frac{2E'}{C_1 S_y}\right) - 1\right] \tag{2.76}$$

$$\frac{F_c}{L} = \pi R \frac{\left(C_1 S_y\right)^2}{E'} \tag{2.77}$$

$$A_c = 4LR\frac{C_1 S_y}{E'} \tag{2.78}$$

In Eq. (2.76), (2.77) and (2.78), S_y is typically assumed to equal the yield strength of the material with the lower value of S_y. For the plane stress condition, $C_1 = 1$, and for the plane strain condition,

$$C_1 = \frac{1}{\sqrt{1+4(\upsilon-1)\upsilon}}, \qquad \upsilon \leq 0.1938 \tag{2.79}$$

$$C_1 = 1.164 + 2.975\upsilon - 2.906\upsilon^2, \ \upsilon > 0.1938 \tag{2.80}$$

Recently, Sharma and Jackson [15-16] analyzed the elastic-plastic cylindrical contact for a wide range of material properties and plane-stress conditions. Analyzing the FEM results, Sharma et al. [15] provided the following equations to predict the contact area when the material model includes only 1% bilinear hardening:

$$\frac{A}{A_{Hertz}} = 2\left(\frac{F}{F_c}\right)^{5/18} - 1 \tag{2.81}$$

$$\frac{A}{A_{Hertz}} = 4.8\left(\frac{S_y}{E'}\right)^{-1/25}\left(\frac{\delta}{\delta_c}\right)^{0.106} - 4.8\left(\frac{S_y}{E'}\right)^{-\frac{1}{25}} + 1 \tag{2.82}$$

The above two equations are valid when half-width of the contact to the initial radius of the cylinder ratio, $b/R < 0.4$.

To analyze the effect of different amounts of hardening and material properties, Sharma et al. [16] provided the following equation for the effective yield strength:

$$S_e = S_y + 0.4E_t\left(\frac{\delta-\delta_c}{R}\right)^{0.62\left(\frac{E_t}{E}\right)^{0.09}} \tag{2.83}$$

In the above equation, S_y is the virgin yield strength and $E_t$is the tangential modulus. The equation can be used for all the analyzed cases except when $E_t \leq 0.0001E$. The half contact width, b can be calculated as a function of applied force, F from the following equation:

$$\frac{b}{b_{Hertz}} = \left(\frac{F}{F_c}\right)^{0.463} \tag{2.84}$$

During the calculation of F_c for the above equation, effective yield strength needs to be used in Eq. (2.77) to account for variations in hardening and b_{Hertz} can be calculated from Eq. (2.23). However, to predict the initiation of yielding, virgin yield strength has to be used in Eq. (2.76)-(2.78). The half contact width, b as a function of applied displacement, ω is given by the following formula:

$$\frac{b}{b_{Hertz}} = 7.1\left(\frac{E'}{S_e}\right)^{0.01}\left[\left(\frac{\omega}{\omega_c}\right)^{0.1} - 1\right] + 1 \tag{2.85}$$

In the above equation also, during the calculation of ω_c, effective yield strength has to be used. Eq. (2.84) and (2.85) are applicable when $\frac{b}{R} \leq 0.5$. During the curve fitting of Eq. (2.85), the cases that are effectively in the elastic regime $\left(\frac{\omega}{\omega_c} < 2\right)$ has been omitted. The equations should only be used in the range of material properties $\left(0.001 \leq \frac{S_y}{E} \leq 0.128, 0.0001E \leq E_t \leq 0.1E\right)$ and deformations considered in this work. Average contact pressure normalized by the yield strength has also been analyzed as a function of normalized contact half-width in [49], however, no empirical equation has been provided. Their analysis shows that, maximum value of $\frac{\bar{P}}{S_y}$ ratio varies from 1.8 to 2 with the change in $\frac{b}{R}$ ratio. Cinar and Sinclair [50] found that, for the cylindrical contact at the plane-strain condition, hardness or pressure was approximately $2.24S_y$. Therefore

both for the plane strain and plane stress condition of the cylindrical contact, hardness to yield strength ratio is a lot smaller than spherical case. Using slip-line theory, recently Jackson [51] provided the following equation for $\frac{\bar{p}}{S_y}$ for the case of indentation of a rigid cylinder into a flat surafce where $\bar{p}$ is the average pressure during fully plastic plane strain contact.

$$\frac{\bar{p}}{S_y} = \frac{F}{2bLS_y}$$

$$= \frac{1}{2\sqrt{3}}\left(\frac{b}{R}\right)^{-1}\left[\begin{matrix}\frac{\pi^2}{4} + \pi - \left(cos^{-1}\left(\frac{b}{R}\right)\right)^2 - 2cos^{-1}\left(\frac{b}{R}\right) \\ + \left\{cos^{-1}\left(\frac{b}{R}\right) + 1\right\}\sin\left(2cos^{-1}\left(\frac{b}{R}\right)\right) + \left(\frac{b}{R}\right)^2\end{matrix}\right] \quad (2.86)$$

2.3.4 Gao et al. Elastic-perfectly plastic Sinusoidal Surface Model for 2D Plain Strain

Inspired by the fractal rough surface model developed by Ciavarella [52], and using Westergaard wavy surface model for 2D elastic plain strain [4], Gao et al. [53] performed a detailed analysis of the contact between a 2D elastic-perfectly plastic sinusoidal asperity and a rigid flat for the plane strain case. The work gives a broader look of the elastic-plastic contact behavior for a wide range of material properties and surface roughness. According to their analysis, two parameters: $\alpha = \frac{a}{\lambda}$, where a is the contact area and λ is the wavelength of the sinusoidal asperity and $\psi = \frac{E'}{S_y}\frac{\Delta}{\lambda}$ can be used to characterize the behavior of contact deformation. Analyzing the results based on these two parameters, it has been concluded in the paper that there are eight general types of behavior for the asperity contacts: elastic, elastic-plastic or fully plastic isolated Hertz type contacts; elastic or elastic-plastic non-Hertzian isolated contact; elastic, elastic-plastic or fully plastic, interacting contacts. Change in mean asperity contact pressure, contact pressure to yield strength ratio, residual stress in these eight-contact regions with indentation depth, contact fraction, and ψ have

also been observed for different material properties and loading conditions. Like the Jackson-Green model, their analysis shows that the hardness to yield strength ratio is not a constant as suggested by Tabor and also shows that depending on the material properties, geometry, and loading condition, the ratio may increase up to around 5.6. Curve fitting the FEA results, they provided empirical equations for contact pressure distribution, contact size, the total area of contact, number of contacts and average pressure to yield strength ratio [54].

2.3.5 Manner rigid-perfectly plastic sinusoidal surface model

Manner [35] theoretically analyzed the flattening of a sinusoidal wavy surface using rigid-perfectly plastic material behavior. Rigid-perfectly plastic means the effect of elastic behavior or elastic-plastic interaction has been neglected; only fully plastic behavior has been considered during material modeling. Both the mechanisms for isolated and interacting contacts have been investigated. In this work, analysis using rigid-perfectly plastic modeling has been defined as upper bound analysis and analysis employing perfectly elastic modeling has been defined as lower bound analysis. Although in this work, the contact behavior has been analyzed using the upper bound analysis; however, to check the upper limit of the pressure to yield strength ratio, both upper and lower bound analysis have been done. From the upper bound analysis, Manner provided the following formula for average and mean contact pressure:

$$\bar{p} = k\left(2 - \frac{2a}{\lambda}\right)\left[\frac{d}{\left(1-\frac{2a}{\lambda}\right)} - \frac{\frac{2a}{\lambda}}{d}\right] \tag{2.87}$$

$$p_m = \frac{2k\left(2-\frac{2a}{\lambda}\right)}{\sqrt{\frac{2a}{\lambda}\left(1-\frac{2a}{\lambda}\right)}} \tag{2.88}$$

When $d = \sqrt{\frac{2a}{\lambda}\left(1 - \frac{2a}{\lambda}\right)}$, Eq. (2.87) becomes maximum,

$$\bar{p} = k\left(2 - \frac{2a}{\lambda}\right)\left[\frac{\frac{2a}{\lambda}}{\left(1-\frac{2a}{\lambda}\right)}\right] \tag{2.89}$$

Both Eq. (2.88) and (2.89) show that, with the increase of contact area fraction, $\bar{p}$ and p_m gradually increases, and at complete contact when $2a = \lambda$, they become infinite. k is the shear yield stress. Performing a lower bound analysis for an axisymmetric cylinder, Manner showed that for the lower bound analysis also average pressure can become infinite and concluded that elastic-plastic interaction and boundary conditions are the most possible reason of the finite value of pressure to yield strength ratio for the cases analyzed by Gao et al. [53].

2.3.6 Krithivasan and Jackson 3D Elastic-perfectly plastic Sinusoidal Asperity Model

Krithivasan and Jackson [55] analyzed the contact of a 3D elastic-perfectly plastic wavy surface in contact with a rigid flat. The geometry of this problem is similar to that used by Johnson, Greenwood, and Higginson model [5] for the elastic wavy surface contact modeling; however, the material model is elastic-perfectly plastic. To analyze the contact behavior and to formulate empirical equations, a parametric study has been performed in their work varying Young's modulus from 150 GPa to 350 GPa, yield strength from 0.75 GPa to 2.25 GPa and amplitude to wavelength ratios of the sinusoidal asperity, $\frac{\Delta}{\lambda}$, from 0.01 to 0.04. The range of parametric analysis was limited to the mentioned range due to convergence difficulties at higher values of $\frac{\Delta}{\lambda}$ ratios. Analyzing all the results, empirical equations have been formulated for average contact pressure at complete contact and contact area from early contact all the way up to complete contact. Later, Jackson et al. [34] derived an equation for the critical value of amplitude below which a wavy surface will behave elastically over the entire range of contact using the analytical solution for stress derived by Tripp et al. [56] and the von Mises yield criterion. However, recently a

discrepancy was found in the equation provided by Jackson et al. for the critical value of amplitude. Ghaednia et al. [13] has corrected the equation for the critical value of amplitude and extended the analysis performed by Krithivasan et al. [55] for a broader range of material properties and surface roughness. In the extended model, yield strength is varied from 0.1 GPa to 2.5 GPa, Young's modulus varied from 50 GPa to 400 GPa, Poisson ratio varied from 0.01 to 0.49 and the amplitude to wavelength ratio is considered over the range of $\frac{\Delta}{\lambda}$ from 0.001 to 0.05. At the beginning of the contact, spherical and sinusoidal asperities behave in a very similar way. Hence, the equations formulated by the Jackson-Green model to determine the interference, contact area, and force during the initiation of yielding can be modified for sinusoidal asperity contact using the radius of curvature of a sinusoidal asperity. Now substituting the equation of radius of curvature at the tip of a 3D sinusoidal asperity, $R = \frac{\lambda^2}{4\pi^2\Delta}$ into Eq. (2.61)-(2.63), the following equations for critical interference, contact area and force for 3D sinusoidal contact can be obtained:

$$\omega_c = \left(\frac{\pi C S_y}{2E'}\right)^2 \frac{\lambda^2}{4\pi^2\Delta} \tag{2.90}$$

C is the same as used in the Jackson-Green model (see Eq. (2.59)).

$$A_c = \frac{2}{\pi}\left(\frac{C S_y \lambda^2}{8\Delta E'}\right)^2 \tag{2.91}$$

$$F_c = \frac{1}{6\pi}\left(\frac{\lambda^2}{\Delta E'}\right)^2 \left(\frac{C}{2} S_y\right)^3 \tag{2.92}$$

According to the modified model, the critical value of amplitude can be expressed by the following equation [13]:

$$\Delta_c = \frac{\sqrt{2} S_y \lambda}{\pi E' \left[3e^{-2(\upsilon+1)/3} + 2\left(\frac{1-2\upsilon}{1-\upsilon}\right)\right]} \tag{2.93}$$

Using the above equation instead of using the equation provided in [36], a new equation for average contact pressure required to react at complete contact for the elastic-perfectly plastic case has been obtained as [13]:

$$\frac{p_{ep}^*}{p_e^*} = 0.992\left[\left\{\left(\frac{\Delta}{\Delta_c}\right)^{\left(\frac{10}{3}\left(\frac{\Delta}{\Delta_c}\right)^{-0.39}+\frac{9}{4}\upsilon^4+0.64\right)}\right\}^{-1}\right] \tag{2.94}$$

In the above equation, when $\Delta = \Delta_c$, $p_{ep}^* = p_e^*$ and the pressure required to reach complete contact for the elastic-plastic case cannot be greater than the elastic case. Therefore, when $\Delta \leq \Delta_c$, all the cases become elastic. Using Eq. (2.80) and (2.81), the modified model obtained the following equation for contact area [13]:

$$A = A_p\left[1-\left(\frac{\bar{p}}{p_{ep}^*}\right)^{1.51}\right] + \left(A_{JGH}\right)_2\left(\frac{\bar{p}}{p_{ep}^*}\right)^{1.04} \tag{2.95}$$

where

$$A_p = 2\left(\frac{A_c}{2}\right)^{\frac{1}{(1+d)}}\left(\frac{3\bar{p}\lambda^2}{4C_2S_y}\right)^{\frac{d}{(1+d)}} \tag{2.96}$$

$$d = 3.8\left(\frac{E'}{S_y}\frac{\Delta}{\lambda}\right)^{0.11} \tag{2.97}$$

$$(A_{JGH})_2 = \lambda^2\left(1-\frac{3}{2\pi}\left[1-\frac{\bar{p}}{p_{ep}^*}\right]\right) \tag{2.98}$$

For the same contact problem, Rostami and Jackson [19] provided the following equations to predict the change in surface separation as a function of contact pressure from early contact to the complete contact:

$$G = \left(1 - \left(p_{ep}\right)^{A_1 P_{ep} + A_2}\right)^{5/2} \tag{2.99}$$

where

$$A_1 = -0.08 ln(B^*)$$

$$A_2 = \frac{1}{15}(B^* - 1)^{0.44} + 0.99^{0.41(B^* - 1)} - \frac{1}{2}$$

In Eq. (2.99), $p_{ep} = \frac{\bar{p}}{p^*_{ep}}$, $B^* = \frac{B}{B_c}$, and $B = \frac{\Delta}{\lambda}$.

2.3.7 Axisymmetric Sinusoidal Asperity Model

Liu, and Liu and Proudhon studied axisymmetric sinusoidal asperity in contact with a rigid flat with linear strain hardening [57] and power-law hardening [58]. In [57], aspect ratios of the sinusoidal asperity were varied; however, the analysis was performed only for gold. An equation for the contact area modifying the truncation model and contact pressure to yield strength ratio has also been provided. However, as the analysis did not consider the change in material properties, the derived equations work only for gold and a narrow range of surface roughness which will be shown later in Chapter 3. Besides that, a large domain has been considered around the axisymmetric sinusoidal asperity, which reduces the asperity interaction effect in the model. In another study of Liu et al. [58], the ratio of yield strength to Young's modulus ratio was varied; however, the asperity aspect ratio was held constant at 0.1. No empirical equation was derived in that work; although, the work showed the effect of the variation of yield strength to Young's modulus ratio on the evolution of contact deformation. It has been shown later in Chapter 3 that elastic-plastic contact deformation is not only a function of material properties or surface

roughness, rather a combined effect of surface roughness and material properties govern the whole contact behavior.

2.4 Summary

A comprehensive literature review has been performed on elastic and elastic-plastic asperity models in this chapter. The literature review shows that:

- Elastic asperity models for elliptical or mildly elliptical contact is available; however, only for the early contact and near the complete contact. No elliptical or mildly-elliptical contact models are available for the whole range of contact.
- Details investigation has been done on the spherical asperity model with circular contact. Empirical equations are available for the contact area and force for the early contact, average pressure or hardness to yield strength ratio, which should be useful in rough surface modeling. Besides these, complete spherical flattening, change in radius of curvature with the geometric deformation, change in hardness to yield strength ratio for heavily deformed spherical asperities at different boundary conditions have also been analyzed, which should be helpful to model particle flattening modeling and so on.
- Cylindrical contacts are generally not used for rough surface contact modeling. However, there are many plane strain and plane stress cases for example, wheel-road contacts, cylindrical roller bearings, lubricated gear and cams, and so on where cylindrical contact modeling should be very useful. Empirical equations to analyze elastic cylindrical contact and to predict the initiation of yielding are available. Detail investigation has been done and empirical equations have been formulated for elastic-plastic cylindrical contact (plane stress boundary conditions) for wide range of material properties, hardening and loading

conditions. Analysis has also been performed on how the average pressure to yield strength ratio changes for the plane strain and plane stress boundary conditions.

- Research has been done on 2D elastic and elastic-perfectly plastic plane-strain wavy asperity. Empirical equations to predict the elastic contact behavior are available for the whole range of contact. A detailed investigation has been done on the elastic-perfectly plastic contact and the parameters that control the contact behavior; however, no empirical equations are provided for the elastic-perfectly plastic case. Like the spherical asperity model, the 2D plane strain sinusoidal asperity case also shows that hardness to yield strength ratio is not a constant, and rise continuously with the increase in the contact area.
- A detailed examination has also been done on the 3D elastic and elastic-perfectly plastic sinusoidal asperity contact. Empirical equations to predict the contact area, pressure, and surface separation, as a function of contact pressure are available both for the elastic and elastic-perfectly plastic cases. An empirical equation has also been provided for the critical value of amplitude below which an asperity will deform elastically from initial to complete contact.
- Analysis has been done on the axisymmetric sinusoidal asperity model with hardening; however, none of the analysis gives a clear idea about which parameters are controlling the contact behavior. Empirical equations are available for contact area, and average pressure to yield strength ratio, although their application is limited as the analysis did not perform a thorough investigation of the material properties, surface roughness, and their combined effect on the evolution of the contact behavior.

Reference

1. Keer, L. M. (2013). History of contact mechanics. Encyclopedia Tribol., 1682-4.
2. Xu, Y., Jackson, R. L., & Marghitu, D. B. (2014). Statistical model of nearly complete elastic rough surface contact. International Journal of Solids and Structures, 51(5), 1075-1088.
3. Xu, Y. (2017). Statistical Models of Nominally Flat Rough Surface Contact. Doctoral dissertation, Auburn University.
4. Westergaard, H. M. (1939). Bearing pressures and cracks. Trans AIME, J. Appl. Mech., 6, 49-53.
5. Johnson, K. L., Greenwood, J. A., & Higginson, J. G. (1985). The contact of elastic regular wavy surfaces. International journal of mechanical sciences, 27(6), 383-396.
6. Hertz, H., Jones, D. E., & Schott, G. A. (1896). Miscellaneous papers. Macmillan and Company.
7. Johnson, K. L., & Johnson, K. L. (1987). Contact mechanics. Cambridge university press.
8. Jackson, R. L., Ghaednia, H., Lee, H., Rostami, A., & Wang, X. (2013). Contact mechanics. In Tribology for scientists and engineers (pp. 93-140). Springer, New York, NY.
9. Jackson, R. L., & Streator, J. L. (2006). A multi-scale model for contact between rough surfaces. Wear, 261(11-12), 1337-1347.
10. Nayak, P. R. (1971). Random process model of rough surfaces. J. of Lubrication Tech., 93(3), 398-407.
11. Greenwood, J. A. (2006). A simplified elliptic model of rough surface contact. Wear, 261(2), 191-200.

12. Stanley, H. M., & Kato, T. (1997). An FFT-based method for rough surface contact. J. Tribol., 119(3), 481-485.
13. Ghaednia, H., Wang, X., Saha, S., Xu, Y., Sharma, A., & Jackson, R. L. (2017). A review of elastic–plastic contact mechanics. Applied Mechanics Reviews, 69(6), 060804.
14. Hamrock, B. J. (1994). Fundamentals of Fluid Film Lubrication McGraw-Hill. Inc. Hightstown, NJ, 8520.
15. Sharma, A., & Jackson, R. L. (2016). A finite element study of elasto-plastic cylindrical contact against a rigid flat. In STLE Annual Meeting, Las Vegas, NV, May (pp. 15-19).
16. Sharma, A., & Jackson, R. L. (2017). A finite element study of an elasto-plastic disk or cylindrical contact against a rigid flat in plane stress with bilinear hardening. Tribology Letters, 65(3), 112.
17. Paris, P. C., & Sih, G. C. (1965). Stress analysis of cracks. In Fracture toughness testing and its applications, edited by ASTM Committee E-24 (West Conshohocken, PA: ASTM International), 30-81.
18. Kuznetsov, Y. A. (1978). A periodic contact problem accounting for the additional load acting beyond the indenter. Izv. Acad. Nauk SSSR, Mekh. Tverd. Tela, 6(35), 44.
19. Rostami, A., & Jackson, R. L. (2013). Predictions of the average surface separation and stiffness between contacting elastic and elastic–plastic sinusoidal surfaces. Proceedings of the Institution of Mechanical Engineers, Part J: Journal of Engineering Tribology, 227(12), 1376-1385.
20. Kassir, M. K., & Sih, G. C. (1967). Griffith's theory of brittle fracture in three dimensions. International Journal of Engineering Science, 5(12), 899-918.

21. Shah, R. C., & Kobayashi, A. S. (1971). Stress intensity factor for an elliptical crack under arbitrary normal loading. Engineering Fracture Mechanics, 3(1), 71-96.
22. Sneddon, I. N. (1979). The stress intensity factor for a flat elliptical crack in an elastic solid under uniform tension. International Journal of Engineering Science, 17(2), 185-191.
23. Martin, P. A. (1986). Orthogonal polynomial solutions for elliptical cracks under shear loadings. The Quarterly Journal of Mechanics and Applied Mathematics, 39(4), 519-534.
24. Abbott, E. J., & Firestone, F. A. (1995). Specifying surface quality: a method based on accurate measurement and comparison. Spie Milestone Series MS, 107, 63-63.
25. Davis, J. R. (1988). Metal Handbook. Metal park.
26. Francis, H. A. (1976). Phenomenological analysis of plastic spherical indentation. J. Eng. Mater. Technol., 98(3), 272-281.
27. Oliver, W. C., & Pharr, G. M. (1992). An improved technique for determining hardness and elastic modulus using load and displacement sensing indentation experiments. Journal of materials research, 7(6), 1564-1583.
28. Mesarovic, S. D., & Fleck, N. A. (2000). Frictionless indentation of dissimilar elastic–plastic spheres. International Journal of Solids and Structures, 37(46-47), 7071-7091.
29. Kral, E. R., Komvopoulos, K., & Bogy, D. B. (1993). Elastic-plastic finite element analysis of repeated indentation of a half-space by a rigid sphere. J. Appl. Mech., 60(4), 829-841.
30. Kral, E. R., Komvopoulos, K., & Bogy, D. B. (1995). Finite element analysis of repeated indentation of an elastic-plastic layered medium by a rigid sphere, Part II: Subsurface results. J. Appl. Mech., 62(1), 29-42.
31. Streator, J. L. (2003). Dynamic contact of a rigid sphere with an elastic half-space: a numerical simulation. J. Trib., 125(1), 25-32.

32. Chang, W. R., Etsion, I., & Bogy, D. B. (1987). An elastic-plastic model for the contact of rough surfaces. J. Tribol., 109(2), 257-263.
33. Tabor, D. (2000). The hardness of metals. Oxford university press.
34. Jackson, R. L., & Green, I. (2005). A finite element study of elasto-plastic hemispherical contact against a rigid flat. J. Trib., 127(2), 343-354.
35. Manners, W. (2008). Plastic deformation of a sinusoidal surface. Wear, 264(1-2), 60-68.
36. Jackson, R. L., Krithivasan, V., & Wilson, W. E. (2008). The pressure to cause complete contact between elastic—plastic sinusoidal surfaces. Proceedings of the Institution of Mechanical Engineers, Part J: Journal of Engineering Tribology, 222(7), 857-863.
37. Zhao, Y., Maietta, D. M., & Chang, L. (2000). An asperity microcontact model incorporating the transition from elastic deformation to fully plastic flow. J. Trib., 122(1), 86-93.
38. Kogut, L., & Etsion, I. (2002). Elastic-plastic contact analysis of a sphere and a rigid flat. J. Appl. Mech., 69(5), 657-662.
39. Jackson, R. L., Green, I., & Marghitu, D. B. (2010). Predicting the coefficient of restitution of impacting elastic-perfectly plastic spheres. Nonlinear Dynamics, 60(3), 217-229.
40. Chaudhri, M. M., Hutchings, I. M., & Makin, P. L. (1984). Plastic compression of spheres. Philosophical Magazine A, 49(4), 493-503.
41. Quicksall, J. J., Jackson, R. L., & Green, I. (2004). Elasto-plastic hemispherical contact models for various mechanical properties. Proceedings of the Institution of Mechanical Engineers, Part J: Journal of Engineering Tribology, 218(4), 313-322.

42. Wadwalkar, S. S., Jackson, R. L., & Kogut, L. (2010). A study of the elastic—plastic deformation of heavily deformed spherical contacts. Proceedings of the Institution of Mechanical Engineers, Part J: Journal of Engineering Tribology, 224(10), 1091-1102.
43. Ghaednia, H., & Jackson, R. L. (2013). The effect of nanoparticles on the real area of contact, friction, and wear. Journal of Tribology, 135(4).
44. Jackson, R. L., & Kogut, L. (2007). Electrical contact resistance theory for anisotropic conductive films considering electron tunneling and particle flattening. IEEE Transactions on Components and Packaging Technologies, 30(1), 59-66.
45. Dumas, G., & Baronet, C. N. (1971). Elastoplastic indentation of a half-space by an infinitely long rigid circular cylinder. International journal of mechanical sciences, 13(6), 519-530.
46. Komvopoulos, K. (1989). Elastic-plastic finite element analysis of indented layered media.
47. Akyuz, F. A., & Merwin, J. E. (1968). Solution of nonlinear problems of elastoplasticity by finite element method. AIAA Journal, 6(10), 1825-1831.
48. Liu, G., Zhu, J., Yu, L., & Wang, Q. J. (2001). Elasto-plastic contact of rough surfaces. Tribology transactions, 44(3), 437-443.
49. Green, I. (2005). Poisson ratio effects and critical valus in spherical and cylindrical Hertzian contacts. Applied Mechanics and Engineering, 10(3), 451.
50. Cinar, A., & Sinclair, G. B. (1986). Quasi-static normal indentation of an elasto-plastic half-space by a rigid circular cylinder of infinite length. International journal of solids and structures, 22(8), 919-934.
51. Jackson, R. L. (2016). A Solution of Rigid Plastic Cylindrical Indentation in Plane Strain. STLE Tribology Frontiers, Chicago, IL.

52. Ciavarella, M., Demelio, G., Barber, J. R., & Jang, Y. H. (2000). Linear elastic contact of the Weierstrass profile. Proceedings of the Royal Society of London. Series A: Mathematical, Physical and Engineering Sciences, 456(1994), 387-405.
53. Gao, Y. F., Bower, A. F., Kim, K. S., Lev, L., & Cheng, Y. T. (2006). The behavior of an elastic–perfectly plastic sinusoidal surface under contact loading. Wear, 261(2), 145-154.
54. Gao, Y. F., & Bower, A. F. (2006). Elastic–plastic contact of a rough surface with Weierstrass profile. Proceedings of the Royal Society A: Mathematical, Physical and Engineering Sciences, 462(2065), 319-348.
55. Krithivasan V, Jackson RL. (2007). An analysis of threedimensional elasto-plastic sinusoidal contact. Tribol Lett., 27(1), 31–43.
56. Tripp, J. H., Van Kuilenburg, J., Morales-Espejel, G. E., & Lugt, P. M. (2003). Frequency response functions and rough surface stress analysis. Tribology transactions, 46(3), 376-382.
57. Liu, M. (2014). Finite element analysis of large contact deformation of an elastic–plastic sinusoidal asperity and a rigid flat. International Journal of Solids and Structures, 51(21-22), 3642-3652.
58. Liu, M., & Proudhon, H. (2016). Finite element analysis of contact deformation regimes of an elastic-power plastic hardening sinusoidal asperity. Mechanics of Materials, 103, 78-86.

Chapter 3

Elastic and Elastic-perfectly plastic Analysis of an Axisymmetric Sinusoidal Asperity Contact

3.1 Introduction

This chapter will discuss the importance, implication, and implementation of an axisymmetric sinusoidal asperity model. There are many asperity models available, as discussed in the previous chapter, and different asperity models work well in different applications. Although, in many cases, spherical asperity models work well; however, to model the multiscale nature of the rough surface, a separate asperity model is necessary because real surface barely looks like sphere upon another sphere. Besides that, the spherical asperity model works well with rough surface models when the applied force is small, or deformation of the asperity is limited to the tip of the asperity. The developed spherical asperity models also do not consider the effect of the substrate at the base of the asperity, and the effect of the substrate becomes important during large deformation of the asperity. Several researchers [1-6] suggested that sinusoidal shapes may be a more realistic depiction of surface asperity contact, than spherical ones, especially when the asperity interaction gets important due to large deformation of the surface. Stanley and Kato[7], Ciavarella et al. [1], Jackson [2], and also some other works [3-6, 8-12] considered multiple scales of roughness and represented the rough surfaces by either a Fourier series (taking the FFT of the rough surface data) or the Weierstrass-Mandelbrot fractal function. Fig. 3.1 is showing the formation of the rough surface superimposing sine waves. Besides this, intuitively, the asperities on surfaces would be more like rolling hills that do not meet their base at right angles, as is the case with sphere models (See Fig. 2.4 (a) and (b) in chapter 2). In contrast to the spheres, the slope of the sinusoidal or wavy

asperity decreases gradually at the base to conform to the supporting surface. A detailed description of the changes in the shape of the sinusoidal asperity models with load found from the FEA has shown later in Fig. 3.5. Also, when the deformation of the asperity is limited to the tip of the asperity, spherical and sinusoidal models act in a very similar way. Therefore, using a sinusoidal (wavy) model seems more applicable than a spherical one. In 2016, Greenwood [13] proposed a model that would extend the Greenwood-Williamson rough surface model (GW model) [14] by replacing Hertz contact with a model of a quartic bump asperity. The quartic bump is similar to the sinusoidal wave geometry developed in this dissertation.

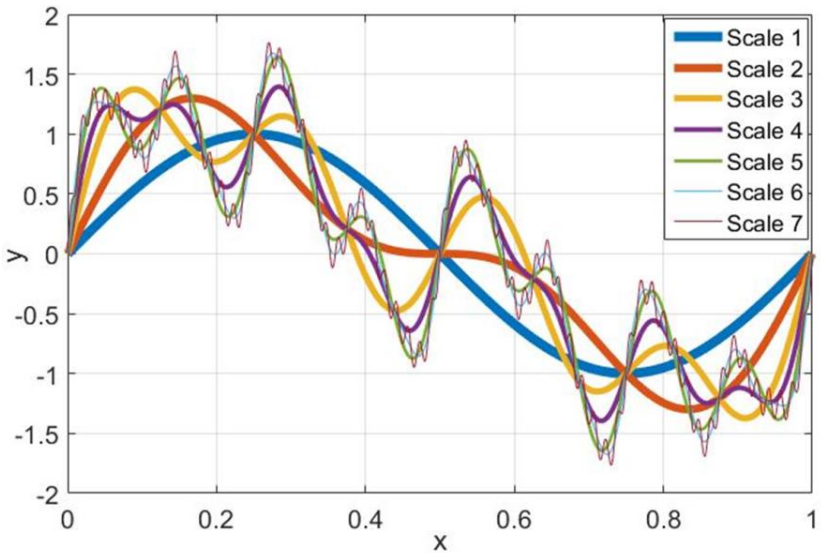

Fig. 3.1 Formation of rough surface superimposing sine waves.

As discussed in the previous chapter, research has been done on 3D periodic or bi-sinusoidal asperity models [4-5, 15-19]; however, these 3D models are computationally very expensive, especially if other mechanisms such as adhesion or coupled electro-thermo-mechanical analysis are included. Analysis has also been done on the 2D sinusoidal asperity [6, 20-21] at the plane-strain condition; however, it is pertinent for specific applications only. Therefore, the following aspects are considered during the new asperity modeling:

- Consider interaction with adjacent asperities,
- Consider the effect of the substrate at the base of the asperity,
- Reduce the computational expense of bi-sinusoidal models and also provide a 3D analysis of the asperity.

Besides that, the aim of the present work are:

1) To quantify the transition from elastic to elastic-perfectly plastic behavior,

2) Validation of the model comparing all the cases analyzed with the Hertz elastic and Jackson Green elastic-plastic model,

3) To analyze and discern the parameters that govern the contact behavior from low load to very high load that causes complete contact,

4) To formulate equations for the contact pressure, contact area and contact pressure as a function of surface separation both for elastic and elastic-perfectly plastic cases at which two surfaces reach complete contact for a wide range of material properties and surface roughness,

5) Characterize the relation of the nominal pressure (i.e., hardness) to the yield strength for all the cases considered in the present work from initial to complete contact.

3.2 Methodology

3.2.1 Axisymmetric Sinusoidal Geometry:

In the current study, the profile of the axisymmetric sinusoidal surface is described using the following equation,

$$h(r) = \Delta\left(1 + cos\left(\frac{2\pi r}{\lambda}\right)\right),\ r \leq \frac{\lambda}{2} \tag{3.1}$$

where *h* is the surface height, and *r* is the radial location from the axis of symmetry of the sinusoidal surface (see Fig.3.2 (a)). A three-dimensional view of this geometry is shown in Fig. 3.2(b). The amplitude of the asperity has been magnified for clarity.

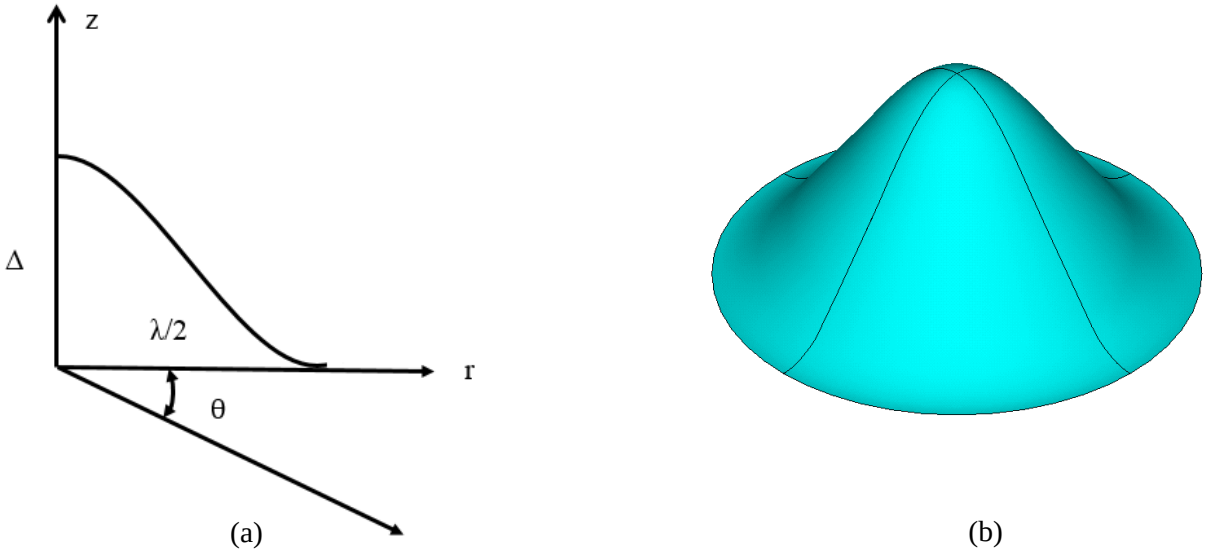

(a) (b)

Fig. 3.2 (a) 2D plot and (b) 3D surface of the sinusoidal asperity.

3.2.2 Finite Element Model (FEM):

To model the axisymmetric sinusoidal asperity contact, one sinusoidal asperity in contact with a rigid flat is considered by using the following equation for the equivalent elastic modulus:

$$\frac{1}{E'} = \frac{(1-\upsilon_1^2)}{E_1} + \frac{(1-\upsilon_2^2)}{E_2} \tag{3.2}$$

where E_i and ν_i are the Young' modulus and Poisson's ratio respectively of two contacting bodies and i =1, 2.

The cross-section of the axisymmetric sinusoidal surface loaded against a rigid flat is shown in Fig. 3.3. Fig. 3.4 is showing the schematic of the asperity before and after deformation. As it is an axisymmetric model, only the right half of the axis is considered in the FEA. The commercial FEM software ANSYS is used in this work. During modeling, the following assumptions have been made:

1) When there is a gap between the two surfaces, no contact will be established and vice versa.
2) For elastic cases, a linear elastic isotropic material is assumed, and for the elastic-plastic cases, a nonlinear isotropic elastic-perfectly plastic material model is assumed. Elastic-perfectly plastic means no strain hardening is included in the model. The elastic-perfectly plastic model will be helpful in modeling elastic-plastic cases with different amounts of hardening in future works.
3) The von Mises criteria is used to predict yielding.
4) The large deformation effect is included during the analysis to include the effect of geometric non-linearity.
5) The contact is assumed to be frictionless and without adhesion.

For meshing the entire sinusoidal surface and its substrate, PLANE183, an 8 node plane element with mid-nodes, is used. CONTA 172, a 3-node contact element with a mid-node and TARGE 169, a 2-node target element are used to model the contact between the sinusoidal surface and the rigid flat. The Augmented Lagrange method is used as the contact algorithm. Two other common

methods are the Normal Lagrange method, which has a chattering problem, often making convergence difficult, and the Multi-Point Constraint method, which is best suited for a bonded and unseparated contact. Besides this, the Augmented Lagrange method results in more detection points at the contact than the Normal Lagrange and Multi-Point Constraint method. Essentially, it is effective at restricting interference at the contact, while still converging relatively easily. The other boundary conditions that are considered in the present study are:

- The axisymmetric boundary condition is applied at the axis of symmetry, which is U_r (0, z) =0. Boundary conditions that consider interaction with adjacent asperities are applied to the displacement in the radial direction along the side surface, L_2, such that U_r (0, z) =U_r ($\lambda/2$, z) = 0 and to the value of shear stress which is zero at $\lambda/2$ (σ_{rz} ($\lambda/2$, z) = 0). This is very similar to a periodic boundary condition (see Fig.3.3).
- The nodes at the base of the substrate (z=0) are fixed in all directions.
- Only displacement in the negative z-direction is allowed on the rigid flat.

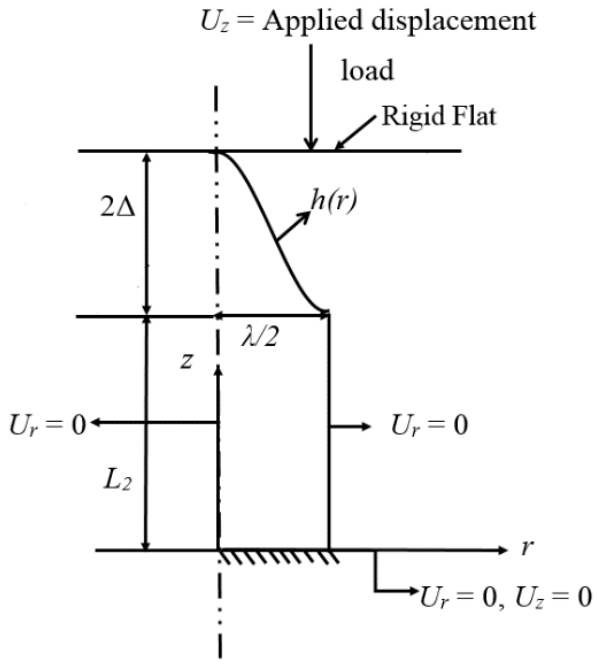

Fig. 3.3 Schematic of an axisymmetric sinusoidal asperity loaded with a rigid flat.

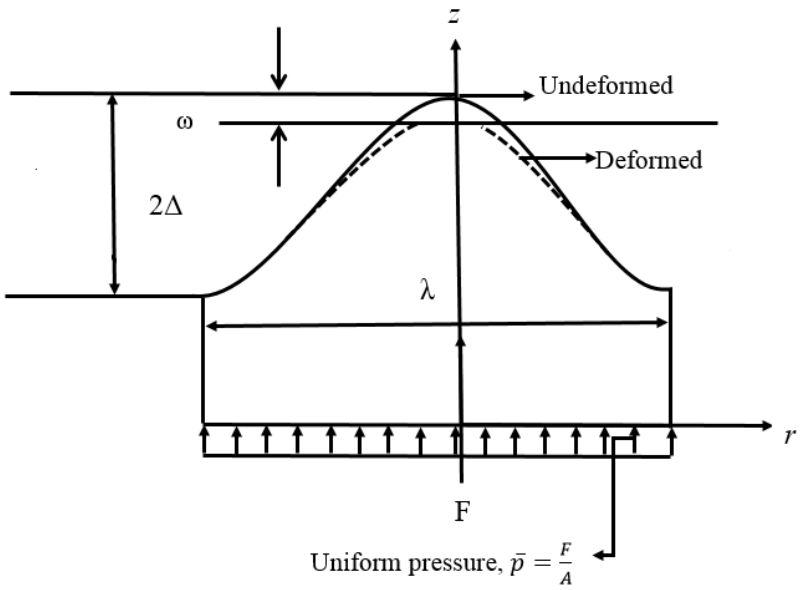

Fig. 3.4 Schematic of a sinusoidal asperity before and after deformation. (ω= Displacement, *F*=Reaction force).

Although the asperity contact considered in this work is not perfectly periodic, it does effectively include interactions with adjacent asperities by having a confined boundary at the outer radius of the base. This is drastically different from a single spherical asperity model, which does not have this confinement and lateral interaction and also from the 'non-axisymmetric' bi-sinusoidal models. In the present analysis, a parametric study has been performed for the modeling of the elastic and elastic-perfectly plastic axisymmetric sinusoidal surface, varying both the geometry and the material properties.

From the spectral analysis of different rough surfaces, it has been found that the Δ/λ ratio generally varies in the range of approximately 10^{-7} to 0.1 [22-24]. For the elastic case, five different values of amplitude to wavelength ratios (Δ/λ) are considered in the range of $0.00005 < \Delta/\lambda < 0.025$. In the current model, λ is set to 1 mm throughout the calculation. Then the analysis is performed for three different values of Young's modulus (E= 50 GPa, 200 GPa, and 400 GPa) at each Δ/λ ratio. For each Young's modulus case, three different values of Poisson's ratio (0.20, 0.33, and 0.45) have also been considered. During the simulation, only one parameter is varied at a time while keeping the other two parameters constant. A total of 45 cases are performed for the elastic case.

For the elastic-perfectly plastic case, six different values of amplitude to wavelength ratios (Δ/λ) are considered in the range of $0.00005 < \Delta/\lambda < 0.025$ and three different values of Young's modulus (E= 50 GPa, 200 GPa, and 400 GPa) are considered at each Δ/λ ratio. For each Young's modulus case, six different values of Young's Modulus (E) to yield strength (S_y) ratios (E/S_y = 10, 50, 200, 500, 1000 and 2000) are considered i.e. S_y is varying. This results in eighteen different values of yield strength in the range 25MPa < S_y < 40000 MPa for each Δ/λ case. As mentioned before, it is important to consider this wide range of E/S_y because yield strength changes with scale and asperities can change over many length scales. During the simulation of the elastic-perfectly plastic

case also, only one parameter is varied at a time, keeping the other parameters constant. Since six different values of Δ/λ are considered, in total, 108 cases are performed for the elastic-perfectly plastic analysis. Poisson's ratio has been kept constant at 0.33 for all the elastic-perfectly plastic cases.

To confirm the FE model contact stiffness and penetration tolerance values are acceptable, FE simulations have performed for three different Δ/λ ratios (0.025, 0.005, and 0.00005) at E/S_y=10 and E/S_y=2000. Contact element stiffness is the stiffness of the numerical contact elements. Contact elements act like spring between two contacting surfaces. To enforce zero penetration at the contact, the stiffness of the contact elements have to be very high, and that can cause convergence difficulties. Based on the applied stiffness factor, the bulk modulus of the contact material, and some other parameters, ANSYS makes an initial guess for the contact stiffness. The contact element stiffness is updated during each substep of the FE simulation based on the current mean stress of the underlying element. If a small stiffness factor is assumed, then the contact stiffness will be small, and there will be larger penetrations at the contact, and the FEM will give inaccurate results. Different values of the contact stiffness factor have been tried, and from the simulation results, it was found that an ANSYS contact stiffness factor equal to 1.0 and a penetration tolerance factor equal to 0.01 are adequate to make the solution independent of contact element stiffness and to enforce almost zero penetration at the contact for the cases considered in this work.

To observe the effect of substrate length or to make the model applicable for the semi-infinite solid case (half-space), simulations have performed for the same cases as the contact stiffness test. From the results, it is found that the results are independent of the length of geometry at the base of the asperities when $L_2 \leq 3\lambda$. The cases where the asperity deforms easily, i.e., more plasticity is observed, a higher substrate length is necessary to mitigate the effect of the generated high stress.

In the plane strain model of Gao et al. [21], it is found that the substrate will act as a semi-infinite solid when $L_2 \geq 3\lambda$ while noting that in their study, the Δ/λ ratio varied from 0.01 to 0.1.

The mesh convergence test has been performed for the same cases as the contact stiffness, and substrate depth tests to check the validity of the FEM model used. Simulations have performed for different element sizes, and it has found that depending on the Δ/λ ratio and substrate depth, 106,963–153,466 elements are enough to capture the results accurately.

3.2.3 Validation of the FEM Model:

At low load and at the beginning of the contact, when the deformation is limited to the tip of the asperity, the contact behavior of spherical and sinusoidal asperities are very similar. At these low loads, the axisymmetric sinusoidal asperity model is compared with the spherical contact models. Besides that, material generally deforms elastically at the beginning of the contact, and plastic deformation may be confined to an insignificant volume. That's why both elastic and elastic-perfectly plastic cases of the FEM results have been compared with the Hertz model [16, 25-26], i.e., Eq. (2.17) and Eq. (2.18). The elastic-perfectly plastic cases have also been compared with the Jackson-Green (JG) elastic-plastic spherical contact model [27], i.e., Eq. (2.66)-(2.69). In the JG model, equations are formulated such that in the elastic region, it uses the Hertz solution, while the transition from elastic to elastic-plastic behavior is continuous in nature and considered by another equation. To adapt the formulas for spherical contact to sinusoidal contact at low load, the curvature at the tip of the axisymmetric sinusoidal surface needs to be replaced by the following equation,

$$R = \frac{\lambda^2}{4\pi^2\Delta} \tag{3.3}$$

where Δ is the amplitude of the sinusoidal asperity, and λ is the wavelength of the sinusoidal surface. A comparison of the current results with the Hertz elastic spherical contact model shows that all the cases, whether elastic or elastic-perfectly plastic, match well at the beginning of the contact, except for a few elastic-perfectly plastic cases. For those cases, the value of initial interference was greater than the value of critical interference. Critical interference means the interference that causes initial yielding at the surface. However, all of the elastic-perfectly plastic cases agreed very well with the JG elastic-plastic spherical contact model [27]. Fig 3.5 (a) shows the comparison of the elastic sinusoidal asperity with the Hertz equation and Fig. 3.5(b) and 3.4(c) show the comparison of the elastic-perfectly plastic sinusoidal asperity model with Hertz and JG model, respectively. These three figures have magnified at the low load region to make the comparison clear. From the figures, it is clear that at the beginning of the contact, sinusoidal and spherical asperity model matches reasonably well; however, with the increase of load, they behave differently. Fig. 3.6(a) describes the overall phenomena more clearly. An isolated spherical contact (Hertz and JG model) will evolve with deformation to more of a column or barrel shape, which has been analyzed and shown in detail by Wadwalkar et al. [28], See Fig. 2.4(a) and (b) in chapter 2. However, a sinusoidal asperity will not follow this trend, as the geometry and boundary conditions are different. Fig. 3.6(b) is showing the gradual change in the behavior of the sinusoidal asperity with loading found from the FEA.

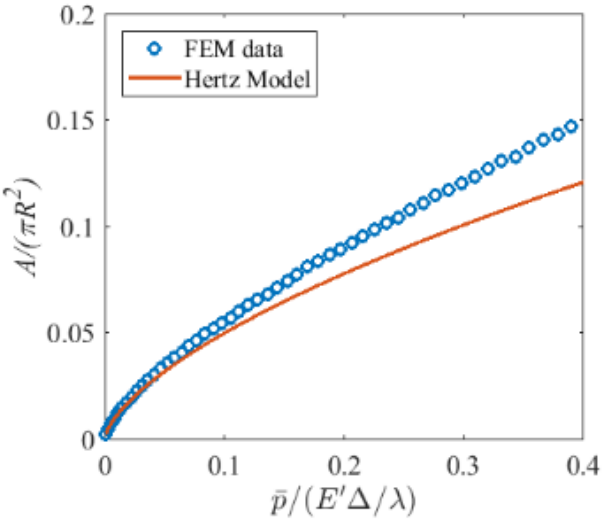

(a)

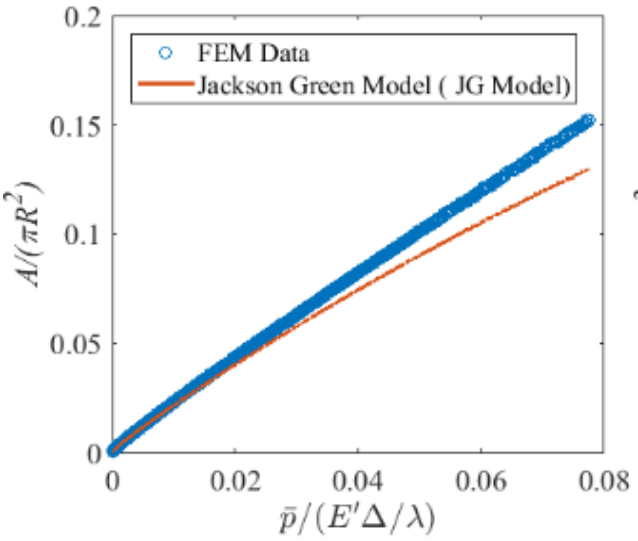

(b)

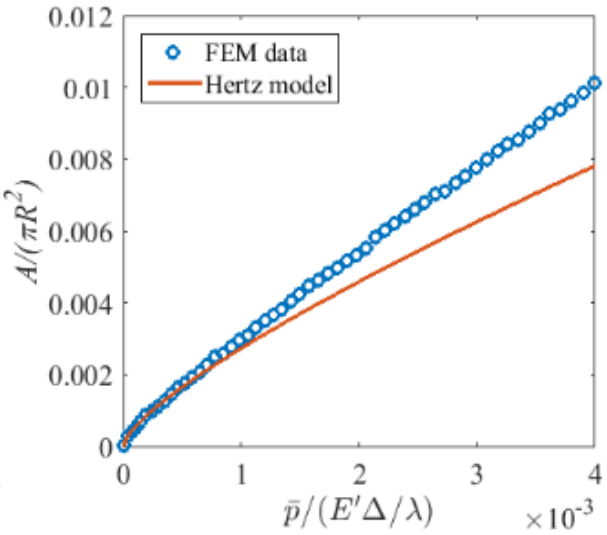

(c)

Fig. 3.5(a) Comparison of the elastic case Δ/λ=0.00005, E=200 and υ=0.33 with the Hertz model, (b) Comparison of elastic-perfectly plastic case Δ/λ=0.01, E=200, E/S_y=500 and υ=0.33 with the Hertz model, (c) Comparison of elastic-perfectly plastic case Δ/λ=0.005, E=200, E/S_y=1000 and υ=0.33 with the JG model. (In the figures, $R = \frac{\lambda}{2}$ and $\bar{p}$ is the nominal pressure i.e.$\bar{p} = \frac{F}{\pi R^2}$).

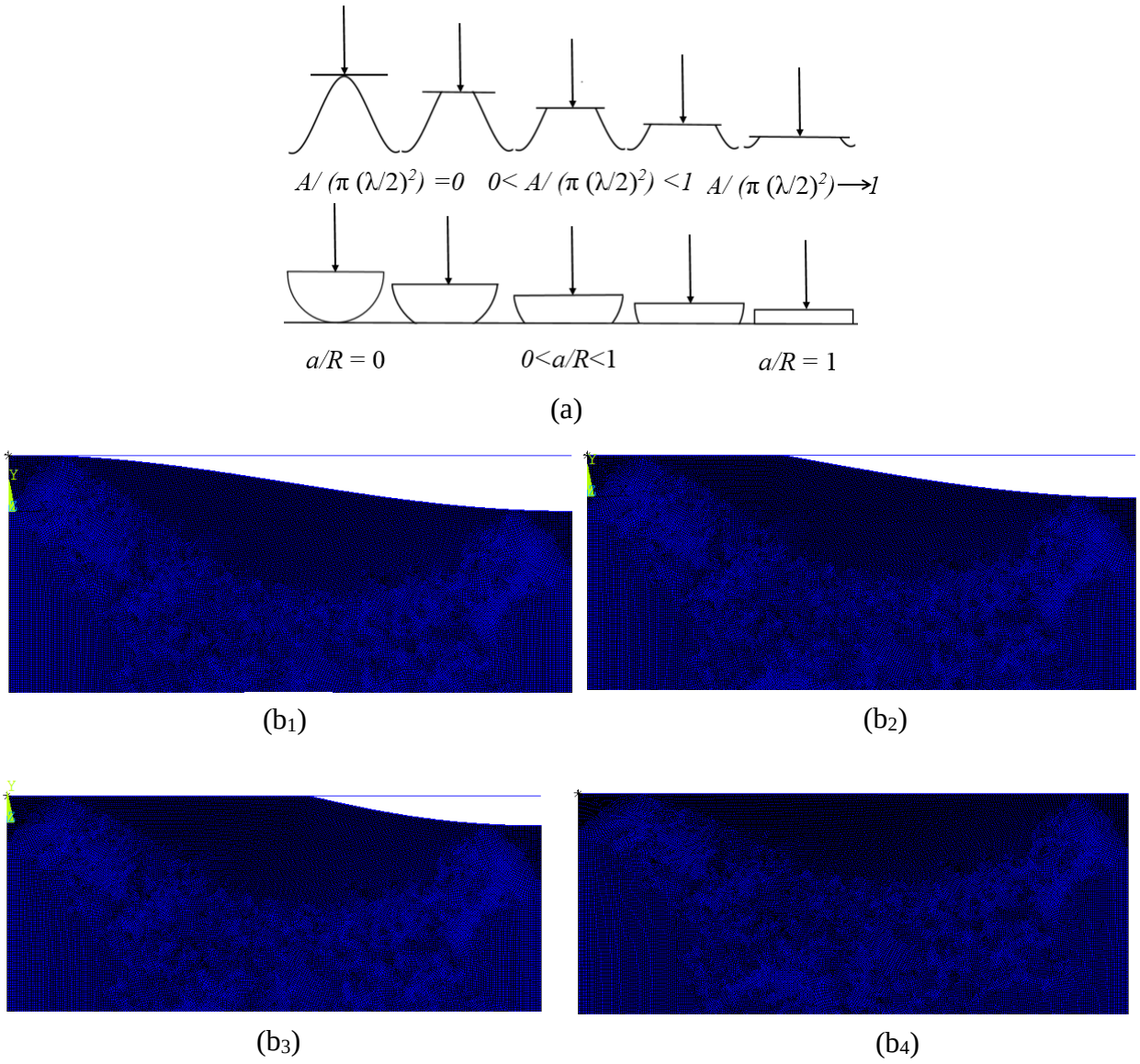

(a)

(b$_1$) (b$_2$)

(b$_3$) (b$_4$)

(b)

Fig.3.6 (a) An approximate conceptual depiction is showing the gradual change with loading for spherical and sinusoidal asperities in contact with a rigid flat (b) Change in the shape of the sinusoidal asperity from very low load to high load (Complete flattening of the sinusoidal asperity). (b$_1$) δ=0.65μm, (b$_2$) δ=0.013mm, (b$_3$) δ=0.026mm and (b$_4$) δ=0.065mm.

3.3 Results and Discussion

3.3.1. Elastic Sinusoidal Asperity Model

3.3.1.1 Empirical Equation for Average Pressure at Complete Contact

As described in the methodology section, a parametric study has performed to predict the contact behavior of the elastic sinusoidal asperity in contact with a rigid flat. Figure 3.7(a) presents the effect of Young's modulus on the relation between the average contact pressure, $\bar{p}$, and the contact area, A. The Young's modulus spans an order of magnitude, ranging from E=50GPa to E= 400 GPa, while the amplitude to wavelength ratio is held constant at $\frac{\Delta}{\lambda} = 0.025$ and Poisson's ratio is υ=0.33. As shown in Fig. 3.7(a), the different values of Young's modulus result in different curves for the contact area as a function of the average contact pressure. The required average contact pressure to reach the state of complete contact increases proportionally with the increase of Young's modulus. Figure 3.7(b) shows the average contact pressure–area curves for different Poisson's ratios at E=200GPa and $\frac{\Delta}{\lambda} = 0.025$. Higher values of Poisson's ratio result in higher average contact pressures required to reach complete contact. Figure 3.7(c) shows several examples of the average contact pressure–area curves for the different amplitude to wavelength ratios, $\frac{\Delta}{\lambda}$ at $E = 200$GPa and υ=0.33. Higher value of $\frac{\Delta}{\lambda}$ results in a higher pressure required to reach complete contact. Normalizing A by $\pi\left(\frac{\lambda}{2}\right)^2$ and $\bar{p}$ by $E'\frac{\Delta}{\lambda}$, the corresponding dimensionless relation becomes independent of the material properties and geometrical parameters. Figures 3.8(a)–3.8(c) represent the dimensionless average contact pressure–area curve for the same three cases described above and shown in Figs. 3.7(a)–3.7(c). In each of the figures, the normalized results are consolidated into a single curve. For the other cases also, Young's modulus, Poisson's

ratio, and amplitude to wavelength ratio showed the same effect on the dimensional and dimensionless contact pressure-area relation; that is why all the cases have not shown here. From all the numerical simulations, performed over the entire range of the input parameters, the value of pressure at which the two surfaces reach complete contact, p_e^* has found, which can be expressed by the following equation:

$$p_e^* = 1.85E' \left(\left(\frac{\Delta}{\lambda} \right)^{\left(0.93 \left(\frac{\Delta}{\lambda} \right)^{-0.005} \right)} \right) \tag{3.4}$$

The average difference between the FEM results and Eq. (3.4) is 1.43%, and the maximum difference is 2.84%.

3.3.1.2. Empirical Equation for Contact Area:

Equation (3.4) is now used to normalize the nominal pressure, $\bar{p}$. By curve fitting the normalized contact pressure-area plots found from the FEA, an equation is derived empirically for the contact area. The fitted equation for contact area is,

$$\frac{A}{\pi \left(\frac{\lambda}{2} \right)^2} = 0.425 \left(\frac{\bar{p}}{p_e^*} \right)^{2/3} \left(1 - \frac{\bar{p}}{p_e^*} \right)^{1.4} + \left(0.8 + (1 - 0.8) \left(\frac{\bar{p}}{p_e^*} \right)^{a} \right) \left(\frac{\bar{p}}{p_e^*} \right)^{1.6} \tag{3.5}$$

where,

$$a = 10 \left(\frac{\Delta}{\lambda} \right)^{0.7} + 10.75$$

The difference between the FEM results and Eq. (3.5) is 1.73% on average, and the maximum error is 8.81%. The equation is applicable for the wide range of material properties and $\frac{\Delta}{\lambda}$ ratios

considered in this work. As an example, Fig. 3.9 shows the comparison of the fitted equation with the results of two FEM cases.

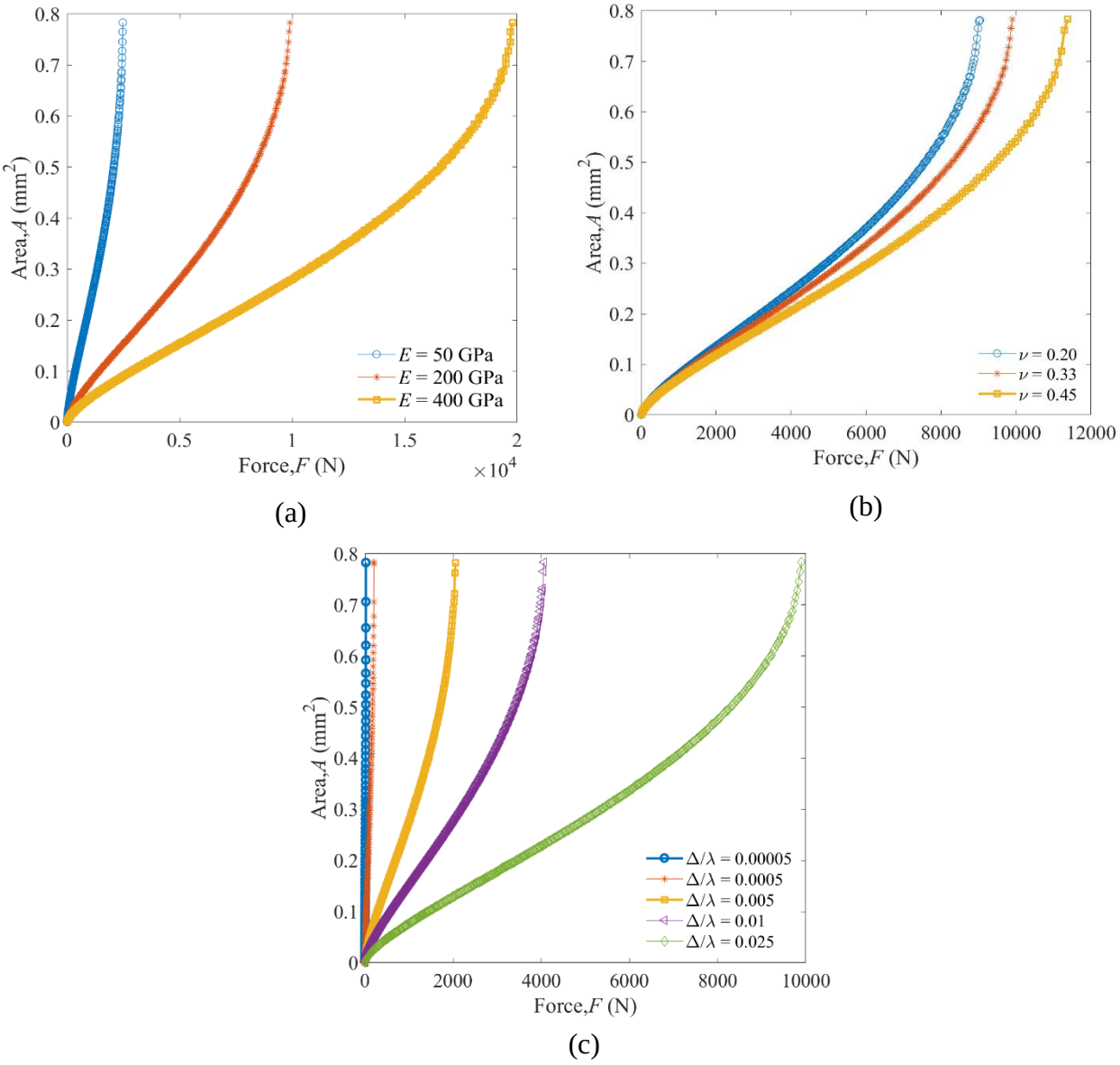

Fig.3.7 (a) Dimensional contact pressure-area relation for different Young's modulus at a Δ/λ of 0.025 and Poisson's ratio of 0.33. (b) Dimensional contact pressure-area relation for different Poisson's ratio at Δ/λ of 0.025 and Young's modulus of 200 GPa (c) Dimensional contact pressure-area relation for different amplitude to wavelength ratios (Δ/λ) at a Young's Modulus of 200 GPa and Poisson's ratio 0.33.

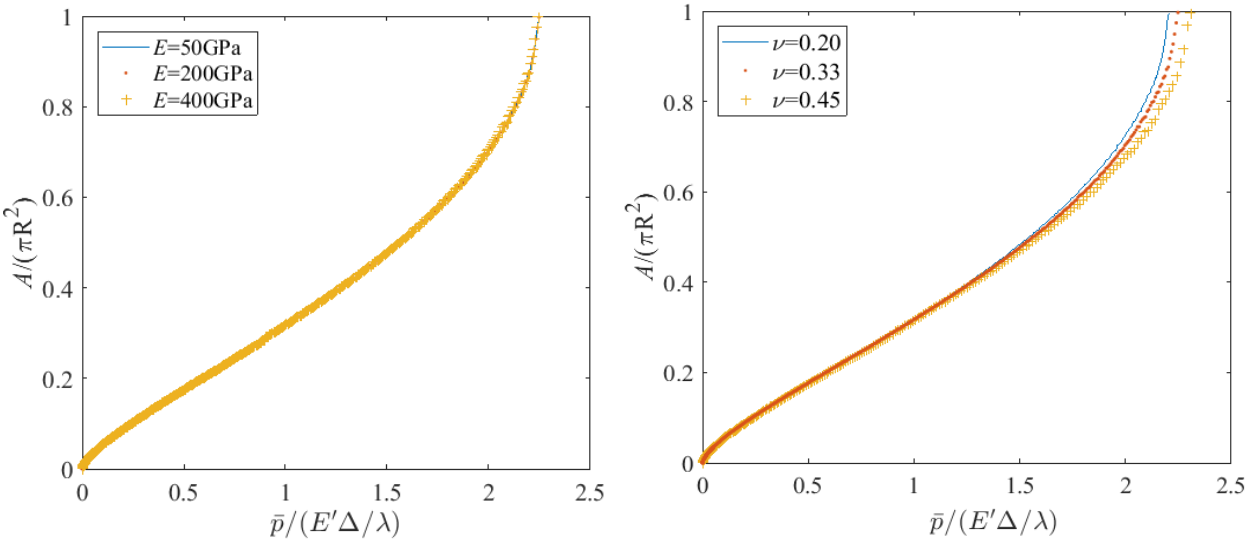

(a)

(b)

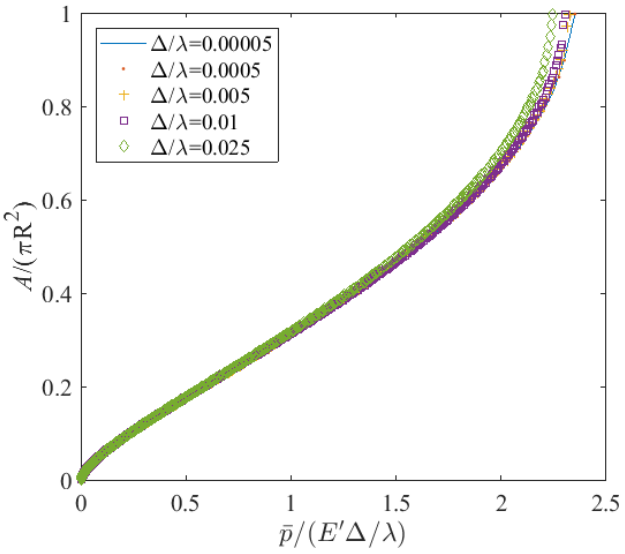

(c)

Fig. 3.8 (a) Dimensionless contact pressure-area relation for different Young's modulus at a Δ/λ of 0.025 and Poisson's ratio of 0.33. (b) Dimensionless contact pressure-area relation for different Poisson's ratio at Δ/λ of 0.025 and Young's modulus of 200 GPa (c) Dimensionless contact pressure-area relation for different amplitude to wavelength ratios (Δ/λ) at a Young's Modulus of 200 GPa and Poisson's ratio 0.33. (In the figures, $R = \frac{\lambda}{2}$ and $\bar{p}$ is the nominal pressure i.e.$\bar{p} = \frac{F}{\pi R^2}$).

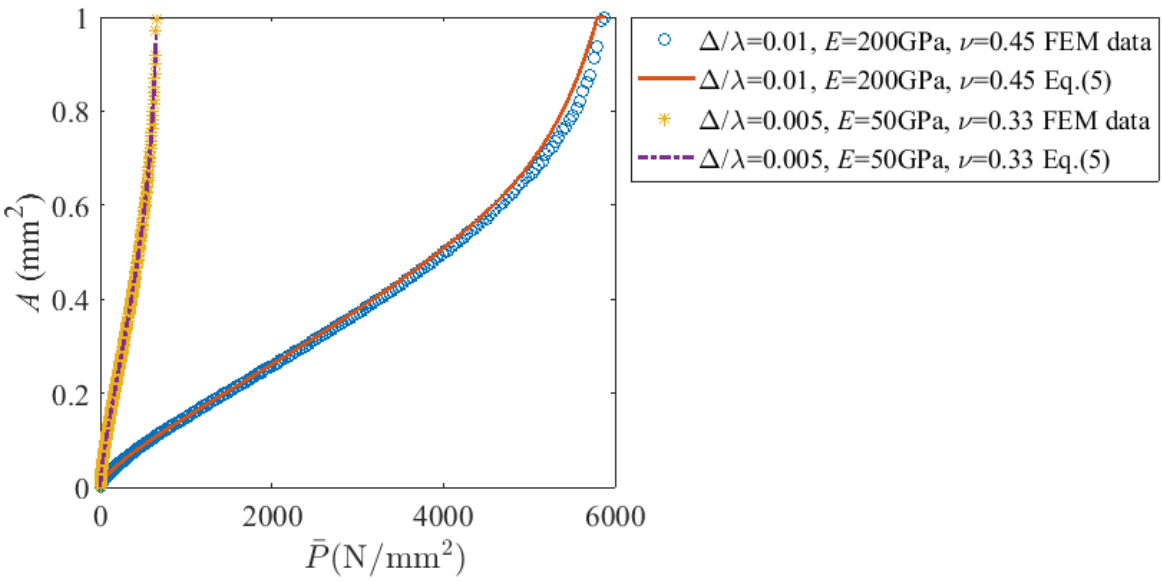

Fig. 3.9 Comparison of the FEM data with the fitted Eq. (3.5).

3.3.1.3. Empirical Equation for Nominal Pressure as a Function of Surface Separation:

The gap between the axisymmetric sinusoidal asperity considered in this work and rigid flat at zero load can be calculated from the following equation:

$$g = 2\Delta - \Delta\left(1 + cos\left(\frac{2\pi r}{\lambda}\right)\right) \tag{3.6}$$

The average gap at zero displacement or at the beginning is defined by $\overline{g_o}$ and the average gap at any displacement is defined by $\bar{g}$. The average contact gap at zero displacement, $\overline{g_o}$ is calculated from the following equation:

$$\overline{g_o} = \frac{\int_0^{\lambda/2}\int_0^{2\pi} gr d\theta dr}{\pi\left(\frac{\lambda}{2}\right)^2} \tag{3.7}$$

Substituting Eq. (3.6) into Eq. (3.7), the following equation for the average gap at zero load is obtained:

$$\overline{g_o} = \Delta\left(1 + \frac{4}{\pi^2}\right) \tag{3.8}$$

To observe the effect of different parameters on the gap, the predictions of average surface separation, $\overline{g}$ versus nominal pressure, $\overline{p}$ are plotted in Fig. 3.10 (a), (b) and (c). Fig. 3.10 (a) shows that with the increase of the Δ/λ ratio more contact pressure is required to fill the gap between the contacting surfaces. The same behavior is observed with the increase of Poisson's ratio and Young's modulus as shown in Fig. 3.10(b) and 3.10(c), respectively.

Then the nominal pressure and average surface separation is normalized by p_e^* and $\overline{g_o}$ respectively and the same cases shown in Fig. 3.10 are plotted in Fig. 3.11(a), 3.11(b) and 3.11(c). It is found that like the contact area, this normalization collapses the data onto one curve. Considering all of the cases, the following empirical equation for nominal pressure as a function of surface separation is found:

$$\frac{\bar{p}}{p_e^*} = \left[1 - G_n^{\left(1.77\left(\frac{\Delta}{\lambda}\right)^{2.46} + 0.045G_n + 0.384\right)}\right]^{\left(1.525(G_n)^{0.21} - 0.0029\right)} \tag{3.9}$$

In the above equation, $G_n = \frac{\bar{g}}{\overline{g_o}}$. The difference between the FEM results and Eq. (3.9) is 1.29% on average and maximum error is 5.86%.

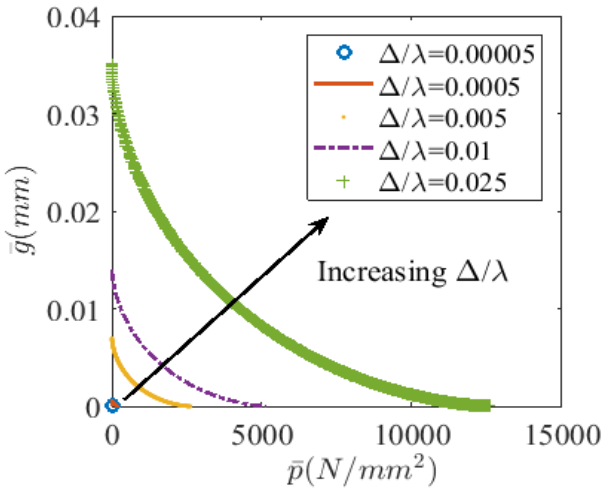

(a)

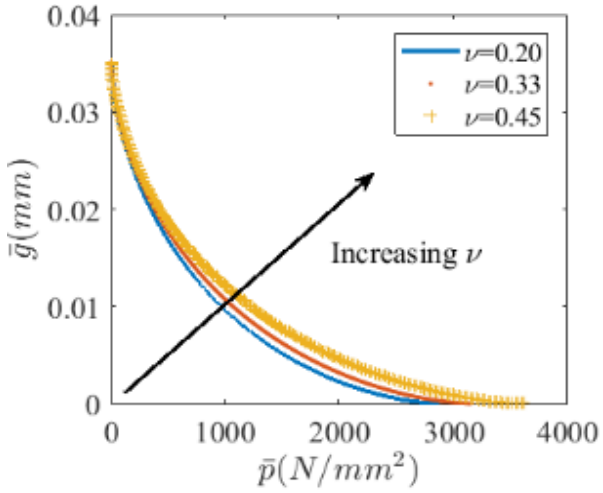

(b)

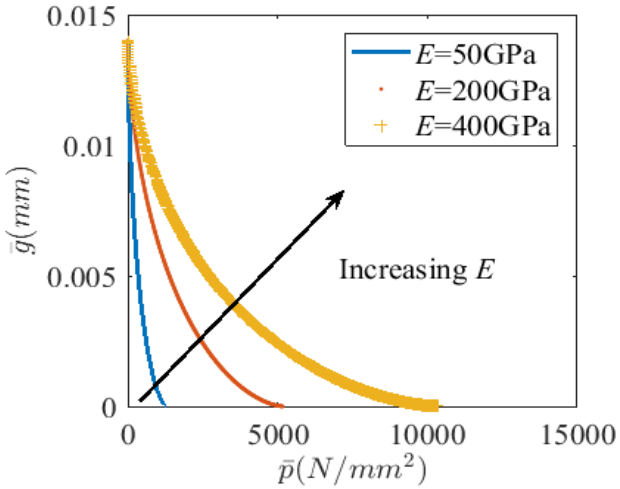

(c)

Fig.3.10 (a) Nominal pressure vs. average surface separation for E=200 GPa, υ=0.33 at different values of Δ/λ ratio (b) Nominal pressure vs. average surface separation for E=50 GPa, Δ/λ =0.025 at different values of Poisson's ratio (c) Nominal pressure vs. average surface separation for Δ/λ =0.01, υ=0.33 at different values of Young's modulus. (In the figures, $R = \frac{\lambda}{2}$ and $\bar{p}$ is the nominal pressure i.e.$\bar{p} = \frac{F}{\pi R^2}$).

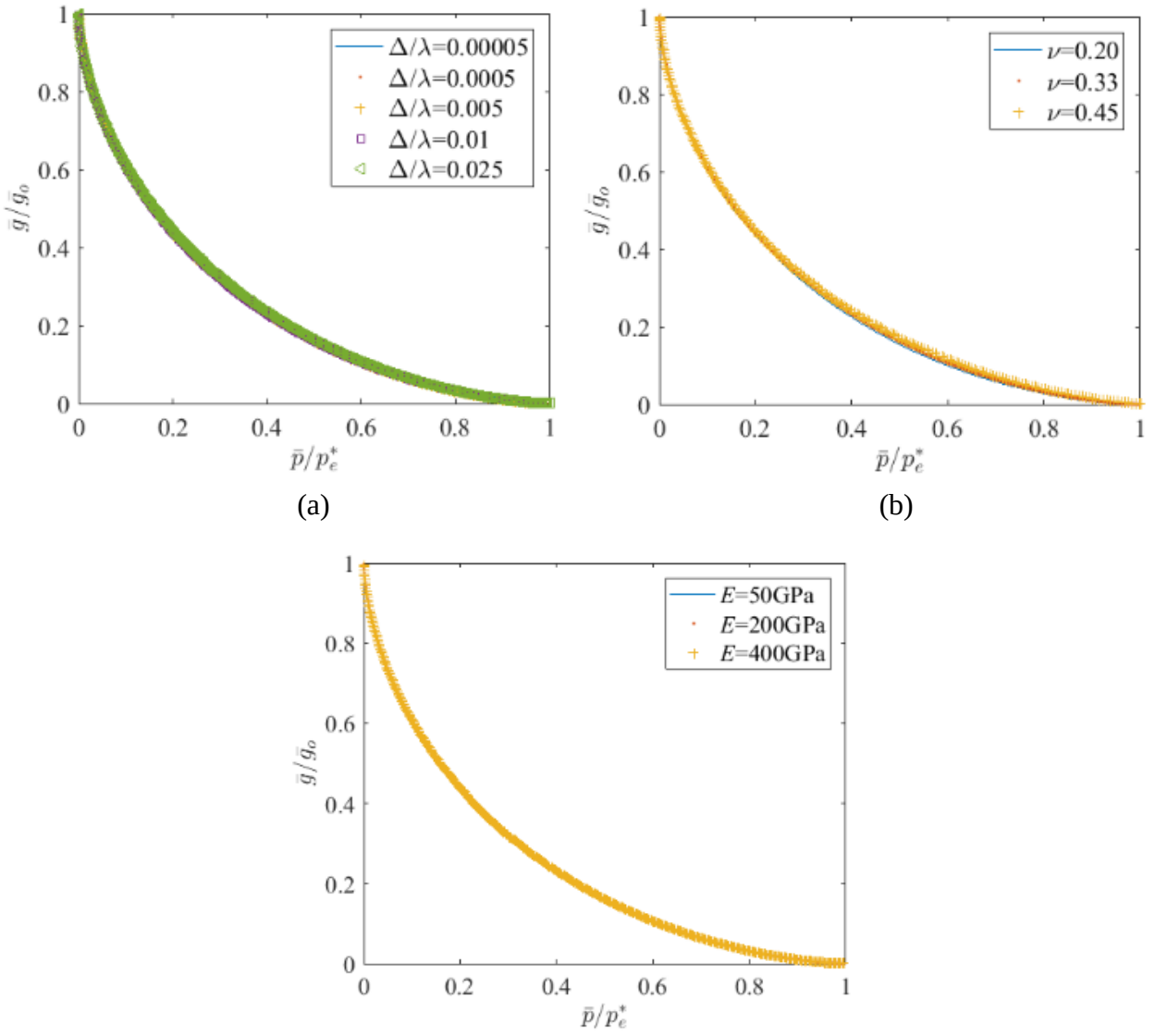

Fig.3.11 (a) Normalized nominal pressure vs. normalized surface separation for E=200 GPa, υ=0.33 at different values of Δ/λ ratio (b) Normalized nominal pressure vs. normalized surface separation for E=50 GPa, Δ/λ =0.025 at different values of Poisson's ratio (c) Normalized nominal pressure vs. normalized surface separation for Δ/λ =0.01, υ=0.33 at different values of Young's modulus. (In the figures, $R = \frac{\lambda}{2}$ and $\bar{p}$ is the nominal pressure i.e.$\bar{p} = \frac{F}{\pi R^2}$).

3.3.2. Elastic-perfectly plastic Sinusoidal Asperity Model

3.3.2.1. Empirical Equation for Average Pressure at Complete Contact, p_{ep}^{*} and Critical Amplitude, Δ_c

For the analysis of the elastic-perfectly plastic behavior, the effect of different parameters (E, E/S_y, and Δ/λ ratio) on the contact pressure-area relation is examined. Poisson's ratio is constant throughout this analysis.

Similar to elastic asperity contact, in elastic-perfectly plastic asperity contact, an increase of Young's modulus also increases the amount of pressure required to reach complete contact, as shown in Fig. 3.12(a). Contact area is normalized by $\pi\left(\frac{\lambda}{2}\right)^2$ and nominal pressure by $E'\frac{\Delta}{\lambda}$. Again note that nominal pressure is contact force divided by the nominal contact area. After normalization, at a constant value of E/S_y and Δ/λ ratio, curves for different Young's moduli collapse into a single curve. Therefore, the dimensionless contact pressure-area relation for a constant value of E/S_y and Δ/λ ratio does not depend on Young's modulus, E. This normalization is demonstrated in Fig. 3.12(b) for E/S_y=50 and Δ/λ=0.005.

Next, the effect of E/S_y and the Δ/λ ratio on the normalized contact pressure-area relation is analyzed. For different Δ/λ ratios, the effect of E/S_y is shown in Fig. 3.13. The Young's modulus is now held constant at 200 GPa, as the normalized contact pressure-area relation doesn't depend on Young's modulus. Some interesting results are found from the analysis. Fig. 3.13(a) shows the effect of E/S_y ratios on the normalized contact area to pressure relation for Δ/λ = 0.025. From Fig. 3.13 (a), it is observed that the higher the value of E/S_y ratio (that means lower yield strength values) the lower the force required to reach complete contact.

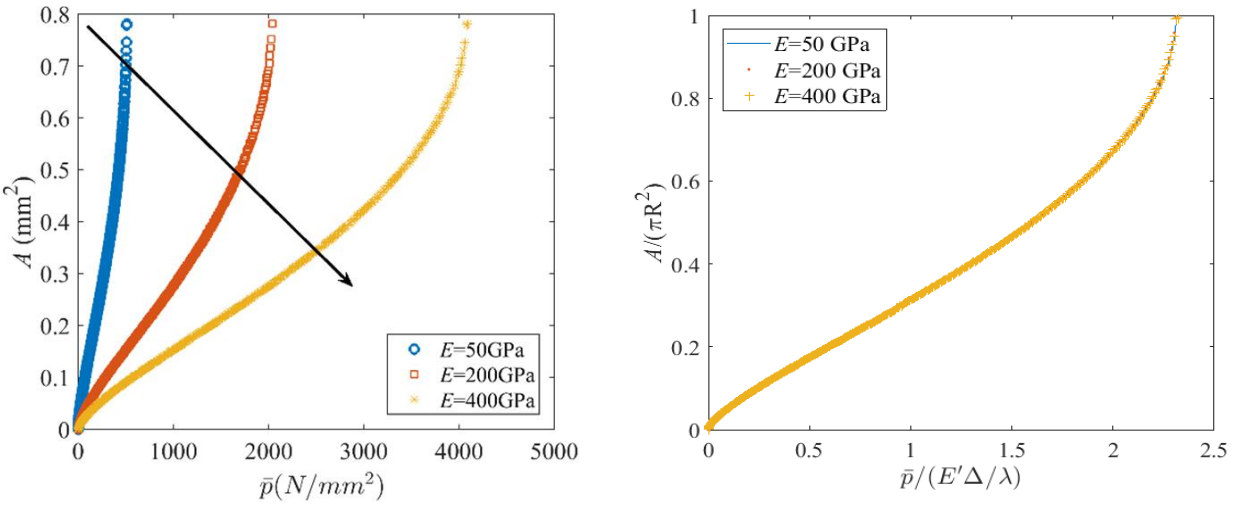

(a) (b)

Fig.3.12 (a) Dimensional nominal pressure-area relation (b) Dimensionless nominal pressure-area relation for different values of Young's modulus at Δ/λ equal to 0.005 and υ=0.33. (In the figures, $R = \frac{\lambda}{2}$ and $\bar{p}$ is the nominal pressure i.e.$\bar{p} = \frac{F}{\pi R^2}$).

For the same E/S_y ratios, when Δ/λ equals to 0.01, higher values of contact pressure are required to reach complete contact, as shown in Fig. 3.13(b). In Fig. 3.13(c), for the same cases, further decrease in the Δ/λ ratio causes the curves for E/S_y=10 and E/S_y=50 to coincide with each other and require more contact pressure to reach complete contact. The same trend is observed for the case in Fig. 3.13(d). Additional decreases in the Δ/λ ratios cause the curves for E/S_y=10, 50, 200, and 500 to coincide with each other, as shown in Fig. 3.13(e). In Fig. 3.13(f), and when Δ/λ ratio equals to 0.00005, the curves for all the ratios of E/S_y coincide with each other. This means that the effect of E/S_y is decreasing with the decrease of the Δ/λ ratio. This is because the cases are becoming more and more elastic with the decrease in the Δ/λ ratio.

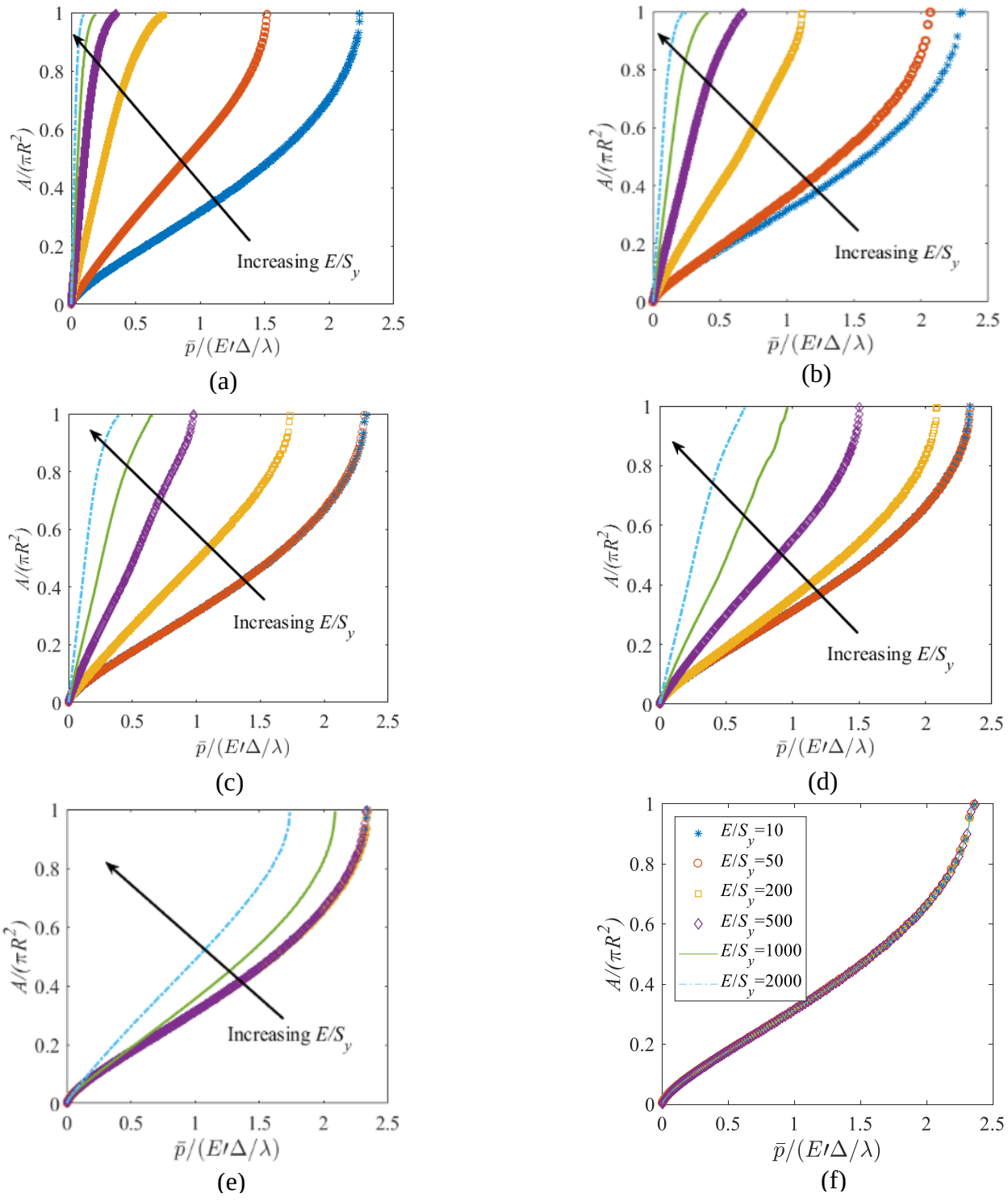

Fig. 3.13 Dimensionless contact pressure-area relation for different values of E/S_y at Young's modulus 200, Poisson's ratio 0.33 and (a) $\Delta/\lambda = 0.025$, (b) $\Delta/\lambda = 0.01$, (c) $\Delta/\lambda = 0.005$, (d) $\Delta/\lambda =$

0.0025, (e) Δ/λ=0.0005(f) Δ/λ=0.00005. (In the figures, R=λ/2 and $\bar{p}$ is the nominal contact pressure).

To investigate the reason, the average pressure, p_{ep}^*, that causes complete contact, is evaluated from the finite element model data for each of the considered cases. This value corresponds to the average pressure when the area ratio, $\frac{A}{\pi\left(\frac{\lambda}{2}\right)^2}$ is equal to 1. p_{ep}^*/p_e^* , for all the considered cases, is then plotted against $\frac{E'\Delta}{S_y\lambda}$ in Fig 3.14. This plot seems very useful, as it is successful at collapsing all of the data into a single curve.

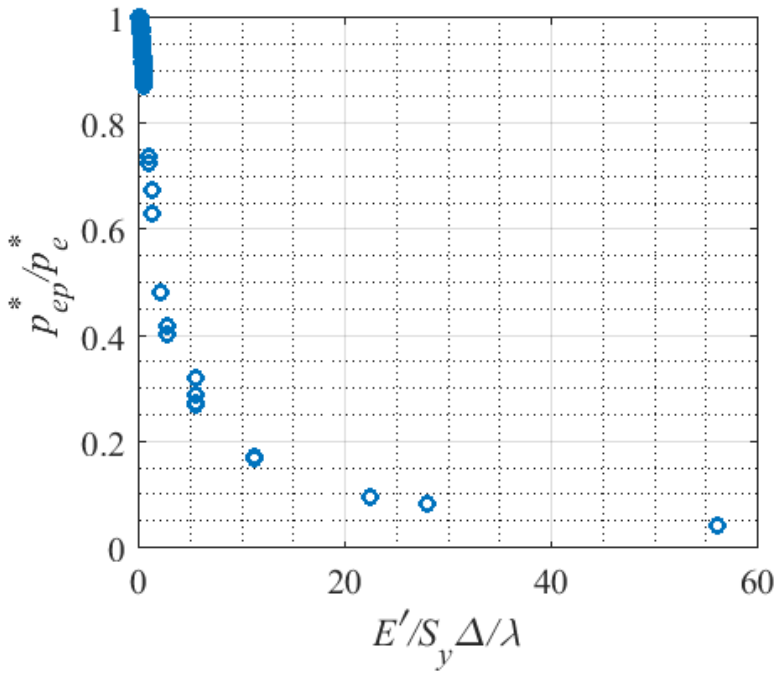

Fig. 3.14 Relation between p_{ep}^*/p_e^* with $\frac{E^*\Delta}{S_y\lambda}$ for all the cases analyzed.

From Fig.3.14, it is observed that there is a cluster of points near $p_{ep}^*/p_e^* = 1$. To investigate the transition from the elastic regime to the elastic-plastic regime, a magnified view of that region is examined in Fig.3.15, and it is found that at low values of $\frac{E^*\Delta}{S_y\lambda}$, the values of p_{ep}^*/p^* approach 1.

The cases where p_{ep}^*/p_e^* is equal to 1 are elastic because the pressure required to cause complete contact for the elastic-plastic case cannot be equal to or greater than the pressure required for the elastic case[5]. Therefore, it is important to characterize the transition point. To find out the transition point below which all cases will be elastic, additional cases are run near the cluster, and then extrapolation is made of the points approaching 1, which results in an approximate value of $\frac{E'}{S_y}\frac{\Delta}{\lambda}$ at the transition. The approximate value is,

$$\frac{E'}{S_y}\frac{\Delta}{\lambda} = 0.23 \tag{3.10}$$

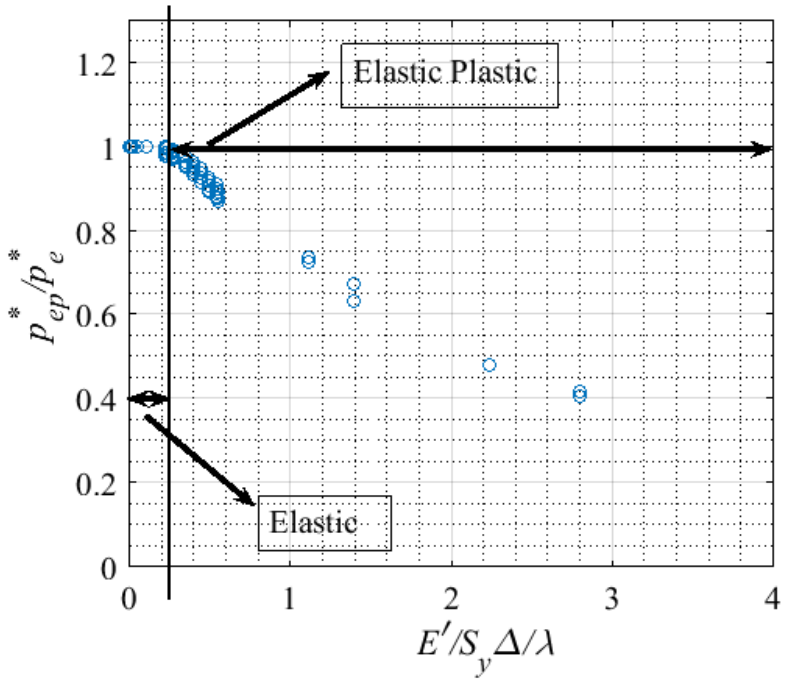

Fig. 3.15 Magnified view of the region near p_{ep}^*/p_e^*equals 1.

Defining $\Delta = \Delta_c$ at the transition point, as when $p_{ep}^* \approx p_e^*$ then the value of Δ_c (the critical amplitude) can be written as,

$$\Delta_c = 0.23\frac{S_y\lambda}{E'} \tag{3.11}$$

Therefore, when the value of Δ is less than $\Delta_{c,}$ the contact is considered to be perfectly elastic. The cases that are found elastic using Eq. (3.11) are confirmed by observing the von Mises stress from the finite element data following the distortion energy yield criterion. Based on Eq. (3.11), separating the elastic data from the elastic-plastic data, the elastic-perfectly plastic complete contact pressure curve is effectively fitted by the following equation,

$$\frac{p_{ep}^*}{p_e^*} = \left[\frac{1.009}{\left(2.634\frac{\Delta}{\Delta_c}\right)^{\left(0.25\frac{\Delta}{\lambda}+0.7307\right)^{-0.925}} + \left(0.0118\frac{\Delta}{\Delta_c}\right)^{\left(0.155\left(\frac{\Delta}{\Delta_c}\right)^{-0.789}+0.106\frac{\Delta}{\lambda}\right)}} \right]^{\left(1.605\frac{\Delta}{\Delta_c}-0.28\right)} \tag{3.12}$$

The difference between the FEM result and Eq. (3.12) is 1.21% in average and maximum error is 5.93%.

Figure 3.16(a) shows the data of all the cases, which are elastic, based on eq. (3.11). For these cases, empirical equations for the elastic case can be used to predict the contact behavior. As an example, Fig. 3.16(b) is showing the comparison of a few of the elastic cases that have been separated based on Eq. (3.11) with the elastic contact area empirical equation, i.e., Eq. (3.5).

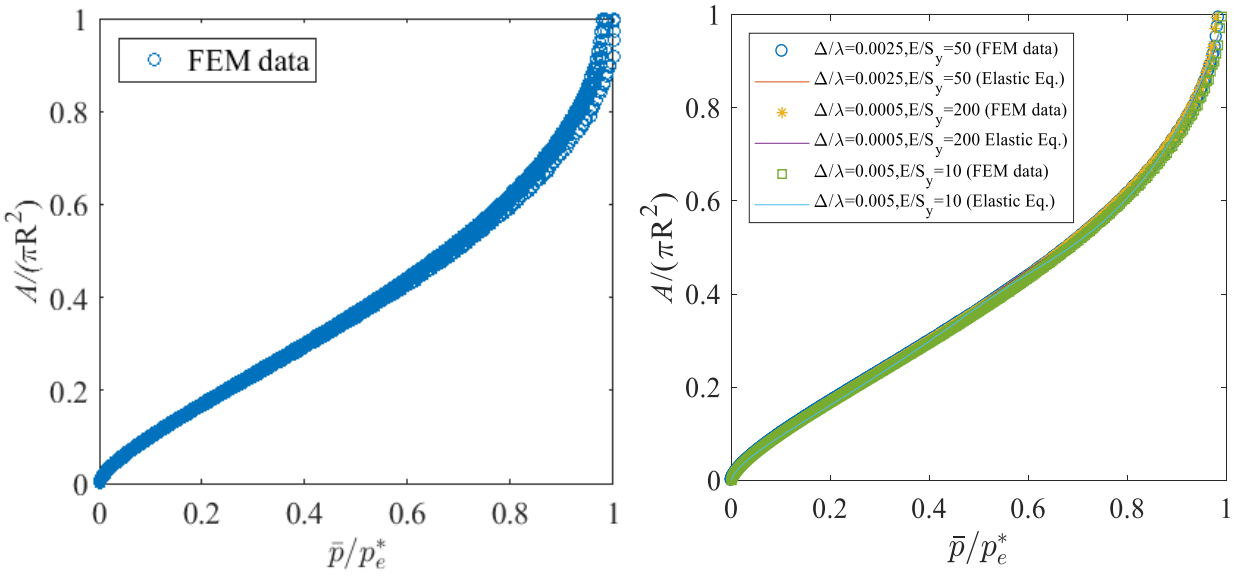

(a) (b)

Fig. 3.16 (a) Dimensionless area as a function of dimensionless contact force for all the elastic cases, (b) Comparison among Eq. (3.5) and a few of the elastic cases that have been separated based on Eq. (3.11)

3.3.2.2. Empirical Equation for Contact Area

Figure 3.17(a) shows the behavior of the normalized area as a function of normalized contact force for all the elastic-perfectly plastic cases. For the elastic-perfectly plastic cases analyzed, the value of Δ/Δ_c or $\frac{E\prime}{S_y}\frac{\Delta}{\lambda}\Big/_{0.23}$ varies in the range of 1.0 to 243.96. From the figure, it is visible that, with the increase in loading, all the curves gradually diverge due to plastic deformation. However, they converge again near the complete contact. The difference might be due to the tendency of elastic contact to compress while contacts dominated by plastic deformation tend to expand laterally. From Fig. 3.17(a), it seems that all the cases are almost on the same curve at low load while it is not. The magnified view at low load is shown in Fig. 3.17(b). When $\frac{\Delta}{\Delta_c}$ equals 1.0, the shape of the

curve is similar to Hertz contact at low load. Then, with the increase of $\frac{\Delta}{\Delta_c}$ values, the range where the Hertz model works decreases, and the normalized contact pressure-area relation also becomes more and more linear. From Fig. 3.17(b), it is clear that when $\frac{\Delta}{\Delta_c}$ Equals to 243.96, the normalized contact-pressure area relation is almost linear in behavior at the beginning of the contact. Again from Fig. 3.17(a), when Δ/Δ_c equals to 1.0, i.e., just at the transition point from elastic to elastic-perfectly plastic contact, the normalized contact pressure-area behavior is very similar to the normalized elastic contact pressure-area behavior. Then, when Δ/Δ_c becomes 12.2, an almost linear relationship is observed. With the increase of $\Delta/\Delta c$ ratios, the cases are becoming more and more plastic, and more and more area is coming into contact at the same amount of applied contact force. To investigate this behavior in detail, $\frac{w_c}{\Delta_c}$ has been plotted against $\frac{\Delta}{\Delta_c}$, w_c is the critical value of interference at which initial yielding starts (see Fig. 3.17(c)). When $\frac{\Delta}{\Delta_c}$ is close to 1.0, a high value of displacement is required for initial yielding. At the small value of $\frac{\Delta}{\Delta_c}$, the required value of initial yielding changes very dramatically with little change in $\frac{\Delta}{\Delta_c}$. From Fig. 3.17(c) it is clear that, the data point for $\frac{\Delta}{\Delta_c}$ equal to 12.2 is situated at this dramatic change or transition. When $\frac{\Delta}{\Delta_c}$ is greater than 12.2, very small values of displacement can cause initial yielding. Based on the observed transitions in Fig. 3.17(a-c), equations are fit into two different ranges of data. One is for $1 \leq \frac{\Delta}{\Delta_c} \leq 12.2$ and another is for $12.2 \leq \frac{\Delta}{\Delta_c} \leq 243.96$.

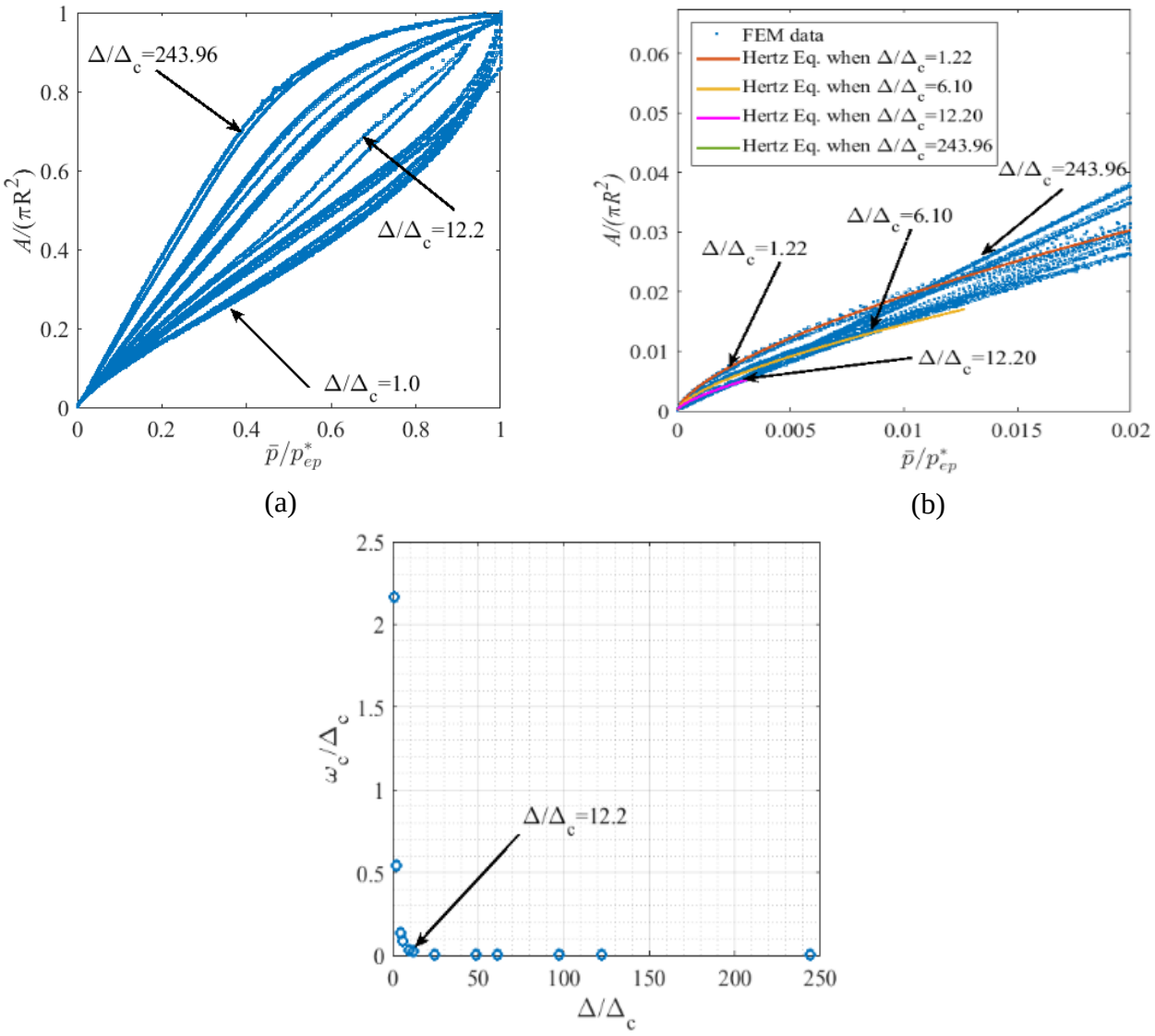

Fig. 3.17 (a) Dimensionless area as a function of dimensionless contact force for all the elastic-plastic cases. (In the figures, $R = \frac{\lambda}{2}$ and $\bar{p}$ is the nominal pressure i.e.$\bar{p} = \frac{F}{\pi R^2}$), (b) Magnified view of Fig.14(a) at low load, (c) Dimensionless interference as a function of dimensionless amplitude for all the elastic-perfectly plastic cases.

The fit equations are:

Contact pressure-area relation when $\mathbf{1} \leq \frac{\Delta}{\Delta_c} \leq \mathbf{12.2}$:

$$\frac{A}{\pi\left(\frac{\lambda}{2}\right)^2} = 0.4\left(\frac{\bar{p}}{p_{ep}^*}\right)^{(2/3+a)}\left(1-\frac{\bar{p}}{p_{ep}^*}\right)^{(1.4+b)} + \left(0.8+(1-0.8)\left(\frac{\bar{p}}{p_{ep}^*}\right)^c\right)\left(\frac{\bar{p}}{p_{ep}^*}\right)^{(1.6+d)} \quad (3.13)$$

where,

$$a = 0.007\left(\frac{\Delta}{\Delta_c}\right) - 0.007$$

$$b = 0.1 - 0.1\left(\frac{\Delta}{\Delta_c}\right)$$

$$c = 11\left(\frac{\Delta}{\Delta_c}\right)^{-0.42}\left(\frac{\Delta}{\lambda}\right)^{-0.1} + 2.0$$

$$d = 0.03 - 0.03\left(\frac{\Delta}{\Delta_c}\right)$$

The average difference between Eq. (3.13) and the FEM results is 2.55%, and the maximum error is 9.96%. The format of Eq.(3.13) is very similar to the equation of the contact area for the elastic cases when $\frac{\Delta}{\Delta_c}$ equal to 1.0. The equation is valid from initial contact up to the complete contact. When $\frac{\bar{p}}{p_e^*} < 0.0005$, the spherical Hertz equation for the contact area can be used.

Contact pressure-area relation when $\mathbf{12.2} \leq \frac{\Delta}{\Delta_c} \leq \mathbf{243.96}$:

$$\frac{A}{\pi\left(\frac{\lambda}{2}\right)^2} = 0.908\left(\frac{\bar{p}}{p_{ep}^*}\right)^{(0.33+a)}\left(1-\frac{\bar{p}}{p_{ep}^*}\right)^b + \left(\frac{\bar{p}}{p_{ep}^*}\right)^{c-0.24} \quad (3.14)$$

In Eq. (3.14),

$$a = 0.5185\left(\frac{\Delta}{\Delta_c}\right)^{\left(0.9\left(\frac{\Delta}{\lambda}\right)^{2.1}+0.018\right)}$$

$$b = 0.26\left(\frac{\Delta}{\lambda}\right)^{-0.03} + 0.95$$

$$c = \left(\left(5.5\left(\frac{\bar{p}}{S_y}\right)^{-1.06} - 0.072\right)\frac{\bar{p}}{p_{ep}^*} + 0.00006^{\left(0.014\left(\frac{\bar{p}}{S_y}\right)^{\left(3.3+1.5\frac{\Delta}{\lambda}+0.125\right)}\right)}\right)$$

The difference between Eq. (3.14) and the FEM results is 1.54% on average, and the maximum error is 10.6%. Equation (3.14) is valid when $\frac{\bar{p}}{p_e^*} \geq 0.001$. The data below $\frac{\bar{p}}{p_e^*} < 0.001$ agrees well with the JG model. So when $\frac{\bar{p}}{p_e^*} < 0.001$, the JG model can be used.

3.3.2.3. Empirical Equation for Nominal Pressure as a Function of Surface Separation

In addition to determining the contact area, it is important to predict pressure as a function of surface separation. Therefore, the effect of different parameters ($\frac{E\prime}{S_y}$ and $\frac{\Delta}{\lambda}$) have been observed. Fig. 3.18(a) shows that, for increasing E/S_y ratios, the average contact pressure required to reach complete contact gradually decreases. The same trend is also observed with the decrease in $\frac{\Delta}{\lambda}$ ratios, as shown in Fig. 3.18(b). In Fig. 3.18(b), the curves for E/S_y=10, 50, 200 and 500, $\frac{\Delta}{\lambda} = 0.025$ coincide with each other as those cases are elastic. All the cases considered are not shown or discussed here because they show the same trends, i.e., with the decrease in $\frac{\Delta}{\lambda}$ ratio, the effect of E/S_y decreases, and at Δ/λ =0.00005, the curves for all the E/S_y cases collapse into a single curve and are completely elastic (according to the Eq. (3.11)).

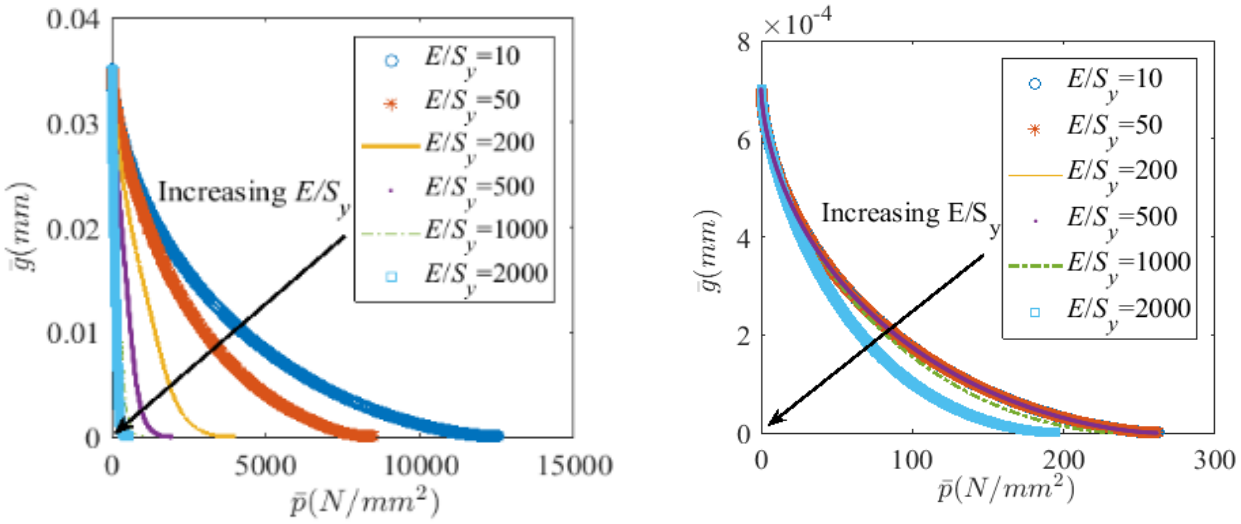

Fig. 3.18 (a) Nominal pressure vs. average surface separation for E=200 GPa, υ=0.33, for different values of E/S_y ratio at Δ/λ=0.025 (b) Nominal pressure vs. average surface separation for E=200 GPa, υ=0.33, for different values of E/S_y ratio at Δ/λ=0.0005. (In the figures, $R = \frac{\lambda}{2}$ and $\bar{p}$ is the nominal pressure i.e. $\overline{p} = \frac{F}{\pi R^2}$).

After normalizing the nominal pressure, $\bar{p}$ and average surface separation, $\bar{g}$ by p_{ep}^* and $\overline{g_o}$ respectively, the same cases shown in Fig. 3.18(a) and (b) are shown in Fig. 3.19(a) and 3.19(b). The normalized curves do not coincide with each other, as found for the elastic cases (see sec. 3.3.1.3). As with the contact area for elastic-plastic cases, the normalized surface separation doesn't depend on only the normalized contact pressure.

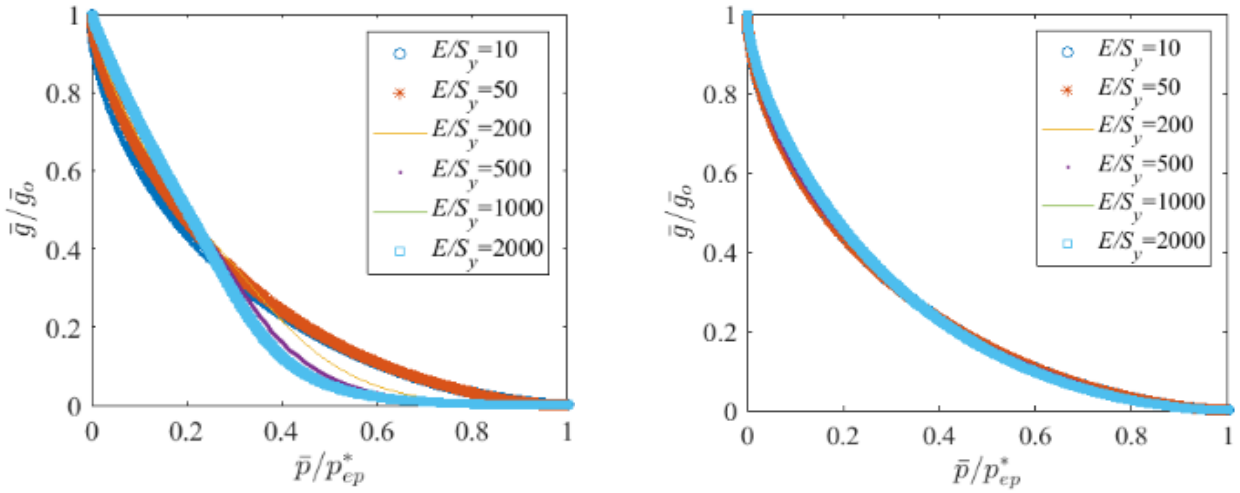

(a) (b)

Fig. 3.19 (a) Normalized nominal pressure vs. normalized surface separation for E=200 GPa, υ=0.33, for different values of E/S_y ratio at Δ/λ=0.025 (b) Normalized nominal pressure vs. normalized surface separation for E=200 GPa, υ=0.33, for different values of E/S_y ratio at Δ/λ=0.0005.

To quantify the surface separation so that it can be applied to rough surface contact modeling for solving practical engineering problems, three empirical equations have been found. The results are divided into three ranges. One is for $1 \leq \frac{\Delta}{\Delta_c} \leq 12.2$, another one is for $12.2 < \frac{\Delta}{\Delta_c} \leq 48.8$ and $48.8 < \frac{\Delta}{\Delta_c} \leq 243.96$

When $1 \leq \frac{\Delta}{\Delta_c} \leq 12.2$:

$$\frac{\bar{p}}{p^*_{ep}} = (1 - {G_n}^a)^b \tag{3.15}$$

where,

$$a = 0.185\left(\frac{E'}{S_y}\frac{\Delta}{\lambda}\right)^{\left(1.03{G_n}^2\right)} + 1.28\left(\frac{\Delta}{\Delta_c}\right)^{\left(0.72\left(\frac{\Delta}{\lambda}\right)^{1.4}\right)} - 0.91$$

$$b = \left[0.027\left(\frac{\Delta}{\Delta_c} - 1\right)^{0.44}\right]G_n + 1.5$$

The average difference between Eq. (3.15) and the FEM results is 2.75% on average, and the maximum difference is 9.49%. The equation is valid from initial contact to complete contact.

When $\mathbf{12.2 < \frac{\Delta}{\Delta_c} \leq 48.8}$:

$$\frac{\bar{p}}{p^*_{ep}} = (1 - {G_n}^a)^b \tag{3.16}$$

where,

$$a = 0.75{G_n}^{\left(-0.039\left(\frac{\Delta}{\Delta_c}\right)^{0.12}\right)}$$

$$b = c{G_n}^{\left(-0.9\left(\frac{\Delta}{\lambda}\right)^{0.012}\right)} + 7.17\left(\frac{\Delta}{\Delta_c}\right)^{-0.051} - 5.066$$

In the above expression,

$$c = \left[64.401\left(\frac{E'}{S_y}\frac{\Delta}{\lambda}\right)^{\left(0.0044\left(\frac{E\prime}{S_y}\right)^{-0.0476}\right)} - 64.338\right]$$

The average difference between Eq. (3.16) and the FEM results is 3.14%, and the maximum error is 10.6%. The above equation is valid when $\frac{\bar{p}}{p^*_{ep}} \geq 0.0004$. Below that it behaves elastically, which is confirmed by comparing with Eq. (3.9). Therefore when $\frac{\bar{p}}{p^*_{ep}} \leq 0.0004$, Eq. (3.9) can be used.

When $48.8 < \frac{\Delta}{\Delta_c} \leq 243.96$:

$$\frac{\bar{p}}{p_{ep}^*} = (1 - {G_n}^a)^b \tag{3.17}$$

where,

$$a = 0.781 G_n^{\left(-0.03\left(\frac{\Delta}{\Delta_c}\right)^{0.13}\right)}$$

$$b = c G_n^{\left(-0.92\left(\frac{\Delta}{\bar{\lambda}}\right)^{0.017}\right)} + 7.01\left(\frac{\Delta}{\Delta_c}\right)^{-0.052} - 4.912$$

In the above expression,

$$\boldsymbol{c} = \left[68.745\left(\frac{E'}{S_y}\frac{\Delta}{\lambda}\right)^{\left(0.004\left(\frac{E\prime}{S_y}\right)^{-0.0405}\right)} - 68.675\right]$$

The difference between the above equation and the FEM results is 3.70% on average, and the maximum difference is 9.94%. For almost the entire range of pressure, the behavior is elastic-plastic.

3.3.3. The Nominal Pressure to Yield Strength Ratio

Analyzing all the elastic-perfectly plastic results, it is found that, Δ/Δ_c and $\frac{a}{\lambda/_2}$, actually, control how the behavior of the nominal pressure to yield strength changes. In Fig. 3.20(a), i.e., when $1 \leq \frac{\Delta}{\Delta_c} \leq 12.2$, for all the cases $\frac{\bar{p}}{S_y}$ reaches a maximum value but then decreases with $\frac{a}{\lambda/_2}$. With the increase of Δ/Δ_c, this maximum value of $\frac{\bar{p}}{S_y}$ gradually increases. When Δ/Δ_c equals 12.2, $\frac{\bar{p}}{S_y}$ reaches

a maximum value of about 2.9 and then changes very little. This is the case where an almost linear contact pressure-area relationship is observed. With a further increase in Δ/Δ_c values, i.e., when $12.2 < \frac{\Delta}{\Delta_c} \leq 243.96$, $\frac{\bar{p}}{S_y}$ increases linearly and then become nearly constant with the increase of $\frac{a}{\lambda/_2}$, until increasing again at a high value of $\frac{a}{\lambda/_2}$. Then with further increases in $\frac{a}{\lambda/_2}$, $\frac{\bar{p}}{S_y}$ continuously increases up to values above 3. Both of these trends are shown in Fig. 3.20(a) and 3.20(b), have also been observed in the work of Gao et al. [21] for 2D plain-strain sinusoidal contact. Although in their work more concentration was given to higher Δ/λ ratios ($0.01 \leq \frac{\Delta}{\lambda} \leq 0.1$), the maximum value of $\frac{E'}{S_y}\frac{\Delta}{\lambda}$ was 54.95 whereas the maximum value of $\frac{E'}{S_y}\frac{\Delta}{\lambda}$ for the current research is 56.11 ($0.00005 \leq \frac{\Delta}{\lambda} \leq 0.025$). The maximum value of $\frac{\bar{p}}{S_y}$ in their research was about 5.9. Liu model [29] has given a general expression for average contact pressure to yield strength ratio, which is only a function of $\frac{\Delta}{\lambda}$ and normalized interference, $\frac{\omega}{\Delta}$. However, the current analysis clearly shows that the nominal pressure to yield strength ratio depends on Δ/Δ_c and $\frac{a}{\lambda/_2}$. In the work of Krithivasan et al. [4], the maximum observed value of $\frac{\bar{p}}{S_y}$ was approximately 6.0 at the maximum value of $\frac{E'}{S_y}\frac{\Delta}{\lambda}$ =20.51. The work of Manners [6] showed that both for the upper and lower bound analysis the value of $\frac{\bar{p}}{S_y}$ may rise to infinity; however, it was concluded that elastic-plastic interaction and boundary conditions are responsible for the finite value in the analysis of Gao et al. [21]. To investigate this upper limit of $\frac{\bar{p}}{S_y}$, a simulation is performed at a very high value of $\frac{E'}{S_y}\frac{\Delta}{\lambda}$ =280.55, i.e., ≈ 1220 and the value of $\frac{\bar{p}}{S_y}$ at complete contact is 5.8 for this case. So it seems that although with the increase of $\frac{E'}{S_y}\frac{\Delta}{\lambda}$, the value of $\frac{\bar{p}}{S_y}$ at complete contact has increased, for most of

the materials the value of $\frac{\bar{p}}{S_y}$ at complete contact will be less than 6. Change of $\frac{\bar{p}}{S_y}$ at complete contact with $\frac{E'}{S_y}\frac{\Delta}{\lambda}$ has shown in Fig. 3.21.

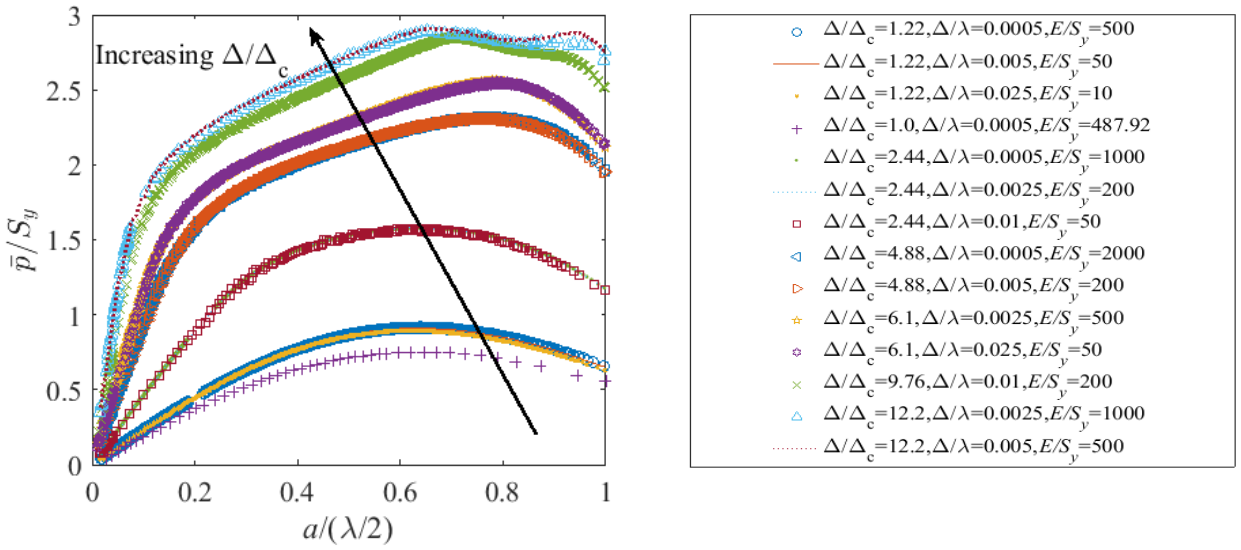

(a)

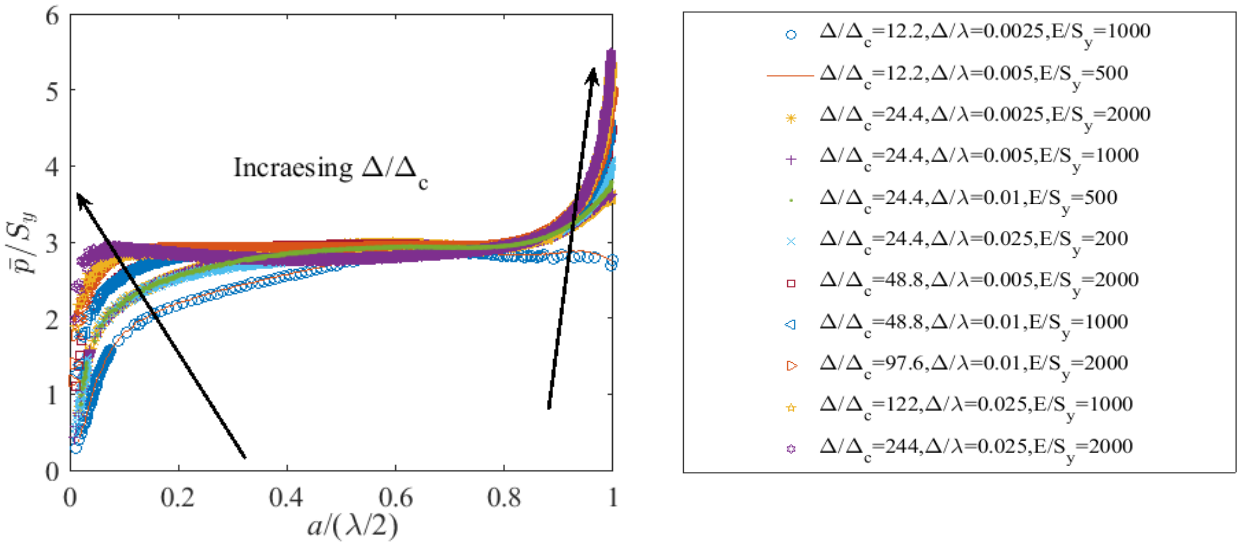

(b)

Fig. 3.20(a) $\frac{\bar{p}}{S_y}$ vs. $\frac{a}{\lambda/2}$ for $1 \leq \frac{\Delta}{\Delta_c} \leq 12.2$, (b) $\frac{\bar{p}}{S_y}$ vs. $\frac{a}{\lambda/2}$ for $12.2 \leq \frac{\Delta}{\Delta_c} \leq 243.96$

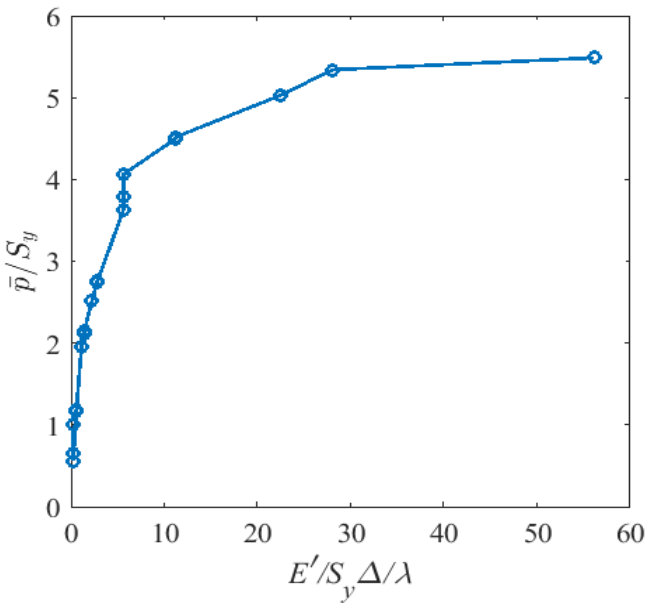

Fig. 3.21 Change of $\frac{\bar{p}}{S_y}$ at complete contact with $\frac{E'}{S_y}\frac{\Delta}{\lambda}$.

3.3.4. Comparison with the Available 2D Axisymmetric Sinusoidal Asperity Models:

As discussed in chapter 2, Liu [29] has performed an analysis on elastic-plastic axisymmetric sinusoidal asperity contact with linear hardening (less than 2%*E* bilinear hardening, *E* is Young's modulus). Previous research [30] shows that isotropic material with upto 5%*E* bilinear hardening has a negligible hardening effect on the contact behavior. Therefore, the results of this chapter will be compared with the Liu model. In the Liu model, the surface asperity height to width ratio was varied in the range of 0.01 to 0.4, and the analysis was done only for gold. However, they provided a general expression for the normalized contact radius. The equation for the contact radius is the following:

$$a_\lambda = \frac{\arccos(1-k_a d_g)}{\pi} \tag{3.18}$$

where,

$a_\lambda = \frac{a}{\lambda/2}$, ($a$ is the contact radius, and λ is the wavelength of the sinusoidal asperity)

$d_g = \frac{d}{g}$, (d is the interference, and g is the amplitude of the sinusoidal asperity)

$k_a = \frac{2.15 g_\lambda}{(0.008 + g_\lambda)}$,$(g_\lambda = \frac{g}{\lambda})$.

According to Liu [29], when k_a is 2.0, Eq. (3.18) represents the truncation model [31]. Truncation model [31] cannot predict elastic-plastic behavior properly. That's why Liu [29] proposed the modified truncation model (Eq. (3.18)). The Liu model agrees well with the ZMC model [32], which also cannot predict the elastic-plastic behavior properly, as discussed in chapter 2. Later in 2016, Liu et al. [33] showed that the $\frac{S_y}{E}$ ratio has a significant effect on the elastic-plastic behavior. Therefore, the modified truncation model given by Liu [29] will not work for all the cases. This has shown in this chapter in Fig. 3.22.

Actually, in 2016, the author showed in one of the published works [34] that, it is not only $\frac{E}{S_y}$ ratio but the combined effect of $\frac{E}{S_y}$ and surface asperity height and width ratio, $\frac{\Delta}{\lambda}$ govern the elastic-perfectly plastic behavior. Later, in another published work [18] (2017), the author provided the following empirical equation to predict the contact area of the axisymmetric elastic-plastic axisymmetric sinusoidal asperity contact:

$$\frac{A}{\pi R^2} = \frac{A}{\pi\left(\frac{\lambda}{2}\right)^2} = \frac{2}{\pi}\left(\frac{\bar{P}}{P^*_{ep}}\right)^{C_2'\left(\bar{P}/P^*_{ep}\right)}\left\{sin^{-1}\left[\left(\frac{\bar{P}}{P^*_{ep}}\right)^{0.16}\right]\right\}^{C_3'} \tag{3.19}$$

$$C_2' = 0.64 + \left[1.14 - \frac{1}{1.25}\left(\frac{E'}{S_y}\frac{\Delta}{\lambda}\right)^{0.32}\right]$$

$$C_3' = 1 + \frac{1}{200}\left(\frac{E'}{S_y}\frac{\Delta}{\lambda}\right)$$

In the above equation, $\bar{P}$ is the nominal pressure and P_{ep}^* can be calculated using the following expression:

$$\frac{P_{ep}^*}{P^*} = \frac{0.67}{0.653\left(\frac{E'}{S_y}\frac{\Delta}{\lambda}\right)^{0.0027} + 0.22\left(\frac{E'}{S_y}\frac{\Delta}{\lambda}\right)^{s}} \tag{3.20}$$

$$s = 1.6\left(\frac{E'}{S_y}\frac{\Delta}{\lambda}\right)^{-0.141}$$

$$P^* = \frac{3}{4}\pi E'\frac{\Delta}{\lambda} \tag{3.21}$$

P^* is the equation of contact pressure at complete contact for the elastic case. Although the above contact area equation (Eq. (3.19)) is a lot simpler compared to the contact area equations described in this chapter, a significant amount of improvements have been made in the current model. Following improvements have been made in the current work, which is also published in 2020 [35]:

- In [18 and 34] the value of $\frac{\Delta}{\Delta_c}$ varied in the range of 1 to 80.16 whereas in the model described in this chapter, $\frac{\Delta}{\Delta_c}$ varied in the range of 1 to 243.96, which covers almost all the metallic materials.
- The model described in this chapter is continuous from the elastic to the elastic-plastic regime and also for the whole range of $\frac{\Delta}{\Delta_c}$ considered in this work. For example, when $\frac{\Delta}{\Delta_c}$ is less than 1.0, the cases are elastic and empirical equations for the elastic contact model

can be used. When $\frac{\Delta}{\Delta_c} \geq 1.0$, the cases are elastic-perfectly plastic in nature, and separate equations have provided. However, this continuity from elastic to elastic-plastic regime has not confirmed in Ref. [19].

- The equations developed in the current work are applicable from very low load to complete contact, as all the cases match with either the Hertz model or the Jackson-Green model at low load. The lower limit has been clearly defined below which the spherical contact model can be applied. These have not shown and confirmed in Ref. [19].
- A stiffness test has been performed for the current model so that there is no effect of contact stiffness on the model, which was not confirmed in [19] and [34].
- Besides these, the number of elements in the current model is higher than [19, 34], and the number of elements has been selected such that it agrees with either Hertz or Jackson-Green model at low load.
- Empirical equations for contact pressure as a function of surface separation have provided both for elastic and elastic-perfectly plastic cases in this chapter and in [35].

Figure 3.22 (a), (b), (c) and (d) are showing the normalized contact pressure-area relation for different values of $\frac{\Delta}{\Delta_c}$. When $\frac{\Delta}{\Delta_c}$ equals 1.22 and 6.10 i.e. the effect of elastic behavior is dominant, FEM data of the current analysis matches well with Ref. [19]. From the previous discussion, with the increase of $\frac{\Delta}{\Delta_c}$, the effect of plasticity becomes dominant. As the model published in [19] has 1%E bilinear hardening, with the increase of $\frac{\Delta}{\Delta_c}$, the current FEM data shows a deviation from the Ref. [19] because the current model is elastic perfectly plastic.

The Liu model [29] was developed by modifying the truncation or Abbott and Firestone model [31]. So when $\frac{\Delta}{\Delta_c}$ is less than 12.2, i.e. the effect of elastic behavior is dominant, the FEM data

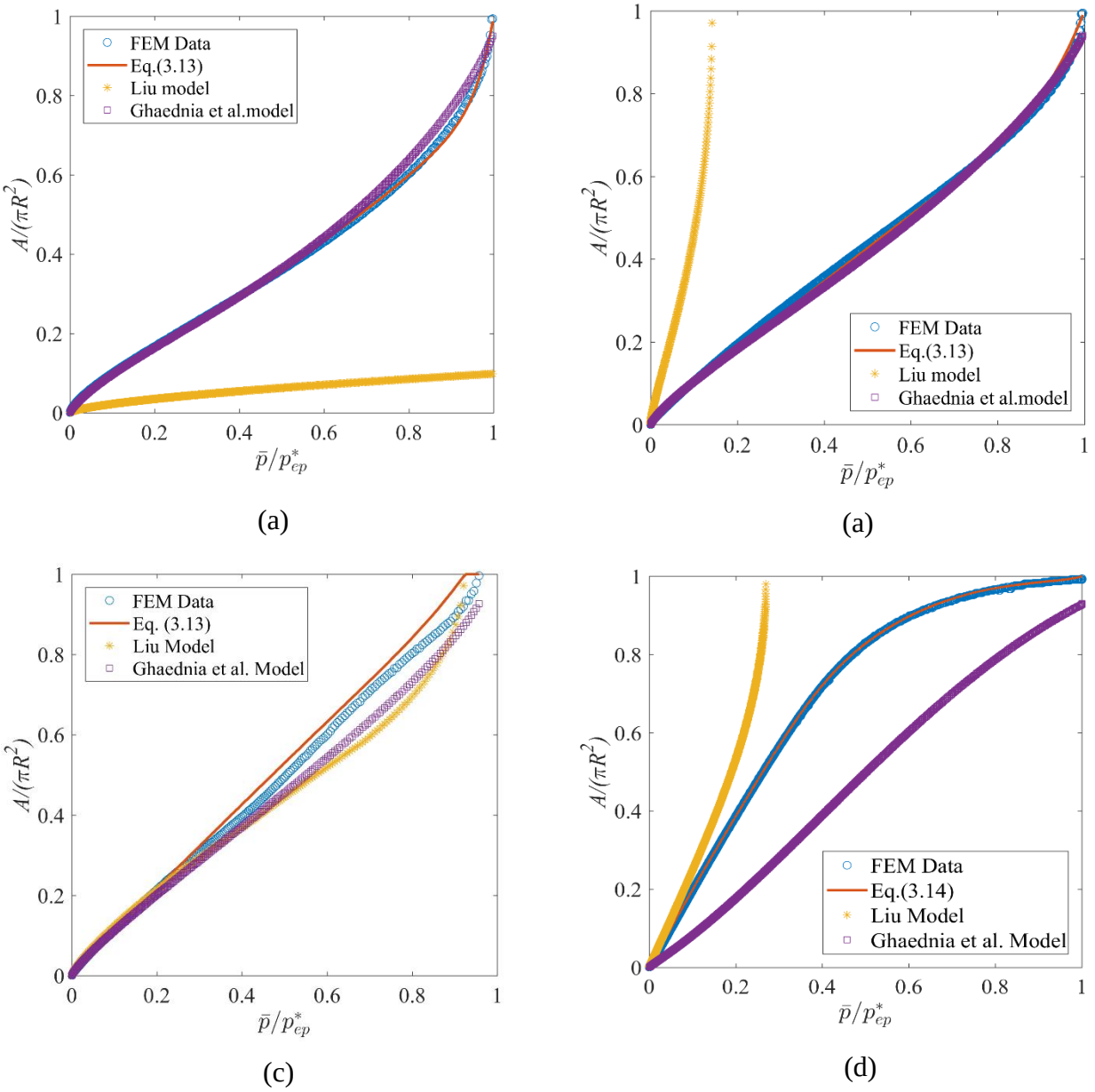

Fig. 3.22 Comparison of the normalized nominal pressure-contact area relation with Liu model and Ghaednia et al. model when (a) $\frac{\Delta}{\Delta_c}$ equal to 1.22 (b) $\frac{\Delta}{\Delta_c}$ equal to 6.10 (c) $\frac{\Delta}{\Delta_c}$ equal to 12.2 (d) $\frac{\Delta}{\Delta_c}$ equal to 243.96.

doesn't match with the Liu model. When $\frac{\Delta}{\Delta_c}$ equals 12.2, that is when small deformation can cause yielding in the material, the FEM data matches with the Liu model [29] to some extent. However, in the Liu model [29], the effect of change in material properties has been completely disregarded. That is why with the increase of $\frac{\Delta}{\Delta_c}$, when the effect of yield strength becomes important, the current analysis does not agree with the Liu model [29].

3.4. Summary

- An axisymmetric sinusoidal asperity model for the elastic and elastic-perfectly plastic cases is developed which reduces computational time to a great extent. Interaction with adjacent asperities and the effect of the substrate below the asperity have also been considered. Interaction with adjacent asperities becomes very important for medium to high load ranges.
- The model matches well with the spherical Hertz and JG model at low loads. The transition point from spherical to sinusoidal asperity model has been quantified and specified.
- Although a few works on the axisymmetric sinusoidal asperity contact have been performed, none of those works properly quantified the parameters that govern the behavior of the elastic and elastic-perfectly plastic axisymmetric sinusoidal asperity behavior. The current analysis shows that not any single parameter but different combinations of material properties and surface roughness govern the whole contact behavior.
- In this work, the transition from elastic to elastic-perfectly plastic behavior has been quantified, and empirical equations for the average contact pressure, contact area, surface separation are formulated for a wide range of material properties and Δ/λ ratios. These

empirical equations are applicable from low load to complete contact and should be useful for complex rough surface modeling and analysis.

- Besides these, an investigation has been done on the average contact pressure to yield strength ratio which is actually controlled by two parameters, $\Delta/\Delta_c \left(\frac{E'}{S_y} \frac{\Delta}{\lambda} \Big/ 0.23 \right)$ and contact width ratio, $\frac{a}{\lambda/2}$. When Δ/Δ_c is equal to or close to one, i.e. at the transition from elastic to elastic-perfectly plastic behavior, the maximum value of $\frac{\bar{p}}{S_y}$ is less than 1, as there is no yielding at the contact surface. Yielding occurs below the surface for those cases. When Δ/Δ_c is less than 12.2, $\frac{\bar{p}}{S_y}$actually increases with contact width and reaches a maximum value and then reduces with further increases in contact width (which is similar to spherical asperity behavior). At Δ/Δ_c=12.2, $\frac{\bar{p}}{S_y}$ reaches a maximum value of three and then changes little. With further increases in Δ/Δ_c, $\frac{\bar{p}}{S_y}$ increases continuously. However, for most of the metallic materials, the value does not appear to exceed the value 6.0 at complete contact.

References

1. Ciavarella, M., Demelio, G., Barber, J. R., & Jang, Y. H. (2000). Linear elastic contact of the Weierstrass profile. Proceedings of the Royal Society of London. Series A: Mathematical, Physical and Engineering Sciences, 456(1994), 387-405.
2. Gao, Y. F., & Bower, A. F. (2006). Elastic–plastic contact of a rough surface with Weierstrass profile. Proceedings of the Royal Society A: Mathematical, Physical and Engineering Sciences, 462(2065), 319-348.
3. Jackson, R. L. (2010). An analytical solution to an Archard-type fractal rough surface contact model. Tribology Transactions, 53(4), 543-553.
4. Krithivasan V, Jackson RL. (2007). An analysis of threedimensional elasto-plastic sinusoidal contact. Tribol Lett. 27(1), 31–43.
5. Jackson, R. L., Krithivasan, V., & Wilson, W. E. (2008). The pressure to cause complete contact between elastic-plastic sinusoidal surfaces. Proceedings of the Institution of Mechanical Engineers, Part J: Journal of Engineering Tribology, 222(7), 857-863.
6. Manners, W. (2008). Plastic deformation of a sinusoidal surface. Wear, 264(1-2), 60-68.
7. Stanley, H. M., & Kato, T. (1997). An FFT-based method for rough surface contact, J. Tribol. 119(3), 481-485.
8. Wilson, W. E., Angadi, S. V., & Jackson, R. L. (2010). Surface separation and contact resistance considering sinusoidal elastic–plastic multi-scale rough surface contact. Wear, 268(1-2), 190-201.
9. Jackson, R. L., Ghaednia, H., Elkady, Y. A., Bhavnani, S. H., & Knight, R. W. (2012). A closed-form multiscale thermal contact resistance model. IEEE Transactions on Components, Packaging and Manufacturing Technology, 2(7), 1158-1171.

10. Jackson, R. L., Crandall, E. R., & Bozack, M. J. (2015). Rough surface electrical contact resistance considering scale dependent properties and quantum effects. Journal of Applied Physics, 117(19), 195101.
11. Jackson, R. L., & Streator, J. L. (2006). A multi-scale model for contact between rough surfaces. Wear, 261(11-12), 1337-1347.
12. Jackson, R. L., Malucci, R. D., Angadi, S., & Polchow, J. R. (2009). A simplified model of multiscale electrical contact resistance and comparison to existing closed form models. In 2009 Proceedings of the 55th IEEE Holm Conference on Electrical Contacts, 28-35. IEEE.
13. Greenwood, J. A. (2015, September). Half a century of the Greenwood and Williamson Paper. In 42nd Leeds-Lyon Symposium on Tribology, Lyon, France, 7-9.
14. Greenwood, J. A., & Williamson, J. P. (1966). Contact of nominally flat surfaces. Proceedings of the royal society of London. Series A. Mathematical and physical sciences, 295(1442), 300-319.
15. Johnson, K. L., Greenwood, J. A., & Higginson, J. G. (1985). The contact of elastic regular wavy surfaces. International journal of mechanical sciences, 27(6), 383-396.
16. Johnson, K. L., & Johnson, K. L. (1987). Contact mechanics. Cambridge university press.
17. Shah, S., Krithivasan, V., & Jackson, R. L. (2011). An electro-mechanical contact analysis of a three-dimensional sinusoidal surface against a rigid flat. Wear, 270(11-12), 914-921.
18. Rostami A, Jackson RL. (2013). Predictions of the average surface separation and stiffness between contacting elastic and elastic–plastic sinusoidal surfaces. Proc Inst mech Eng, Part J., 227(12):1376–1385.

19. Ghaednia, H., Wang, X., Saha, S., Xu, Y., Sharma, A., & Jackson, R. L. (2017). A review of elastic–plastic contact mechanics. Applied Mechanics Reviews, 69(6), 060804.
20. Westergaard, H. M. (1939). Bearing pressures and cracks. Trans AIME, J. Appl. Mech., 6, 49-53.
21. Gao, Y. F., Bower, A. F., Kim, K. S., Lev, L., & Cheng, Y. T. (2006). The behavior of an elastic–perfectly plastic sinusoidal surface under contact loading. Wear, 261(2), 145-154.
22. Zhang, X., Xu, Y., & Jackson, R. L. (2017). An analysis of generated fractal and measured rough surfaces in regards to their multi-scale structure and fractal dimension. Tribology International, 105, 94-101.
23. An, B., Wang, X., Xu, Y., & Jackson, R. L. (2019). Deterministic elastic-plastic modelling of rough surface contact including spectral interpolation and comparison to theoretical models. Tribology International, 135, 246-258.
24. Wang, X., Xu, Y., & Jackson, R. L. (2018). Theoretical and finite element analysis of static friction between multi-scale rough surfaces. Tribology Letters, 66(4), 146.
25. Xu, Y. (2017). Statistical Models of Nominally Flat Rough Surface Contact, Doctoral dissertation, Auburn University.
26. Hertz, H., Jones, D. E., & Schott, G. A. (1896). Miscellaneous papers. Macmillan and Company.
27. Jackson, R. L., & Green, I. (2005). A finite element study of elasto-plastic hemispherical contact against a rigid flat. J. Trib., 127(2), 343-354.
28. Wadwalkar, S. S., Jackson, R. L., & Kogut, L. (2010). A study of the elastic—plastic deformation of heavily deformed spherical contacts. Proceedings of the Institution of Mechanical Engineers, Part J: Journal of Engineering Tribology, 224(10), 1091-1102.

29. Liu, M. (2014). Finite element analysis of large contact deformation of an elastic–plastic sinusoidal asperity and a rigid flat. International Journal of Solids and Structures, 51(21-22), 3642-3652.
30. Kadin, Y., Kligerman, Y., & Etsion, I. (2008). Loading–unloading of an elastic–plastic adhesive spherical microcontact. Journal of Colloid and Interface Science, 321(1), 242-250.
31. Abbott, E. J., & Firestone, F. A. (1995). Specifying surface quality: a method based on accurate measurement and comparison. Spie Milestone Series MS, 107, 63-63.
32. Zhao, Y., Maietta, D. M., & Chang, L. (2000). An asperity microcontact model incorporating the transition from elastic deformation to fully plastic flow. J. Trib., 122(1), 86-93.
33. Liu, M., & Proudhon, H. (2016). Finite element analysis of contact deformation regimes of an elastic-power plastic hardening sinusoidal asperity. Mechanics of Materials, 103, 78-86.
34. Saha, S., & Jackson, R. L. (2016). Elastic-plastic axisymmetric sinusoidal surface asperity contact. In 2016 IEEE 62nd Holm Conference on Electrical Contacts (Holm), 17-24. IEEE.
35. Saha, S., & Jackson, R. L. (2020). Elastic and elastic-perfectly plastic analysis of an axisymmetric sinusoidal surface asperity contact. Tribology-Materials, Surfaces & Interfaces, 14(1), 1-21.

Chapter 4

Literature Review on Rough Surface Contact Models and Determination of Electrical Contact Resistance

4.1 Introduction

Whether natural or synthetic, one surface varies from the other a lot depending on their formation, finishing, and the requirement for any particular application. As already discussed in Chapter 1, there are different numerical and analytical methods available to predict the behavior of rough surfaces in contact. This chapter will describe the previous research works on the rough surface contact models. However, before reviewing the literature, the terminologies that are generally used to explain the rough surface contact models will be described.

4.2 Characterization of Rough Surface

4.2.1 Moment Calculation of the Real Rough Surface

Based on the Longuet-Higgins random process model [1], Nayak [2] developed a random process model for the isotropic rough surface. According to Nayak's random theory, the spectral moments of a rough surface can be calculated using the following equation [2-4]:

$$m_{pq}^{h} = \iint_{-\infty}^{\infty} \omega_x^p \omega_y^q S^h\left(k_x, k_y\right) dk_x dk_y \tag{4.1}$$

where, $\omega_x$and ω_y are angular frequency components in the x and y-direction and $\omega_x = 2\pi k_x, \omega_y = 2\pi k_y$. k_x and k_y are frequency components or wavenumbers. $S^h\left(k_x, k_y\right)$ represents the power

spectral density (PSD) of a rough surface that can be determined by employing the following formula:

$$S^h(k_x, k_y) = \left| \frac{fft2(h(x,y))}{\left(\frac{N_x}{L_x} * \frac{N_y}{L_y}\right)} \right|^2 \Big/ \left(L_x * L_y\right) \tag{4.2}$$

In the above equation, $fft2(h(x,y))$ represents the 2D Fast Fourier Transform (FFT) of the rough surface data. N_x and N_y represent the number of data points, and L_x and L_y are the scan lengths along the x and y-directions, respectively. Spectral moments can also be calculated using the following equation [3-4]:

$$m_{pq}^h = 0, \text{ if } p \text{ or } q \text{ is odd}$$

$$m_{pq}^h = \langle \left(\frac{\partial^{\left(\frac{p}{2}+\frac{q}{2}\right)} h}{\partial x^{\left(\frac{p}{2}\right)} \partial y^{\frac{q}{2}}} \right)^2 \rangle \text{ , } p \text{ and } q \text{ are even} \tag{4.3}$$

$\langle \cdot \rangle$ represents the ensemble average. Xu [4] showed proof that Eq. (4.1) and (4.3) are equal to each other. Xu and Jackson [3] also performed a rough surface analysis using both of the methods, and the results showed that the difference between the two methods is negligible. In this dissertation, Eq. (4.3) has been used for all the rough surface contact analysis. If the rough surface is isotropic, then the spectral moments are independent of the direction of measurement. There are infinite possibilities of this direction; therefore, two orthogonal directions parallel to the x and y-axes are considered in this study. According to Eq. (4.3), spectral moments in the x and y-directions can be written as [3]:

$$m_{n0}^h = \frac{1}{N_x N_y} \sum_{k=1}^{N_x} \sum_{l=1}^{N_y} \left[\frac{dh^{n/2}(x_k, y_l)}{dx^{n/2}} \right]^2 , n = 0,2,4 \cdots \text{ (for } x \text{ direction)} \tag{4.4}$$

$$m_{0n}^h = \frac{1}{N_x N_y} \sum_{k=1}^{N_x} \sum_{l=1}^{N_y} \left[\frac{dh^{n/2}(x_k, y_l)}{dy^{n/2}} \right]^2 , n = 0,2,4 \cdots \text{ (for } y \text{ direction)} \tag{4.5}$$

Taking an average of the Eq. (4.4) and (4.5), the spectral moment of the rough surface, m_n^h can be determined. Using these averages, the Nayak bandwidth parameter, α^h is [2]:

$$\alpha^h = m_0^h m_4^h / \left(m_2^h\right)^2 \tag{4.6}$$

A "pressure surface" has been defined at the beginning of Chapter 2, and it is useful for the near-complete contact analysis. To calculate the spectral moments of a "pressure surface" Ciavarella [5] and Xu and Jackson [3-4] gave the following equation:

$$m_n^p = \frac{n+2}{4(n+1)} (E')^2 m_{n+2}^h \quad n = 0,2,4\cdots \tag{4.7}$$

The Nayak bandwidth parameter for the "pressure surface" is [3-4]:

$$\alpha^p = m_0^p m_4^p / \left(m_2^p\right)^2 \tag{4.8}$$

According to Eq. (4.7) the first three non-zero moments are:

$$m_0^p = \frac{1}{2}(E')^2 m_2^h, m_2^p = \frac{1}{3}(E')^2 m_4^h, m_4^p = \frac{3}{10}(E')^2 m_6^h \tag{4.9}$$

4.2.2 Moment Calculation for the Fractal Rough Surface

Two methods are widely used to generate the fractal surface. One of them is that for a given Power Spectral Density (PSD), the surface can be reconstructed by taking the inverse FFT of the PSD [6-7]. Another method is using the Weierstrass-Mandelbrot (W-M) function [8-11]. Here the surface parameter calculation for the first method of surface generation will be discussed. Hu and Tonder [12] proposed a Fourier based filtering algorithm, which allows generating topographies with PSD approximately given by the following equations and, as shown in Fig. 4.1[3-4, 14]:

$$S^h(k) = \begin{cases} Ck^{-2(1+H)} & k \in [k_r, k_s], \\ Ck_r{}^{-2(1+H)} & k \in [k_l, k_r), \\ 0 \qquad Otherwise \end{cases} \tag{4.10}$$

where C is the constant determining the roughness amplitude, k_s and k_l are the cut-off wavenumbers associated with the shortest (λ_s) and the longest (λ_l) wavelengths, respectively. k_r is the roll-off wavenumber, and H is the Hurst exponent. Rough surfaces generated using this PSD are self-affine, which means the surface geometry is not scaled uniformly in the x, y, and z-directions with the decrease of scale. During fractal surface generation, the linear part with continuous decreasing slope of Fig. 4.1 has been used because for the PSD of many measured rough surfaces, the k_r and k_l are almost identical [13]. Therefore, the plateau is not present and $k_r = k_l$. Spectral moments for this type of fractal rough surface can be calculated using the following equation [3-4]:

$$m_n^h = (2\pi)^{n+1} \frac{\prod_{k=1}^{n/2}(2k-1)C}{\prod_{k=1}^{n/2}(2k)} \left[\frac{k_r^{-2(1+H)}}{n+2} (k_r^{n+2} - k_l^{n+2}) + \frac{1}{n-2H} (k_s^{n-2H} - k_r^{n-2H}) \right] \quad (4.11)$$

where $\prod_{k=1}^{0}(\cdot) = 1$ and $n = 0,2,4,6\cdots$

Now if we assume $k_r = k_l$, Eq. (4.11) reduces to the following [4, 14]:

$$m_n^h = \frac{\prod_{k=1}^{n/2}(2k-1)}{\prod_{k=1}^{n/2}(2k)} \frac{(2\pi)^{n+1}C}{n-2H} (k_s^{n-2H} - k_r^{n-2H}) \quad (4.12)$$

Therefore, the first four spectral moments can be written as:

$$m_0^h = \frac{\pi C}{H} (k_l^{-2H} - k_s^{-2H}) \quad (4.13)$$

$$m_2^h = \frac{1}{4} \frac{(2\pi)^3 C}{(1-H)} (k_s^{2-2H} - k_l^{2-2H}) \quad (4.14)$$

$$m_4^h = \frac{3}{16} \frac{(2\pi)^5 C}{(2-H)} (k_s^{4-2H} - k_l^{4-2H}) \quad (4.15)$$

$$m_6^h = \frac{5}{32} \frac{(2\pi)^7 C}{(3-H)} (k_s^{6-2H} - k_l^{6-2H}) \quad (4.16)$$

For this fractal surface, the spectral moments for the "pressure surface" is [3-4]:

$$m_n^p = (E')^2 \frac{\prod_{k=1}^{n/2}(2k-1)}{\prod_{k=1}^{n/2}(2k)} \frac{(2\pi)^{n+3}C}{4(n+2-2H)} (k_s^{n+2-2H} - k_l^{n+2-2H}) \quad (4.17)$$

According to Eq. (4.17), the first three non-zero moments are [4]:

$$m_0^p = (E')^2 \frac{1}{8} \frac{(2\pi)^3 C}{(1-H)} (k_s^{2-2H} - k_l^{2-2H}) \tag{4.18}$$

$$m_2^p = (E')^2 \frac{1}{16} \frac{(2\pi)^5 C}{(2-H)} (k_s^{4-2H} - k_l^{4-2H}) \tag{4.19}$$

$$m_4^p = (E')^2 \frac{3}{64} \frac{(2\pi)^7 C}{(3-H)} (k_s^{6-2H} - k_l^{6-2H}) \tag{4.20}$$

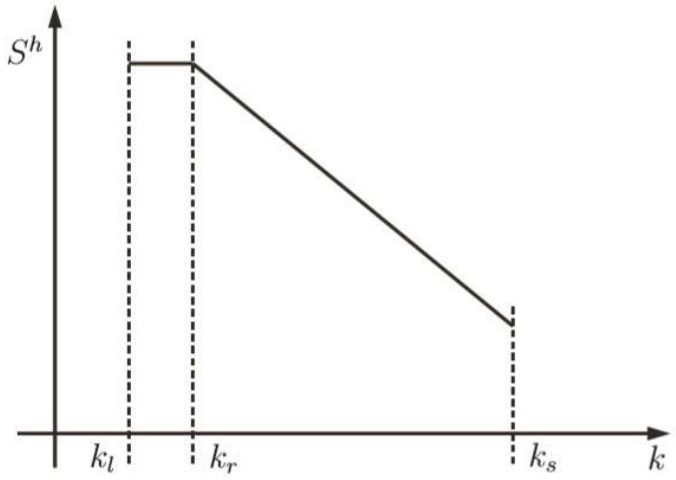

Fig. 4.1 Schematic representation of the PSD of a self-affine rough surface as a function of wavenumber, k (wavenumber=1/wavelength).

4.2.3 Probability Distribution Function (PDF) for the Rough Surface and "pressure surface"

Nayak [2] developed a radical random process model for an isotropic rough surface and provided a probability distribution function (PDF) for the summit of an asperity on the rough surface. The PDF is such that it can be modified to use with different shaped asperity models. According to Nayak, the probability that an arbitrary point on the surface will be a stationary point is [2]:

$$P_{sum}\left(\xi^{h*}, t_1, t_2, t_3, (stat.pt)\right) = \left(\frac{m_4}{m_2}\right) \frac{[C_1 \alpha^h]^{\frac{1}{2}}}{3(2\pi)^3} exp\left[-C_1 \xi^{h*^2}\right] \iiint_{V'} |t_1^2 - t_2^2 - t_3^2|$$

$$\times exp\left\{-\frac{1}{2}[C_1 t_1^2 + t_2^2 + t_3^2 + C_2 t_1 \xi^{h*}]\right\} dt_1 dt_2 dt_3 \quad (4.21)$$

In the above equation,

$\xi^{h*} = \frac{\xi^h}{\sigma}$, σ is the standard deviation of the probability distribution function and $\sigma = \sqrt{m_0^h}$

$t_1 = = \sqrt{\frac{3}{m_4^h}} \frac{\left(\frac{\partial^2 \xi^h}{\partial x^2} + \frac{\partial^2 \xi^h}{\partial y^2}\right)}{2}$, $t_2 = \sqrt{\frac{3}{m_4^h}} \frac{\partial^2 \xi^h}{\partial x \partial y}$ and $t_3 = \sqrt{\frac{3}{m_4^h}} \frac{\left(\frac{\partial^2 \xi^h}{\partial x^2} - \frac{\partial^2 \xi^h}{\partial y^2}\right)}{2}$, the domain of integration V' is defined by, $t_1 < 0$ and $t_2^2 + t_3^2 \leq t_1^2$

$C_1 = \alpha^h/(2\alpha^h - 3)$, $C_2 = C_1(12/\alpha)^{1/2}$, α^h is known as the Nayak parameter or bandwidth parameter. Using Eq. (4.21) and integrating the following equation, Nayak obtained the mathematical expression for area asperity density [2]:

$$D_{sum} = \eta = \int_{-\infty}^{\infty} P_{sum}\left(\xi^{h*}, t_1, t_2, t_3, (stat.pt)\right) d\xi^{h*} dt_1 dt_2 dt_3$$

Substituting Eq. (4.21) in the above integration and solving,

$$\eta = \frac{1}{6\pi\sqrt{3}}\left(\frac{m_4^h}{m_2^h}\right) \quad (4.22)$$

Dividing Eq. (4.21) by Eq. (4.22), the PDF equation for the summit of an asperity on the rough surface can be obtained. Employing Eq. (4.21) and (4.22), Nayak obtained the following two PDF for the summit of the asperity [2]:

PDF as a function of only the surface asperity height, ξ^{h*}

$$\emptyset^h(\xi^{h*}) = \frac{3}{2\pi}\frac{\sqrt{2\alpha^h - 3}}{\alpha^h}\xi^{h*} \exp[-C_1(\xi^{h*})^2] + \frac{3\sqrt{3}}{2\sqrt{2\pi}}\frac{1}{\alpha^h}[(\xi^{h*})^2 - 1] \times$$

$$exp\left[-\frac{1}{2}(\xi^{h*})^2\right][1+erf(\beta)]+\sqrt{\frac{\alpha^h}{2\pi(\alpha^h-1)}}\times exp\left[\frac{-\alpha^h\left(\xi^{h*}\right)^2}{2(\alpha^h-1)}\right][1+erf(\gamma)] \quad (4.23)$$

where $\beta=\xi^{h*}\sqrt{\frac{3}{2(2\alpha^h-3)}}$, $\gamma=\xi^{h*}\sqrt{\frac{\alpha^h}{2(\alpha^h-1)(2\alpha^h-3)}}$, $\mathrm{erf}(x)=\frac{2}{\sqrt{\pi}}\int_0^x e^{-t^2}\,dt$

PDF as a function of the surface asperity height, $\boldsymbol{\xi^{h*}}$ and asperity mean curvature, $\boldsymbol{k_m^{h*}}$

$$\emptyset^h(\xi^{h*},k_m^{h*})=\frac{3\sqrt{C_1}}{2\pi}exp[-C_1(\xi^{h*})^2]\left\{3(k_m^{h*})^2-2+2exp\left[-\frac{3}{2}\,(k_m^{h*})^2\right]\right\}\times$$

$$exp\left\{-\frac{1}{2}\left[3C_1(k_m^{h*})^2-\sqrt{3}C_2k_m^{h*}\xi^{h*}\,\right]\right\} \quad (4.24)$$

where $C_1=\alpha^h/(2\alpha^h-3)$ and $C_2=C_1\sqrt{12/\alpha^h}$.

Gaussian distribution

In Eq. (4.23), when $\alpha^h\to\infty$, the surface asperity distribution becomes Gaussian [2]. Jackson and Green provided the following equation for the normalized Gaussian distribution [15]:

$$\emptyset^h(\xi^{h*})=\frac{1}{\sqrt{2\pi}}\left(\frac{\sigma}{\sigma_s}\right)exp\left[-0.5\left(\frac{\sigma}{\sigma_s}\right)^2(\xi^{h*})^2\right] \quad (4.25)$$

In the above equation, σ is the standard deviation of the surface heights, σ_s is the standard deviation of the asperity heights. Adopting Nayak's random process model, Bush et al. [16] provided the equation of the mean summit curvature, R and the standard deviation of the summit heights, σ_s about the summit mean height:

$$R=\frac{8}{3}\sqrt{\frac{m_4}{\pi}} \quad (4.26)$$

$$\sigma_s^2 = \sigma^2 - \frac{3.717.10^{-4}}{\eta^2 R^2} \tag{4.27}$$

$$\sigma = \sqrt{m_0^h} \tag{4.28}$$

Bush et al. [16, 17] gave the following equation for the distance between the mean asperity height and the mean surface height:

$$y_s = \frac{0.045944}{\eta R} \tag{4.29}$$

Eq. (4.26)-(4.29) are generally used to employ the original statistical or GW model. McCool [18] organized all these parameters together to analytically express the inputs for the GW model. That is why these parameters are also known as McCool's parameter. Jackson and Green [15] provided an exact closed-form solution for the original GW model employing McCool's parameters. Fig. 4.2(b) is showing the schematic representation of a rough surface with Gaussian distribution and McCool's parameters.

PDF as a function of surface asperity height, ξ^{h*} and principal curvatures, k_1^{h*} and k_2^{h*}

Based on Nayak's random theory, Bush et al. obtained a PDF for elliptical asperity model, which is a function of asperity height, ξ^{h*} and two principal curvatures of the asperity, k_1^{h*} and k_2^{h*}[16]:

$$\emptyset^h\left(\xi^{h*}, k_1^{h*}, k_2^{h*}\right) = \frac{27}{8\pi}\sqrt{C_1} exp\left[-C_1\left(\xi^{h*} - \frac{3\left(k_1^{h*} + k_2^{h*}\right)}{4\sqrt{\alpha^h}}\right)^2\right] k_1^{h*} k_2^{h*}\left(k_2^{h*} - k_1^{h*}\right)$$

$$\times exp\left\{-\frac{9}{16}\left[\left(k_1^{h*}\right)^2 + \left(k_2^{h*}\right)^2 - \frac{2}{3}k_1^{h*}k_2^{h*}\right]\right\} \tag{4.30}$$

PDF as a function of surface asperity height, ξ^{h*} and asperity geometric curvature, k_g^{h*}

Greenwood gave the following PDF using Nayak's random theory, which varies as a function of summit height, ξ^{h*} and summit geometric curvature, k_g^{h*} [19]:

$$\emptyset^h\left(\xi^{h*}, k_g^{h*}\right) = \frac{9}{2\sqrt{2\pi}}\sqrt{\frac{\alpha^h}{\alpha^h-1}}\left(k_g^{h*}\right)^3 erfc\left[\mu\left(3k_g^{h*} - \frac{\xi^{h*}\sqrt{\alpha^h}}{\alpha^h-1}\right)\right] exp\left[\frac{-\alpha^h\left(\xi^{h*}\right)^2}{2(\alpha^h-1)} + \frac{3\left(k_g^{h*}\right)^2}{2}\right] \quad (4.31)$$

where $\mu = \sqrt{\frac{1}{2}\frac{\alpha^h-1}{2\alpha^h-3}}$

The above PDF is derived from Eq. (4.21) so only valid for isotropic surfaces. The PDFs for the asperity of the "pressure surface" are the same as the PDFs of the asperity of the rough surface. Only superscript *p* has to be used, instead of using superscript *h*, i.e., the parameters for the "pressure surface" [3-4].

4.2.4 Surface Parameter Calculation for an Equivalent or Composite Rough Surface

Barber showed that [20], purely normal elastic contact between two rough surfaces is identical to the contact of a rigid and imaginary equivalent rough sum surface. Greenwood and Tripp [21] also investigated it mathematically for misaligned asperities with a Gaussian distribution, and O'Callaghan and Cameron [22] numerically examined by using Longuet-Higgins two-dimensional Gaussian random surface model. Francis [23] obtained the relations that correlate the roughness parameters of the equivalent rough surface to the values of individual surfaces. So based on the previous research works, if $h_1(x,y)$and $h_2(x,y)$ define the surface roughness of the two contacting surfaces then the rough surface contact problem can be simplified to a composite rough surface with surface roughness, $h(x,y) = h_1(x,y) + h_2(x,y)$ in purely normal contact with a rigid flat, as shown in Fig. 4.2(a). The equivalent elastic modulus and radius of curvature of the

composite surface can be calculated using Eq. (2.9) and (2.19), respectively. The spectral moments of the composite rough surface are:

$$(m_i^h)_{composite\_surface} = (m_i^h)_{surface1} + (m_i^h)_{surface2}, \text{ i= 0, 2, 4}\cdots \quad (4.32)$$

Root Mean Square (RMS) surface roughness or standard deviation, σ, surface slope, σ', and surface curvature, σ'' of the composite surface can be calculated from the following formula [24]:

$$\sigma_{composite\_surface} = \sqrt{(m_0^h)_{composite\_surface}} = \sqrt{(\sigma_{surface1})^2 + (\sigma_{surface2})^2}$$

$$\sigma'_{composite\_surface} = \sqrt{(m_2^h)_{composite\_surface}} = \sqrt{(\sigma'_{surface1})^2 + (\sigma'_{surface2})^2}$$

$$\sigma''_{composite\_surface} = \sqrt{(m_4^h)_{composit\_surafce}} = \sqrt{(\sigma''_{surface1})^2 + (\sigma''_{surface2})^2} \quad (4.33)$$

To get an idea about the different scales of the rough surface, spectral analysis is a useful method. For the spectral analysis, rough surface data can be converted into a series of stacked sine waves by performing an FFT on the rough surface data. Then amplitude and wavelength can be calculated from the FFT. For 2D rough surface data or a line scan by a profilometer, amplitude can be calculated from the following formula:

$$\beta_i = \left| \frac{fft(h(x))}{N} \right|$$

where N is the total number of points along the scan length. The measured data points using a profilometer are evenly spaced. The above operation will create a $N \times 1$ matrix of amplitudes. To prevent aliasing in the analyzed data, amplitude, Δ_i and wavelength, λ_i at each scale will be

considered only up to the Nyquist frequency. Therefore, only half of the scanned data will be considered, and the equation for Δ_i and λ_i at each scale, i will be:

$$\Delta_i = \begin{cases} 2\beta_i, \text{for } i = 2 \; to \frac{N}{2} \\ \beta_i, \text{for } i = 1, \frac{N}{2} + 1 \end{cases} \tag{4.34}$$

$$\lambda_i = \frac{L}{i}, i = 1, \cdots \frac{N}{2}, \tag{4.35}$$

For the 3D rough surface data, amplitude can be calculated from the following formula:

$$\Delta_{i,j} = \sqrt{\frac{S^h(k_x,k_y)}{L_x L_y}} = \frac{1}{\sqrt{L_x L_y}} \times \left(\left| \frac{fft2(h(x,y))}{\left(\frac{N_x}{L_x} * \frac{N_y}{L_y}\right)} \right|^2 \Big/ \left(L_x * L_y\right) \right)^{0.5} = \left| \frac{fft2(h(x,y))}{N_x N_y} \right| \tag{4.36}$$

where N_x and N_y are the number of data points along x and y-direction. Eq. (4.36) will generate a $N_x \times N_y$ matrix of amplitudes. However, most of the developed asperity models need a single amplitude for a particular frequency. Therefore, it is important to accurately represent the amplitude information from a 2D FFT to a 1D representation. The following relations can be used to obtain the signal amplitude at a given frequency level, i [25-26]:

$$\beta_i = \frac{1}{2} \sqrt{\sum_{j=1}^{N_y} |(\Delta(i,j))|^2 + \sum_{k=1}^{N_x} |(\Delta(k,i))|^2} \tag{4.37}$$

$$\Delta_i = 2\beta_i, \text{ when } 1 < i < \frac{N_x}{2} + 1 \text{ and } \Delta_i = \beta_i \text{ when } i = 1, \frac{N_x}{2} + 1 \tag{4.38}$$

λ_i can be calculated using Eq. (4.35) and for the 3D rough surface data also all the measured data points are evenly spaced. Now if $N_x = N_y$, the amplitude for the composite rough surface is:

$$(\Delta_i)_{Composite\_surface} = (\Delta_i)_{Surface\_1} + (\Delta_i)_{Surface\_2} \tag{4.39}$$

If the number of the sampling points are the same on the contacting surfaces, the wavelength of the composite surface will be the same as the contacting surfaces, i.e., $(\lambda_i)_{Composite\_surface} = (\lambda_i)_{Surface\_1} = (\lambda_i)_{Surface\_2}$. However, if the number of the sampling points is different on the individual contacting surfaces, then λ_i of the individual and composite surfaces will be different and have not been discussed here.

4.3 Rough Surface Models

4.3.1 Rough Surface Models for the Elastic Contact

4.3.1.1 Statistical Models for the Early Contact

In 1966, Greenwood and Williamson [27] (GW model) developed a model to predict the rough surface contact behavior based on the statistical characterization of the surface. Surfaces are generally random in nature, so it seems logical to model the surface statistically. The model predicts the real contact area and contact force using the following equations:

$$A^* = \eta \int_d^\infty \overline{A}_\iota \varphi^h(\xi^h) d\xi, \quad P^* = \eta \int_d^\infty \overline{P}_\iota \varphi^h(\xi^h) d\xi \tag{4.40}$$

In the above equation, A^* denotes the normalized contact area i.e. $\frac{A_r}{A_n}$ where A_r is the real contact area, and A_n is the nominal contact area. P^* denotes the average pressure i.e. $\frac{F}{A_n}$ where F is the contact force, and A_n is the nominal contact area. d specifies the surface separation between the mean plane of the contacting rough surfaces (see Fig. 4.2(b)) and $\xi^h > d$. $\overline{A}_\iota$ and $\overline{P}_\iota$ denote the single asperity contact area and contact force model. The original GW model adopted the Hertz single asperity model with circular contact (Eq. (2.17) and (2.18)) and made the following assumptions during the rough surface modeling:

- Surface height follows either an exponential or Gaussian distribution

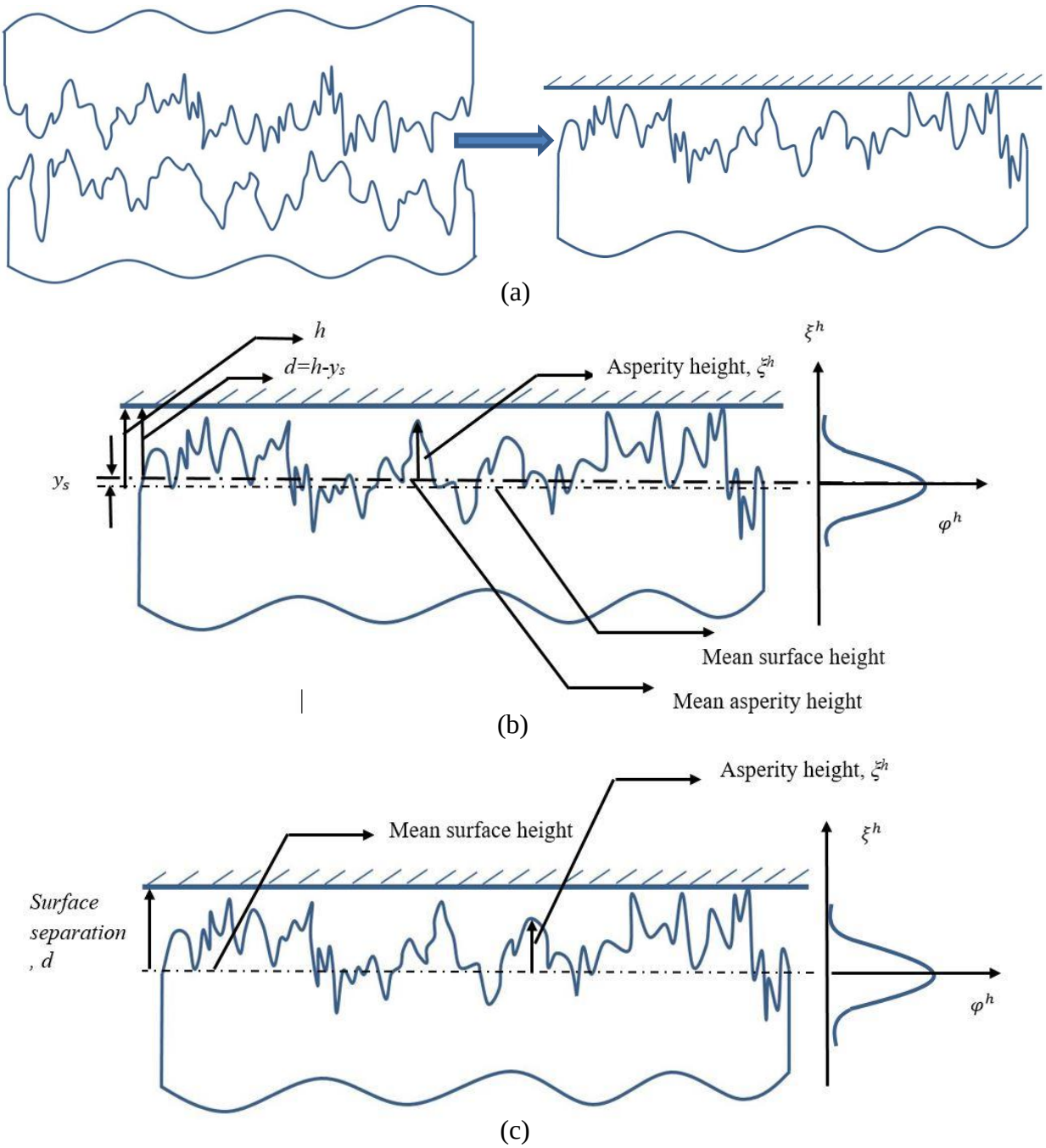

Fig. 4.2 Schematic representation of (a) the contact between two rough surfaces, the contact between an equivalent rough sum surface and smooth surface or rigid flat for (b) GW model with McCool's parameter (c) all other models.

- The radius of curvature of the asperities are constant, only the surface height varies
- Does not consider the effect of the substrate at the base of the asperities
- Does not consider interaction with adjacent asperities

The surface parameters for the Greenwood and Williamson model can be determined from the McCool's parameters, i.e. Eq. (4.26) - Eq. (4.29) and Gaussian distribution is given in Eq. (4.25). Although there are many real surfaces that follow a Gaussian distribution [13], however, there are many other surface distributions, for instance, the Weibull distribution [28-29], asymmetric distribution as a function of skewness and kurtosis [30], etc. Therefore, the first assumption is not always correct. Surface roughness varies over many scales. At the finest scale, the radius of curvature is a lot smaller than the curvature at the larger scales [31]. Therefore, the second assumption is wrong. The third and fourth assumptions are valid only if the applied load is very small, and the amount of deformation is limited to the tip of the asperity.

In 1970, Whitehouse and Archard [31] derived a PDF as a function of asperity height and radius of curvature. Later, Onions and Archard [32] used this probability distribution function in the framework of the GW model. As described in sec. 4.2.3, in 1971, Nayak developed equation, Eq. (4.21) and Eq. (4.22) to describe the surface asperity distribution of the rough surface, which can be adapted for different shaped asperity models to employ the statistical model. Nayak and later others [2, 3-4, 16, 19] used this equation to obtain different PDFs for the rough surface (sec. 4.2.3). The following conventions have been applied to normalize the parameters used in the rough surface models [3-4]:

- To normalize surface height, ξ^h, surface separation, d or interfacial gap, g and interference, δ, parameters have been divided by $\sqrt{m_0^h}$ and curvature has been divided by $\sqrt{m_4^h}$. For instance, $d^* = \frac{d}{\sqrt{m_0^h}}$, $k_m^{h*} = \frac{k_m^h}{\sqrt{m_4^h}}$.

- To normalize average pressure, $\bar{p}$, it has been divided by $\sqrt{m_0^p}$. For instance, $\bar{p}^* = \frac{\bar{p}}{\sqrt{m_0^p}} = \frac{\bar{p}}{\sqrt{\frac{1}{2}(E')^2 m_2^h}}$.

Adapted Greenwood-Williamson Model:

It has been mentioned before in sec. 4.2.3 that, Nayak [2] provided two probability distribution functions. One of them varies only as a function of surface asperity height, ξ^{h*} (Eq. (4.23)). Gaussian distribution is also a function of only surface asperity height; however, Gaussian distribution is a special case of Eq. (4.23) (see sec. 4.2.3 for details). Nayak [2] showed that bandwidth parameter, α controls whether a surface asperity distribution will be Gaussian or another asymmetric distribution with different skewness and kurtosis. When α is small, the Power Spectral Density (PSD) of a rough surface has a narrow band of wavelengths, however with the increase of α, the range of wavelengths in the PSD also increases. Therefore, instead of using Gaussian distribution in Eq. (4.40), it seems more accurate to use Eq. (4.23) for the probability distribution function. Using Eq. (4.23), areal asperity density (Eq. 4.22), and Hertzian circular contact with constant radius of curvature (Eq. (2.17), (2.18) and (4.26)), original GW model (Eq. 4.40) can be modified to the following as a function of α [4]:

$$A^*(d^*) = \frac{\sqrt{\pi}}{16\sqrt{3}}\sqrt{\alpha^h}\int_{d^*}^{\infty}(\xi^{h*} - d^*)\emptyset^h(\xi^{h*})d\xi^{h*} \tag{4.41}$$

$$\bar{p}^*(d^*) = \frac{1}{9(\pi)^{3/4}}(\alpha^h)^{3/4}\int_{d^*}^{\infty}(\xi^{h*} - d^*)^{3/2}\emptyset^h(\xi^{h*})d\xi^{h*} \quad (4.42)$$

Expressing equations as a function of α^h helps to observe the effect of α^hon the rough surface contact modeling.

Bush, Gibson, and Thomas model (BGT model)

In 1975, Bush, Gibson, and Thomas (BGT model) proposed the most complete random process model for the linear elastic Gaussian rough surface model. BGT model was developed based on the assumption that each asperity in the GW model will be replaced by a paraboloid asperity with elliptical contact and Gaussian or exponential PDF will be replaced by a PDF, which is a function of the surface asperity heights, ξ^{h*} and principal curvatures, k_1^{h*} and k_2^{h*} i.e. Eq. (4.30). Fig. 4.2(c) is showing the conventions used to model the contact between a rigid flat and the equivalent sum surface. Employing the PDF from Eq. (4.30) and utilizing the Hertz asperity model with elliptical contact (Eq. (2.10) and (2.11)) under the framework of the GW model, Bush et al. proposed the following two equations to the determine the real contact area and contact force [16, 33]:

$$A^*(d^*) = \eta^h\int_{d^*}^{\infty}\int_0^{k_2^{h*}}\int_0^{\infty}A_i\left(\xi^h, k_1^h, k_2^h\right)\emptyset\left(\xi^{h*}, k_1^{h*}, k_2^{h*}\right)d\xi^{h*}dk_1^{h*}dk_2^{h*} \quad (4.43)$$

$$\bar{p}(d^*) = \eta^h\int_{d^*}^{\infty}\int_0^{k_2^{h*}}\int_0^{\infty}P_i\left(\xi^h, k_1^h, k_2^h\right)\emptyset\left(\xi^{h*}, k_1^{h*}, k_2^{h*}\right)d\xi^{h*}dk_1^{h*}dk_2^{h*} \quad (4.44)$$

In the above equations, $k_1^{h*} < k_2^{h*}$.

Substituting the equation of area asperity density (Eq. (4.22)) into the BGT model, Eq. (4.43) and Eq. (4.44) can be modified to the following two equations [4]:

$$A^*(d^*) = \frac{1}{6\sqrt{3}}\sqrt{\alpha^h}\int_{d^*}^{\infty}\int_0^{k_2^{h*}}\int_0^{\infty}(\xi^{h*}-d^*)\left(k_1^{h*}k_2^{h*}\right)^{-\frac{1}{2}}\frac{{F_1}^2(e)}{F_2(e)}\emptyset^h\left(\xi^{h*},k_1^{h*},k_2^{h*}\right)d\xi^{h*}dk_1^{h*}dk_2^{h*} \tag{4.45}$$

$$\bar{P}^*(d^*) = \frac{2\sqrt{2}}{9\sqrt{3}\pi}(\alpha^h)^{\frac{3}{4}}\int_{d^*}^{\infty}\int_0^{k_2^{h*}}\int_0^{\infty}(\xi^{h*}-d^*)^{\frac{3}{2}}\left(k_1^{h*}k_2^{h*}\right)^{-\frac{1}{4}}F_2^{\left(-\frac{3}{2}\right)}(e)$$

$$\times\emptyset^h\left(\xi^{h*},k_1^{h*},k_2^{h*}\right)d\xi^{h*}dk_1^{h*}dk_2^{h*} \tag{4.46}$$

The equations expressed as a function of α^h (Eq. (4.45) and (4.46)) and the main equations (Eq. (4.43) and (4.44)) are the same equations but different forms.

Nayak and Bush model

Bush [34] developed another multi-asperity model using mean curvature, k_m^{h*} in the Hertz spherical asperity model with circular contact (Eq. (2.17) and (2.18)), in conjunction with the PDF developed by Nayak (Eq. (4.24)), which is a function of surface asperity height, $\xi^{h*}$and mean curvature, k_m^{h*}:

$$A^*(d^*) = \eta^h\int_{d^*}^{\infty}\int_0^{\infty}A_i(\xi^h,k_m^h)\emptyset(\xi^{h*},k_m^{h*})d\xi^{h*}dk_m^{h*} \tag{4.47}$$

$$\bar{p}(d^*) = \eta^h\int_{d^*}^{\infty}\int_0^{\infty}P_i(\xi^h,k_m^h)\emptyset(\xi^{h*},k_m^{h*})d\xi^{h*}dk_m^{h*} \tag{4.48}$$

Representing η^h by Eq. (4.22), Eq. (4.47) and (4.48) can be modified to the following equations as a function of α [4]:

$$A^*(d^*) = \frac{1}{6\sqrt{3}}\sqrt{\alpha^h}\int_{d^*}^{\infty}\int_0^{\infty}(\xi^{h*}-d^*)(k_m^{h*})^{-1}\emptyset^h(\xi^{h*},k_m^{h*})d\xi^{h*}dk_m^{h*} \tag{4.49}$$

$$\bar{p}^*(d^*) = \frac{2\sqrt{2}}{9\sqrt{3}\pi}(\alpha^h)^{3/4}\int_{d^*}^{\infty}\int_0^{\infty}(\xi^{h*}-d^*)(k_m^{h*})^{-1/2}\emptyset^h(\xi^{h*},k_m^{h*})d\xi^{h*}dk_m^{h*} \tag{4.50}$$

Bush, Gibson and Thomas asymptotic solution

Bush et al. [16, 33] also provided an extremely simple asymptotic solution to their complete model (BGT model) for very large surface separations, d^*:

$$A^* = \frac{1}{4} erfc\left(\frac{d^*}{\sqrt{2}}\right) \tag{4.51}$$

$$\bar{p}^* = \frac{1}{2\sqrt{2}\sqrt{\pi}} erfc\left(\frac{d^*}{\sqrt{2}}\right) \tag{4.52}$$

$$A^* = \sqrt{\frac{\pi}{2}}\bar{p}^* \tag{4.53}$$

Asymptotic relations show that the contact area is related solely to the elastic properties and the RMS slope of the surface. However, recently this has been questioned by Jackson et al. [35], and also some other researchers found that this not always true [35-37], which will be discussed later in this chapter. To calculate the normalized average pressure, $\bar{p}^*$, the convention showed in Fig. 4.2(c) has been used.

Greenwood model:

Although the BGT model provides a more realistic implementation of the statistical model than the other statistical models available, the triple integration makes the model very complex and computationally expensive. To simplify the BGT model, Greenwood developed a PDF (Eq. (4.31)) which is a function of surface asperity height, ξ^{h*} and geometric curvature, k_g^{h*}. Employing this PDF and using geometric curvature, k_g^{h*} in the Hertz spherical asperity model with circular contact (Eq. (2.17) and (2.18)), Greenwood developed the following statistical model [19]:

$$A^*(d^*) = \eta^h \int_{d^*}^{\infty} \int_0^{\infty} A_i\left(\xi^h, k_g^h\right) \emptyset\left(\xi^{h*}, k_g^{h*}\right) d\xi^{h*} dk_g^{h*} \tag{4.54}$$

$$\bar{p}(d^*) = \eta^h \int_{d^*}^{\infty} \int_0^{\infty} P_i\left(\xi^h, k_g^h\right) \emptyset\left(\xi^{h*}, k_g^{h*}\right) d\xi^{h*} dk_g^{h*} \tag{4.55}$$

Representing η^h by Eq. (4.22) and substituting the equations for asperity models $\left(A_i\left(\xi^h, k_g^h\right)\right.$ and $\left.P_i\left(\xi^h, k_g^h\right)\right)$and PDF $\left(\emptyset\left(\xi^{h*}, k_g^{h*}\right)\right)$, the above two equations, i.e. Eq. (4.54) and (4.55) can be expressed as a function of α [4]:

$$A^*(d^*) = \frac{1}{6\sqrt{3}} \sqrt{\alpha^h} \int_{d^*}^{\infty} \int_0^{\infty} (\xi^{h*} - d^*) \left(k_g^{h*}\right)^{-1} \emptyset^h\left(\xi^{h*}, k_g^{h*}\right) d\xi^{h*} dk_g^{h*} \tag{4.56}$$

$$\bar{p}^*(d^*) = \frac{2\sqrt{2}}{9\sqrt{3}\pi} (\alpha^h)^{3/4} \int_{d^*}^{\infty} \int_0^{\infty} (\xi^{h*} - d^*)^{3/2} \left(k_g^{h*}\right)^{-1/2} \emptyset^h\left(\xi^{h*}, k_g^{h*}\right) d\xi^{h*} dk_g^{h*} \tag{4.57}$$

For this model, the convention shown in Fig. 4.2 (c) has also been used.

Carbone and Bottiglione model:

In 2008, Carbone and Bottiglione [33] performed a detailed investigation comparing the Persson model (see sec.4.3.1.4) with different multi-asperity models (i.e., BGT models [16], Nayak-Bush model [34] and the GW model [27] in conjunction with McCool's parameters [18] for the early contact). It was concluded in their work that all the multi-asperity contact models that take into account the statistical distribution of the summit curvatures give similar results, and all of them have the same asymptotic solution when surface separation is very large. Recently, Xu performed a very similar study [4] and showed that $\frac{k_1^h}{k_2^h}$ has a significant effect on multi-asperity model behavior, and the more this ratio decreases from unity, Hertzian mildly elliptical model with geometric/mean curvature show more deviation from the elliptical model (see sec. 2.2.3). However, both Xu [4] and Greenwood [19] found from their analysis that, statistical model with

geometric curvature gives better rough surface contact approximation than the statistical model with mean curvature. In 2009, to simplify the BGT model, Carbone proposed a new model [39]. Carbone defined this model as the GW-modified model. According to this model, instead of having a wide range of curvatures for a particular height, there will be a single curvature for a particular height. Carbone [39] developed this multi-asperity model by employing the PDF derived by Nayak, which is a function of surface height only, ξ^{h*} (Eq. (4.23)). The Hertz asperity model with a circular cross section (Eq. (2.17) and Eq. (2.18)) has been used instead of an asperity with an elliptical cross section. For each asperity height, the following equation for the radius of curvature has been suggested:

$$\bar{k}_A^*(\xi) = -\frac{\xi^{h*}}{\sqrt{\alpha^h}} + \frac{1}{\emptyset^h(\xi^{h*})}\frac{3\sqrt{3}}{\sqrt{2\pi}} exp\left[-\frac{(\xi^{h*})^2}{2}\right]$$

$$\times\left\{-\frac{2}{3\sqrt{3}}\frac{1}{\sqrt{2\pi}}\frac{1}{C_1\sqrt{C_1}(1+C_1)} exp\left(-\frac{3C_1}{2}\frac{(\xi^{h*})^2}{\alpha^h}\right) - \frac{1}{3C_1}\frac{\xi^{h*}}{\sqrt{\alpha^h}}\left[1+erf\left(\sqrt{\frac{3C_1}{2}}\frac{\xi^{h*}}{\sqrt{\alpha^h}}\right)\right]\right.$$

$$\left. + \frac{\sqrt{C_1}}{3\sqrt{(1+C_1)^3}}\frac{\xi^{h*}}{\sqrt{\alpha^h}}\left[1+erf\left(\sqrt{\frac{C_1}{2(\alpha^h-1)}}\xi^{h*}\right) exp\left(-\frac{1}{2}\frac{(\xi^{h*})^2}{\alpha^h-1}\right)\right]\right\} \quad (4.58)$$

$\emptyset^h(\xi^{h*})$ can be obtained from Eq. (4.23). The GW-modified [33] model showed the same behavior as the asymptotic BGT model for large surface separation, d^*. For this model, the convention showed in Fig. 4.2(c) has also been used.

4.3.1.2 Jackson, Saha and Xu Statistical Model from Early Contact to Complete Contact:

It has been discussed in Chapter 2 that Jackson and Streator [40] obtained a solution to predict the contact area-pressure relation for the elastic sinusoidal asperity model, which is valid from early contact to complete contact. Jackson et al. [41] employed this sinusoidal asperity model (Eq. (2.46) and (2.47)) and Gaussian surface distribution in conjunction with McCool's parameters in the structure of the GW model (Eq. (4.40)) to predict the elastic rough surface contact behavior. The original GW model was developed for low load or early contact where the real contact area is very small compared to the nominal contact area. Therefore, all the contact areas are isolated and do not interact with each other. However, the concept of the Jackson et al. model [41] is that as the boundary conditions of the 3D sinusoidal asperity is such that it considers interaction with adjacent asperities and also consider the effect of the substrate at the base of the asperity, therefore, early contact to complete contact can be effectively modeled by replacing the Hertz asperity model with the sinusoidal asperity model in the framework of the GW model. Jackson et al. [41] employed three different methods to apply the sinusoidal asperity model in the GW model:

1. **Method-1:** The amplitude of the sinusoidal asperity is equal to the surface height, and the wavelength is constant based on the asperity density. It has been assumed that asperities are evenly spaced. Therefore, according to this method, $\Delta = \xi^h$ and $\lambda = 2\left(\frac{L}{\eta}\right)^{1/2}$ where L is the scan length of the sample. Substituting the value of Δ and λ, the radius of curvature at the summit of the asperity can be calculated from $R = \frac{\lambda^2}{4\pi^2\Delta}$. The gap between the contacting surface is, g=?
2. **Method-2:** For this method, amplitude of the sinusoidal asperity is also equal to the surface height; however, R is constant and can be calculated according to the McCool's equation

(Eq. (4.26)). Therefore, $\Delta = \xi^h$, $R = \frac{8}{3}\sqrt{\frac{m_4}{\pi}}$ and λ can be calculated from $R = \frac{\lambda^2}{4\pi^2\Delta}$. For this method, the interfacial gap, $g = d$.

3. **Method-3:** According to this method, the radius of curvature, *R*, is constant and can be calculated from McCool's equation (Eq. (4.26)). Just as with method 1, the wavelength can be calculated from, $\lambda = 2\left(\frac{L}{\eta}\right)^{1/2}$. Then substituting *R* and λ in the equation, $R = \frac{\lambda^2}{4\pi^2\Delta}$ the value of Δ can be calculated. This method does not work well unless the asperity level surface separation is $g = d - \delta$, δ is interference.

Jackson et al. [41] performed a comparison of these three methods with the other analytical models available and concluded at the end of the analysis that the results using the second method gives a closer prediction with the original GW model. For these models, the convention showed in Fig. 4.2(b) has been used to model the contact between the equivalent sum surface and rigid flat.

4.3.1.3 Statistical Model at Nearly Complete Contact

Xu and Jackson [3] first proposed several statistical models near the complete contact based on single asperity models, which were developed for nearly complete contact using the fracture mechanics approach (see sec.2.2.8-2.2.10). The concept of the statistical models for nearly complete contact is very similar to the statistical models for early contact. It has been assumed in their models that near the complete contact at the contact interface, there are numerous non-contact regions, which can be treated as cracks. These cracks are generally circular or elliptical in shape and surrounded by the contact area. Like contact area at the early contact, non-contact area at the nearly complete contact are also isolated and do not interact with each other, and therefore, can be

expressed as the superposition of the corresponding results of the non-contact area for a single crack. The statistical models for the nearly complete contact have been discussed below.

Xu and Jackson Modified Greenwood-Williamson Model:

This model [3-4] is very similar to the GW model employing McCool's parameters for the early contact. However, instead of using the Hertzian asperity model, a penny shaped crack model (Eq. (2.55) and (2.56)) is used. A Gaussian distribution for the pressure surface, $\emptyset^p$ (Eq. (4.25)) is assumed. According to this model, the non-contact region and average interfacial gap can be calculated from the following two equations [3-4]:

$$1 - A^*(\bar{p}^*) = \eta^p \int_{\bar{p}^*}^{\infty} A_i(\xi^p - \bar{p}, k^p)\, \emptyset^p(\xi^{p*}) d\xi^{p*} \tag{4.59}$$

$$\bar{g}(\bar{p}^*) = \eta^p \int_{\bar{p}^*}^{\infty} V_i(\xi^p - \bar{p}, k^p)\, \emptyset^p(\xi^{p*}) d\xi^{p*} \tag{4.60}$$

η^p and $k^{\,p} = \frac{1}{R^p}$, can be determined from Eq. (4.22) and Eq. (4.26). Please note that, it has been mentioned before, the PDF for the "pressure surface" will be the same as the PDF for the summit of the asperity of the rough surface (see at the end of the sec. 4.2.3) and $\bar{p}^*$ is analogous to the $\bar{d}^*$ in the statistical early rough surface model. Eq. (4.59) and (4.60) can also be expressed as a function of α^p using the following two equations:

$$1 - A^*(\bar{p}^*) = \frac{\sqrt{3}}{16}\sqrt{\pi}\sqrt{\alpha^p} \int_{\bar{p}^*}^{\infty} (\xi^{p*} - \bar{p}^*)\, \emptyset^p(\xi^{p*}) d\xi^{p*} \tag{4.61}$$

$$\bar{g}^*(\bar{p}^*) = \frac{3}{20\sqrt{2}} (\pi)^{-1/4} (\alpha^p)^{1/4} (\alpha^h)^{-1/2} \int_{\bar{p}^*}^{\infty} (\xi^{p*} - \bar{p}^*)^{5/2}\, \emptyset^p(\xi^{p*}) d\xi^{p*} \tag{4.62}$$

Xu and Jackson Modified Nayak-Bush Model:

This model is very similar to the previously discussed Nayak-Bush model for early contact. Instead of Hertzian mildly elliptical contact with mean curvature, a mildly elliptical crack model with mean curvature (see sec. 2.2.10) has been used in this model. According to this model, the non-contact area and average interfacial gap are [3-4]:

$$1 - A^*(\bar{p}^*) = \eta^p \int_{\bar{p}^*}^{\infty} \int_0^{\infty} A_i(\xi^p - \bar{p}, {k_m}^p)\, \emptyset^p(\xi^{p*}, {k_m}^{p*}) d{k_m}^{p*} d\xi^{p*} \tag{4.63}$$

$$\bar{g}(\bar{p}^*) = \eta^p \int_{\bar{p}^*}^{\infty} \int_0^{\infty} V_i(\xi^p - \bar{p}, {k_m}^p)\, \emptyset^p(\xi^{p*}, {k_m}^{p*}) d{k_m}^{p*} d\xi^{p*} \tag{4.64}$$

The above two equations as a function of α^p can be expressed by the following two equations:

$$1 - A^*(\bar{p}^*) = \frac{1}{2\sqrt{3}} \sqrt{\alpha^p} \int_{\bar{p}^*}^{\infty} \int_0^{\infty} (\xi^{p*} - \bar{p}^*)\, ({k_m}^{p*})^{-1} \emptyset^p(\xi^{p*}, {k_m}^{p*}) d{k_m}^{p*} d\xi^{p*} \tag{4.65}$$

$$\bar{g}^*(\bar{p}^*) = \frac{4\sqrt{3}}{15\pi} (\alpha^p)^{1/4} (\alpha^h)^{-1/2} \int_{\bar{p}^*}^{\infty} \int_0^{\infty} (\xi^{p*} - \overline{p^*})^{5/2}\, \emptyset^{p*}(\xi^{p*}, {k_m}^{p*}) d{k_m}^{p*} d\xi^{p*} \tag{4.66}$$

For the above equations, η^p, $\emptyset^p$, α^p and α^h can be determined using Eq. (4.22), (4.24), (4.8), and (4.6), respectively.

Xu and Jackson Modified Greenwood Model:

This model has been developed by modifying the PDF developed by Greenwood [19] for the asperity of the rough surface, which is a function of surface height and geometric curvature [3-4]. For the asperity model, the mildly elliptical crack model with geometric curvature (see sec. 2.2.10) has been used. Therefore, the non-contact area and gap are [3-4]:

$$1 - A^*(\bar{p}^*) = \eta^p \int_{\bar{p}^*}^{\infty} \int_0^{\infty} A_i\left(\xi^p - \bar{p}, {k_g}^p\right) \emptyset^p\left(\xi^{p*}, {k_g}^{p*}\right) d{k_g}^{p*} d\xi^{p*} \tag{4.67}$$

$$\bar{g}(\bar{p}^*) = \eta^p \int_{\bar{p}^*}^{\infty} \int_0^{\infty} V_i\left(\xi^p - \bar{p}, {k_g}^p\right) \emptyset^p\left(\xi^{p*}, {k_g}^{p*}\right) d{k_g}^{p*} d\xi^{p*} \tag{4.68}$$

The non-contact area and gap as a function of α^p is:

$$1 - A^*(\bar{p}^*) = \frac{1}{2\sqrt{3}} \sqrt{\alpha^p} \int_{\bar{p}^*}^{\infty} \int_0^{\infty} (\xi^{p*} - \bar{p}^*) \left({k_g}^{p*}\right)^{-1} \emptyset^p\left(\xi^{p*}, {k_g}^{p*}\right) d{k_g}^{p*} d\xi^{p*} \tag{4.69}$$

$$\bar{g}^*(\bar{p}^*) = \frac{4\sqrt{3}}{15\pi} (\alpha^p)^{1/4} (\alpha^h)^{-1/2} \int_{\bar{p}^*}^{\infty} \int_0^{\infty} (\xi^{p*} - \overline{p^*})^{5/2} \emptyset^{p*}\left(\xi^{p*}, {k_g}^{p*}\right) d{k_g}^{p*} d\xi^{p*} \tag{4.70}$$

For the above equations, η^p, $\emptyset^p$, α^p and α^h can be determined using Eq. (4.22), (4.31), (4.8), and (4.6), respectively.

Greenwood Nearly Complete Contact Analysis for Different Pressure Distributions:

Xu and Jackson [3-4] developed the statistical model for nearly complete contact based on their asperity models developed for nearly complete contact [4, 42]. They developed both parabolic pressure asperity with an elliptical cross-section and parabolic pressure asperity with a penny-shaped or mildly elliptical cross-section. For the elliptical cross-section, it has been shown that when $\frac{k_1^p}{k_2^p} \to 0$, where $k_1^p < k_2^p$, the parabolic pressure asperity with an elliptical cross-section becomes ill defined. That is why they proposed statistical models near-complete contact using only penny-shaped crack with different curvatures. They also concluded that when $\frac{k_1^p}{k_2^p} \to 0$, the contact pressure distribution is not parabolic anymore, but becomes something very complicated. Inspired from this conclusion, Greenwood [43] analyzed the nearly complete contact region for different shaped-pressure distributions, for instance, parabolic shape, cosine shape, quartic, and a wavy pressure distribution extending Sneddon's equations [44]. It has been inferred in the paper that different shaped pressure distributions applied to the tensile region does not alter the total pressure

distribution. However, to keep the total pressure distribution unaltered, the non-contact area is always greater than the tensile pressure contact area. The amount of increase depends on the pressure that is acting on the tensile area. For the cases analyzed by Greenwood [43], this increase varies from ~17% to ~40.76%. Xu et al. [42] provided a simple relation between the non-contact area and the tensile area of a single crack:

$$A_{non-contact} = \frac{3}{2} A_{tensile-area} = \frac{3}{2} \pi R(p - \bar{p})$$

$\pi R(p - \bar{p})$ is very similar to the Hertz contact area equation, $\pi R(\xi^h - d)$, however, for the above equation $(p - \bar{p})$ is for the "pressure surface" asperity, and the definition of *R* is also different. Greenwood showed that multiplying the above equation by a factor of $\frac{4}{3}$ and using Eq.(4.63) an excellent agreement can be obtained with the Persson's model provided that $\bar{p}^*$is very large, or the non-contact area is about $0.01A_{nominal}$ or less, where $A_{nominal}$ is the nominal contact area.

Ciavarella Asymptotic Model for Nearly Complete Contact:

Ciavarella [45] proposed the following asymptotic solution for the nearly complete contact when $\bar{p}^*$is very large:

$$A^*(\bar{p}^*) = 1 - \tfrac{3}{4} erfc\left(\frac{\bar{p}^*}{\sqrt{2}}\right) \tag{4.71}$$

Using a different approach Xu [4] found the similar result as Ciavarella [45]. Xu [4] derived the following asymptotic solution for the interfacial gap when $\bar{p}^*$is very large:

$$\bar{g}^*(\bar{p}^*) = \frac{12}{5\sqrt{2}(\pi)^{3/2}} (\alpha^h)^{-1/2} \int_{\bar{p}^*}^{\infty} (\xi^{p*})^{1/2} (\xi^{p*} - \bar{p}^*)^{5/2} exp\left[-\frac{(\xi^{p*})^2}{2}\right] d\xi^{p*} \tag{4.72}$$

4.3.1.4 Multiscale Model:

Archard [46] was the probably first who developed a rough surface contact model in 1957. The Archard model considers the multiscale nature of the surface, i.e., with the magnification of the rough surface from the macro scale to the atomic level, roughness will be observed at all the scales. Figure 4.3 is showing an Archard type multiscale rough surface. Archard described his model as "protuberance upon protuberance" and employed the Hertz spherical asperity model, whereas real surfaces under scanning or tunneling microscope barely look like one sphere upon another sphere. The developed model by Archard is self-similar in nature. Self-similar means scaling ratio of the asperities is the same in all directions of the surface. The model shows a linear relationship between contact pressure and the real contact area. However, the Hertz model shows a non-linear behavior between contact pressure and the real contact area. There are several different ways to model the multiscale nature of the surface, which will also be discussed subsequently.

Stacked Multiscale Modeling Method

Jackson and Streator [40] developed a multiscale rough surface model based on the surface spectrum and asperity models. The Fast Fourier Transform (FFT) was applied to determine the amplitude and wavelength of the rough surfaces (see sec. 4.2.4) and asperity models [47-49] were used to determine the contact area and pressure. The FFT of the rough surfaces is a reliable way to characterize them. This multiscale model was also developed based on Archard's idea of "protuberance upon protuberance." To develop an elastic rough surface contact model, Jackson and Streator employed both the Hertz elastic spherical contact model (Eq. 2.17 and 2.18) and the extended version of the JGH model (Eq. (2.46) and (2.47)) and observed the effect of asperity models on the rough surface contact modeling. To develop an elastic-plastic rough surface contact

model Jackson et al. [40] used the Jackson-Green elastic-plastic spherical contact model [49]. It will be discussed in detail later in the elastic-plastic rough surface literature review (see sec.4.3.2.2). Later the Jackson-Streator model has been expanded using elastic-plastic sinusoidal asperity models (see sec. 4.3.2.2) and applied to many different applications [50-52]. See Fig. 3.1 in Chapter 3, which shows the formation of surface profile superimposing sine waves of different amplitudes and wavelengths at different scales. The following assumptions were made in the Jackson-Streator model to consider the multiscale nature of the surface contact.

- Asperities of smaller cross-sectional surface areas are located at the top of the larger asperities.
- Each scale carries the same total load.
- The load is shared equally among all the asperities at each scale.
- At a particular scale, each asperity will deform according to an elastic or elastic-plastic asperity contact model, irrespective of the presence of asperities with a smaller wavelength upon it.
- The area at a particular scale cannot be greater than the area at a smaller frequency domain or larger wavelength scale.

Jackson et al. [40] proposed the following equations to describe the multiscale contact model:

$$\frac{A_r}{A_n} = \left(\prod_{i=1}^{i_{max}} \bar{A}_i \eta_i\right) \tag{4.73}$$

$$F = \bar{F}_i \eta_i A_{i-1} \tag{4.74}$$

In Eq. (4.73) and Eq. (4.74), $\bar{A}_i$ and $\bar{F}_i$ are single asperity contact area and force for a particular frequency level, i represents the frequency level and η_i represents the asperity density at a particular frequency level.

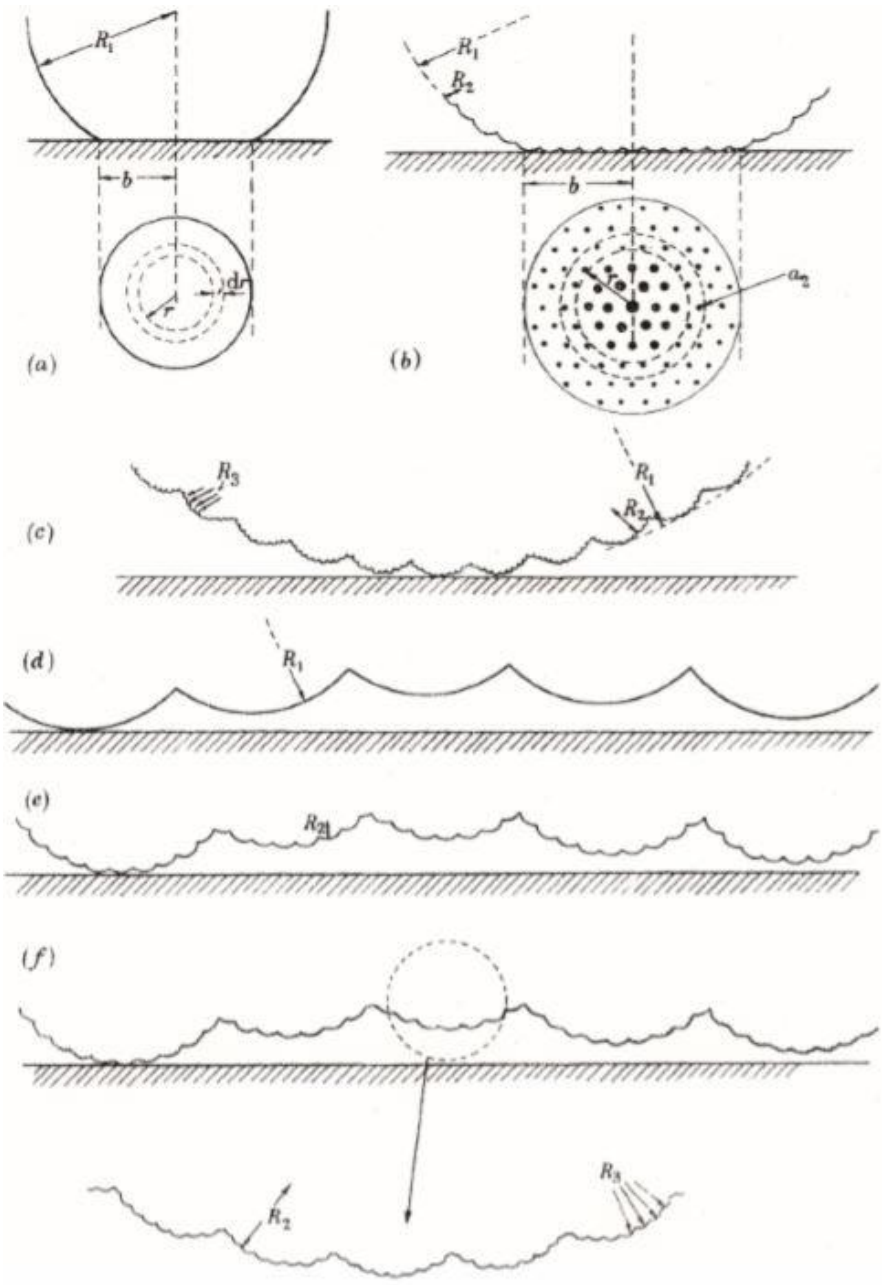

Fig. 4.3 (a) Contact between a rigid flat and spherical asperity, (b) Contact between a rough surface and rigid flat (c-f) Archard proposed model to represent multiscale nature of rough surafce. Archard, J.F., Elastic deformation and the laws of friction. Proceedings of the Royal Society of London A: Mathematical, Physical and Engineering Sciences, 1957, 243(1233), pp. 193, by permission of the Royal Society.

Fractal Method

Surfaces can be easily generated using the fractal methods, and the effect of different surface parameters for any specific application can be determined without lots of sample preparation and surface measurement. That is why fractal curves are widely used to describe the multiscale nature of surfaces. A rough surface following a repeating pattern over many scales is fractal. Weierstrass and Mandelbrot (W-M) proposed a 2D fractal geometry [53]. Later Ausloos and Berman [54] and Yan and Komvoupolous [55] proposed a 3D fractal geometry. Fractal surfaces can be characterized by two parameters, the fractal dimension, *D* and fractal roughness, *G*. There are two kinds of geometry, Euclidean and Non-Euclidean. Euclidean geometries are used to describe the geometry with integer dimensions, i.e., 1D, 2D and 3D geometry. Non-Euclidean geometries are used to describe geometry with non-integer dimensions such as, the Koch curve shown in Falconer [56], the Sierpinski fractal shown in Karplus [57] and so on. The fractal dimension, *D*, can describe both the Euclidean geometry, i.e., a fractal dimension with integer numbers only, and also Non-Euclidean geometry, i.e., a fractal dimension with non-integer values. Fractal dimension, *D*, equals one for a perfect line, *D* equals two for a surface, and *D* equals three for space. Therefore, fractal surface can characterize "rough" phenomena in both natural and artificial worlds. Fractal surfaces are either self-similar or self-affine in nature. Persson [13] described self-similar and self-affine surfaces nicely. "If $z = h(x, y)$is the equation of a self-similar surface, then its magnified version $z = \lambda h(\frac{x}{\lambda}, \frac{y}{\lambda})$ cannot be distinguished from the original. A self-affine surface is analogous, except that the magnification factor along the *z*-direction differs from the in-plane magnification factor λ. The transformed surface $\lambda^H h(\frac{x}{\lambda}, \frac{y}{\lambda})$ looks exactly like the original one, $z = h(x, y)$." λ defines the wavelengths found from the surface spectrum. The calculation of the surface spectrum is different depending on the method used for the fractal surface generation [6-7, 10]. Two popular methods

of fractal rough surface generation are- the Weierstrass-Mandelbrot fractal function [6, 8-10, 53] and the inverse FFT of the PSD where PSD, where the PSD of the rough surface is known [3, 4, 7, 13-14].

Majumdar and Bhusan [8] first proposed a rough surface contact model using fractal geometry to represent the multiscale nature of the surface. According to this method, the contact area can be calculated by truncating an interfering flat surface with the fractal rough surface, and contact force can be determined using the Hertz asperity model along with a fully plastic contact model in the truncated areas. The results showed that the number of contact spot sizes follow a power-law behavior and can be characterized by the fractal dimension of the surface. This model was criticized by other researchers [58] because this model assumes that surfaces will deform plastically at smaller scales and will deform elastically at larger scales; as a result, with the increase of the load, plastic deformation will decrease. Besides this, the model used truncation theory to predict the contact area, and it has been mentioned before that truncation theory cannot predict the contact behavior properly as it does not consider the gradual loading and deformation of the asperities in calculating the contact area.

Later, Ciavarella et al. [9] developed a 2D rough surface model using the W-M function using Archard's "protuberance upon protuberance" concept (see Fig. 4.3). The W-M function can be decomposed into sine waves with different frequencies, where higher frequencies are located at the top of smaller frequencies. To derive the contact pressure relation between successive scales, the Westergaard 2D sinusoidal wavy surface model developed for the plane strain case [59] was employed. Then performing recursive numerical integration of this relation obtained contact area as a function of scale. According to this model, with the decrease of the scale, the contact area decreases. As a result, when an infinite number of scales are included, the contact area will

approach zero. Therefore, two surfaces will never reach complete contact, or it will take infinite pressure to reach complete contact.

Jackson [10] performed a detail investigation and provided a closed-form analytical solution for contact area as a function of pressure to fractal contact based on the concept of stacked asperities presented by Archard. However, instead of using spheres, this work assumed that asperities can be modeled by sinusoidal asperities as fractal surfaces are a superimposition of the sine waves with different amplitudes and wavelengths. According to the Archard model, the smaller scale of asperities will be on the top of larger asperities. As the successive scales are included, the contact area gradually decreases, and contact pressure increases. Contact pressure and contact area at each scale will be:

$$p_i = \frac{F}{(A_r)_i} \tag{4.75}$$

$$(A_r)_i = \frac{F}{p_i} \tag{4.76}$$

According to the analysis, for some surfaces, with the increase of the asperity aspect ratios, contact pressure continuously increases, and it will require infinite pressure to reach at complete contact. All self-affine fractal surafce show this behavior. This case is very similar to the previously described Ciavarella model [9]. On the other hand, there could also be some cases where the aspect ratio continuously decreases or is constant or behave randomly with the increase of the frequency i.e. at the smaller scale. For such cases, it is possible to obtain a value of pressure at which surface will reach complete contact. The analytical derivation in the paper shows that the pressure profile for complete contact of a surface is:

$$p(x) = \max[p_1^*, p_2^*, \cdots\cdots p_\infty^*] + \sum_{n=1}^{\infty} p_n^* \cos(2\pi n \frac{x}{\lambda} + \emptyset_n)$$

Only the first part of the above equation i.e. the average contact pressure contributes to the calculation of the real area of contact between surfaces. Therefore from the above equation, the average contact pressure of the surface is:

$$p_{ave} = max[p_1^*, p_2^*, \cdots\cdots p_\infty^*]$$

Now, using FFT or W-M fractal surface, surface can be reduced to a series of superimposed sinusoidal surfaces. By assuming elastic contact and using superposition the pressure required to flatten all of these sinusoidal asperities can be obtained from the following equation:

$$p_e^* = max[p_1^*, p_2^*, \cdots\cdots p_\infty^*] = p^*(B_{max})$$

In the above equation, $p^*(B_{max})$ means the average pressure required for complete flattening of the scale whose aspect ratio, *B* is maximum. Then employing the equation of p_e^*, derived by Westergaard for 2D plane strain [59] the following approximate equation for total real contact area for the multiscale fractal surface can be obtained:

$$A_r = \frac{F}{p_e^*} = \frac{F}{\pi E' B_{max}} \tag{4.77}$$

and for 3D elasto-static case, the formula for average pressure required for complete flattening of 3D sinusoidal wavy surface derived by Johnson, Greenwood, and Higginson [47] can be used to determine the real contact area:

$$A_r = \frac{F}{p_e^*} = \frac{F}{\sqrt{2}\pi E' B_{max}} \tag{4.78}$$

These closed-form solutions derived by Jackson are also known as the simplified multiscale model.

Recently, Zhang et al. [6-7, 60] thoroughly investigated the characterization of fractal rough surfaces and tried to reconstruct real surfaces using fractal methods. However, results show that different methods for fractal surface characterization do not give a consistent result, and for a small change in the fractal dimension, *D*, the fractal roughness, *G* changes over several orders of magnitude. After analyzing all the results, it was concluded that fractal surfaces need to be used with great care.

Persson Model

Persson developed a diffusion model based on the probability distribution of the contact pressure to describe the contact behavior between a viscoelastic rubber against a rough rigid flat [61]. Later this model has been successfully applied to many other applications [62-69]. However, many researchers have found the model difficult to understand. In 2006, Manner and Greenwood [70] simplified the Persson model and provided the following diffusion equation, which is equivalent to the Persson's model:

$$\frac{\partial P}{\partial(m_0^p)} = \frac{1}{2}\frac{\partial^2 P}{\partial p^2} \tag{4.79}$$

In the above equation, P is the probability distribution of the contact pressure, p, $\sqrt{m_0^p}$ is the Root Mean Square (RMS) surface roughness of the "pressure surface" and $m_0^p = \frac{1}{2}(E')^2 m_2^h$. The above equation describes how the PDF of the contact pressure evolves with the Power Spectral Density (PSD), which includes a wide range of frequencies. To employ the above equation to solve the rough surface contact problem, the following two boundary conditions were applied [70]:

- When $m_0^p \to \infty$, contact pressure, $p = 0$, that is at the beginning of the contact
- When $m_0^p \to 0$, contact pressure, $p \to \infty$, that means the rough surface has been completely flattened

Applying the above two boundary conditions, the following solution for the diffusion equation was derived [70]:

$$P\left(p, m_0^p\right) = \frac{1}{\sqrt{2\pi m_0^p}}\left\{exp\left[-\frac{(p-\bar{p})^2}{2m_0^p}\right] - exp\left[-\frac{(p+\bar{p})^2}{2m_0^p}\right]\right\} \tag{4.80}$$

Integrating the above equation from $[0, \infty]$, the following equation for contact ratio, A^* was obtained [70]:

$$A^* = \frac{A_r}{A_n} = 1 - erfc\left(\frac{\bar{p}^*}{\sqrt{2}}\right) \tag{4.81}$$

The above equation is applicable from early contact to complete contact. When $\bar{p}^* \to 0$, i.e., for light contacts, Eq. (4.80) becomes [70]:

$$P\left(p, m_0^p\right) = \frac{1}{\sqrt{2\pi m_0^p}}\left(\frac{2p\bar{p}}{m_0^p}\right)\left\{exp\left[-\frac{(p)^2}{2m_0^p}\right]\right\} \tag{4.82}$$

and contact area for small $\bar{p}^*$ is [70]:

$$\frac{A_r}{A_n} \approx 1 - \frac{2}{\sqrt{\pi}}\left(\frac{\bar{p}^*}{\sqrt{2}}\right) \tag{4.83}$$

According to Persson and some other models [16], real contact area is only a function of the average pressure normalized by the equivalent elastic modulus and the Root Mean Square (RMS) slope. McGhee et al. [71] showed the same kind of behavior performing in situ contact measurement for 3D printed self-affine fractal rough surface. However, Jackson et al. [35] recently

performed BEM analysis employing several real rough surfaces, and found that for real rough surfaces the above statement is not always true and discussed possible reasons. One of the reasons mentioned in the paper is that real surfaces are not always a perfectly self-affine fractal as assumed in the Persson model; especially with the increase of wavelength, they showed significant deviation from the self-affine fractal surface behavior. Also, for some cases, the spectrum of the rough surface showed a combination of self-similar and self-affine fractal surface behavior. Another reason mentioned in the paper that contact behavior only depends on the RMS slope of the part of the surface that is really in contact. They have defined the RMS slope of the real contact area as the effective RMS slope. For the surfaces analyzed in their work, effective RMS slope was plotted as a function of truncation height, h. For a certain truncation height, h only the surface heights, which were taller than the truncation heights, were used to calculate the effective RMS slope. The plot shows that at the beginning of the contact, the effective RMS slope is higher than the entire surface RMS slope. With the decrease of the truncation height, i.e., with the increase of the load, effective RMS slope continuously decreases and approaches the RMS slope of the entire surface at a h value of approximately $-\sigma$ or -2σ which is just after passing the mean height of the surface. Besides Jackson et al., Yastrebov [38], Campana and Muser [36], Putignano [37] also showed that in addition to RMS slope, other factors govern the real contact area.

4.3.1.5 Analysis of the Elastic Contact Behavior using BEM:

BEM is a computationally expensive method and difficult to implement. However, due to its high computational accuracy, especially for the linear elastic material contact behavior analysis, it can be used as the validation tool for the other contact mechanics models. In Chapter 1, the basic working principle of BEM has already been described. It has been mentioned that BEM estimates the solution by solving the Boundary Integral Equation (BIE) over the elements on the boundary

using different solutions, such as the Kelvin solution [72-74], Boussinesq-Cerutti [75-76], Flamant [77-78], Westergaard solution [59], etc. depending on the applications. The BEM that solves the problem using the Kelvin or Mindlin solution [72-74] are known as general-purpose BEM, and the BEM that uses any of the other solutions [59, 75-78] to solve the problem are known as Special BEM. Anderson et al. [79] first applied the BEM to solve the contact mechanics problems. Most of the works in tribology using BEM [80-81] are based on the special BEM that means the equations that are used to solve the BIE over the elements on the boundary were developed for the half-space or half-plane problems. Recently, Li showed the difference between the sub-surface stress with and without the half-space assumption [82], and Xu and Jackson proved that BEM can not only be applied to the half-space/half-plane problem but also be applied successfully to the rough surface contact problem [74]. To solve the rough surface contact problem, Xu et al. [74] used the Kelvin solution to solve the BIE. Xu et al. [74] also showed that the widely used Boussinesq-Cerutti solution [75-76] for the 3D linear elasto-static problem and the Flamant solution [77-78] for the 2D plane strain/stress problem can be derived from the Kelvin solution, and that means these two cases are special cases of the Kelvin solution. However, still, BEM using the Boussinesq-Cerutti solution or the Flamant solution are a good approximations for the rough surface contact problem if the contact area is very small compared to the nominal area, or the surface slope is really very small so that it can be assumed as a half-space problem.

To compare different rough surface models, Xu and Jackson [3-4] generated a surface that is fractal, isotropic, and Gaussian at the same time so that the analytical models whether developed for fractal or isotropic-Gaussian surfaces can be compared. Xu [4] performed a BEM analysis on the generated fractal, isotropic-Gaussian surface for different surface properties and also provided a curve-fitted solution to predict the contact behavior for the surfaces analyzed. The surface

generated by Xu et al. [3-4] and the curve-fitted solution will be used in this dissertation for the rough surface model development and validation purpose and have been described in detail below.

Xu and Jackson [3-4] developed the rough surface model based on the algorithms proposed by Hu and Tonder [83] and Wu [84]. For fractal surface generation Eq. (4.10) has been used. To ensure the isotropy of the surface it has been assumed that $k_r = k_l$, so the rough surface has an axisymmetric power spectral density (PSD). The surface slope m_2^h has been assumed to be very small so that the surface can be considered as half-space. This assumption is very important as the fundamental assumption of the BEM implemented by Xu [4] is that the surface domain needs to be a half-space. The roughness amplitude in Eq. (4.10) can be determined using the following equation:

$$C = \frac{4(1-H)m_2^h}{(2\pi)^3\left[k_s^{2-2H} - k_l^{2-2H}\right]} \tag{4.84}$$

In order to ensure that the generated surface is Gaussian, the following convolution has been applied:

$$h(x,y) = \int_{-\infty}^{\infty}\int_{-\infty}^{\infty} f(x-x', y-y')h_0(x',y')dx'dy' \tag{4.85}$$

In Eq. (4.85), $h_0(x',y')$ is a Gaussian surface of size *m* x *n*. Due to the applied convolution, $h(x,y)$ is also Gaussian [81]. Now using a Fourier transform, Eq. (4.85) can be written as:

$$\mathcal{F}[h]\left(k_x,k_y\right) = \mathcal{F}[f]\left(k_x,k_y\right)\mathcal{F}[h_0]\left(k_x,k_y\right) \tag{4.86}$$

In the above equation, $\mathcal{F}[f]\left(k_x,k_y\right)$ is a transfer function. The absolute value of the transfer function can be determined using the following relation:

$$\left|\mathcal{F}[f]\left(k_x, k_y\right)\right| = \sqrt{S^h(k_x, k_y)/S[h_0]\left(k_x, k_y\right)} \tag{4.87}$$

where, $S^h(k_x, k_y)$can be calculated from Eq. (4.10). During the PSD calculation, it has been assumed that the rough surface is equally spaced along the *x* and *y*-directions. Therefore, the wavelength of the rough surface, $\lambda_{x(y)} = \frac{L_{x(y)}}{i},\ i = 1,2,\cdots m(n)/2$, the wavenumber is, $k_{x(y)} = \frac{1}{\lambda_{x(y)}}$, and the size of the generated PSD will be $\frac{m}{2} \times \frac{n}{2}$. To calculate the transfer function from Eq. (4.87), the PSD of the Gaussian surface, $h_0(x', y')$, has also been calculated and only 1/4th of the *m* x *n* matrix, that is $\frac{m}{2} \times \frac{n}{2}$, is considered when using Eq. (4.87). Then using the following equation, $\mathcal{F}[f]\left(k_x, k_y\right)$ can be obtained from its absolute value:

$$\mathcal{F}[f]\left(k_x, k_y\right) = \left|\mathcal{F}[f]\left(k_x, k_y\right)\right|[\cos(\theta) + isin(\theta)] \tag{4.88}$$

where, θ is the random phase varied between 0 and 2π. Since $h(x, y)$ is real, using the following Hermitian symmetry the complete *m* x *n* sized $\mathcal{F}[f]\left(k_x, k_y\right)$ has been constructed.

$$\mathcal{F}[f]\left(-k_x, -k_y\right) = conj\left(\mathcal{F}[f]\left(k_x, k_y\right)\right) \tag{4.89}$$

Now, from the inverse Fourier transform of $\mathcal{F}[h]\left(k_x, k_y\right)$, the surface, $h(x, y)$ can be constructed, which is isotropic, Gaussian, and fractal at the same time. To ensure the isotropy and Gaussianity of the fractal surface, Xu [4] enforced the following conditions:

$$k_l \gg \frac{1}{L_{x(y)}} \text{ and } k_s \ll \frac{N_{x(y)}}{L_{x(y)}} \tag{4.90}$$

In the above equation, L_x and L_y are the length of the generated surfaces along *x* and *y* direction, N_x and N_y are the numbers of sampling points in the *x* and *y*-direction. Yastrebov et al. [14]

performed a very similar analysis; however, they did not provide any conditions to make the surface isotropic and Gaussian. Xu [4] performed BEM analysis on several groups of surfaces varying lower cut off wavenumber, k_l, upper cut off wavenumber, k_s, and Hurst exponent, H, However, the surface slope, $\sqrt{m_2^h}$ and equivalent elastic modulus, E' were kept constant. Plots of the normalized contact area and contact pressure for different rough surfaces found from the BEM analysis fall onto one master curve, which means normalized contact area is only a function of surface slope and equivalent elastic modulus. Some other researchers also found the similar result [16]. Xu obtained the following curve-fitted equation for the analyzed surfaces:

$$A^*(\bar{p}^*) = \begin{cases} I(\bar{p}^*)f(\bar{p}^*) & \bar{p}^* \in [0,2] \\ I(\bar{p}^*) & \bar{p}^* \in (2,\infty) \end{cases} \tag{4.91}$$

In the above equation, $I(\bar{p}^*)$ represents the contact ratio predicted from the Xu and Jackson [3] modified Greenwood model:

$$I(\bar{p}^*) = A^*(\bar{p}^*) = 1 - \frac{1}{2\sqrt{3}}\sqrt{\alpha^p}\int_{\bar{p}^*}^{\infty}\int_0^{\infty}(\xi^{p*} - \bar{p}^*)\left(k_g{}^{p*}\right)^{-1}\emptyset^p\left(\xi^{p*}, k_g{}^{p*}\right)dk_g{}^{p*}d\xi^{p*}$$

and $f(\bar{p}^*)$ can be determined using the following equation:

$$f(\bar{p}^*) = a \cdot exp(b\bar{p}^*) + c \cdot exp(d\bar{p}^*)$$

Where, a = -c. The value of a, b, c, and d vary from surface to surface and will be discussed later in Chapter 5. In Chapter 5, Eq. (4.91) has been used for the validation of the newly developed rough surface models.

4.3.2 Rough Surface Models for the Elastic-plastic Contact and Contact Resistance Determination

4.3.2.1 Statistical Model or Multi-asperity Model

The statistical model was originally developed to model the low load elastic rough surface contact cases. However, this rough surface model was developed based on the statistical characterization of the rough surface and single asperity. Therefore, any single asperity model that represents the particular application should be able to predict the contact behavior when employed in the statistical or multi-asperity rough surface model. Based on this idea, the GW statistical model has been applied to model other contact cases [85-89]. However, as the development of the statistical model depends on the asperity model, if the asperity model has pitfall, it inherently transfers to the asperity based statistical model. That is why the rough surface models developed to predict the elastic-plastic contact behavior using the truncation, ZMC, CEB and other single asperity models have serious limitations (see sec 2.3). Later Kogut and Etsion [89] and Jackson and Green [87] developed elastic-plastic rough surface contact models using the KE and JG single asperity models respectively (see sec 2.3 and 2.3.1). When the deformation is small, or the plasticity index of a rough surface is less than 10, the KE and JG models predict almost the same contact behavior. Greenwood and Williamson [27] defined the plasticity index from the surface properties and critical interference of the material, which is given as [27, 87]:

$$\psi = \sqrt{\frac{\sigma_s}{w_c}} \tag{4.92}$$

In the above equation, σ_s is the standard deviation of the asperity heights and w_c is the critical interference of the average asperity i.e. the amount of interference that causes initial yielding in

the material. When this plasticity index value is greater than 10, KE and JG elastic-plastic rough surface models do not behave in the same way. Reasons that cause the difference between these two models have been discussed in detail in sec. 2.3.1. At the beginning of the contact, JG and KE asperity models predict almost the same result with a very negligible amount of difference; however, for the large deformation JG model is more suitable than the KE model. The JG elastic-plastic rough surface model has been developed such that when interference, ω, is less than the critical value of interference, ω_c, the rough surface model uses Hertz single asperity model (i.e. Eq. (2.65)) to predict the contact area and contact force. However, when interference, ω, is greater than the critical value of interference, ω_c, rough surafce model uses Eq. (2.66) to (2.69) to predict the elastic-plastic contact behavior. When employing this single asperity model in the framework of the statistical model, it needs to be applied with caution as the JG single asperity model can predict contact behavior only when $\frac{a}{R} \leq 0.41$, where a and R are the contact radius and radius of curvature of the single asperity respectively. Although this limitation has been eliminated later by Jackson, Green and Marghitu [90] and Wadwalkar and Jackson [91].

Wilson, Angadi and Jackson [88] applied the JG rough surface model to determine the electrical contact resistance between two rough surafce. Electrical contact resistance has already been defined in Chapter 1. When two surfaces come into contact, the electricity passes only through the real contact area. If the contact pressure is infinitesimally small, the total real contact area can be assumed as the summation of isolated "a-spots" distributed randomly at the interface of the mating parts as shown in Fig. 4.4. In 1958, Holm [93] obtained an equation to determine the electrical contact resistance of these "a-spots." If the mating parts are made of different materials, the electrical contact resistance will be:

$$R_{Holm} = \frac{\rho_1+\rho_2}{4a} \tag{4.93}$$

where, ρ_1 and ρ_2 are the electrical resistivity of the contacting surfaces and a is the contact radius. However if the matting parts are made of the same materials, then the above equation reduces to the following:

$$R_{Holm} = \frac{\rho}{2a} \tag{4.94}$$

Later in 1966, Greenwood and Williamson (GW model) [27] employed the Holm equation in their statistical rough surface model to determine the electrical contact resistance between two rough surfaces. According to the GW model, the total contact resistance at the interface will be:

$$\frac{1}{E_r} = A_n\eta \int_d^\infty \frac{2a}{\rho} \varphi^h(z)dz \tag{4.95}$$

In the above equation, E_r is the total contact resistance, A_n is the nominal contact area, η is the areal asperity density, a is the contact radius of the "a-spots" and can be calculated using a single asperity model, $\varphi^h(z)$ is the probability distribution function of the asperity of the rough surface and d is the separation distance between the mean height of the contacting surfaces. The above described contact resistance model works well when the contact pressure is small. The model assumes that as the "a-spots" are sufficiently separated to be mechanically independent and therefore current flow through them is also independent. However, due to heat generation or with the increase of applied pressure, the effect of asperity interaction becomes important. To consider the effect of the adjacent asperity interactions, Wilson et al. [88] modified Eq. (4.95) to the following equation:

$$\frac{1}{E_r} = \frac{A_n\eta}{\psi} \int_d^\infty \frac{2a_{ep}}{\rho} \varphi^h(z)dz \tag{4.96}$$

Where, ψ is the alleviation factor and considers the effect of the asperity interaction in the electrical contact. There are various ways to calculate this alleviation factor [94], however, Wilson and Jackson used the following simplified version offered by Copper et al. [95]:

$$\psi = \left(1 - \sqrt{\frac{A_r}{A_n}}\right)^{1.5} \tag{4.97}$$

A_r is the real contact area and A_n is the nominal contact area. Wilson et al. [88] also developed a multi-asperity model for the elastic contact to determine the electrical contact resistance employing Hertz single asperity model for the contact area and contact force, i.e., Eq. (2.17) and (2.18).

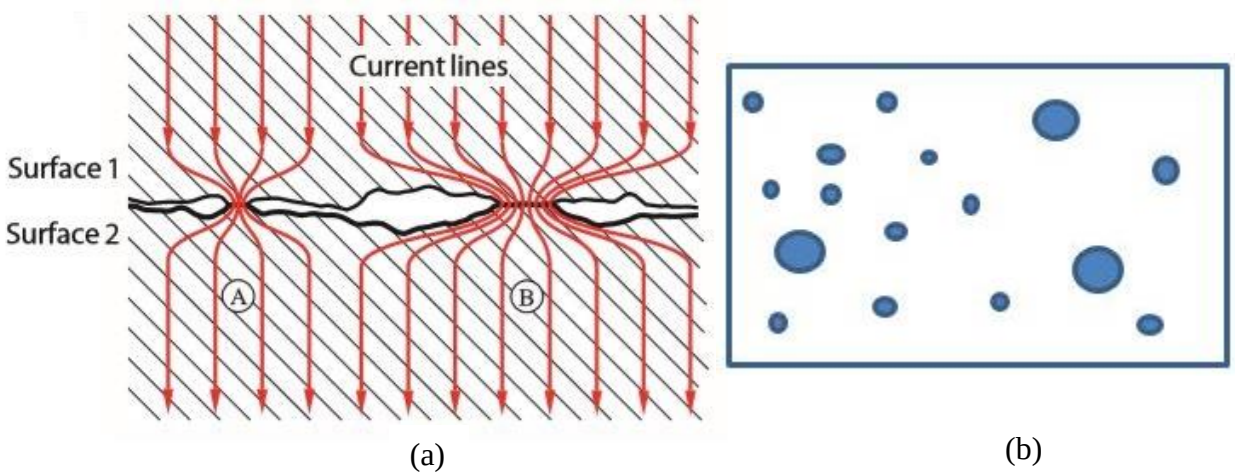

(a) (b)

Fig. 4.4 (a) Schematic of the current flow through the constriction between the contacting surfaces, reprinted from "Taheri, P., Hsieh, S., & Bahrami, M. (2011). Investigating electrical contact resistance losses in lithium-ion battery assemblies for hybrid and electric vehicles. Journal of Power Sources, 196(15), 6525-6533", taking permission from Elsevier, (b) Schematic of the "a-spots" at the contact.

4.3.2.2 Multiscale Model

Stacked Multiscale Modeling Method

Archard [46] first developed the concept of stacked multiscale rough surface modeling. Archard rough surface contact model and multiscale elastic rough surface modeling based on Archard's concept have been discussed in detail in sec 4.3.1.4. Research works that have been done on the development of the stacked multiscale elastic-plastic rough surface contact modeling and determination of the electrical contact resistance will be discussed in the next few paragraphs.

Jackson and Streator [40] first developed multiscale rough surface contact model based on the FFT of the rough surface. Jackson et al. [40] used Jackson and Green (JG model) single asperity model [49] to analyze the elastic-plastic multiscale rough surface contact. With the increase of load, the stresses in the asperity at each scale gradually increases. When the interference, ω due to the applied load is less than the critical value of interference, ω_c, Jackson-Streator model used Hertz equation (Eq. (2.65)) in the framework of the multiscale model (Eq. (4.73) and (4.74)). When the interference, ω is greater than the critical value of interference, ω_c, Eq. (2.66) to (2.69) have been employed for the asperity model in the multiscale model. However, Eq. (2.68) and (2.69) are valid only when $\frac{a}{R} \leq 0.41$. Depending on the degree of loading and the details of the frequency spectrum, in many cases $\frac{a}{R}$ may exceed the value of 0.41. For such cases, when $\frac{a}{R} > 0.41$, Jackson and Streator provided the following equation [40]:

$$\left(\frac{H_G}{S_y}\right)_{ext} = 7.32\left(\frac{a}{R}\right)^3 - 14.1\left(\frac{a}{R}\right)^2 + 6.28\left(\frac{a}{R}\right) + 1.52 \tag{4.98}$$

The above equation has some limitation, that is why later Jackson, Green and Marghitu [90] provided another equation for $\frac{H_G}{S_y}$ which is valid from $0 < \frac{a}{R} < 1$ and also Wadwalkar and Jackson [91] provided empirical equations for heavily deformed spherical contact which are discussed in detail in Chapter 2 (see sec. 2.3.1 and sec. 2.3.2). Almeida, Ramadoss, Jackson, Ishikawa and Yu [96] investigated a laterally actuated multicontact MEMS relay experimentally and compared the experimental results with the theoretical electrical contact resistance calculated by employing the Jackson-Streator multiscale model [40]. The multiscale model showed good qualitative agreement with the experimental measurement. The author showed that for that particular electrical contact case, there were also other factors such as, liquid meniscus adhesion, scale dependent material properties etc. that were important to obtain good quantitative agreement.

Wilson, Angadi and Jackson [88] performed an elastic-plastic rough surface contact analysis based on the Jackson-Streator multiscale model [40]. However, different asperity models have been used in the structure of the multiscale model. Wilson et al. [88] employed the empirical equations for the 3D elastic-plastic sinusoidal asperity model developed by Krithivasan et al. [97] and Jackson et al. [98]. The empirical equations developed by [97] and [98] (Eq. (4.99)-Eq. (4.101)) have not been described in Chapter 2, as Ghaednia et al. [99] have refined the 3D elastic-plastic sinusoidal asperity model later. According to Wilson et al., for the multiscale rough surface contact model, when the average contact pressure, $\bar{p}$ is less than the average pressure during initial yielding, p_c, the JGH elastic 3D sinusoidal asperity model i.e. Eq. (2.46) and Eq. (2.47) can be employed in the multiscale modeling. When the average contact pressure, $\bar{p}$ is greater than p_c, the following equations developed for the 3D elastic-plastic asperity model have been employed [97, 98]. For the 3D sinusoidal asperity model, the radius of curvature at the tip of the asperity is, $R =$

$\frac{\lambda^2}{4\pi^2\Delta}$. Substituting the equation for radius of curvature in Eq. (2.62) and (2.63), the average contact area and contact pressure at the initiation of yielding can be obtained:

$$A_c = \frac{2}{\pi}\left(\frac{CS_y\lambda^2}{8\Delta E'}\right)^2$$

$$p_c = \frac{1}{6\pi}\left(\frac{\lambda^2}{\Delta E'}\right)^2\left(\frac{C}{2}S_y\right)^3$$

The contact area from initial to complete contact at any scale, *i*, is:

$$\bar{A_\iota} = (A_p)\left(1 - \left[\frac{\bar{p}}{p^*_{ep}}\right]^{1.51}\right) + (A_{JGH})_2\left[\frac{\bar{p}}{p^*_{ep}}\right]^{1.04} \tag{4.99}$$

where,

$$A_p = 2\left(\frac{A_c}{2}\right)^{\frac{1}{1+d}}\left(\frac{3\bar{p}\lambda^2}{4CS_y}\right)^{\frac{d}{1+d}}$$

$$d = 3.8\left(\frac{E'}{S_y}\frac{\Delta}{\lambda}\right)^{0.11}$$

The pressure to cause complete contact during the elastic-plastic deformation is [97]:

$$\frac{p^*_{ep}}{p^*_e} = \left(\frac{11}{4\frac{\Delta}{\Delta_c}+7}\right)^{3/5} \tag{4.100}$$

where,

$$\Delta_c = \frac{\sqrt{2}S_y\lambda}{3\pi E'}exp\left(\frac{2\nu}{3}\right) \tag{4.101}$$

p_e^* can be calculated from Eq. (2.43) and Δ_c is the amplitude below which 3D sinusoidal asperity will deform elastically from early contact to complete contact. As mentioned before, Eq. (4.99)-4.101 have been refined by Ghaednia et al. [99] (Eq. (2.93)-(2.98)), therefore, to improve the above discussed rough surface model, instead of Eq. (4.99-4.101), Eq. (2.93)-(2.98) have to be used. Wilson et al. also calculated electrical contact resistance considering the multiscale nature of the surface. If the asperities distributed on each scale are 3D sinusoidal in shape then the contact area for each of the asperities will be:

$$\frac{A_i}{A_{i-1}} = \frac{2\pi {a_i}^2}{{\lambda_i}^2} \Rightarrow\gg a_i = \sqrt{\frac{{\lambda_i}^2 A_i}{2\pi A_{i-1}}} \tag{4.102}$$

Now the total contact resistance at each scale, *i* can be calculated by summing the reciprocal of the resistance of each individual asperity on each scale as this multiscale model assumes that the asperities are electrically in parallel.

$$\frac{1}{R_c} = \sum_{n=1}^{N} \frac{1}{R_{asp}}$$

Since according to the assumption of the multiscale model, all the asperities at this frequency will be identical, the above equation reduces to the following equation:

$$R_c = \frac{R_{asp}}{N_i} = \frac{R_{asp}}{\eta_i A_{i-1}}$$

N_i is the number of asperities at scale, *i* and A_{i-1} is the contact area at the previous scale, *i*-1. Then summing over all the considered scales the total resistance for the entire surface in contact can be calculated.

$$E_r = \sum_{i=1}^{i_{max}} \frac{R_{asp}}{N_i} \psi_i = \sum_{i=1}^{i_{max}} \frac{\rho}{2a} \frac{1}{N_i} \psi_i \tag{4.103}$$

$$N_i = 2 \frac{A_{i-1}}{\lambda_i^2} \tag{4.104}$$

ψ_i is the alleviation factor. For the multiscale rough surface contact model, alleviation factor has to be calculated using the following formula:

$$\psi_i = \left(1 - \sqrt{\frac{A_i}{A_{i-1}}}\right)^{1.5} \tag{4.105}$$

For 3D periodic sinusoidal elastic-plastic model, the contact area and pressure equation considers the factor 2 (two asperity) that is why when employing Eq. (4.104) in the multiscale model, the factor 2 in the numerator does not need to be considered. Using the same empirical equations and multiscale model as described above [88], Zhang and Jackson [100] analyzed surfaces with different finishes which represent different manufacturing processes and observed the effect of surface finishes on the contact pressure-area relation and contact resistance behavior. They have also compared their result with the conventional method of dividing the contact force by the hardness (2.8 times the yield strength, S_y) to calculate the electrical contact resistance. The conventional method did not show a good qualitative agreement with the multiscale model.

To determine the electrical contact resistance, Holm's equation is widely used. However, when the size of the "a-spots" become less than the electron mean free path length, *l*, the electrical conduction mechanism changes from a diffusive mechanism (Maxwell) to a ballistic mechanism (Sharvin). Jackson, Crandall and Bozack [101] developed the previously described Wilson et al. [88] multiscale electrical contact resistance model considering the quantum and size-dependent

contact and electrical conduction mechanisms. To model size dependent contact, scale dependent mechanical and electrical properties have been considered.

Fractal Method

Gao and Bower [102] developed an elastic-perfectly plastic rough surface contact model for the 2D plane-strain condition. To develop the model they analyzed the contact between a rigid cylindrical indenter and an elastic-perfectly plastic solid with a fractal surface roughness. The fractal surface roughness was idealized by a Weierstrass profile, which can be described by the following equation:

$$h(x) = G_0 \sum_{m=0}^{\infty} \gamma^{(D-2)m} \cos\left(\frac{2\pi x \gamma^m}{\lambda_0}\right) \tag{4.106}$$

In the above equation, $h(x)$ is the surface profile height, G_0 is the fractal roughness, m is the fractal scale index, γ is the fractal scaling parameter, D is the fractal dimension and λ_0 is the wavelength at the largest scale. In the analysis, it has been assumed that, $\gamma \gg 1$ so that the successive scales are decoupled or widely separated from each other. In this condition, each scale can be considered as a sinusoidal surface, indented by a rigid flat. Although it is not an actual representation of the rough surface, it can still represent the multiscale nature of the rough surafce. To couple the successive scales, it has been assumed that nominal pressure acting on scale i is equal to the true pressure acting on scale i-1. According to their analysis, the following three dimensionless functions control the elastic-perfectly plastic contact behavior at the plane-strain condition:

$$\Sigma = \sqrt{\frac{PE'}{RS_y^2}}, \psi = \left(\frac{G_0 E'}{\lambda_0 S_y}\right), K = \left(\frac{\gamma \lambda_0^2}{G_0 R}\right) \tag{4.107}$$

In the above equation, $\sum is$ the dimensionless load parameter, ψ and *K* together characterize the surface roughness and its resistance to the plastic flow, *P* is the load per unit length out of plane, *R* is the radius of the cylinder. The parameter $\psi^D K^{D-1}$is the plasticity index for the fractal rough surface. When the value of $\psi^D K^{D-1}$is small, most of the surface scales remain elastic and with the increase of $\psi^D K^{D-1}$the number of plastic roughness scales and the depth of the plastically deformed layer gradually increases. Curve fitting the FEA results, they provided empirical equations for contact pressure distribution, contact size, the total area of contact and number of contacts for each scale of roughness. Also analyzed the change in nominal pressure to yield strength ratio and mean pressure to yield strength ratio with the change in contact fraction and provided empirical equations by curve fitting to the FEA results. Their results show that when the contact fraction is close to 1.0, both the nominal and mean pressure reach a value of 5.8 times the yield strength. Like the previously described Ciavarella elastic fractal rough surface contact model [9] this mode also provided an unphysical prediction of the true contact size and the number of contact spots when $m \to \infty$. It has been suggested in the paper that when $m \to \infty$, by considering the effect of adhesion and the deviation of the real surface from the fractal behavior at the smaller scales, may be a finite contact area or logical result can be obtained. Although the model developed by Gao and Bower was for the Weierstress fractal rough surface, the empirical equations provided in their paper are applicable to any discrete approximation to a Power Spectral Density, provided that successive scales are widely separated from each other.

In section 4.3.1.4, the simplified multiscale model for elastic contact developed by Jackson [10] has been discussed in detail. Although the model was developed using fractal rough surface profiles, the model is applicable to both fractal and real surfaces. Simplified multiscale model was approximated using the elastic superposition principal; apparently, it seems that this model should

not work for the elastic-plastic cases. However, the result found from the 3D elastic-plastic model developed by Krithivasan et al. [97] and Jackson et al. [98] show that for the elastic-plastic sinusoidal surfaces in complete contact the deformation appears to effectively revert to elastic deformation. Actually, the stress becomes hydrostatic at complete contact and theoretically, there will be no further plastic deformation there. Therefore, the elastic superposition principal may be applicable to the complete contact for the 3D elastic-plastic case also. Now employing the equation of p_{ep}^{*} derived by Jackson et al. for 3D elastic-plastic case [98], the following approximate equation for total real contact area can be obtained:

$$(A_r)_{elastic-plastic} = \frac{F}{p_{ep}^{*}} \tag{4.108}$$

Substituting the value of p_{ep}^{*} from Eq. (4.100), the real contact area for elastic-perfectly plastic case can be obtained.

$$(A_r)_{elastic-plastic} = \frac{F}{\sqrt{2}\pi E' B_{max}} \left(\frac{\frac{12\pi E'}{2} B_{max} + 7}{\sqrt{2} S_y e^{\frac{3}{2}\upsilon}} \right)^{3/5} \tag{4.109}$$

Eq. (4.109) has been formulated using Eq. (4.100) and (4.101) which have been improved by Ghaednia et al. [99]. Therefore, to employ this simplified elastic-perfectly plastic asperity model instead of Eq. (4.100) and (4.101), Eq. (2.93) and Eq. (2.94) have to be used in Eq. (4.116). Using this simplified multiscale model, Jackson, Malucci, Angadi and Polchow [103] obtained a simplified model of multiscale electrical contact resistance. For this model, the real contact area equation for 3D elastic and elastic-perfectly plastic model have been modified to the following:

$$(P_r)_{elastic} = \sqrt{2}\pi E' C B_{max} = \frac{F}{A_r} \tag{4.110}$$

$$(P_r)_{elastic-plastic} = \sqrt{2}\pi E' C B_{max} \left(\frac{11}{\frac{12\pi E'}{\sqrt{2} S_y e^{\frac{2}{3}\upsilon}} B_{max} + 7} \right)^{3/5} \tag{4.111}$$

In the above two equation, the value of *C* is 0.8. To make these two equations applicable from early contact to complete contact, the following equation has been suggested:

$$(P_r)_{eff} = P_r(CB_{max}) + [P_r(B_{max}) - P_r(CB_{max})] \left(\frac{F}{A_r P_r(B_{max})} \right)^{\beta} \tag{4.112}$$

For elastic contact, β=2 and for the elastic-perfectly plastic contact $\beta = 4$. Therefore, the new equation for real contact area will be:

$$A_r = \frac{F}{(P_r)_{eff}}$$

The electrical contact resistance according to the simplified multiscale electrical contact resistance model is given by:

$$R = \sqrt{\frac{\pi}{8}} \left(\frac{\rho \lambda_{max}}{F} \right) (P_r)_{eff} \tag{4.113}$$

If for a particular scale, the value of amplitude, Δ, is less than Δ_c it will deform elastically, otherwise it will deform elastic-perfect plastically. Jackson et al. [103] compared the simplified multiscale electrical contact resistance model with the "Fully Plastic" model given by Malucci [104] and the GW perfectly elastic model [27]. However, in the GW perfectly elastic model instead of a Gaussian distribution, an exponential distribution suggested by Greenwood and Williamson has been used so that equations can be solved analytically. The comparison shows that the simplified electrical contact resistance model matches well with "Fully plastic" model given by

Malucci [104]. According to Holm [93] and Greenwood [105], electrical contact resistance between rough surfaces is:

$$R = \frac{\rho}{2na} + \frac{\rho}{D} \tag{4.114}$$

In the above equation, *n* is the number of asperity contacts in the diameter of 'macro' contact, *D*. According to the "Fully plastic" model derived by Malucci [104], the micro-scale multi-spot contact resistance is given by the following equations:

$$n = 196F\left(\frac{0.24\times10^{-6}}{\sigma}\right)^2\left(1 + \frac{F}{2.84S_yA_n}\right)^{-1} \tag{4.115}$$

$$na = \left[\frac{3nF}{2.84S_y\pi}\left(1 + \frac{F}{2.84S_yA_n}\right)^{-1}\right]^{1/2} \tag{4.116}$$

$$A = \frac{F}{H}\left(1 + \frac{F}{2.84S_yA_n}\right)^{-1} = \frac{F}{2.84S_y}\left(1 + \frac{F}{2.84S_yA_n}\right)^{-1} \tag{4.117}$$

σ is the standard deviation or RMS surface roughness and *A* is the contact area. Substituting Eq. (4.116) into Eq. (4.114), electrical contact resistance can be determined. Using an exponential distribution instead of Gaussian distribution in the GW perfectly elastic model, the following equation for ECR has been obtained [103]:

$$R = \frac{\rho\sigma E'}{F} \tag{4.118}$$

Persson Model

Persson [106] developed both an elastic and elastic-plastic contact model for fractal rough surfaces based on the following diffusion type of equation:

$$\frac{\partial P}{\partial \zeta} = G'(\zeta)\sigma_0^2 \frac{\partial^2 P}{\partial \sigma^2} \tag{4.119}$$

In the above diffusion type of equation, time is replaced by the magnification, ζ, and the spatial co-ordinate by stress, σ. $P(\zeta) = \frac{A(\lambda)}{A(L)}$ denotes the relative fraction of the surface where contact occurs. $A(L)$ is the macroscopic contact area and $A(\lambda)$ is the real contact area if the surface is flattened on all length scales shorter than λ. $\lambda = \frac{L}{\zeta}$ where $\zeta \geq 1$ and L is the largest wavelength of the rough surface spectrum. $G'(\zeta)$ denotes the ζ derivative of the function:

$$G(\zeta) = \frac{\pi}{4}\left[\frac{E}{(1-\nu^2)\sigma_0}\right]^2 \int_{k_L}^{\zeta k_L} dk\, k^3 S(k) \tag{4.120}$$

If F is the applied force on the rough surface, then $\sigma_0 = \frac{F}{A_0}$, A_0 is the nominal contact area. k_L is the wavenumber at the smallest length scale or upper cut off wavenumber and $k_L = \frac{2\pi}{L}$. $S(k)$ is the Power Spectral Density (PSD) of the rough surface. The developed model by Persson is only valid for the self-affine fractal rough surface. To generate the self-affine rough surface, Persson employed the following definition of PSD:

$$S(k) = C_0 \left(\frac{k}{k_0}\right)^{-2(1+H)} \text{ when } k > k_0$$

$$S(k) = C_0 \qquad \text{when } k < k_0 \tag{4.121}$$

where, H is the Hurst exponent and related to the fractal dimension, D by D=3-H. C_0 can be determined from the following equation:

$$C_0 = \alpha \left(\frac{h_0}{k_0}\right)^2 \frac{H}{2\pi} \tag{4.122}$$

where, $h_0^2 = \langle h^2 \rangle$, and $\langle h^2 \rangle$ is the RMS surface roughness or amplitude. α can be calculated using the following equation:

$$\alpha = \frac{1}{1+H-\left(\frac{k_L}{k_0}\right)^2 H} \tag{4.123}$$

k_0 is the lower cutoff wavenumber. Substituting Eq. (4.121) into Eq. (4.120), defining $k = k_L\zeta$ and assuming $k \gg k_0$ gives,

$$G(\zeta) \approx \left(\frac{k_0 h_0}{4(1-\nu^2)}\right)^2 \frac{\alpha H}{(1-H)} \left(\frac{E}{\sigma_0}\right)^2 \left(\frac{k}{k_0}\right)^{2(1-H)} \tag{4.124}$$

For the elastic case, two boundary conditions have been applied:

1. Detachment will occur when local stress, $\sigma \to 0$, i.e. $P(0,\zeta) = 0$. No adhesion is considered in the model.
2. Yield will occur only when $\sigma \to \infty$, i.e. $P(\infty,\zeta) = 0$

Applying these two boundary conditions in Eq. (4.119), the area of contact on the length scale, $\lambda = \frac{2\pi}{k}$ is:

$$A(\lambda) = \frac{4(1-\nu^2)}{k_0 h_0} \left(\frac{1-H}{\pi\alpha H}\right)^{1/2} \frac{F}{E'} \left(\frac{\lambda}{\lambda_0}\right)^{1-H} \tag{4.125}$$

If, $\lambda_0 = L \; and \; k_0 = \frac{2\pi}{L}$, then the above equations becomes:

$$A(\lambda) = \frac{2L(1-\nu^2)}{\pi h_0} \left(\frac{1-H}{\pi\alpha H}\right)^{1/2} \frac{F}{E'} \left(\frac{\lambda}{L}\right)^{1-H} \tag{4.126}$$

To consider plasticity in the rough surface model, Persson provided the following equation:

$$P_{el}(\zeta) + P_{non}(\zeta) + P_{pl}(\zeta) = 1 \tag{4.127}$$

In the above equation, $P_{el}(\zeta), P_{pl}(\zeta)\ and\ P_{non}(\zeta)$ are the fraction of the contact area that is elastic, plastic and not in contact respectively. To solve Eq. (4.119) for the elastic-plastic case Persson considered the following two boundary conditions:

1. $P(0,\zeta) = 0$, and 2. $P(\infty,\zeta) = 0$

$P_{pl}(\zeta)\ and\ P_{non}(\zeta)$ can be calculated using the following equations:

$$P_{non} = \frac{2}{\pi}\sum_{n=1}^{\infty}\frac{sin\alpha_n}{n}\{1 - exp[-\alpha_n^2 G(\zeta)]\} \tag{4.128}$$

$$P_{pl} = -\frac{2}{\pi}\sum_{n=1}^{\infty}(-1)^n\frac{sin\alpha_n}{n}\{1 - exp[-\alpha_n^2 G(\zeta)]\} \tag{4.129}$$

Where $\alpha_n = \frac{n\pi\sigma_0}{S_y}$ and $G(\zeta)$ is given by Eq. (4.120). The fraction of the macro-contact area where elastic contact occurs can be determined by substituting P_{non} and P_{pl} in Eq. (4.127).

4.3.2.3 Analysis of the Elastic-plastic Contact Using FEM/ Deterministic Modeling:

The previously described rough surface contact models (statistical model, multiscale rough surface models); all were developed based on different assumptions to simplify the rough surface model and to reduce the computational expenses. Therefore, it is important to validate these idealized theoretical rough surface models and Deterministic modeling can serve this purpose. For Deterministic rough surface contact modeling, generally all the data points measured using a surface measurement instrument are directly used in the model. In 2007. Thompson [107] showed that it is possible to import measured surface data into ANSYS and to analyze rough surface contact using FEM. Later in 2010, Thompson et al. [108] performed another rough surface contact

analysis using FEM and introduced different factors that may help to develop rough surface contact modeling using the directly measured rough surface data. According to their analysis, identifying "representative" surfaces, shape of surface geometry i.e. whether to connect the sampling points by a simple straight line or spline interpolation, surface layers and impurities, mesh density, incorporating material non-linearity, effect of different contact parameters, boundary conditions, and solving method, etc. are noteworthy and may improve the FEA. The largest model solved by Thompson et al. in 2010 consists of 377,556 elements and the computational time was 105 hr.

Liu et al. [109] performed a Deterministic FEA of a microswitch contact by scanning the contact surface using AFM. They used different resolution for their FEA and analyzed force-displacement, force-contact area, force-contact resistance and different other contact behavior. It has been mentioned in their paper that for proper determination of the contact spot it will require a very fine mesh, which needs an outrageous solving duration. Jackson et al. [110] employed a multiscale model (similar to previously described Wilson, Angadi and Jackson multiscale elastic-plastic rough surface model) to determine contact area, pressure to yield strength ratio, number of contact spots and compared the results with the deterministic result of Liu et al. [109]. Good qualitative agreement has been found for all the contact parameters, however, the contact area-pressure and real contact pressure to yield strength ratio were almost identical to the Deterministic FEA result.

Jackson and his research group [111-113] recently have also done detailed analysis on rough surface contact modeling using FEA and compared the FEA results with the available theoretical models. They have analyzed the effect of different parameters, such as- smoothing of the surface data points using linear and spectral/ harmonic interpolation, number of total elements and contact elements, contact modeling using the Gauss and Nodal point method, effect of normal load, both normal and tangential load, plasticity index, and different amounts of hardening. They showed the

effect of these parameters on the contact pressure-area relation, static friction co-efficient, average gap, average contact pressure to yield strength ratio, von Mises stress, and other contact parameters. Their results show that sampling resolution has a significant effect on the contact behavior. The smallest resolution they have tried in their analysis is 0.25 μm. Using this resolution the model has in total 868,806 elements and the computational time was 20 days using a 20-processor high performance cluster. For low load or at the beginning of contact it requires very fine elements to capture the contact behavior and very fine elements will increase the number of elements and computational time significantly. That is why the theoretical models in their analysis match better with the FEA at high load or large contact region. Although during their analysis, they did not reach mesh convergence; their study provides methodology to the FEA of rough surface contact that may push the simulation results closer to the reality.

4.3.2.4 Determination of the Electrical Contact Resistance (ECR) if Thin Films/Oxides are Present at the Interface:

Due to surface roughness, current flows through the asperity peaks, as a result current will effectively be "bottlenecked" and causes in contact resistance (See Fig. 1.1 and 4.4(a)). Previous research shows that the presence of thin film /oxides is also a common phenomenon in the electrical contact [114-116]. Therefore, total ECR at each microcontact consists of constriction resistance due to convergence and divergence of the current flow and tunnel resistance due to the presence of an insulating film. If two electrodes are separated by a sufficiently thin insulating film, current can flow between the electrodes by means of the tunneling effect. Sommerfield and Bethe [117] were the first who investigated it theoretically for very low and high voltages and Holm [118] extended their study for the intermediate voltages. Sommerfield and Bethe [117] and Holm and Kirschstein [119] assumed a symmetric parabola shaped potential barrier to simplify the

analysis and to derive analytical equations. However, this assumption limits the range and applicability of their models. Simmons [120] derived current-voltage formulas for electric tunneling through an arbitrary shape or generalized potential barrier, existing in a thin insulating film that separates two similar electrodes. Then Simmons applied the generalized barrier formulas to the rectangular shape potential barrier with and without the image forces effect. These formulas are applicable for true image force problems for all voltage ranges. Image force reduces the area of the potential barrier by rounding off the corners of its distribution; as a result, this reduces the thickness of the barrier and increases the current flow between the electrodes. Now, if we consider a single microcontact of area A_i, covered by a thin insulating film of thickness t, dielectric constant, *K*, and energy height above the Fermi level of the conductive surfaces, $\emptyset_0$, then for a rectangular shaped potential barrier with the image force effect, the current through the microcontacts for different voltage drop are given by the following formulas [120]:

When $V_i \cong 0$,

$$I_i = (3.16 \times 10^{10}/\Delta S)\emptyset_L^{1/2} \times exp\left(-1.025\Delta S\emptyset_L^{1/2}\right)V_i A_i \tag{4.130}$$

$\emptyset_L$ is the mean barrier height and is given by:

$$\emptyset_L = \emptyset_0 - \left[\frac{5.75}{K\Delta S}\right] ln\left[\frac{S_2(t - S_1)}{S_1(t - S_2)}\right]$$

$$\Delta S = S_2 - S_1$$

S_2 and S_1 are the limits of the barrier at Fermi level and can be calculated using the following formula:

$$S_1 = \frac{6}{K\emptyset_0} \text{ and } S_2 = t - \frac{6}{K\emptyset_0}$$

The tunnel resistance, R_{ti} when $V_i \cong 0$ will be:

$$R_{ti} = \frac{V_i}{I_i} = \frac{\Delta S exp(1.025\Delta S\emptyset_L^{1/2})}{3.16\times10^{10}\emptyset_L^{1/2}} \frac{1}{A_i} \tag{4.131}$$

If the voltage drop across the microcontact is not very small then:

$$I_i = \frac{6.2\times10^{10}}{(\Delta S)^2}\left\{\varphi_L exp\left(-1.025\Delta S\emptyset_L^{1/2}\right) - (\emptyset_L + V_i)exp\left[-1.025\Delta S(\emptyset_L + V_i)^{1/2}\right]\right\}A_i \tag{4.132}$$

where,

$$\emptyset_L = \emptyset_0 - \left[\frac{V_i}{2t}\right](S_1 + S_2) - \left[\frac{5.75}{K\Delta S}\right] ln\left[\frac{S_2(t - S_1)}{S_1(t - S_2)}\right]$$

If $V_i < \emptyset_0$,

$$S_1 = \frac{6}{K\emptyset_0} \text{ and } S_2 = t\left[1 - \frac{46}{(3\emptyset_0 Kt + 20 - 2V_i Kt)}\right] + \frac{6}{K\emptyset_0}$$

If $V_i > \emptyset_0$,

$$S_1 = \frac{6}{K\emptyset_0} \text{ and } S_2 = \frac{(\emptyset_0 Kt - 28)}{KV_i}$$

So the tunneling resistance will be:

$$R_{ti} = \frac{V_i}{I_i} \tag{4.133}$$

Now substituting the value of I_i from Eq. (4.130) and the value of V_i into Eq. (4.131) the tunneling resistance can be determined.

Jackson and Kogut [121] analyzed and modeled the electrical contact resistance between two surfaces separated by an anisotropic conductive film, which is made up of an epoxy with conductive spherical metallic particles dispersed within. For the metallic particle flattening they used the extended version of the JG single asperity model which can model the cases when $\frac{a}{R} \geq 0.41$(Eq. (2.66-2.67, 2.70)). To model the ultra-thin insulating film between the particles and the surfaces they applied the above-discussed tunneling theory. Their analysis shows that including the effect of tunneling current through the thin film at the electrical contact significantly improves the prediction of the theoretical model when compared with the experimental results. Jackson et al. [116] performed another analysis to observe the effect of repeated initial connector insertions and roughness on electrical contact resistance. Their analysis showed that multiscale ECR theoretical model shows good agreement with the experimental measurements after the inclusion of the oxide resistance in the theoretical model.

4.4 Summary

1. Archard is probably the first who developed a rough surface contact model based on the "protuberance upon protuberance" concept, which considers the multiscale nature of the surface. However, Archard employed spherical asperities to model the multiscale rough surface (i.e. smaller sphere upon another sphere) which is not realistic. That is why lots of research has been done to develop the multiscale rough surafce model. Among them, the fractal method, and FFT method are noteworthy. These methods consider the wide range of frequency spectrum of the rough surface and then employing different elastic and elastic-

plastic asperity models with different boundary conditions to predict the contact behavior. Persson's model also considers the multiscale nature of the surface. However, Persson's model has been developed based on the diffusion type of equation, not the asperity models.

2. Greenwood and Williamson (GW model) developed a rough surface contact model based on the statistical characterization of rough surfaces. This model is known as the statistical or multiasperity model. The statistical model assumes that surfaces are random in nature. Greenwood and Williamson employed the Hertz spherical asperity model and assumed a Gaussian distribution to model the rough surface contact behavior. Several other assumptions that have been made in the GW model are that the radius of curvature of the asperity is constant and the rough surface model is applicable when the load is very small. Later research has been done to alleviate these assumptions. Among them employing different elastic asperity models in conjunction with different probability distribution functions are noteworthy, which can model different surface and radius of curvature distribution of the asperities. Models have also been developed by employing elastic asperity models, with adhesion, elastic-plastic asperity models, and 3D elastic wavy asperity models in the framework of the statistical model. Recently, the statistical model has also been formulated for near the complete contact regime using the fracture mechanics approach. The statistical model for infinitesimally small contact and near complete contact both were validated using the Boundary Element Method. However, no statistical rough surface model is available which works over the whole range of the contact.
3. Both the Statistical and Multiscale rough surface contact models have been developed based on several assumptions. The advantage of these models are that they reduce the computational expense to a great extent. However, these models need to be validated and

BEM/FEM can serve this purpose. BEM are generally used for the validation of the elastic models and are computationally less expensive than the FEM. Recently works have been done to validate the elastic-plastic rough surface contact models using FEM. No mesh convergence has been obtained in those works as rough surface contact analysis employing FEM are computationally very expensive and may take months or even years.

4. Electrical contact behavior is a very complicated phenomenon. The presence of different kinds of oxides, impurities or wear debris make the electrical contact behavior more complicated. Experimental and theoretical work have been done to determine electrical contact resistance employing statistical and multiscale rough surface models. Previous research work show that depending on the applications and surface roughness, consideration of the oxides, quantum and size dependent electrical conduction mechanism and adhesion may improve the prediction of the theoretical electrical contact resistance models.

Reference

1. Longuet-Higgins, M. S. (1957). Statistical properties of an isotropic random surface. Philosophical Transactions of the Royal Society of London. Series A, Mathematical and Physical Sciences, 250(975), 157-174.
2. Nayak, P. Ranganath. (1971). Random process model of rough surfaces. Journal of Lubrication Technology, 93(3), 398-407.
3. Xu, Y., & Jackson, R. L. (2017). Statistical models of nearly complete elastic rough surface contact-comparison with numerical solutions. Tribology International, 105, 274-291.
4. Xu, Y., (2017). Statistical Models of Nominally Flat Rough Surface Contact. Doctoral dissertation, Auburn University.
5. Ciavarella, M. (2015). Adhesive rough contacts near complete contact. International Journal of Mechanical Sciences, 104, 104-111.
6. Zhang, X., Xu, Y., & Jackson, R. L. (2017). An analysis of generated fractal and measured rough surfaces in regards to their multi-scale structure and fractal dimension. Tribology International, 105, 94-101.
7. Zhang, X., Xu, Y., & Jackson, R. L. (2019). A mixed lubrication analysis of a thrust bearing with fractal rough surfaces. Proceedings of the Institution of Mechanical Engineers, Part J: Journal of Engineering Tribology, 1350650119867242.
8. Majumdar, A., & Bhushan, B. (1990). Role of fractal geometry in roughness characterization and contact mechanics of surfaces. ASME Journal of Tribology, 112(2), 205-216.

9. Ciavarella, M., Demelio, G., Barber, J. R., & Jang, Y. H. (2000). Linear elastic contact of the Weierstrass profile. Proceedings of the Royal Society of London. Series A: Mathematical, Physical and Engineering Sciences, 456(1994), 387-405.
10. Jackson, R. L. (2010). An analytical solution to an Archard-type fractal rough surface contact model. Tribology Transactions, 53(4), 543-553.
11. Zhang, X., & Jackson, R. L. (2017). An analysis of the multiscale structure of surfaces with various finishes. Tribology Transactions, 60(1), 121-134.
12. Hu, Y. Z., & Tonder, K. (1992). Simulation of 3-D random rough surface by 2-D digital filter and Fourier analysis. International journal of machine tools and manufacture, 32(1-2), 83-90.
13. Persson, B. N., Albohr, O., Tartaglino, U., Volokitin, A. I., & Tosatti, E. (2004). On the nature of surface roughness with application to contact mechanics, sealing, rubber friction and adhesion. Journal of physics: Condensed matter, 17(1), R1.
14. Yastrebov, V. A., Anciaux, G., & Molinari, J. F. (2015). From infinitesimal to full contact between rough surfaces: evolution of the contact area. International Journal of Solids and Structures, 52, 83-102.
15. Jackson, R. L., & Green, I. (2011). On the modeling of elastic contact between rough surfaces. Tribology Transactions, 54(2), 300-314.
16. Bush, A. W., Gibson, R. D., & Keogh, G. P. (1976). The limit of elastic deformation in the contact of rough surfaces. Mechanics Research Communications, 3(3), 169-174.
17. Front, I. (1990). The effects of closing force and surface. Roughness on leakage in radial face seals. MS Thesis Technion, Israel Institute of Technology.

18. McCool, J. I. (1986). Comparison of models for the contact of rough surfaces. Wear, 107(1), 37-60.
19. Greenwood, J. A. (2006). A simplified elliptic model of rough surface contact. Wear, 261(2), 191-200.
20. Barber, J. R. (2003). Bounds on the electrical resistance between contacting elastic rough bodies. Proceedings of the royal society of London. Series A: mathematical, physical and engineering sciences, 459(2029), 53-66.
21. Greenwood, J. A., & Tripp, J. H. (1970). The contact of two nominally flat rough surfaces. Proceedings of the institution of mechanical engineers, 185(1), 625-633.
22. O'Callaghan, M., & Cameron, M. A. (1976). Static contact under load between nominally flat surfaces in which deformation is purely elastic. Wear, 36(1), 79-97.
23. Francis, H. A. (1977). Application of spherical indentation mechanics to reversible and irreversible contact between rough surfaces. Wear, 45(2), 221-269.
24. Bhushan, B. (2000). Surface roughness analysis and measurement techniques. In Modern Tribology Handbook, Two Volume Set (pp. 79-150). CRC press.
25. Bansal, D. G. P. (2009). Tribological investigation of electrical contacts. Doctoral dissertation, Georgia Institute of Technology.
26. Rostami, A., & Streator, J. L. (2015). Study of liquid-mediated adhesion between 3D rough surfaces: a spectral approach. Tribology International, 84, 36-47.
27. Greenwood, J. A., & Williamson, J. P. (1966). Contact of nominally flat surfaces. Proceedings of the royal society of London. Series A. Mathematical and physical sciences, 295(1442), 300-319.

28. McCool, J. I. (1992). Non-Gaussian effects in microcontact. International Journal of Machine Tools and Manufacture, 32(1-2), 115-123.
29. Yu, N., & Polycarpou, A. A. (2002). Contact of rough surfaces with asymmetric distribution of asperity heights. ASME Journal of Tribology, 124(2), 367-376.
30. Jeng, Y. R., & Peng, S. R. (2006). Elastic-plastic contact behavior considering asperity interactions for surfaces with various height distributions. ASME Journal of Tribology, 128, 245-251.
31. Whitehouse, D. J., & Archard, J. F. (1970). The properties of random surfaces of significance in their contact. Proceedings of the Royal Society of London. A. Mathematical and Physical Sciences, 316(1524), 97-121.
32. Onions, R. A., & Archard, J. F. (1973). The contact of surfaces having a random structure. Journal of Physics D: Applied Physics, 6(3), 289.
33. Carbone, G., & Bottiglione, F. (2008). Asperity contact theories: Do they predict linearity between contact area and load? Journal of the Mechanics and Physics of Solids, 56(8), 2555-2572.
34. Bush, A.W. (1982). Contact mechanics, in: Thomas, T.R. (Ed), Rough Surfaces, First ed. Longman, London.
35. Jackson, R.L., Xu, Y., Saha, S., & Schulze, K. (2020). Elastic Rough Surface Contact and the Root Mean Square Slope of Measured Surfaces. 30th International Conference on Electrical Contacts, 1-8.
36. Campaná, C., & Müser, M. H. (2007). Contact mechanics of real vs. randomly rough surfaces: A Green's function molecular dynamics study. EPL (Europhysics Letters), 77(3), 38005.

37. Putignano, C., Afferrante, L., Carbone, G., & Demelio, G. (2012). The influence of the statistical properties of self-affine surfaces in elastic contacts: A numerical investigation. Journal of the Mechanics and Physics of Solids, 60(5), 973-982.
38. Yastrebov, V. A., Anciaux, G., & Molinari, J. F. (2017). The role of the roughness spectral breadth in elastic contact of rough surfaces. Journal of the Mechanics and Physics of Solids, 107, 469-493.
39. Carbone, G. (2009). A slightly corrected Greenwood and Williamson model predicts asymptotic linearity between contact area and load. Journal of the Mechanics and Physics of Solids, 57(7), 1093-1102.
40. Jackson, R. L., & Streator, J. L. (2006). A multi-scale model for contact between rough surfaces. Wear, 261(11-12), 1337-1347.
41. Jackson, R.L., Saha, S., & Xu, Y., (2015). The influence of single asperity models on predicting contact between rough surfaces using statistical methods. STLE Tribology Frontiers Conference, Denver, CO.
42. Xu, Y., Jackson, R. L., & Marghitu, D. B. (2014). Statistical model of nearly complete elastic rough surface contact. International Journal of Solids and Structures, 51(5), 1075-1088.
43. Greenwood, J. A. (2015). On the almost-complete contact of elastic rough surfaces: The removal of tensile patches. International Journal of Solids and Structures, 56, 258-264.
44. Sneddon, I. N. (1946). The distribution of stress in the neighborhood of a crack in an elastic solid. Proceedings of the Royal Society of London. Series A. Mathematical and Physical Sciences, 187(1009), 229-260.

45. Ciavarella, M. (2016). Rough contacts near full contact with a very simple asperity model. Tribology International, 93, 464-469.
46. Archard, J. F. (1957). Elastic deformation and the laws of friction. Proceedings of the Royal Society of London. Series A. Mathematical and Physical Sciences, 243(1233), 190-205.
47. Johnson, K. L., Greenwood, J. A., & Higginson, J. G. (1985). The contact of elastic regular wavy surfaces. International journal of mechanical sciences, 27(6), 383-396.
48. Hertz, H., Jones, D. E., & Schott, G. A. (1896). Miscellaneous papers. Macmillan and Company.
49. Jackson, R. L., & Green, I. (2005). A finite element study of elasto-plastic hemispherical contact against a rigid flat. J. Trib., 127(2), 343-354.
50. Wenk, J. F., Stephens, L. S., Lattime, S. B., & Weatherly, D. (2016). A multi-scale finite element contact model using measured surface roughness for a radial lip seal. Tribology International, 97, 288-301.
51. Angadi, S. V., Wilson, W. E., Jackson, R. L., Flowers, G. T., & Rickett, B. I. (2008). A multi-physics finite element model of an electrical connector considering rough surface contact. In 2008 Proceedings of the 54th IEEE Holm Conference on Electrical Contacts, 168-177.
52. Liu, H., & McBride, J. W. (2016). A finite element based electrical resistance study for rough surfaces: Applied to a Bi-layered Au/MWCNT composite for micro-switching applications. In 2016 IEEE 62nd Holm Conference on Electrical Contacts, 65-71.
53. Mandelbrot, B. B. (1983). The fractal geometry of nature. 173, 51. New York: WH freeman.

54. Ausloos, M., & Berman, D. H. (1985). A multivariate Weierstrass–Mandelbrot function. Proceedings of the Royal Society of London. A. Mathematical and Physical Sciences, 400(1819), 331-350.

55. Yan, W. and Komvopoulos, K., 1998. Contact analysis of elastic-plastic fractal surfaces. Journal of Applied Physics, 84(7), 3617-3624.

56. Falconer, K. (2004). Fractal geometry: mathematical foundations and applications. John Wiley & Sons, Chichester, England.

57. Karplus, A. (2008). Self-similar Sierpinski Fractals. Science Fair, Santa Cruz, CA.

58. Morag, Y., & Etsion, I. (2007). Resolving the contradiction of asperities plastic to elastic mode transition in current contact models of fractal rough surfaces. Wear, 262(5-6), 624-629.

59. Westergaard, H. M. (1939). Bearing pressures and cracks. Trans AIME, J. Appl. Mech., 6, 49-53.

60. Zhang, X., & Jackson, R. L. (2017). An analysis of the multiscale structure of surfaces with various finishes. Tribology Transactions, 60(1), 121-134.

61. Persson, B. N. (2001). Theory of rubber friction and contact mechanics. The Journal of Chemical Physics, 115(8), 3840-3861.

62. Lorenz, B., and Persson, B.N.J. (2009). Leak rate of seals: Comparison of theory with experiment. EPL, 86, 44006.

63. Lorenz, B. and Persson, B.N.J. (2010). On the dependence of the leak rate of seals on the skewness of the surface height probability distribution. European Physics Letters, 90(3), 38002.

64. Lorenz, B. and Persson, B.N.J. (2010). Leak rate of seals: Effective-medium theory and comparison with experiment. The European Physical Journal E, 31(2), 159-167.
65. Persson, B.N.J. & Scaraggi, M. (2009). On the transition from boundary lubrication to hydrodynamic lubrication in soft contacts. Journal of Physics: Condensed Matter, 21(18), 185002.
66. Persson, B. N. (2010). Fluid dynamics at the interface between contacting elastic solids with randomly rough surfaces. Journal of Physics: Condensed Matter, 22(26), 265004.
67. Persson, B. N. J. (2007). Relation between interfacial separation and load: a general theory of contact mechanics. Physical review letters, 99(12), 125502.
68. Carbone, G., Mangialardi, L. and Persson, B.N.J. (2004). Adhesion between a thin elastic plate and a hard randomly rough substrate. Physical Review B, 70(12), 125407.
69. Persson, B. N. J. (2008). Capillary adhesion between elastic solids with randomly rough surfaces. Journal of Physics: Condensed Matter, 20(31), 315007.
70. Manners, W., & Greenwood, J. A. (2006). Some observations on Persson's diffusion theory of elastic contact. Wear, 261(5-6), 600-610.
71. McGhee, A. J., Pitenis, A. A., Bennett, A. I., Harris, K. L., Schulze, K. D., Urueña, J. M., ... & Sawyer, W. G. (2017). Contact and deformation of randomly rough surfaces with varying root-mean-square gradient. Tribology Letters, 65(4), 157.
72. Brebbia, C. A., Telles, J. C. F., & Wrobel, L. C. (2012). Boundary element techniques: theory and applications in engineering. Springer Science & Business Media.
73. Becker, A. A. (1992). The boundary element method in engineering: a complete course. McGraw-Hill Companies.

74. Xu, Y., & Jackson, R. L. (2019). Boundary element method (BEM) applied to the rough surface contact vs. BEM in computational mechanics. Friction, 7(4), 359-371.
75. Boussinesq, J. (1885). Application des potentiels à l'étude de l'équilibre et du mouvement des solides élastiques: principalement au calcul des deformations et des pressions que produisent, dans ces solides, des efforts quelconques exercés sur une petite partie de leur surface ou de leur intérieur; mémoire suivi de notes étendues sur divers points de physique mathématique et d'analyse. Gauthier-Villars.
76. Willner, K. (2008). Fully coupled frictional contact using elastic half-space theory. Journal of Tribology, 130(3), 031405.
77. Johnson, K. L., & Johnson, K. L. (1987). Contact mechanics. Cambridge university press.
78. Sneddon, I. N. (1964). The use of transform methods in elasticity. Air Force Office of Scientific Research, United States Air Force.
79. Andersson, T. (1981). The boundary element method applied to two-dimensional contact problems with friction. In Boundary element methods, 239-258. Springer, Berlin, Heidelberg.
80. Müser, M. H., Dapp, W. B., Bugnicourt, R., Sainsot, P., Lesaffre, N., Lubrecht, T. A. ... & Rohde, S. (2017). Meeting the contact-mechanics challenge. Tribology Letters, 65(4), 118.
81. Vakis, A. I., Yastrebov, V. A., Scheibert, J., Nicola, L., Dini, D., Minfray, C. ... & Molinari, J. F. (2018). Modeling and simulation in tribology across scales: An overview. Tribology International, 125, 169-199.
82. Li, S. (2014). A boundary element model for near surface contact stresses of rough surfaces. Computational Mechanics, 54(3), 833-846.

83. Hu, Y. Z., & Tonder, K. (1992). Simulation of 3-D random rough surface by 2-D digital filter and Fourier analysis. International journal of machine tools and manufacture, 32(1-2), 83-90.
84. Wu, J. J. (2000). Simulation of rough surfaces with FFT. Tribology international, 33(1), 47-58.
85. Ciavarella, M., Xu, Y., & Jackson, R. L. (2018). Some closed-form results for adhesive rough contacts near complete contact on loading and unloading in the Johnson, Kendall, and Roberts regime. Journal of Tribology, 140(1), 011402.
86. Chang, W. R., Etsion, I., & Bogy, D. B. (1987). An elastic-plastic model for the contact of rough surfaces. Journal of Tribology, 109(2), 257-263.
87. Jackson, R. L., & Green, I. (2006). A statistical model of elasto-plastic asperity contact between rough surfaces. Tribology International, 39(9), 906-914.
88. Wilson, W. E., Angadi, S. V., & Jackson, R. L. (2010). Surface separation and contact resistance considering sinusoidal elastic–plastic multi-scale rough surface contact. Wear, 268(1-2), 190-201.
89. Kogut, L., & Etsion, I. (2003). A finite element based elastic-plastic model for the contact of rough surfaces. Tribology transactions, 46(3), 383-390.
90. Jackson, R. L., Green, I., & Marghitu, D. B. (2010). Predicting the coefficient of restitution of impacting elastic-perfectly plastic spheres. Nonlinear Dynamics, 60(3), 217-229.
91. Wadwalkar, S. S., Jackson, R. L., & Kogut, L. (2010). A study of the elastic—plastic deformation of heavily deformed spherical contacts. Proceedings of the Institution of Mechanical Engineers, Part J: Journal of Engineering Tribology, 224(10), 1091-1102.

92. Quicksall, J. J., Jackson, R. L., & Green, I. (2004). Elasto-plastic hemispherical contact models for various mechanical properties. Proceedings of the Institution of Mechanical Engineers, Part J: Journal of Engineering Tribology, 218(4), 313-322.
93. Holm, R. (1958). Elektrische Kontakte/Electric Contacts Handbook. Springer, Berlin Heidelberg, Berlin, Heidelberg.
94. Madhusudana, C. V., & Madhusudana, C. V. (1996). Thermal contact conductance. Springer-Verlag, New York, 1-43.
95. Cooper, M. G., Mikic, B. B., & Yovanovich, M. M. (1969). Thermal contact conductance. International Journal of heat and mass transfer, 12(3), 279-300.
96. Almeida, L. V., Ramadoss, R., Jackson, R. L., Ishikawa, K., & Yu, Q. (2007). Laterally actuated multicontact MEMS relay fabricated using MetalMUMPS process: experimental characterization and multiscale contact modeling. Journal of Micro/Nanolithography, MEMS, and MOEMS, 6(2), 023009.
97. Krithivasan, V., & Jackson, R. L. (2007). An analysis of three-dimensional elasto-plastic sinusoidal contact. Tribology Letters, 27(1), 31-43.
98. Jackson, R. L., Krithivasan, V., & Wilson, W. E. (2008). The pressure to cause complete contact between elastic—plastic sinusoidal surfaces. Proceedings of the Institution of Mechanical Engineers, Part J: Journal of Engineering Tribology, 222(7), 857-863.
99. Ghaednia, H., Wang, X., Saha, S., Xu, Y., Sharma, A., & Jackson, R. L. (2017). A review of elastic–plastic contact mechanics. Applied Mechanics Reviews, 69(6).
100. Zhang, X., & Jackson, R. L. (2014). The influence of multiscale roughness on the real contact area and contact resistance between real reference surfaces. In ICEC 2014; The 27th International Conference on Electrical Contacts, 1-6, VDE.

101. Jackson, R. L., Crandall, E. R., & Bozack, M. J. (2015). Rough surface electrical contact resistance considering scale dependent properties and quantum effects. Journal of Applied Physics, 117(19), 195101.
102. Gao, Y. F., & Bower, A. F. (2006). Elastic–plastic contact of a rough surface with Weierstrass profile. Proceedings of the Royal Society A: Mathematical, Physical and Engineering Sciences, 462(2065), 319-348.
103. Jackson, R. L., Malucci, R. D., Angadi, S., & Polchow, J. R. (2009). A simplified model of multiscale electrical contact resistance and comparison to existing closed form models. In 2009 Proceedings of the 55th IEEE Holm Conference on Electrical Contacts, 28-35. IEEE.
104. Malucci, R. D., & Ruffino, F. R. (2007). Materials considerations in using voltage drop for power rating. In Electrical Contacts-2007 Proceedings of the 53rd IEEE Holm Conference on Electrical Contacts, 25-31. IEEE.
105. Greenwood, J. A. (1966). Constriction resistance and the real area of contact. British Journal of Applied Physics, 17(12), 1621.
106. Persson, B. N. J. (2001). Elastoplastic contact between randomly rough surfaces. Physical Review Letters, 87(11), 116101.
107. Thompson, M. K., & Slocum, A. H. (2007). A multi-scale iterative approach for finite element modeling of thermal contact resistance. Doctoral dissertation, Massachusetts Institute of Technology.
108. Thompson, M. K., & Thompson, J. M. (2010). Considerations for the incorporation of measured surfaces in finite element models. Scanning, 32(4), 183-198.

109. Liu, H., Leray, D., Colin, S., Pons, P., & Broué, A. (2012). Finite element based surface roughness study for ohmic contact of microswitches. In 2012 IEEE 58th Holm Conference on Electrical Contacts (Holm), 1-10. IEEE.

110. Jackson, R. L., Liu, H., & Leray, D. (2013). A Comparison of the Predictions of a Finite Element Model and Multiscale Model for a Rough MEMS Electrical Contact. In 2013 IEEE 59th Holm Conference on Electrical Contacts (Holm), 1-9. IEEE.

111. Wang, X., Xu, Y., & Jackson, R. L. (2018). Theoretical and finite element analysis of static friction between multi-scale rough surfaces. Tribology Letters, 66(4), 146.

112. Wang, X., An, B., Xu, Y., & Jackson, R. L. (2020). The effect of resolution on the deterministic finite element elastic-plastic rough surface contact under combined normal and tangential loading. Tribology International, 144, 106141.

113. An, B., Wang, X., Xu, Y., & Jackson, R. L. (2019). Deterministic elastic-plastic modelling of rough surface contact including spectral interpolation and comparison to theoretical models. Tribology International, 135, 246-258.

114. Timsit, R. S. (1990). The 'melting' voltage in electrical contacts. In 36th IEEE Conference on Electrical Contacts, and the 15th International Conference on Electrical Contacts, 218-224. IEEE.

115. Timsit, R. (1983). On the evaluation of contact temperature from potential-drop measurements. IEEE Transactions on Components, Hybrids, and Manufacturing Technology, 6(1), 115-121.

116. Jackson, R. L., Ashurst, W. R., Flowers, G. T., Angadi, S., Choe, S. Y., & Bozack, M. J. (2007). The effect of initial connector insertions on electrical contact resistance. In

Electrical Contacts-2007 Proceedings of the 53rd IEEE Holm Conference on Electrical Contacts, 17-24. IEEE.

117. A. Sommerfeld & H. Bethe, Handblich de. (1933). Physik von Geiger und Scheel. Julius Springer-Verlag, Berlin, 24(2), 450.

118. Holm, R. (1951). The electric tunnel effect across thin insulator films in contacts. Journal of Applied Physics, 22(5), 569-574.

119. Holm, R., & Kirschstein, B. (1935). Über den Widerstand dünnster fremdschichten in metallkontakten. Z Tech Physik, 16, 488.

120. Simmons, J. G. (1963). Generalized formula for the electric tunnel effect between similar electrodes separated by a thin insulating film. Journal of applied physics, 34(6), 1793-1803.

121. Jackson, R. L., & Kogut, L. (2007). Electrical contact resistance theory for anisotropic conductive films considering electron tunneling and particle flattening. IEEE Transactions on Components and Packaging Technologies, 30(1), 59-66.

Chapter 5

Development and Validation of the Elastic and Elastic-perfectly Plastic Rough Surface Contact Models and Determination of the Electrical Contact Resistance

5.1 Introduction

This chapter focuses on the development of the asperity based rough surface contact modeling and validation. Previous research works on the rough surface contact modeling have been discussed in detail in Chapter 4. For asperity based rough surafce contact modeling, statistical (Section 4.3.1.1, 4.3.1.2, 4.3.1.3, 4.3.2.1) and multiscale (4.3.1.4, 4.3.2.2) rough surafce contact models are widely used. However, several assumptions have been made when these models are formulated. Xu [1] performed an elastic rough surface contact analysis using the Boundary Element Method (BEM) and for the first time compared the results with the statistical models for early contact and nearly complete contact. The comparison shows that statistical model developed by Greenwood (see Section 4.3.1.1) shows excellent agreement with the BEM results when the deformation is small. Near the complete contact, the modified Greenwood model developed by Xu and Jackson (Section 4.3.1.3) showed very good match with the BEM results. To perform the BEM simulation, Xu [1, 2] developed rough surfaces, which are isotropic, fractal and Gaussian. The motivation behind developing such surfaces was to compare different rough surface contact models. Works have also been done to predict the elastic-plastic rough surface contact behavior employing statistical models (Section 4.3.2.1). Original statistical model assumes the Gaussian distribution of the rough surface; however, later research has been done on rough surface contact modeling using both Gaussian and Non-Gaussian probability distribution function (PDF) of the asperity of the rough surface [3-8].

Very few works have been done to extend the statistical model for the whole range of contact (Section 4.3.1.2 and [9-10]) and these models assume a Gaussian distribution of the asperity of the rough surface while modeling the rough surface contact. However, it is well proven that surfaces are not always Gaussian. Therefore, the objective of this chapter are the following:

1. To develop and validate elastic rough surface contact models with the models that worked well in many practical applications. The objective of the development of the rough surface contact models is to reduce the computational expenses and to make the models applicable for a wide range of surfaces. For the development of the rough surface contact model, the surface generated by Xu [1, 2] will be used which is isotropic, fractal and Gaussian in nature. The purpose of using this rough surface is to compare the newly developed rough surface contact models with the curve fit solution of the BEM results provided by Xu (Eq. 4.91) and also with Persson's model (Eq. 4.81). For the development of the rough surface contact model, following steps have been performed:
    - To observe the effect of different probability distribution functions (PDF) of the asperities of the rough surface on the rough surface contact modeling.
    - To observe the effect of the single asperity contact models on the contact behavior when employed with different PDFs of the asperity of the rough surface in the statistical model.
    - To compare the newly developed rough surface contact models with the curve fit solution of the BEM results provided by Xu, Xu nearly complete contact statistical models, Persson's model and multiscale model.
2. To perform the same analysis for the real surface and to compare with the Persson's model and multiscale model.

3. To develop elastic-perfectly plastic rough surface contact models using statistical models. The statistical models that show good agreement with the BEM results/ Persson model when performed objective-1, will be used to formulate elastic-perfectly plastic rough surface contact models. For asperity models, elastic-perfectly plastic asperity models will be used.
4. To compare the results found from the elastic-perfectly plastic statistical models with the multiscale models.
5. To determine the electrical contact resistance.
6. To determine electrical contact resistance between two aluminum surfaces using a four-wire resistance method and to compare the experimental results with the results found from objective 5.

5.2 Development and Validation of the Elastic Rough Surface Contact Models (Generated Surface)

For the development and validation of the elastic rough surface contact models, one of the surfaces generated by Xu [1] has been used, which has the properties listed in Table-5.1. The surface generation method has been discussed in detail in Chapter 4. (see Section 4.3.1.5).

Table 5.1 Fractal, isotropic and Gaussian surface properties

k_l[1/m]	k_s[1/m]	H	$N_x \times N_y$	L_x, L_y(m)	m_2^h
16	64	0.1	1024×1024	1	2.00×10^{-4}

For the surface properties shown in Table 5.1, 50 rough surfaces are generated. The mean of the roughness of each of the surfaces has been determined taking the average of the rows and columns

of that 1024×1024 matrix. For example- the mean of a single column of a $m \times n$ matrix of surface roughness can be calculated using the following formula:

$$Mean = \frac{1}{m}\sum_{i=1}^{m} \xi^h \tag{5.1}$$

Then the mean of the surface roughness has been subtracted from the original rough surface height. For each of the surface, all the surface properties have been calculated using the methodology described in Section 4.2.1(numerical method) and 4.2.4. However, the methodology described in Section 4.2.2 (analytical solution) can also be used to calculate surface properties. Later taking an average of these 50 surfaces, the final value of the surface properties are calculated. Average properties of the rough surface and the corresponding "pressure surface" are shown in Table-5.2 and Table-5.3, respectively.

Table-5.2: Average moments, RMS surface roughness and bandwidth parameter for the rough surface

m_0^h (m^2)	σ orR_q (μm)	m_2^h	m_4^h (m^{-2})	m_6^h (m^{-4})	α^h
7.7946 $\times 10^{-9}$	88	1.9572 $\times 10^{-4}$	12.2030	1.0635$\times 10^{6}$	2.48

Table-5.3: Average moments and bandwidth parameter of the corresponding "pressure surface"

m_0^{p*}	$m_2^{p*}(m^{-2})$	$m_4^{p*}(m^{-4})$	α^p	$m_n^{p*} = \frac{m_n^p}{(E')^2}$
0.98$\times$ 10^{-4}	4.068	3.19$\times 10^{5}$	1.89	where, $n = 0,2,4,6 \ldots$

For the improvement of the statistical rough surface contact model, all the possible combinations of the following PDFs and asperity models have been formulated and analyzed.

Probability Distribution Functions (PDFs)

1. PDF is a function of asperity height only (PDF $= f(\xi^{h*})$)
2. PDF is a function of asperity height only (PDF $= f(\xi^{h*})$), however Gaussian in nature
3. PDF is a function of the asperity height and geometric curvature (PDF $= f(\xi^{h*}, k_g^{h*})$
4. PDF is a function of the asperity height and mean curvature (PDF $= f(\xi^{h*}, k_m^{h*})$

Asperity Models

1. Hertz elastic asperity model (Mildly elliptical contact with mean curvature or geometric curvature, circular contact with constant radius of curvature)
2. Extended Johnson, Greenwood and Higginson model (Extended JGH model- 3D periodic sinusoidal asperity model)
3. New elastic asperity model (developed and described in Chapter 3- elastic axisymmetric sinusoidal asperity model)

5.2.1 Methodology

5.2.1.1 Statistical model (Hertz Asperity Models+ Different PDFs)

The methodology to generate statistical models employing Hertz asperity models (Hertzian circular contact with constant radius of curvature, mildly elliptical contact with geometric/ mean curvature) and different probability distribution functions (Gaussian distribution, PDF $= f(\xi^{h*})$, PDF $= f\left(\xi^{h*}, k_g^{h*}\right)$, PDF $= f(\xi^{h*}, k_g^{h*})$) have been described in detail in the literature review (Section 4.3.1.1). For these models, the surface separation *d* has been varied from -6σ to

+6σ and the radius of curvature is varied from $10^{-4}\sqrt{m_0^h}$ to $10\sqrt{m_0^h}$ to perform the numerical integration. An increase in surface separation from +/- 6σ to +/- 9σ does not cause any change in the results. Here, negative d does not necessarily mean surface penetration. This is because the surfaces are deforming and the asperity distribution does not consider that. In actuality, the distribution would change with deformation and the average height would lower since the taller peaks are smashed down. In the original statistical model the mean height and distribution are held constant, which is not true. It is very difficult to account for that. To the author's knowledge, it is Wilson et al. [10] who performed an investigation on this.

5.2.1.2 Statistical model (3D Periodic Sinusoidal Asperity Model + Different PDFs)

Greenwood-Williamson 3D Sinusoidal Model (GW 3D Sinusoidal Model)

This statistical model has already been developed before (see Section 4.3.1.2). The authors did not provide any name for their model. To keep similarity with the other newly developed statistical models in this section, the statistical model developed by Jackson et al. (Section 4.3.1.2) has been named as the Greenwood-Williamson 3D sinusoidal model. To develop this statistical model, extended JGH model (see Section 2.2.7) has been employed into the framework of the statistical model with a Gaussian PDF, which is a function of surface asperity height only (PDF $= f(\xi^{h*})$). To predict the rough surface contact area and force, the following two equations have been used:

$$\frac{A_r}{A_n} = \frac{\eta^h}{\sqrt{m_0^h}} \int_d^\infty A\,(\xi^h) \emptyset(\xi^{h*}) d\xi^h \tag{5.2}$$

$$\frac{F}{A_n} = \frac{\eta^h}{\sqrt{m_0^h}} \int_d^\infty F(\xi^h)\, \emptyset(\xi^{h*}) d\xi^h \tag{5.3}$$

$A(\xi^h)$ and $F(\xi^h)$ are the single asperity contact area and contact force. $\emptyset(\xi^{h*})$ is the probability distribution function of the asperity of the rough surface. $A(\xi^h)$ is determined from Eqs. (2.46) and (2.47) and $\emptyset(\xi^{h*})$ will be determined using Eq. (4.25). Using Eqs. (2.1) and (2.37), the radius of curvature at the tip of this asperity is, $R = \frac{\lambda^2}{4\pi^2\Delta}$. Therefore, $\lambda = \sqrt{R \times 4\pi^2\Delta}$ where $\Delta = \xi^h$. For this rough surface contact model, the radius of curvature of the asperity, *R*, is assumed constant and is determined using Eq. (4.26). $F(\xi^h)$ is calculated by modifying Eq. (2.48) to the following:

$$\frac{\bar{p}}{p^*} = \left(1 - (G_n)^{2/5}\right)^2 \Rightarrow\gg \bar{p} = \left(1 - (G_n)^{2/5}\right)^2 \times p^*$$

$$F = \bar{p}\frac{\lambda^2}{2} = \frac{\lambda^2}{2}\left(1 - (G_n)^{2/5}\right)^2 \times p^*$$

where, normalized surface separation, $G_n = d/\xi^h$. d is the gap between the mean of the rough surfaces or mean of the composite rough surface and rigid flat. p^*can be calculated from Eq. (2.43). If $\frac{\bar{p}}{p^*} > 1$, it has been set to 1. This is also true for the other models developed in this chapter. The nominal area for the asperity model is λ^2 and there are two asperities in λ^2. η^h (Number of asperity/unit area) can be calculated from Eq. (4.22). Now substituting the equation for contact force, $F(\xi^h)$ on a single asperity and probability distribution function of the asperity of the rough surface,$\emptyset(\xi^{h*})$, Eq. (5.3) becomes:

$$\frac{F}{A_n} = \frac{\eta^h}{\sqrt{m_0^h}}\int_d^\infty \frac{\lambda^2}{2}\left(1 - (G_n)^{2/5}\right)^2 \times p^* \times \frac{1}{\sqrt{2\pi}}\left(\frac{\sigma}{\sigma_s}\right) exp\left[-0.5\left(\frac{\sigma}{\sigma_s}\right)^2\left(\frac{\xi^h}{\sqrt{m_0^h}}\right)^2\right] d\xi^h$$

Substituting the equations ((2.46) and (2.47)) for single asperity contact area, $A(\xi^h)$ and probability distribution function of the asperity of the rough surface,$\emptyset(\xi^{h*})$in Eq. (5.2),

When $\frac{\bar{p}}{p^*} < 0.8$,

$$\frac{A_r}{A_n} = \frac{\eta^h}{2\sqrt{m_0^h}} \int_d^\infty \left[\lambda^2 \pi \left\{ \frac{3}{8\pi} \frac{\bar{p}}{p^*} \right\}^{2/3} \times \left(1 - \left(\frac{\bar{p}}{p^*} \right)^{1.51} \right) + \lambda^2 \left(1 - \frac{3}{2\pi} \left(1 - \frac{\bar{p}}{p^*} \right) \right) \left(\frac{\bar{p}}{p^*} \right)^{1.04} \right]$$

$$\times \frac{1}{\sqrt{2\pi}} \left(\frac{\sigma}{\sigma_s} \right) exp \left[-0.5 \left(\frac{\sigma}{\sigma_s} \right)^2 \left(\frac{\xi^h}{\sqrt{m_0^h}} \right)^2 \right] d\xi^h$$

When $\frac{\bar{p}}{p^*} > 0.8$,

$$\frac{A_r}{A_n} = \frac{\eta^h}{2\sqrt{m_0^h}} \int_d^\infty \lambda^2 \left(1 - \frac{3}{2\pi} \left(1 - \frac{\bar{p}}{p^*} \right) \right) \times \frac{1}{\sqrt{2\pi}} \left(\frac{\sigma}{\sigma_s} \right) exp \left[-0.5 \left(\frac{\sigma}{\sigma_s} \right)^2 \left(\frac{\xi^h}{\sqrt{m_0^h}} \right)^2 \right] d\xi^h$$

A factor of 2 has been used outside of the integral to divide the total result by 2 because the extended JGH asperity contact equations ((2.46) and (2.47)) are for two asperities. Including this model, for all the statistical models developed in this chapter using 3D sinusoidal model and axisymmetric sinusoidal model, the values of d have been varied from $10^{-4}\sqrt{m_0^h}$ to $6\sqrt{m_0^h}$ and the Composite Simpson's rule has been used for numerical integration. Depending on the rough surface contact models, the integration interval has been divided into different subintervals, until the number of subintervals does not have any impact on the integration results. For the 3D sinusoidal and axisymmetric sinusoidal model, the integration limit of d is always considered positive. Because for both sinusoidal asperity models, $\Delta = \xi^h$ and $\lambda = \sqrt{R \times 4\pi^2 \Delta}$ for a negative value of d, Δ becomes negative, then λ will become a complex or imaginary number. That is why

only positive values of *d* have been considered when employing sinusoidal asperity models in the rough surface contact models.

Adapted Greenwood-Williamson 3D Sinusoidal Model (Adapted GW 3D Sinusoidal Model)

This rough surface contact model has been developed in the same way as the previously described GW 3D sinusoidal model. However, for PDF, instead of using Gaussian distribution, the PDF given by Eq. (4.23) has been used.

Greenwood 3D Sinusoidal Model

To develop this rough surface contact model, the extended JGH wavy asperity model (see Section 2.2.7) and the PDF that varies as a function of asperity height and geometric curvature $\left(\text{PDF} = f\left(\xi^{h*}, k_g^{h*}\right)\right)$ have been employed in the framework of the statistical model. The geometric curvature at the tip of the 3D periodic sinusoidal asperity has been determined using Eq. (2.4) and (2.37):

$$k_g^h = \frac{1}{R} = \left[\frac{\partial^2 \xi^h}{\partial x^2}\frac{\partial^2 \xi^h}{\partial y^2} - \left(\frac{\partial^2 \xi^h}{\partial x \partial y}\right)^2\right]^{1/2} = \left[\frac{4\pi^2\Delta}{\lambda^2}\cdot\frac{4\pi^2\Delta}{\lambda^2} - 0\right]^{1/2} = \frac{4\pi^2\Delta}{\lambda^2} \tag{5.4}$$

As $\frac{2\pi x}{\lambda}$ and $\frac{2\pi y}{\lambda}$ in Eq. (2.37) are equal that is why geometric curvature (Eq. (2.4)), mean curvature (Eq. (2.3)) and radius of curvature (Eq. (2.2)) of the 3D periodic sinusoidal model give the same result. The above equation is used to calculate the wavelength, λ for a particular asperity height, $\Delta = \xi^h$. However, when employed the asperity model and PDF into the statistical model, the geometric curvature, k_g^h in the asperity model and PDF will vary over the integration limit of the statistical model. Therefore, in this statistical model for a particular asperity height, the statistical distribution

of the summit geometric curvature has been considered. To predict the rough surface contact area and force using this statistical model, the following two equations are used:

$$\frac{A_r}{A_n} = \frac{\eta^h}{\sqrt{m_0^h m_4^h}} \int_d^\infty \int_0^\infty A\left(\xi^h, k_g^h\right) \emptyset\left(\xi^{h*}, k_g^{h*}\right) dk_g^h d\xi^h \tag{5.5}$$

$$\frac{F}{A_n} = \frac{\eta^h}{\sqrt{m_0^h m_4^h}} \int_d^\infty \int_0^\infty F\left(\xi^h, k_g^h\right) \emptyset\left(\xi^{h*}, k_g^{h*}\right) dk_g^h d\xi^h \tag{5.6}$$

$A\left(\xi^h, k_g^h\right)$ has been determined using (2.46) and (2.47). Wavelength of the asperity, λ is calculated from $R = 1/k_g^h = \frac{\lambda^2}{4\pi^2\Delta} => \lambda = \sqrt{\frac{1}{k_g^h} \times 4\pi^2\Delta}$, where, $\Delta = \xi^h$. Substituting the equations for $A\left(\xi^h, k_g^h\right)$ and probability distribution function for the asperity of the rough surface, $\emptyset\left(\xi^{h*}, k_g^{h*}\right)$ ((Eq. 4.31)), Eq. (5.5) becomes,

When $\frac{\bar{p}}{p^*} < 0.8$,

$$\frac{A_r}{A_n} = \frac{\eta^h}{2\sqrt{m_0^h m_4^h}} \int_d^\infty \int_0^\infty \left(\left[\frac{\pi}{k_g^h} \times 4\pi^2\Delta \times \left\{ \frac{3}{8\pi} \frac{\bar{p}}{p^*} \right\}^{\frac{2}{3}} \right] \times \left(1 - \left(\frac{\bar{p}}{p^*} \right)^{1.51} \right) + \frac{1}{k_g^h} \right.$$

$$\left. \times 4\pi^2\Delta \left(1 - \frac{3}{2\pi} \left(1 - \frac{\bar{p}}{p^*} \right) \right) \left(\frac{\bar{p}}{p^*} \right)^{1.04} \right) \times \frac{9}{2\sqrt{2\pi}} \sqrt{\frac{\alpha^h}{\alpha^h - 1}} \left(\frac{k_g^h}{\sqrt{m_4^h}} \right)^3$$

$$\times erfc \left[\mu \left(3 \frac{k_g^h}{\sqrt{m_4^h}} - \frac{\xi^h \sqrt{\alpha^h}}{\sqrt{m_0^h}(\alpha^h - 1)} \right) \right] exp \left[\frac{-\alpha^h \left(\frac{\xi^h}{\sqrt{m_0^h}} \right)^2}{2(\alpha^h - 1)} + \frac{3 \left(\frac{k_g^h}{\sqrt{m_4^h}} \right)^2}{2} \right] d\xi^h dk_g^h$$

When $\frac{\bar{p}}{p^*} > 0.8$,

$$\frac{A_r}{A_n} = \frac{\eta^h}{2\sqrt{m_0^h m_4^h}} \int_d^\infty \int_0^\infty \left(\frac{1}{k_g^h} \times 4\pi^2 \Delta \times \left(1 - \frac{3}{2\pi} \left(1 - \frac{\bar{p}}{p^*} \right) \right) \right) \times \frac{9}{2\sqrt{2\pi}} \sqrt{\frac{\alpha^h}{\alpha^h - 1}} \left(\frac{k_g^h}{\sqrt{m_4^h}} \right)^3$$

$$\times erfc \left[\mu \left(3 \frac{k_g^h}{\sqrt{m_4^h}} - \frac{\xi^h \sqrt{\alpha^h}}{\sqrt{m_0^h}(\alpha^h - 1)} \right) \right] \times exp \left[\frac{-\alpha^h \left(\frac{\xi^h}{\sqrt{m_0^h}} \right)^2}{2(\alpha^h - 1)} + \frac{3 \left(\frac{k_g^h}{\sqrt{m_4^h}} \right)^2}{2} \right] d\xi^h dk_g^h$$

$F\left(\xi^{h*}, k_g^{h*}\right)$ has been calculated using the same methodology as described for the GW 3D sinusoidal model. Substituting the equations for $F\left(\xi^h, k_g^h\right)$ and probability distribution function for the asperity of the rough surface, $\emptyset\left(\xi^{h*}, k_g^{h*}\right)$ ((Eq. 4.31)) in Eq. (5.6),

$$\frac{F}{A_n} = \frac{\eta^h}{2\sqrt{m_0^h m_4^h}} \int_d^\infty \int_0^\infty \left(\frac{1}{k_g^h} \times 4\pi^2 \Delta \right) \times \left(1 - (G_n)^{2/5} \right)^2 \times p^* \times \frac{9}{2\sqrt{2\pi}} \sqrt{\frac{\alpha^h}{\alpha^h - 1}} \left(\frac{k_g^h}{\sqrt{m_4^h}} \right)^3$$

$$\times erfc \left[\mu \left(3 \frac{k_g^h}{\sqrt{m_4^h}} - \frac{\xi^h \sqrt{\alpha^h}}{\sqrt{m_0^h}(\alpha^h - 1)} \right) \right] \times exp \left[\frac{-\alpha^h \left(\frac{\xi^h}{\sqrt{m_0^h}} \right)^2}{2(\alpha^h - 1)} + \frac{3 \left(\frac{k_g^h}{\sqrt{m_4^h}} \right)^2}{2} \right] d\xi^h dk_g^h$$

Including this rough surface model, for all the statistical models that will consider the change in geometric curvature, the value of k_g^h in the numerical integration is varied from $10^{-4}\sqrt{m_4^h}$ to $10\sqrt{m_4^h}$.

Nayak-Bush 3D Sinusoidal Model

This model has been developed using a similar methodology as the previously described Greenwood 3D sinusoidal model. Total contact area and contact force at the interface of the rough surfaces are calculated using the following two equations:

$$\frac{A_r}{A_n} = \frac{\eta^h}{\sqrt{m_0^h m_4^h}} \int_d^\infty \int_0^\infty A(\xi^h, k_m^h)\, \emptyset(\xi^{h*}, k_m^{h*}) dk_m^h d\xi^h \tag{5.7}$$

$$\frac{F}{A_n} = \frac{\eta^h}{\sqrt{m_0^h m_4^h}} \int_d^\infty \int_0^\infty F(\xi^h, k_m^h)\, \emptyset(\xi^{h*}, k_m^{h*}) dk_m^h d\xi^h \tag{5.8}$$

Instead of radius of geometric curvature, radius of mean curvature, $R = 1/k_m^h$ has been used in the extended JGH model. The value of mean curvature, k_m^h in the asperity model and in the PDF will vary over the integration limit of the statistical model. For PDF, $\emptyset(\xi^{h*}, k_m^{h*})$, Eq. (4.24) has been used. The mean curvature at the tip of a 3D periodic sinusoidal asperity will be, $k_m^h = \frac{1}{R} = \frac{4\pi^2\Delta}{\lambda^2}$. Besides this model, all the statistical models that will consider the change in mean curvature, the value of k_m^h in the numerical integration is varied from $10^{-4}\sqrt{m_4^h}$ to $10\sqrt{m_4^h}$.

5.2.1.3 Statistical model (Axisymmetric Sinusoidal Asperity model + Different PDFs)

Greenwood-Williamson Axisymmetric Sinusoidal Model (GW Axisymmetric Sinusoidal Model)

To develop this statistical model, the axisymmetric sinusoidal asperity model developed by Saha and Jackson (Chapter 3) has been employed into the framework of the statistical model with Gaussian PDF. To predict the rough surface contact area and contact force, Eq. (5.2) and (5.3) have been used. For this model, $\Delta = \xi^h$, interference, $\delta = \xi^h - d$, d is the gap between the mean of the rough surfaces or mean of the composite rough surface and rigid flat. The radius of curvature at the tip of an axisymmetric sinusoidal asperity is, $R = \frac{\lambda^2}{4\pi^2\Delta}$ (from Eq. (2.1) and (3.1)). For this rough surface contact model, the average radius of curvature of the asperity, R is assumed constant and is determined using Eq. (4.26). Therefore, the wavelength of the asperity, $\lambda = \sqrt{R \times 4\pi^2\Delta}$. $F(\xi^h)$ has been calculated from Eq. (3.9), multiplying by $\pi\left(\frac{\lambda}{2}\right)^2$. In Eq. (3.9), the normalized surface separation is, $G_n = d/\xi^h$. The normalized contact pressure, $\frac{\bar{p}}{p_e^*}$ is also calculated from Eq. (3.9) which has been used to calculate the contact area. If $\frac{\bar{p}}{p_e^*} < 10^{-5}$, Hertz model i.e. Eq. (2.17) is used to calculate the contact area and if $\frac{\bar{p}}{p_e^*} > 10^{-5}$, Eq. (3.5) is used to calculate the contact area. Nominal area for the single asperity model is $\pi\left(\frac{\lambda}{2}\right)^2$. $\eta^h, and\ \emptyset(\xi^{h*})$ can be calculated from Eq. (4.22) and (4.25) respectively.

Adapted Greenwood-Williamson Axisymmetric Sinusoidal Model (Adapted GW Axisymmetric Sinusoidal Model)

This statistical model has been developed using the same methodology as described for the GW axisymmetric sinusoidal model. However, for the PDF, instead of Eq. (4.25), Eq. (4.23) has been used.

Greenwood Axisymmetric Sinusoidal Model

To develop this model, axisymmetric sinusoidal asperity model (Chapter 3) and PDF that varies as a function of asperity height and geometric curvature (PDF $= f\left(\xi^{h*}, k_g^{h*}\right)$), have been employed in the framework of the statistical model. Rough surface contact area and force area are calculated using Eq. (5.5) and (5.6). The radius of curvature, R in the axisymmetric sinusoidal asperity model will be the inverse of the geometric curvature, k_g^h. The value of the geometric curvature in the asperity model and in the PDF will vary over the integration limit of the statistical models. The geometric curvature at the tip of the axisymmetric sinusoidal asperity is $k_g^h = \frac{1}{R} = \frac{4\pi^2\Delta}{\lambda^2}$ (using Eq. (2.4) and (3.1)). This asperity wavelength, λ can be calculated from $R = 1/k_g^h = \frac{\lambda^2}{4\pi^2\Delta} => \lambda = \sqrt{\frac{1}{k_g^h} \times 4\pi^2\Delta}$. $F\left(\xi^h, k_g^{h*}\right)$ is calculated multiplying Eq. (3.9) by $\pi\left(\frac{\lambda}{2}\right)^2$. For this model, $\Delta = \xi^h$, interference, $\delta = \xi^h - d$, and normalized surface separation, $G_n = d/\xi^h$. d is the gap between the mean of the rough surfaces. The normalized contact pressure, $\frac{\bar{p}}{p_e^*}$ is also calculated from Eq. (3.9). When $\frac{\bar{p}}{p_e^*} < 10^{-5}$, Hertz model, i.e. Eq. (2.17) is used to calculate contact area, otherwise Eq. (3.5) is used.

Nayak-Bush Axisymmetric Sinusoidal Model (Nayak-Bush Axisymmetric Sinusoidal Model)

This model has been developed using the same methodology as the previously described Greenwood axisymmetric sinusoidal model. To determine rough surface contact area and force, Eq. (5.7) and (5.8) have been used. $R = 1/k_m^h$ in the axisymmetric sinusoidal asperity model. The mean curvature for the axisymmetric sinusoidal asperity is $k_m^h = \frac{1}{R} = \frac{4\pi^2\Delta}{\lambda^2}$ (using Eq. (2.3) and (3.1)) that is used to calculate wavelength, λ. For PDF, $\emptyset(\xi^{h*}, k_m^{h*})$, Eq. (4.24) has been used.

5.2.1.4 Curve Fit Solution for the BEM Result

Xu [1] performed a BEM analysis to predict the contact behavior of a nominally flat, linear elastic rough surface and also provided a curve fitted solution of the results found from the analysis. The equation is valid only for the surfaces analyzed in his dissertation. The curve fitted equation, i.e. Eq. (4.91) has several constants, which varies from surface to surface. For the surface properties, described in Table-5.1, the constants are, a = -1.160, b = -1.923, c = 1.160 and d = -0.062.

5.2.1.5 Multiscale model

Many research works have been done on the multiscale modeling of rough surface contact and there are different ways to develop multiscale models (see Section 4.3.1.4). In this chapter, the newly developed statistical models are compared with the stacked multiscale model developed by Jackson and Streator (JS model, see Section 4.3.1.4). The multiscale model formulated by Jackson and Streator is an asperity-based model. The model assumes that the asperities on each scale have the same height and radius of curvature, however it also considers wide range of scales found from the spectral analysis of the rough surface. For the multiscale elastic rough surface contact analysis, Jackson and Streator employed the Hertz (Section 2.2.2) and extended JGH asperity models (Section 2.2.7). In this chapter, besides the Hertz and extended JGH asperity models, the newly

developed axisymmetric sinusoidal asperity model has been employed in the framework of the JS multiscale model to compare with the statistical models developed and discussed in this chapter. A flowchart has been given in Fig. 5.1 to describe the iterative asperity based JS multiscale contact model.

Multiscale Axisymmetric Sinusoidal Model

It has already been described in Section 4.3.1.4 that, Jackson and Streator multiscale model converts the rough surface data into the frequency domain by performing FFT on the rough surface data. From the FFT of the rough surface, the amplitude, Δ, and wavelength, λ, of the asperities of the rough surface can be determined. The $\frac{\Delta}{\lambda}$ ratio gives an idea about the sharpness and bluntness of the surface roughness. The method to calculate Δ and λ have been described in Section 4.2.4. Radius of curvature of the asperities at each scale can be calculated using, $R_i = \frac{{\lambda_i}^2}{4\pi^2\Delta_i}$, where i indicates the number of frequency scale. For the multiscale model, the force on each asperity can be calculated using Eq. (4.74), based on the total force. For axisymmetric sinusoidal asperity model, nominal contact area is $\pi\left(\frac{\lambda_i}{2}\right)^2$. So from the force, nominal contact area, and the equation for pressure required to completely flatten the single asperity for the elastic case, p_e^*, (Eq. (3.4)), $\frac{\bar{p}}{p_e^*}$ can be calculated. For this asperity model, if $\frac{\bar{p}}{p_e^*} > 1$, the ratio has to be assumed as 1, i.e. $\frac{\bar{p}}{p_e^*} = 1$. If $\frac{\bar{p}}{p_e^*} < 10^{-5}$, the Hertz equation for contact area (Eq. (2.17) and (2.18)) is used, otherwise Eq. (3.5) has been used. The areal asperity density at each scale is:

$$\eta_i = \frac{1}{\pi\left(\frac{\lambda_i}{2}\right)^2} \tag{5.9}$$

Multiscale elastic rough surface contact using the Hertz (Section 2.2.2) and extended JGH model (Section 2.2.7) can be modeled using the same methodology as described in the flow chart (Fig. 5.1). However, for the Hertz and extended JGH model, the nominal contact area for asperity models are $\pi\left(\frac{\lambda_i}{2}\right)^2$ and $(\lambda_i)^2$ respectively. In this work, the areal asperity density for the Hertz single asperity model has been assumed the same as the axisymmetric sinusoidal asperity model i.e. Eq. (5.9). For the extended JGH model, areal asperity density is:

$$\eta_i = \frac{2}{(\lambda_i)^2} \tag{5.10}$$

In the extended JGH model, there are two asperities in the nominal area, $(\lambda_i)^2$, that is why factor 2 has been used in Eq. (5.10). For the Hertz model, Jackson and Streator model used the same nominal area and areal asperity density as the JGH model.

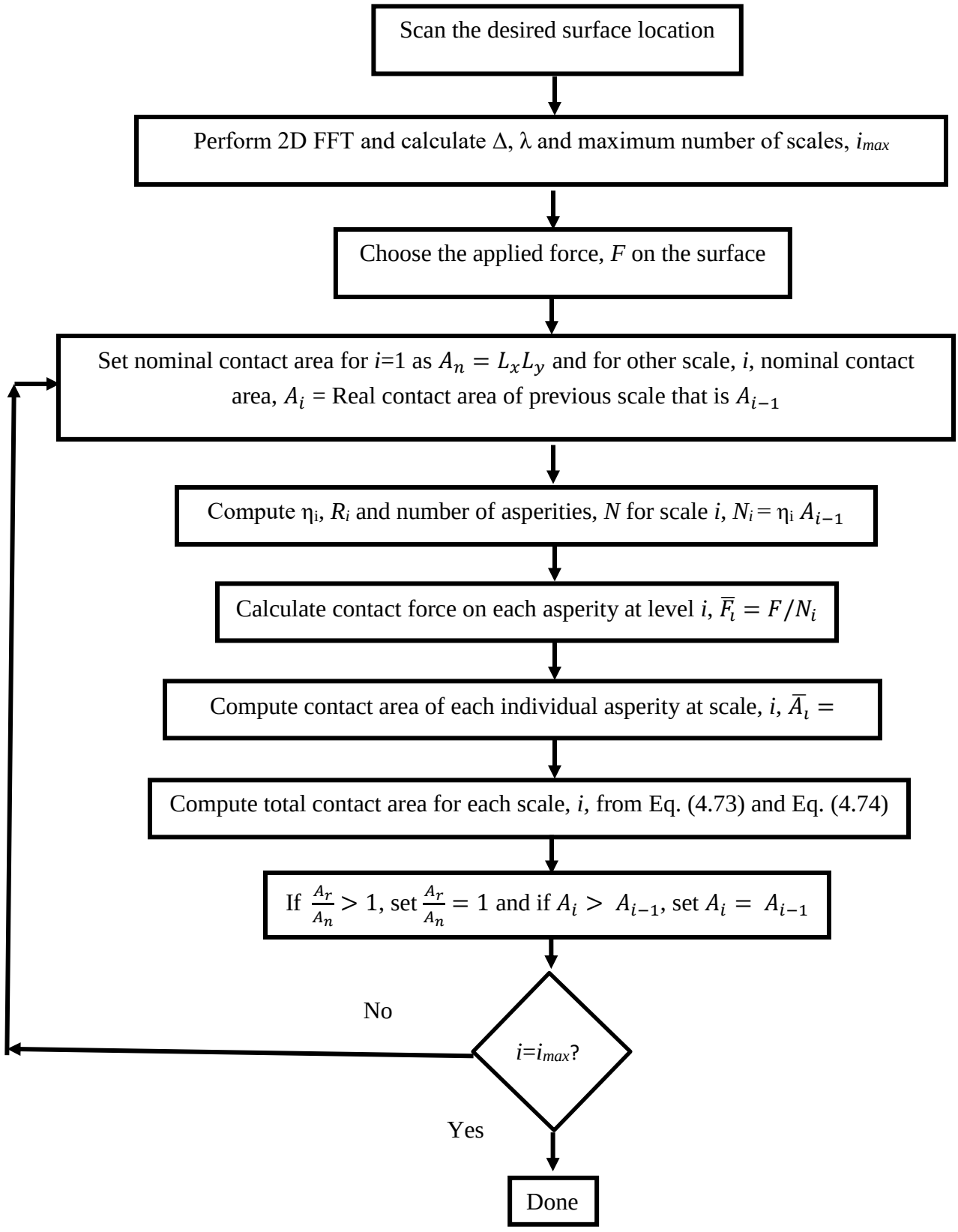

Fig. 5.1 Flowchart of iterative asperity based multiscale contact model

5.2.2 Results and Discussions for the Generated Rough Surface

5.2.2.1 Effect of the PDFs When Employed with the Hertz Model

Fig. 5.2(a) shows the effect of different PDFs on the contact behavior when the asperity model is the same i.e. Hertz model in all the statistical models. At the early contact (~15-20% of the total contact), it seems that all the contact models have coincided with each other except the case when the probability distribution function is a function of surface asperity height, ξ^{h*} (PDF $= f(\xi^{h*})$) and not Gaussian. However, the rough surface contact models gradually diverge from each other when contact area is greater than ~20% of the total contact. Xu [1] compared the Greenwood statistical model with BEM results for the same surface used in this analysis and the result shows that Greenwood model cannot produce results more than ~ 20% of the total contact. This is because in the analysis the surface separation, *d* was limited to the positive value. It has been mentioned before in Section 5.2.1.1 that in this chapter for all the statistical models developed using Hertz asperity models (Section 2.2.2, and 2.2.3), the surface separation value has been varied from -6σ to +6σ, so that the statistical models consider the change in surface mean height with the deformation. As a result, the contact area surpasses the early contact region and produces results up to the complete contact or near the complete contact region. However, all these models show large deviations with each other, with the BEM fit and the Persson model when the contact pressure is high. This is because the Hertz model was developed to model the small elastic deformation region. Fig. 5.2(b-d) show a detailed view of the early contact. From these figures, it is clear that although it seems that all the statistical models have coincided with each other at the low pressure region actually they are not. BEM is generally used as the validation tool for the elastic contact models, however for the small deformation region, it requires a very fine mesh to capture the contact behavior.

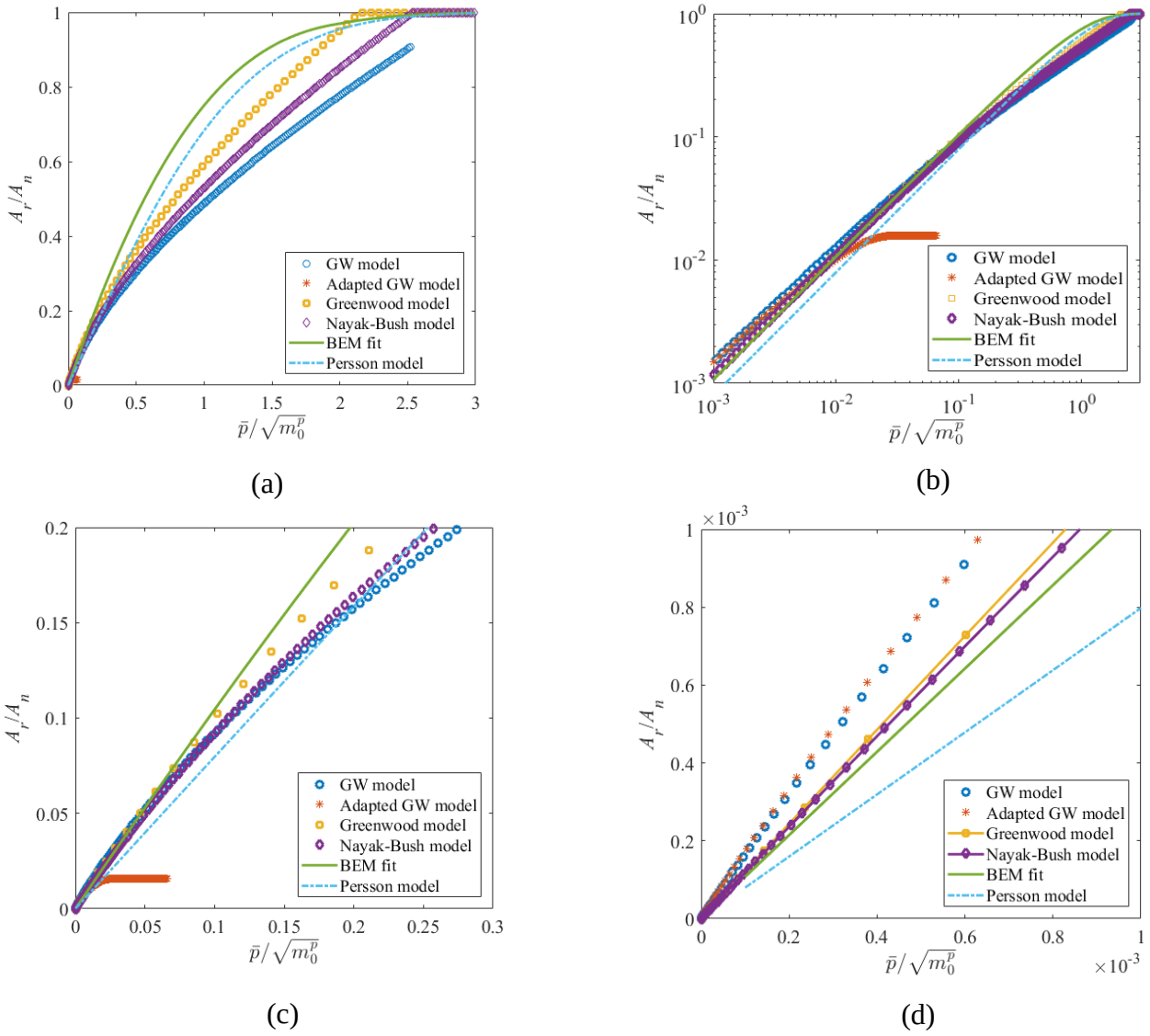

Fig. 5.2 Effect of different PDFs on the rough surface contact behavior when employed with the Hertz elastic single asperity models in the statistical model and comparison with the BEM result and Persson's model, (a) full scale plot (b) log-log plot (c) plot at the small deformation region (d) plot at the very small deformation region compared to Fig. 5.2(c).

Fig. 5.3 (a) is showing the number of asperities in contact vs. the normalized contact area. From the figure, it is clear that when the normalized contact area is 0.1, there are about 200 asperities in contact (total asperities is about 1909) and Fig. 5.3(b) shows that each of the asperities have a far fewer number of nodes, which may not be enough to predict the initial contact behavior. Therefore, for the early contact the prediction that BEM shows is not that accurate. According to the previous research works [1, 11], the Greenwood model shows better agreement with the statistical model generated using the elliptical contact model, i.e. BGT model (Bush, Gibson and Thomas model, Section 4.3.1.1). When the deformation is small, the BGT model is more realistic than the other statistical models. Fig. 5.2 (c-d) shows that the difference between the Greenwood and Nayak-Bush model is very small when the contact area is less than 15% of the total contact. In this small deformation region, although the GW and adapted GW models show very good agreement with each other at the beginning (Fig. 5.2(d)), with the increase of pressure the GW model shows good agreement with the Nayak-Bush model. None of the models shows good agreement with the Persson model. Therefore, it can be concluded that,

- The PDF has an important effect when employing with the Hertz asperity models in the statistical model. The statistical model developed using a Gaussian PDF, i.e. GW model does not consider the statistical distribution of the asperity radius of curvature, still shows a similar trend and close agreement with the Greenwood and Nayak-Bush statistical models when the contact area is less than 20% of the total contact.
- The adapted GW model does not consider the statistical distribution of the asperity radius of curvature and the PDF is not Gaussian. This model can predict contact behavior only when the deformation is very small.
- All the statistical models and BEM result fit show large differences with the Persson model.

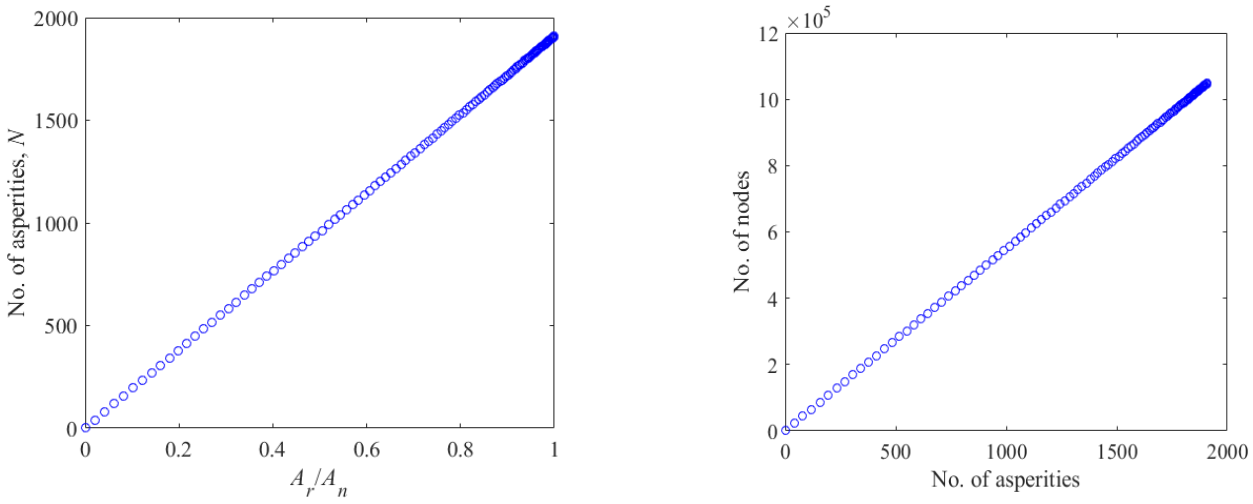

(a) (b)

Fig. 5.3 (a) Number of asperities vs. contact ratio for BEM analysis, (b) Number of nodes vs. number of asperities for the same BEM analysis.

5.2.2.2 Effect of the PDFs When Employed with the 3D Periodic Sinusoidal Model

Original statistical or Greenwood-Williamson model (GW model) was developed using the Hertz asperity model (Section. 2.2.2 and Section 4.3.1.1) for the early contact. The model assumes that when the deformation is small, all the contact spots are isolated and do not interact with each other. However, with the increase of the pressure the effect of interactions among adjacent asperities become important. To consider the effect of the asperity interaction, sinusoidal asperity models have been developed. Extended JGH model is a 3D sinusoidal asperity model which is periodic both in *x* and *y* direction if the distance along *z* direction indicates the height (Section 2.2.7). Statistical models developed using the extended JGH asperity model and different PDFs have been plotted in Fig. 5.4. All the surface parameters and applied interference for the plotted curves in Fig. 5.4 are the same. Fig. 5.4(b-d) show that, GW 3D sinusoidal and adapted GW 3D sinusoidal rough surface contact model under predict the contact area and pressure (both of these two models

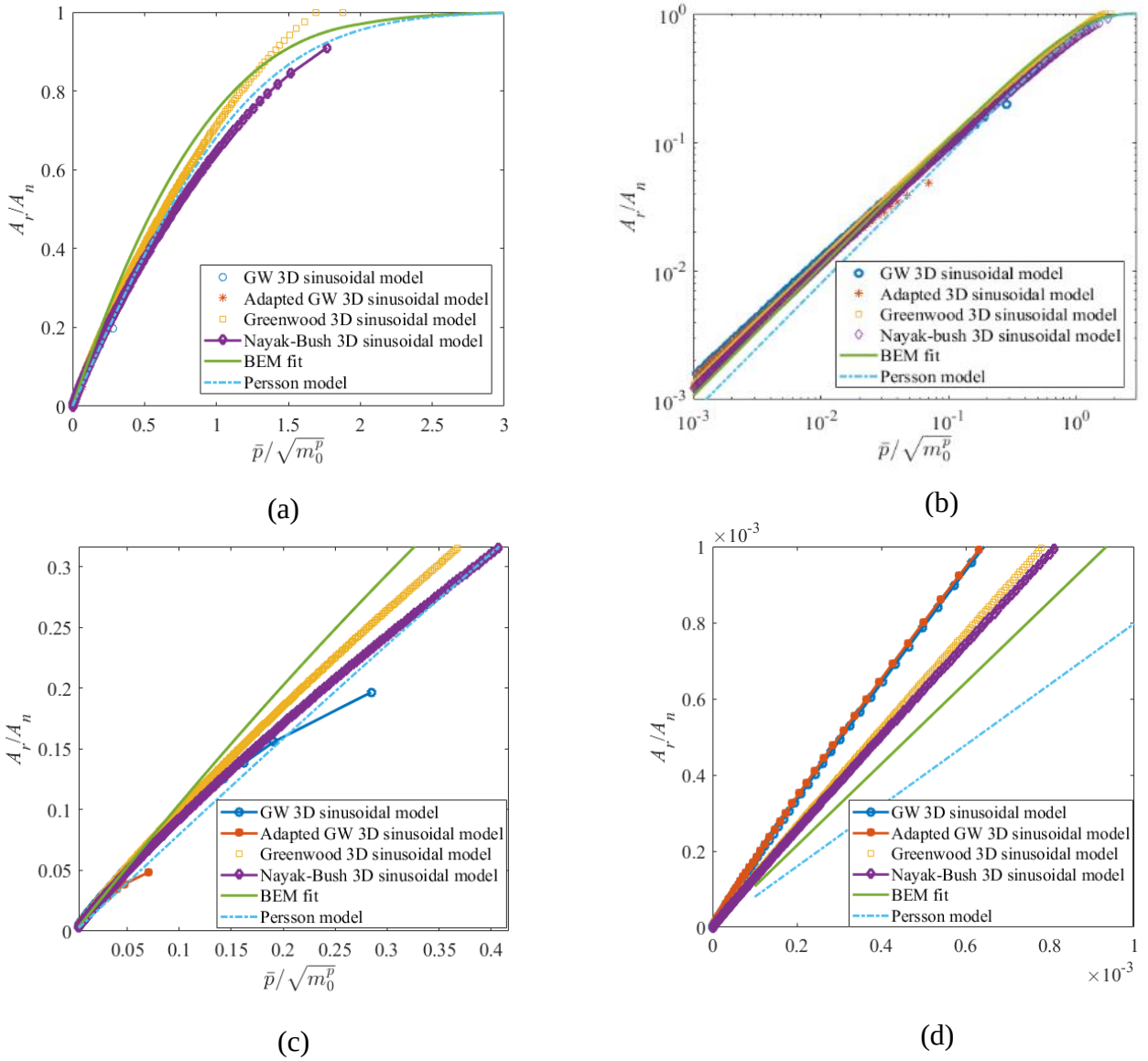

Fig. 5.4 Effect of different PDFs on the rough surface contact behavior when employed with the extended JGH elastic single asperity in the statistical model and comparison with the BEM result and Persson's model, (a) full scale plot (b) log-log plot (c) plot at the small deformation region (d) plot at the very small deformation region compared to Fig. 5.4(c).

assume a constant radius of curvature in the asperity model and PDF). At the low load (Fig. 5.4(d)), they also show large differences with the BEM result compared to the other models. However, from Fig. 5.4(a), the Nayak-Bush 3D sinusoidal and Greenwood 3D sinusoidal rough surface contact model show a similar trend as the BEM and Persson model and can predict the gradual change in the contact area from low to very high pressure. The Greenwood 3D sinusoidal model matches well with the BEM fit from the small deformation region to more than 80% of the total area with an error not more than 12%. When compared with the Persson model, the Greenwood 3D sinusoidal model shows less than 10% error when contact area is about 28-90% of the total area (Fig. 5.5(a)) and the Nayak-Bush 3D sinusoidal model shows less than 10% error when contact area is approximately 12-90% of the total area (Fig. 5.5(b)). The Nayak-Bush 3D sinusoidal model although shows a similar trend as the BEM fit up to near the complete contact, but shows a large difference quantitatively. Therefore, it can be concluded that:

- Similar to the statistical models developed using Hertz asperity models, PDFs have a significant effect on the contact behavior prediction when employed with 3D periodic sinusoidal asperity models in the statistical model.
- For the same surface properties and applied displacement, the GW 3D sinusoidal and adapted GW 3D sinusoidal rough surface models cannot predict the high-pressure contact area, however, the Nayak-Bush 3D sinusoidal model and Greenwood 3D sinusoidal model can.
- The Nayak-Bush 3D sinusoidal and Greenwood models show a very similar trend as the BEM result and Persson model. The Greenwood 3D sinusoidal model shows closer agreement with the BEM fit and the Nayak-Bush 3D sinusoidal model shows a closer agreement with the Persson model.

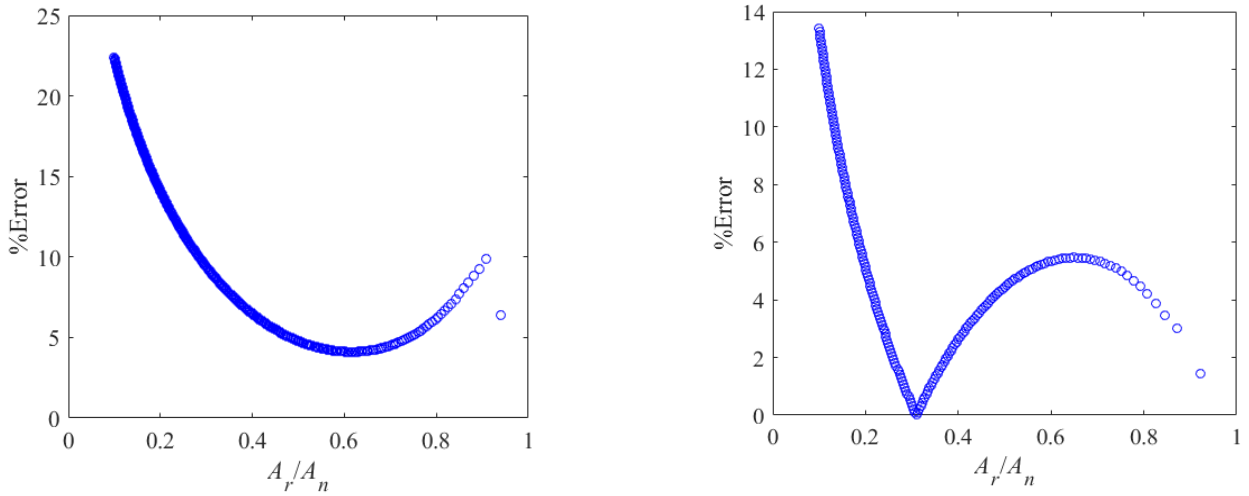

(a) (b)

Fig. 5.5 (a) Percentage of error vs. normalized contact area for Greenwood 3D sinusoidal model, (b) percentage of error vs. normalized contact area for Nayak-Bush 3D sinusoidal model.

5.2.2.3 Effect of the PDFs When Employed with Axisymmetric Sinusoidal Asperity Model

Two important features of the axisymmetric sinusoidal asperity model are (Chapter 3, [12]) are (a) it is computationally less expensive compared to the 3D sinusoidal asperity model, and (b) although the model is not exactly periodic like JGH or the extended JGH model, it effectively considers interaction with the adjacent asperities by having a confined boundary at the outer radius of the base of the asperity. Besides that, as it is a sinusoidal asperity model it considers contact behavior from the low load to the complete contact region.

Fig. 5.6(a) shows that PDFs have an important effect on rough surface contact models when employed with the axisymmetric sinusoidal asperity model. If a PDF is Gaussian or only a function of surface asperity height (PDF $= f(\xi^{h*})$), i.e. GW axisymmetric sinusoidal model and adapted GW axisymmetric sinusoidal model, the rough surface contact models cannot predict the contact

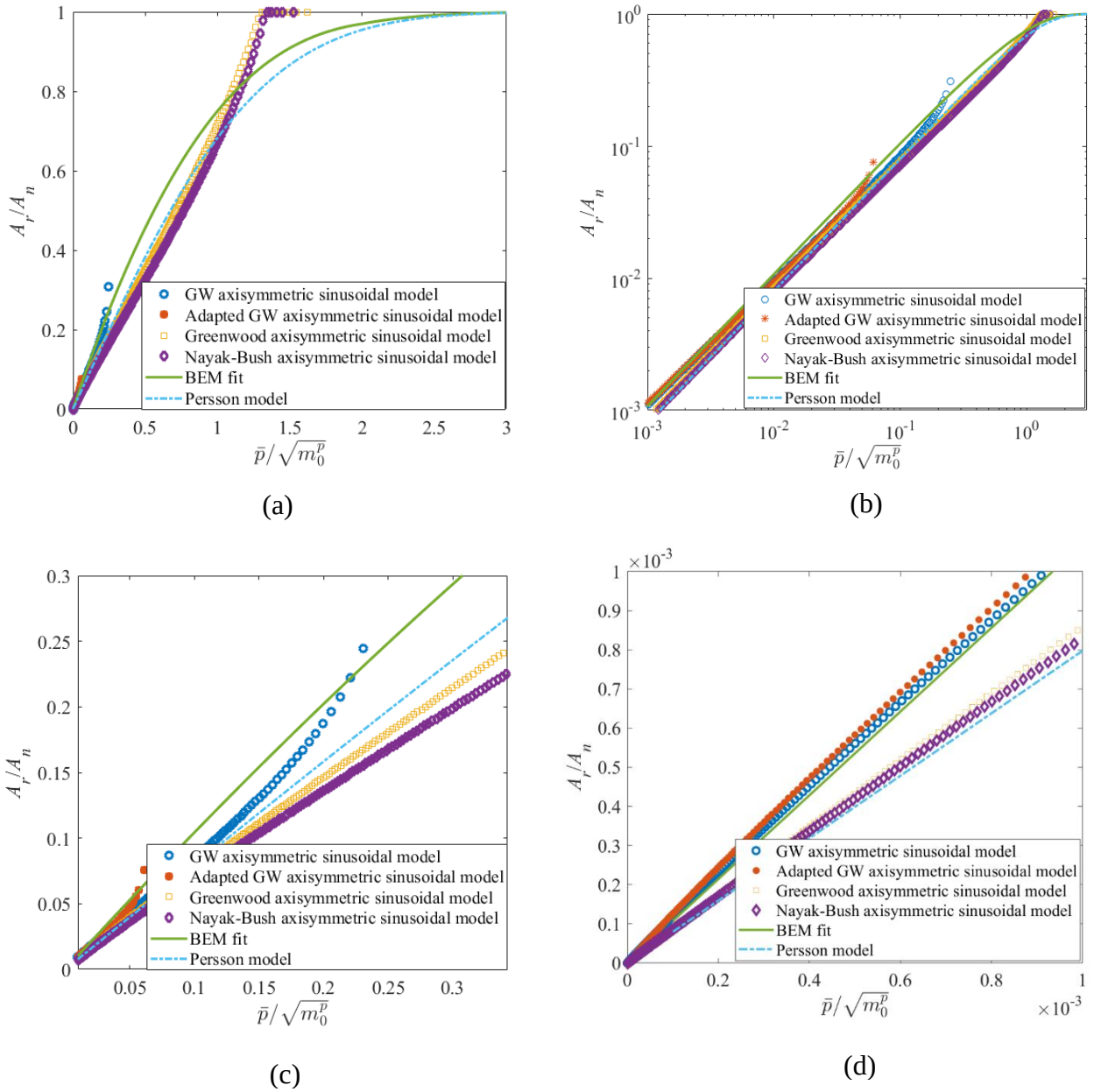

Fig. 5.6 Effect of different PDFs when employed with the axisymmetric sinusoidal single asperity model in the statistical model and comparison with the BEM result and Persson's model, (a) full scale plot (b) log-log plot (c) plot at the small deformation region (d) plot at the very small deformation region compared to Fig. 5.6(c).

behavior when the contact pressure is high. The same behavior was also observed in Section 5.2.2.2. Employment of the PDF $= f\left(\xi^{h*}, k_g^{h*}\right)$ with the axisymmetric sinusoidal asperity model i.e. Greenwood axisymmetric sinusoidal model shows good agreement with the Persson model from 0.01% to about 70% of the total contact area with an error less than 10%. However, near complete contact it does not agree with the Persson model or BEM result and shows a different trend. Fig. 5.6(c) shows that at the small deformation region, both the Nayak-Bush axisymmetric sinusoidal and Greenwood axisymmetric sinusoidal models match well with the Persson model. With the increase of pressure, the Greenwood axisymmetric sinusoidal model matches better with the Persson model than the Nayak-Bush axisymmetric sinusoidal model. Fig. 5.7(a) and (b) are showing the difference in contact area when the Greenwood axisymmetric model and Nayak-Bush axisymmetric model have been compared with the Persson model.

The possible reasons that are causing the difference between the statistical models developed using the 3D periodic sinusoidal asperity model and axisymmetric sinusoidal asperity model will be discussed later in Section 5.2.2.4. From the results of this section, it can be concluded that:

- Like statistical models developed using the 3D periodic sinusoidal asperity model (extended JGH asperity model), the statistical models developed employing an axisymmetric sinusoidal asperity also show that PDFs with constant radius of curvature cannot predict contact behavior at the higher pressure.
- The Greenwood axisymmetric sinusoidal model shows good agreement with the Persson model from the 0.01% to about 70% of the total contact area with less than 10% error. The Nayak-Bush axisymmetric sinusoidal model shows less than 16% error with the Persson model for 0.001-70% of the total contact.

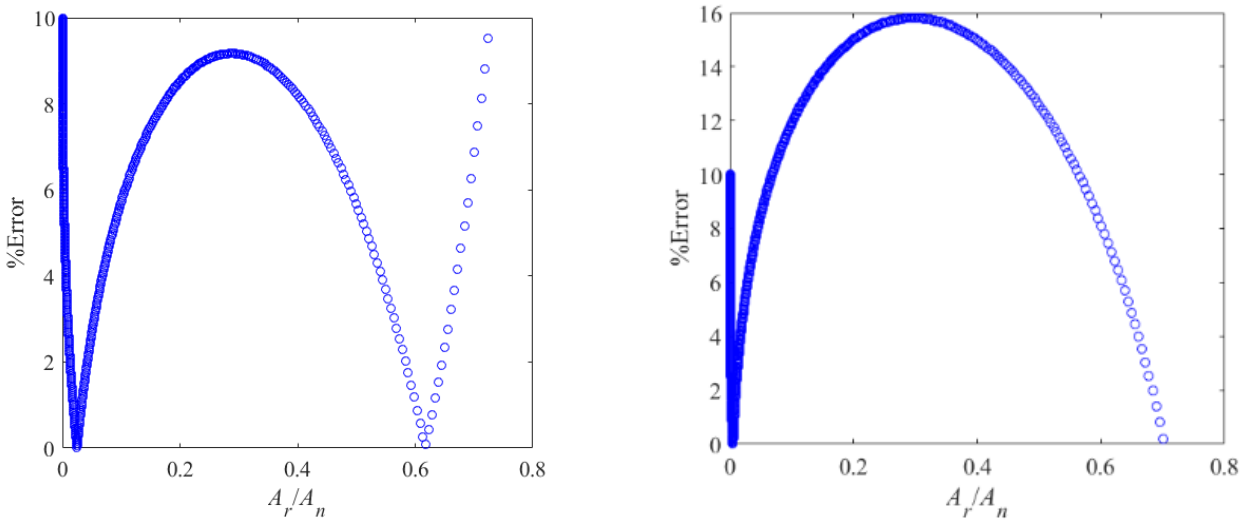

(a) (b)

Fig. 5.7 (a) Percentage of error vs. normalized contact area for Greenwood axisymmetric sinusoidal model, (b) percentage of error vs. normalized contact area for Nayak-Bush axisymmetric sinusoidal model.

- ❖ Both the Greenwood and Nayak-Bush axisymmetric sinusoidal models do not show good agreement with the BEM results.

5.2.2.4 Effect of Asperity Models on the Rough Surface Contact Modeling

The previous sections-5.2.2.1, 5.2.2.2 and 5.2.2.3, give an idea about how the asperity models are affecting the rough surface contact behavior. However, to understand the effect of the various asperity models on the rough surface clearly, the statistical models with different asperity models have been compared, while keeping the PDF same for each of them. Then the probable reasons for the difference among the rough surface models due to the asperity models will be discussed. As the PDFs, which do not consider the change in the asperity radius of curvature under predict the contact area and contact pressure; therefore, the statistical models using those PDFs (Gaussian and (PDF $= f(\xi^{h*})$) will not be used in this section. Fig. 5.8 is showing the effect of different asperity

models on the rough surface contact behavior when PDF $= f\left(\xi^{h*}, k_g^{h*}\right)$. For all the statistical rough surface contact models plotted in Fig. 5.8, the geometric curvature has been varied in the asperity models and in the PDF. These statistical models have been compared with the BEM results and the Persson's model for the purpose of validation. As mentioned before, the main purpose of developing sinusoidal asperity models is to model the asperity interaction at the higher pressures. Although, no validation work has been done before for the statistical models using sinusoidal asperity models for the whole range of contact. Fig. 5.8(a) and (c) are showing the validity of this approximation. Fig. 5.8(a) is showing that for the applied displacement, the Greenwood model, Greenwood 3D sinusoidal model and Greenwood axisymmetric sinusoidal model produce results from the very small deformation region to the complete contact. The Greenwood 3D sinusoidal model matches well with the BEM fit from the very small deformation region to more than 80% of the total contact with an error less than 12% and with the Persson model shows less than 10% error when real contact area is ~28%-90% of the total area (see Fig. 5.5(a)). The Greenwood axisymmetric sinusoidal model shows good agreement with the Persson model from 0.01% to about 70% of the total contact area with less than 10% error (see Fig. 5.7(a)). Although the Greenwood model produces results from small deformation region to the complete contact it only shows very good agreement with the Greenwood 3D sinusoidal model up to 30% of the total contact. Then it gradually diverges, as the Hertz mildly elliptical contact model with geometric curvature is not developed to model the heavy deformation region.

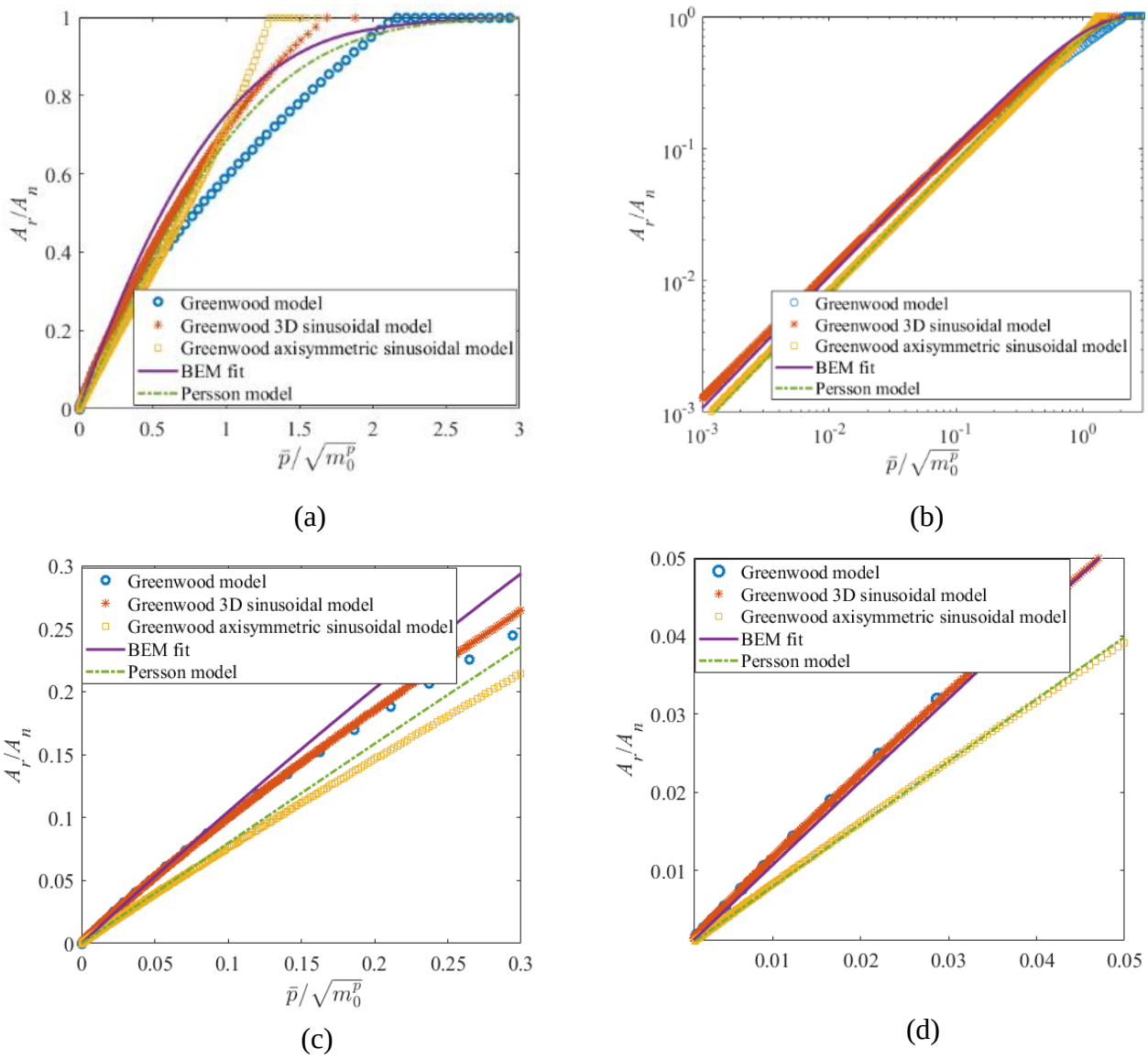

Fig. 5.8 (a) Comparison among the Greenwood, Greenwood 3D sinusoidal, Greenwood axisymmetric sinusoidal rough surface model, BEM fit and Persson's model, (a) full-scale plot (b) log-log plot c) plot at the small deformation region (d) plot at the very small deformation region compared to Fig. 5.8(c).

Several important facts can be noted from Fig. 5.8 and the above discussion:

- Qualitatively, the single asperity contact pressure-area relation is very similar to the rough surface contact result. The contact pressure-area plot near the complete contact region is slightly convex upward for the Greenwood 3D sinusoidal model and slightly concave upward for the Greenwood axisymmetric sinusoidal model, which are very similar to the extended JGH (3D periodic sinusoidal asperity model, see Fig. 2 in [13]), and Saha and Jackson single asperity model (axisymmetric sinusoidal asperity model, see Fig. 3.9 in Chapter 3 [12]) respectively.
- The Greenwood axisymmetric sinusoidal model predicts smaller contact area than the Greenwood 3D sinusoidal model from the small deformation region to the heavy deformation region (from the beginning of the contact to about 70% of the total area for the plot shown in Fig. 5.8). However, then the Greenwood axisymmetric sinusoidal model predicts a larger contact area than the Greenwood 3D sinusoidal model.
- From the small contact area to the intermediate region, the Greenwood 3D sinusoidal and Greenwood axisymmetric sinusoidal model are qualitatively similar. However, from the intermediate to the complete contact, the contact pressure-area trends are different. For the Greenwood 3D sinusoidal model, the contact pressure is continuously increasing even after reaching the complete contact. Therefore, the Greenwood 3D sinusoidal model is hydrostatic in nature at the complete contact. However, the Greenwood axisymmetric sinusoidal model behaves differently near the complete contact. After the intermediate region, although the area is increasing however the pressure is increasing at a very small rate.

Now the probable reasons that are causing the difference between the Greenwood axisymmetric sinusoidal and Greenwood 3D sinusoidal statistical models will be discussed:

For the nearly complete contact analysis, the Johnson, Greenwood and Higginson (JGH model) provided an analytical solution for the 3D periodic sinusoidal asperity (see Section 2.2.6) using a fracture mechanics approach. They also performed an experiment to validate the analytical solution. Their experiment shows that when the $\frac{\bar{p}}{p_e^*}$ ($\bar{p}$ is the nominal pressure and p_e^* is the pressure required to flatten the 3D elastic periodic sinusoidal asperity) is approximately 0.6, the non-contact region becomes circular. Johnson et al. defined that non-contact region as a "penny-shaped" crack and derived the analytical solution for the non-contact area using a fracture mechanics approach (Section 2.2.6). Xu and Jackson also provided a solution for the non-contact area of the "penny-shaped" crack such that the solution can be applied to the statistical model for the nearly complete contact (see Section 2.2.8, 2.2.9, 2.2.10, and 4.3.1.3). Both Johnson et al. (Section 2.2.6, (Eq. (2.39))) and Xu et al. [1-2] assumed that the parabolic pressure distribution is acting on the crack. According to Greenwood [14], for the surfaces like periodic wavy surface, maybe the assumption of the parabolic pressure on the circular non-contact area is valid. However, if the surface is like a fractal or random in nature, the pressure distribution is very complicated and pressure distribution on the concentric ring shape non-contact area (if not more complicated) will be closer to the reality. For the axisymmetric sinusoidal asperity model, the non-contact area is like a concentric ring shape (non-periodic wavy pressure distribution will be created at the interface).

Besides that for the same material and $\frac{\Delta}{\lambda}$ value, the pressure required to reach at complete contact for the 3D sinusoidal model is higher than the pressure required to reach at complete contact for the axisymmetric sinusoidal asperity. This is why when employing this axisymmetric sinusoidal

asperity model to predict rough surface contact behavior it is predicting a contact area larger than the statistical model developed using extended JGH model near the complete contact.

Now, in an average sense it can be assumed that the stress intensity factor (SIF) for the concentric ring shaped crack and circular crack are the same [14]. Then the non-contact area equation for JGH model should be also applicable to the axisymmetric sinusoidal asperity model, however the pressure distribution in the non-contact area equation will be different. The analytical equation for non-contact area developed by Johnson et al. (Section 2.2.6, (Eq. (2.39))) is a function of pressure. Therefore, in that equation if the pressure distribution for the axisymmetric case is applied, the non-contact area for the axisymmetric case and 3D sinusoidal wavy asperity (JGH) should match with each other. The non-contact area equation provided by Johnson et al. (Eq. (2.39)) is:

$$\text{Normalized non-contact area} = \frac{3}{2\pi}\left\{1 - \frac{\bar{p}}{p_e^*}\right\}$$

Fig. 5.9 is showing that, when the pressure distribution for the axisymmetric case has been applied to the above equation, both asperity models almost coincided with each other from the intermediate region to the complete contact. Therefore, it can be said with confidence now that it is the pressure distribution on the non-contact area that is causing the difference between the axisymmetric sinusoidal model, and the 3D periodic sinusoidal asperity model. As a result, this reason is also causing a difference in the rough surface models that have been developed employing these two asperity models.

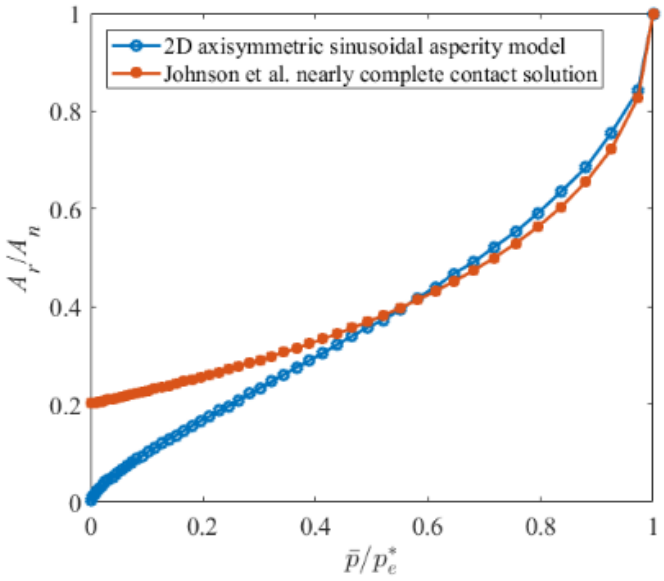

Fig. 5.9 Comparison between axisymmetric sinusoidal asperity model and Johnson et al. [15] nearly complete contact solution (3D periodic sinusoidal asperity model).

The statistical models developed employing mean curvature at the asperity and the PDF, behave in a very similar way as the statistical models developed employing geometric curvature at the asperity and PDF. The statistical models developed using mean curvature i.e. the Nayak-Bush model, Nayak-Bush 3D sinusoidal model and Nayak-Bush axisymmetric sinusoidal model have been shown in Fig. 5.10. Fig. 5.10(a) and (b) show that, employment of the sinusoidal asperity model in the statistical model helps to predict contact behavior from small contact area to the complete contact. The Nayak-Bush 3D sinusoidal model shows a similar trend to the Persson model and BEM fit, but actually shows good agreement with the Persson model from 12% to about 90% of the total contact with less than 10% error. The Nayak-Bush axisymmetric sinusoidal model is qualitatively the same as the Nayak-Bush 3D sinusoidal model, the BEM fit and the Persson model from low load to the intermediate region (more than 60% of the total area). After that, the contact pressure-area curve trend is different. The reason is the same as described for the statistical

models plotted in Fig. 5.8. The comparison between the Nayak-Bush axisymmetric sinusoidal model and the Persson model shows that the difference between the two models is less than 16% when the real contact area is 0.001% to 70% of the total contact. When the pressure is small (Fig. 5.10(c-d), contact area is less than 20% of the total contact), both the Nayak-Bush and Nayak-Bush 3D sinusoidal model match well with each other. These two models show better agreement with the BEM fit at the small pressure region. Therefore, the following points can be concluded:

- The Nayak-Bush model and Nayak-Bush 3D sinusoidal model almost coincide with each other at the small deformation region when the contact area is less than 20% of the total contact. When the deformation is very small, these two models also match well with the BEM fit and with the increase of deformation gradually diverge from BEM fit and from each other.
- The Nayak-Bush 3D sinusoidal model shows good qualitative agreement with the BEM fit and the Persson model, but shows good quantitative agreement with the Persson model (when real contact area is 12-90% of the total area, error is less than 10%).
- The Nayak-Bush axisymmetric sinusoidal model does not show good qualitative agreement with the BEM fit. At the beginning of the contact, when the deformation is very small, the model matches very well with the Persson model. However, with the increase in deformation these two models do not match well qualitatively and after the intermediate contact region, gradually show different trends in the contact behavior. The comparison between these two models shows that the difference between these two models is less than 16% when the contact area is 0.001%-70% of the total contact.

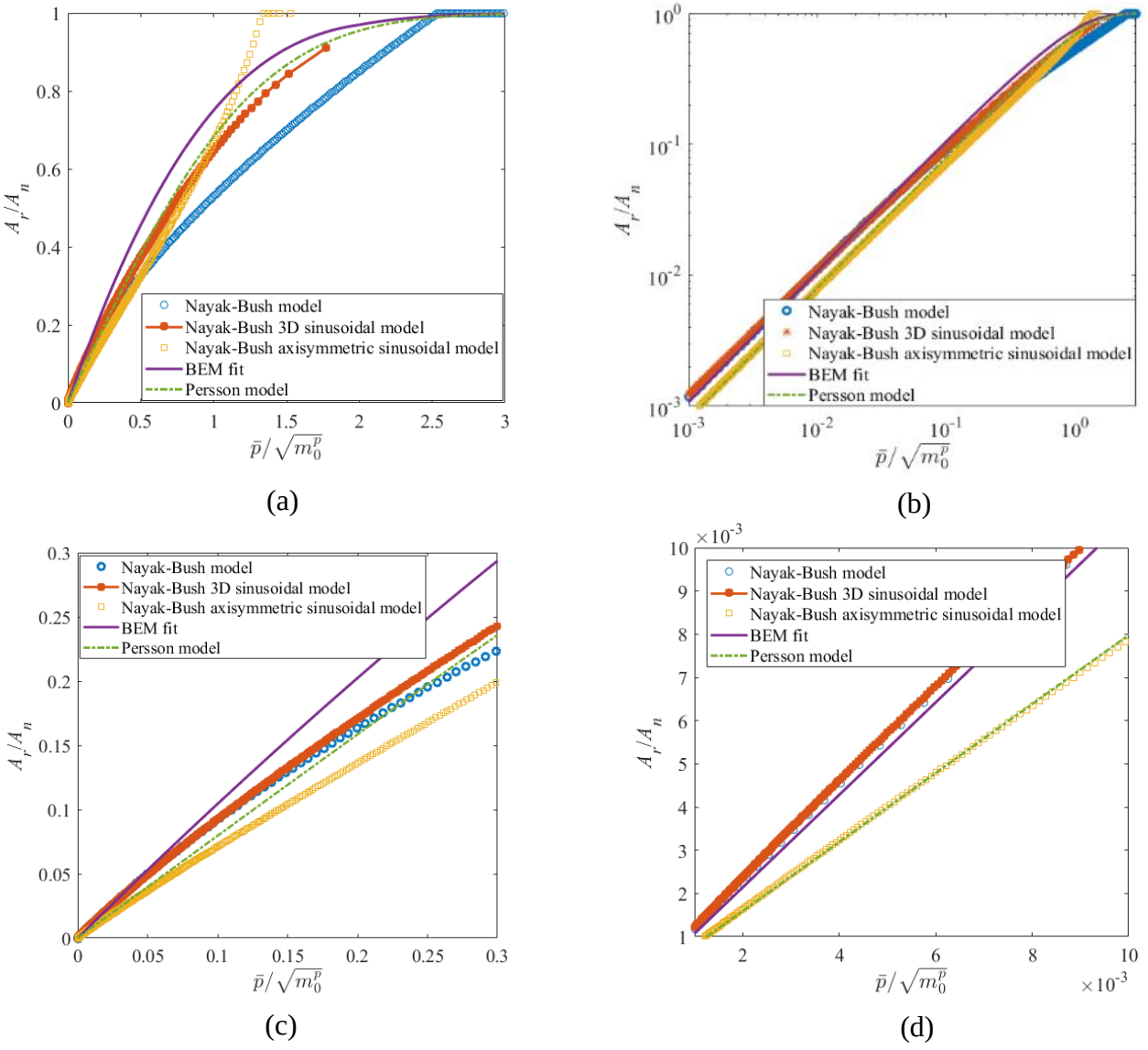

Fig. 5.10 (a) Comparison among Nayak-Bush, Nayak-Bush 3D sinusoidal, Nayak-Bush axisymmetric sinusoidal, BEM fit and Persson's model, (a) full scale plot (b) log-log plot (c) small deformation region (d) very small deformation compared to Fig. 5.10 (c).

5.2.2.5 Comparison of the Newly Developed Statistical Models with the Nearly Complete Contact Statistical Models

In this section, the statistical models developed using 3D periodic sinusoidal asperity model will be plotted together with the statistical models that were developed for the nearly complete contact region using the fracture mechanics approach (see Section 4.3.1.3). The objective is to observe whether the statistical models developed using 3D periodic sinusoidal asperity model and statistical models for the nearly complete contact models together can predict the contact behavior for the whole range of contact. Statistical models developed using axisymmetric sinusoidal asperity model will not be discussed here. Because the nearly complete contact statistical models have been developed assuming parabolic pressure distribution over the circular non-contact area, however, for the axisymmetric sinusoidal asperity case, wavy pressure distribution has been observed on the concentric ring shaped non-contact area.

Fig. 5.11 shows the comparison of the newly proposed statistical models developed employing 3D periodic sinusoidal asperity model with the Greenwood crack model, Nayak-Bush crack model, BEM fit and the Persson model. The Greenwood-crack model is the Xu and Jackson modified Greenwood model, and the Nayak-Bush crack model is the Xu and Jackson modified Nayak-Bush model (see Section 4.3.1.3). The nearly complete contact statistical models show good agreement with the BEM and fit both qualitatively and quantitatively near the complete contact, and shows good qualitative agreement with the Persson model. As mentioned before, Fig. 5.11(a) and Fig. 5.11(b) show that the Greenwood 3D sinusoidal model agrees well with the BEM fit from the very small deformation region (0.1% of the total area) to the heavy deformation region (more than 80% of the total contact). Therefore, the Greenwood 3D sinusoidal model in conjunction with the Greenwood crack model can predict the whole range of contact (assuming the BEM result is

absolutely correct). The amount of error for the whole range of contact is less than 12% when compared with the BEM fit and the normalized contact area is greater than 0.001. The Nayak-Bush 3D sinusoidal model qualitatively shows good agreement with both the Persson model and BEM fit from the small deformation region to the heavy deformation region (more than 90% of the total area for the plot shown in Fig. 5.11(a)), does not show good quantitative agreement with the BEM fit and also cannot predict the complete contact area). To clearly show the combined plot of the Greenwood 3D sinusoidal model, the Greenwood crack model, and the BEM fit, these three results have been plotted together again in Fig. 5.11 (b).

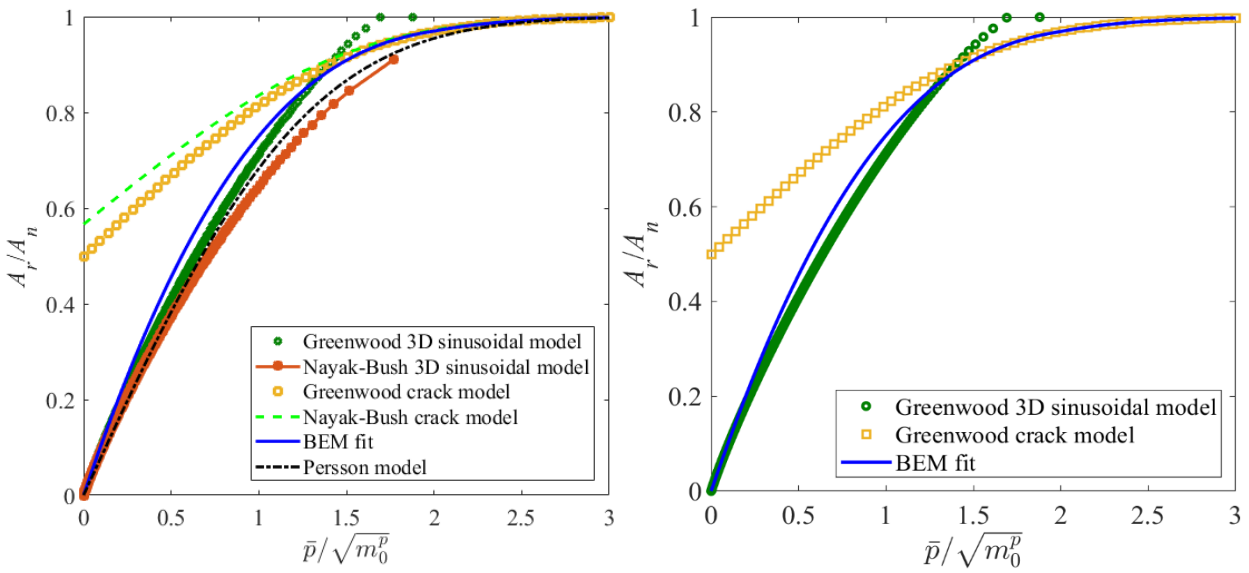

Fig. 5.11 (a) Comparison of the newly developed statistical models using 3D sinusoidal asperity, and PDF $= f\left(\xi^{h*}, k_g^{h*}\right)$ and PDF $= f(\xi^{h*}, k_m^{h*})$ with the nearly complete contact statistical models, BEM fit and Persson's model, (b) Comparison of the Greenwood 3D sinusoidal model and Greenwood-crack model with the BEM fit.

5.2.2.6 Comparison of the Statistical Models with Multiscale Models

In this section, all the statistical model's predictions developed and discussed so far will be compared with the multiscale model. Three different multiscale models have been considered for comparison: multiscale model developed employing 1) Hertz spherical asperity model (Eq. (2.17) and (2.18)), 2) 3D periodic sinusoidal asperity model (Eq. (2.46), (2.47) and (2.48)), and 3) axisymmetric sinusoidal asperity model (Eq. (3.5) and (3.9)), in the framework of the multiscale model (Eq. 4.73 and 4.74). Fig. 5.12(a), 5.12(b), and 5.12(c) are showing the spectrum of the isotropic, fractal and Gaussian rough surface. The spectrum of the rough surface shows that the $\frac{\Delta}{\lambda}$ values for the surafce area very small and there is not much variation in the $\frac{\Delta}{\lambda}$ values. Fig. 5.13 is showing the comparison of the statistical, multiscale, Persson models and BEM fit. Nearly complete contact statistical models have not been plotted in Fig. 5.13. The plots show that when employing different asperity models in the framework of the multiscale model, the contact models show a similar trend as the statistical model, but over predict the contact area compared to all the statistical models, BEM fit and Persson model. The multiscale model developed using the axisymmetric sinusoidal asperity over predicts the contact area most, then multiscale model developed using 3D sinusoidal model and multiscale model developed using Hertz asperity model predicts the least contact area at the same pressure among these three multiscale models.

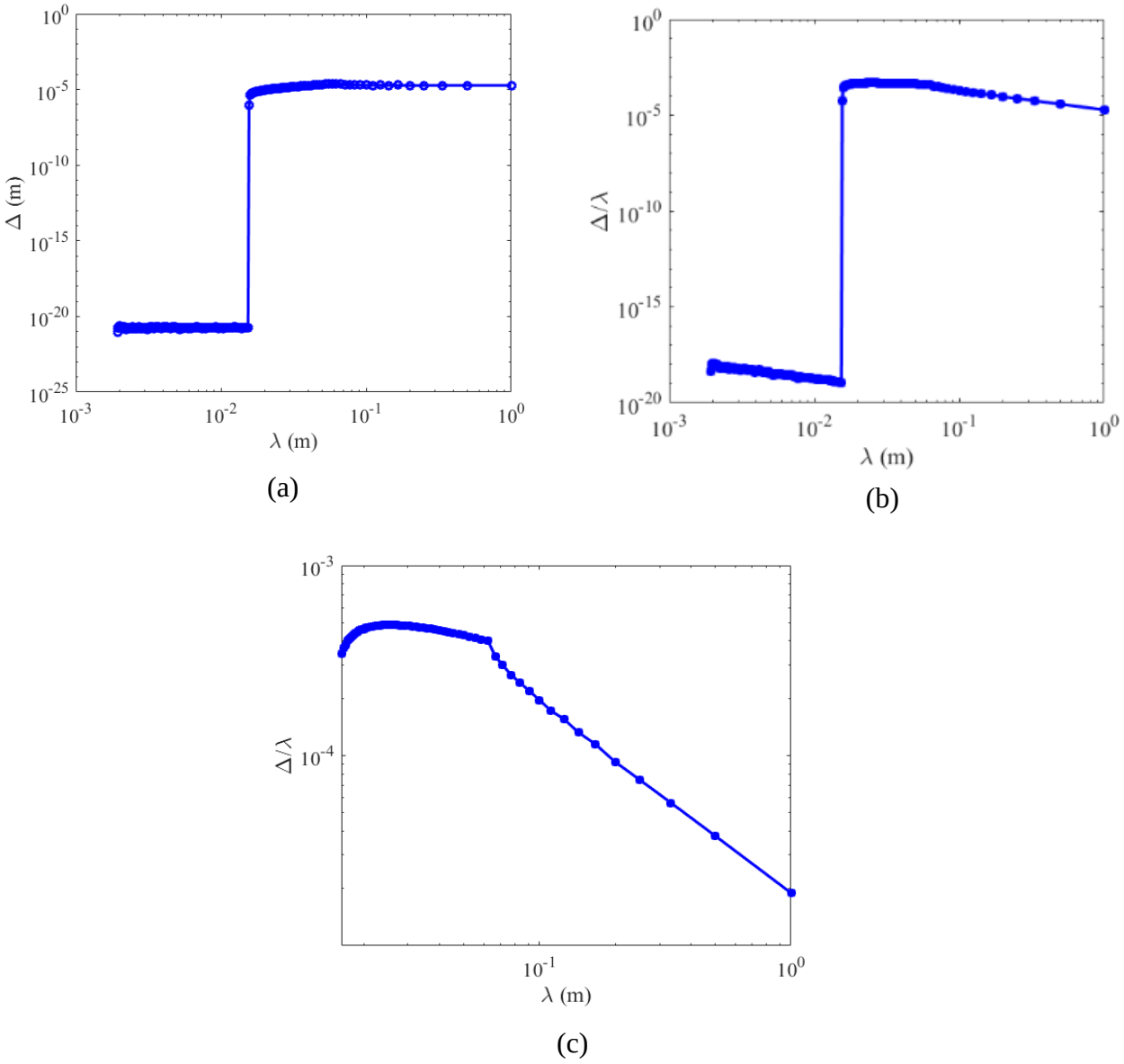

Fig. 5.12 (a) Spectrum of the generated surface with surface properties shown in Table-5.1, (b) Normalized surface spectrum of the same surface, (c) magnified view of the normalized spectrum where $\frac{\Delta}{\lambda}$ value is high.

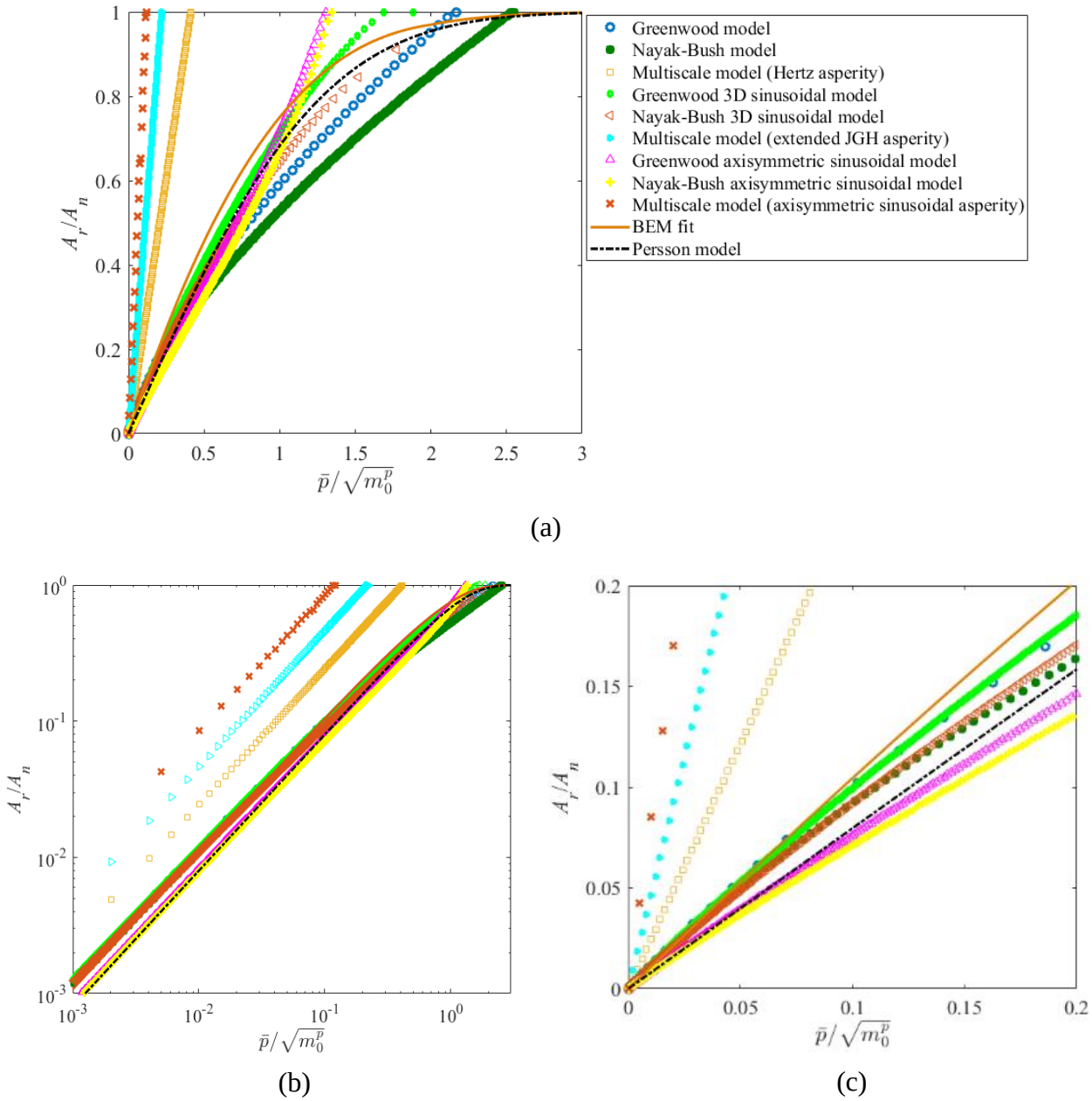

Fig. 5.13 Comparison of the multiscale model with the statistical models and BEM fit, (a) full-scale model (b) log-log plot (c) at the small deformation region.

5.3 Development of the Elastic Rough Surface Contact Models (Real Surface)

The main objective of this section is to observe, how the real surface data effects the prediction of the same rough surface contact models developed and discussed in Section 5.2. It will also be inspected, if there is any difference in the contact behavior trend when these statistical models have been employed for the real surface and generated surface contact analysis.

For real surface analysis, two aluminum alloy cylinders (6061-T6511B) have been chosen, which are then used later to measure the contact resistance between them. Contact resistance measurement between the two aluminum surfaces will be discussed later in Section 5.5.2. Fig. 5.14 (a) shows the aluminum surfaces that have been used for real rough surface contact analysis. For each of the sample surfaces, roughness has been measured at the north, south, east, west, and at the origin as shown in the figure to get an overall idea about the sample surface roughness. Fig. 5.14(b) shows the Scanning White Light Interferometer (SWLI) that has been used for surface roughness measurement. For all the measurements, a 3.429 μm horizontal resolution has been used. After the surface roughness measurement, if there is any missing data, that location has been filled by taking an average of the neighboring surface roughness heights. To level the surface, a plane has been fitted through the surface data. Then that plane has been subtracted from the original surface roughness. The mean has been calculated and subtracted from the roughness heights using the same methodology as described for the generated surface (Section 5.2). The surface properties have been calculated using the methods described in Section 4.2.1 and 4.2.4. The material and surface properties have been shown in Table-5.4, 5.5 and 5.6. The plot of the rough surface, probability distribution of the surface asperity heights and spectral analysis of the surfaces have been shown in Fig. 5.15(a), 5.15(b), and 5.15(c-d) respectively. As the rough surface contact

modeling methodology is the same for both the generated and real surfaces, they is why will not be described in this section.

Table-5.4 Aluminum alloy (6061-T6511B) material properties

Young's Modulus (GPa)	Yield Strength (MPa)	Poisson's Ratio	Equivalent Elastic Modulus (GPa)	Resistivity ($\Omega \cdot m$)
68.9	276	0.33	38.66	3.99×10^{-8}

Table-5.5 Average properties of the composite rough surface

m_0^h (m^2)	σ (μm)	m_2^h	m_4^h (m^{-2})	m_6^h (m^{-4})	α^h
5.0485×10^{-12}	2.25	0.0202	3.7356×10^{9}	8.2979×10^{20}	46.22

Table-5.6 Properties of the corresponding "pressure surface"

m_0^{p*}	$m_2^{p*}(m^{-2})$	$m_4^{p*}(m^{-4})$	α^p	$m_n^{p*} = \frac{m_n^p}{(E')^2}$ Where, $n = 0,2,4,6 \ldots$
3.18×10^{-3}	3.92×10^{8}	7.837×10^{19}	1.62	

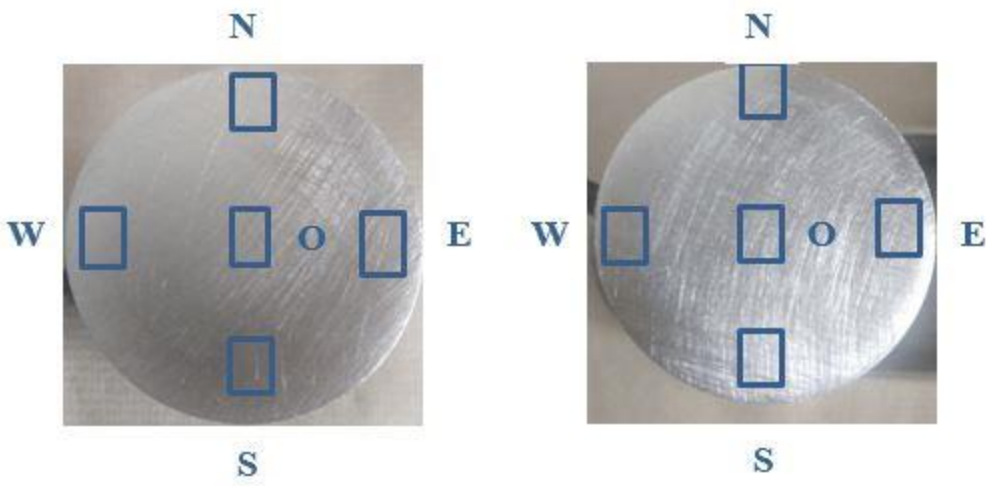

(a)

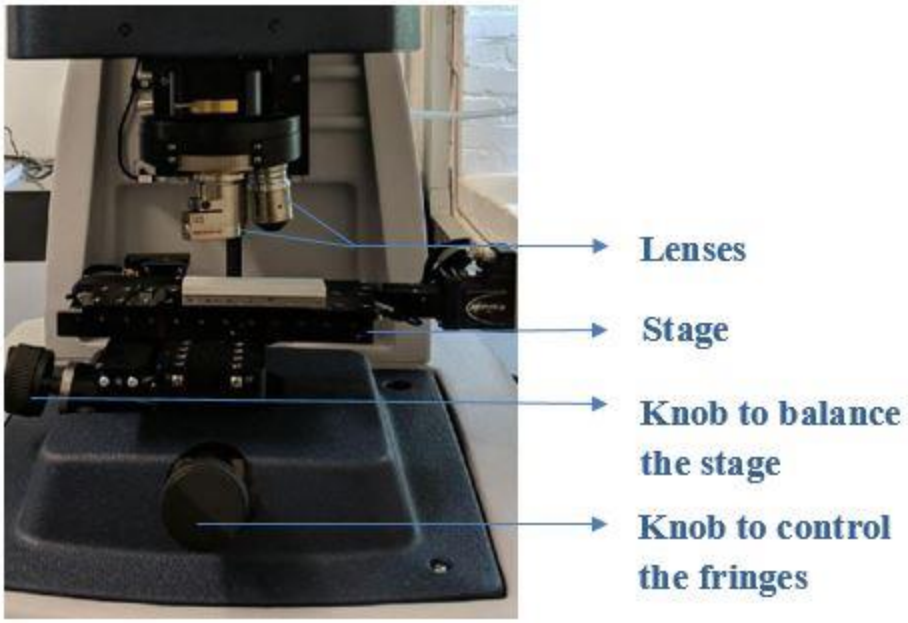

(b)

Fig. 5.14 (a) Aluminum surfaces used for real rough surface contact analysis and contact resistance measurement, (b) Scanning White Light Interferometer (SWLI) used for surface roughness measurement.

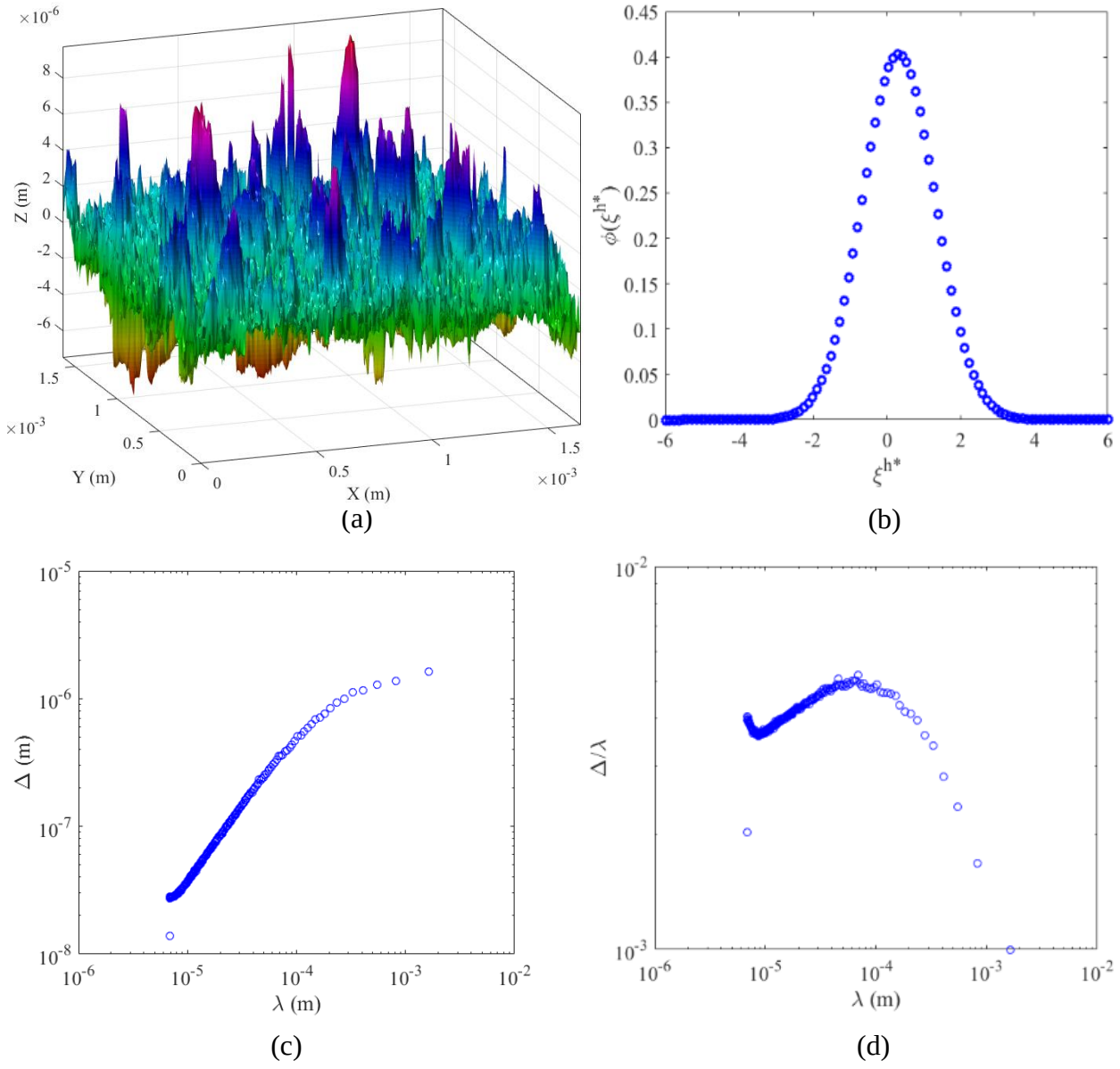

Fig. 5.15 (a) Plot of the aluminum rough surface (b) PDF of the rough surface (c) average spectrum of the rough surface (d) normalized average spectrum of the rough surface.

5.3.1 Results and Discussions for the Real Surface

5.3.1.1 Effect of PDFs when Employed with the Hertz Model

Figure 5.16 shows the effect of different PDFs (Gaussian, $PDF = f(\xi^{h*}), PDF = f(\xi^{h*}, k_g^{h*}), PDF = f(\xi^{h*}, k_m^{h*}))$, when employed with the Hertz models (Circular contact with constant radius of curvature, mildly elliptical contact with geometric curvature, mildly elliptical contact with mean curvature) in the framework of the statistical model. These statistical models have been described in detail in Section 4.3.1.1. For the sample real surface, Nayak's bandwidth parameter, α^h is 46.22 (see Table-5.5). As the value of α^h is very high, so the surface should be nearly Gaussian in nature. Fig. 5.15(b) also shows that the sample surface is very close to Gaussian. The contact behavior trends observed in Fig. 5.16 for the real surface are very similar to the generated elastic surface contact behavior (Fig. 5.2), when the statistical models are the same. For the same surface properties and applied displacement, the rough surface model that has been developed using a PDF which is not Gaussian and $PDF = f(\xi^{h*})$ under predict the contact area and pressure compared to the statistical models developed using a Gaussian PDF, $PDF = f(\xi^{h*}, k_g^{h*})$ and $PDF = f(\xi^{h*}, k_m^{h*})$. Apparently it seems from Fig. 5.16(a-b) that all the models show good agreement with one another when the deformation is very small. However, Fig. 5.16 (c-d) show a clear view of the small deformation region. When the contact area is less than 20% of the total contact, the Nayak-Bush model ($PDF = f(\xi^{h*}, k_g^{h*})$) and Greenwood-Williamson model (Gaussian PDF) show best agreement with each other. All the models plotted in Fig. 5.16 show high deviation from each other after the small deformation region.

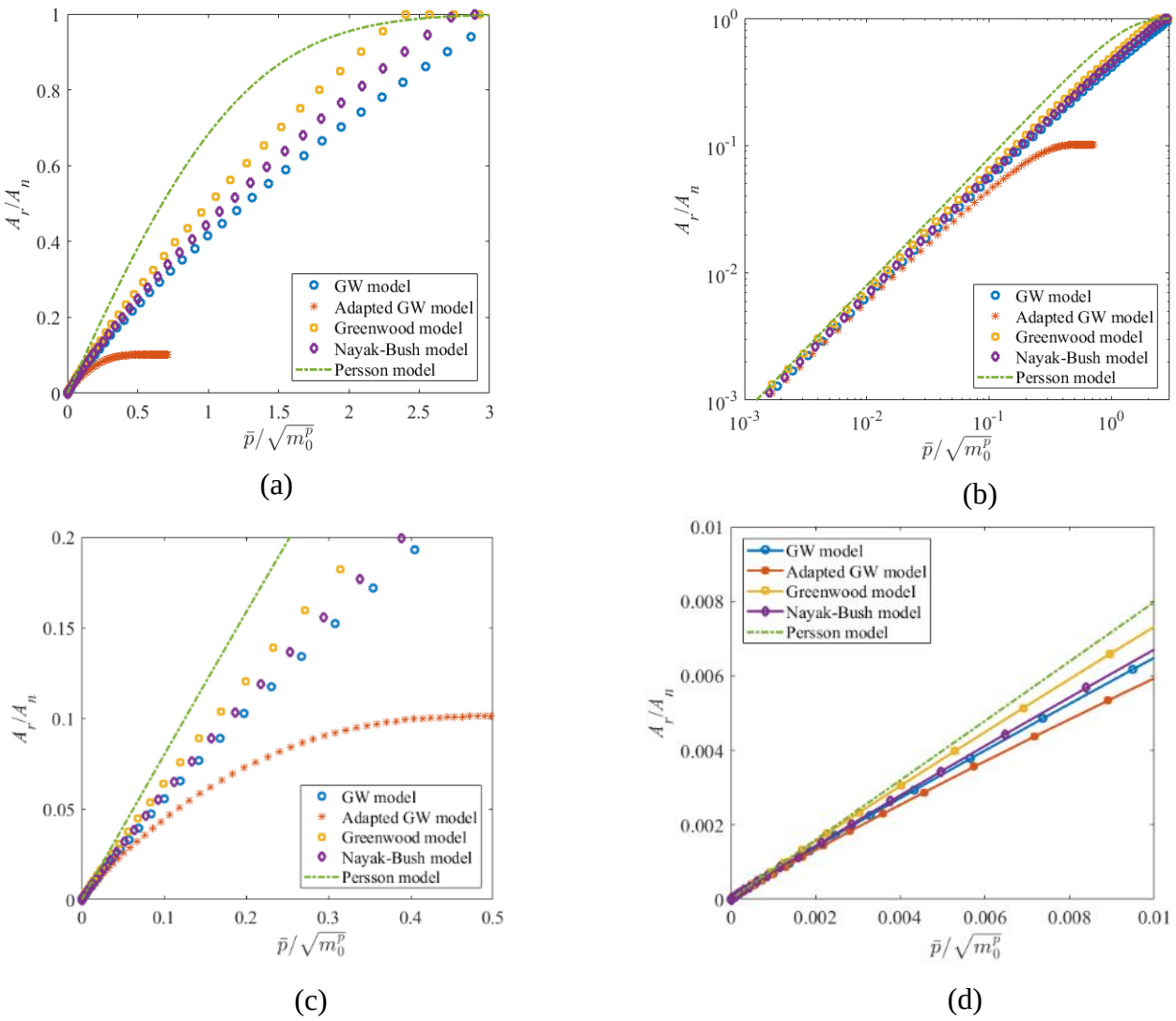

Fig. 5.16 Effect of different PDFs on the rough surface contact behavior when employed with the Hertz elastic single asperity models in the statistical model and comparison with the Persson model, (a) full scale plot (b) log-log plot (c) plot at the small deformation region (d) plot at the very small deformation region compared to Fig. 5.16(c).

5.3.1.2 Effect of PDFs when Employed with the 3D Periodic Sinusoidal Model

Figure 5.17 shows the effect of different PDFs when employed with the 3D periodic sinusoidal asperity models in the statistical model (these statistical models are described in Section 5.2.1.2). For these statistical models, the trend observed in the contact pressure-area curve for the real surface and for the generated surface are very similar (see Fig. 5.4). However, there are very few differences. 1) When the GW 3D sinusoidal statistical model has been employed to predict the contact behavior of the real surface, it shows a similar trend as the Nayak-Bush 3D sinusoidal model and Greenwood 3D sinusoidal model and can predict higher contact areas. The real surface is Gaussian in nature, therefore the result seems logical. In the case of the generated fractal surface, the GW 3D sinusoidal model could not predict the contact behavior after the small deformation region although the generated surface was Gaussian. Therefore, it seems that although the Gaussian distribution equation is easy to employ. However, PDFs, which consider both surface asperity height and mean/geometric curvature are more reliable to predict the contact behavior, whether the surface is Gaussian or not, 2) For the generated surface, the Greenwood 3D sinusoidal model and Nayak-Bush 3D sinusoidal model both show good agreement with the Persson model (For Greenwood 3D sinusoidal, when real contact area is ~30-80% of the total area, error was less than 10% and for Nayak-Bush 3D sinusoidal, when real contact area is ~12-90% of the total area the error was less than 10%). However, for the real surface, the Nayak-Bush 3D sinusoidal model and Greenwood 3D sinusoidal model do not show good agreement with the Persson model. The probable reason of this difference is that the Persson model is derived assuming the rough surface as a self-affine fractal. However, the real surface analyzed here is not a purely self-affine fractal in nature (see Fig. 5.15 (c)-(d)). For pure self-affine fractal rough surfaces, the Δ values will change linearly with λ (as Δ and Power Spectral Density, S^h are proportional to each other, see Eq. (4.36)).

However, in Fig. 5.15(c-d), the Δ or $\frac{\Delta}{\lambda}$ relation with wavelength, λ is not linear for the considered frequency spectrum of the rough surface. Like the generated surface, for the real surface analysis, the Nayak-Bush 3D sinusoidal and GW 3D sinusoidal model also show a good match with each other when the contact area is less than 20% of the total contact.

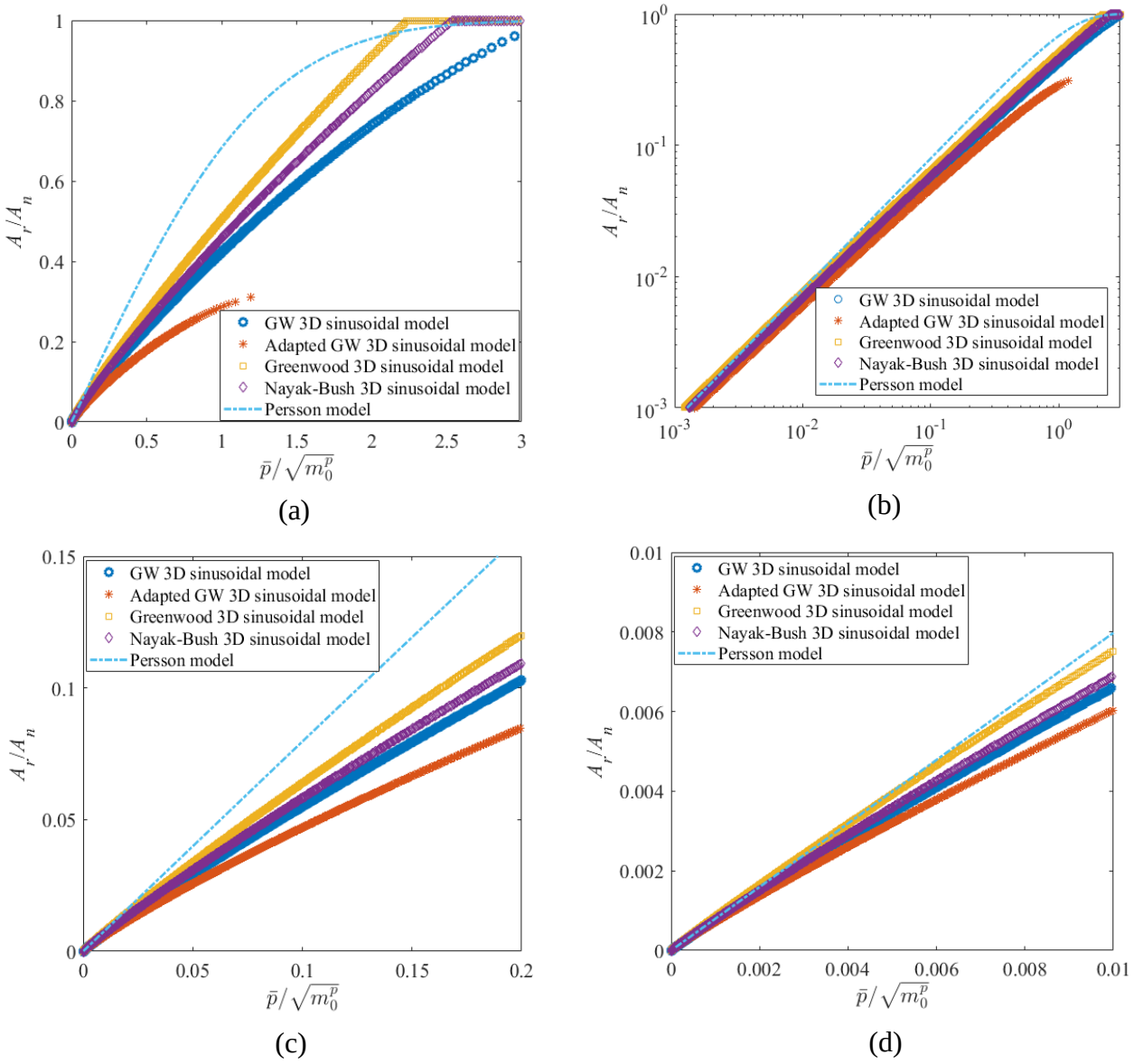

Fig. 5.17 Effect of different PDFs on the rough surface contact behavior when employed with the 3D periodic sinusoidal single asperity in the statistical model and comparison with the Persson

model, (a) full scale plot (b) log-log plot (c) plot at the small deformation region (d) plot at very small deformation region compared to Fig. 5.17(c).

5.3.1.3 Effect of PDFs when Employed with the Axisymmetric Sinusoidal Model

The predictions of the statistical models developed using different PDFs and the axisymmetric sinusoidal asperity are shown in Fig. 5.18 (the statistical models have been described in Section 5.2.1.3). Several differences have been observed when employing these same models for the generated surface. The variations are very similar to the differences as observed in Section 5.3.1.2, 1) For the generated surface, the GW axisymmetric sinusoidal model under predicts the contact area, although the generated surface is Gaussian in nature. However, like the previous Section 5.3.1.2, when employing the GW axisymmetric sinusoidal model to analyze the real surface contact behavior, the contact model can predict higher contact areas and pressure and shows very close agreement with the Nayak-Bush model from the small deformation region to near the complete contact. 2) For the generated surface, both the Greenwood axisymmetric sinusoidal and Nayak-Bush axisymmetric sinusoidal model show very good agreement with the Persson model at the small deformation region (see Fig. 5.8(d) and 5.10(d)). GW axisymmetric sinusoidal model also shows good agreement with Persson's model when contact area is 0.01-70% of the total area with less than 10% error (see Fig. 5.6 and Fig. 5.7(a)). However, for the real surface this statistical model does not match well with Persson's model. As mentioned before, the real surface analyzed here is not a purely self-affine fractal surface Persson's model was derived for the self-affine fractal rough surface. This is probably the reason causing the difference when employing the same models for the generated and real surface.

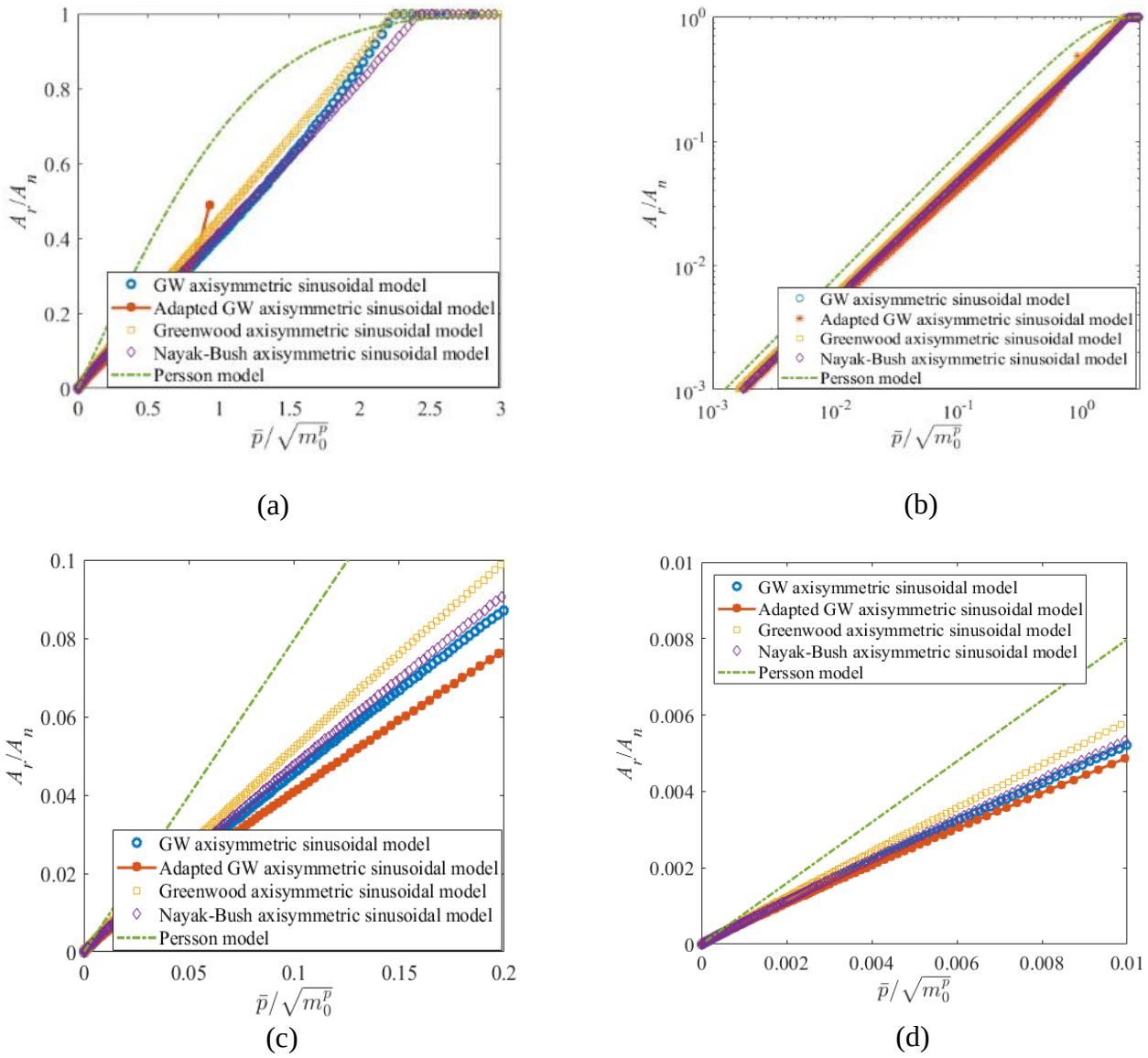

Fig. 5.18 Effect of different PDFs on the rough surface contact behavior when employed with the axisymmetric sinusoidal single asperity in the statistical model and comparison with the Persson model, (a) full scale plot (b) log-log plot (c) plot at the small deformation region (d) plot at the very small deformation region compared to Fig. 5.18(c).

5.3.1.4 Effect of Asperity Models on the Rough Surface Contact Modeling (Real Surface)

The effect of different asperity models on the rough surface contact behavior have been discussed in detail for the generated rough surface (see Section 5.2.2.4). The main difference that has been observed between the generated and real surface analysis are the effect of Gaussian PDF and the difference with the Persson's model. During analyzing the effect of PDFs (while keeping the asperity model the same) on the real surface contact behavior, it has been found that as the real surface is Gaussian the statistical models developed using a Gaussian PDF qualitatively show very similar trends as the statistical models developed using $PDF = f\left(\xi^{h*}, k_g^{h*}\right)$ and $PDF = f(\xi^{h*}, k_m^{h*})$, but quantitatively predict different behavior. The investigations of the asperity models on the contact behavior show that, when employing a Gaussian PDF, the statistical models developed using the 3D periodic sinusoidal asperity model and Hertzian asperity model almost coincided with each other (Fig. 5.19(a)). When employing $PDF = f\left(\xi^{h*}, k_g^{h*}\right)$ and $PDF = f(\xi^{h*}, k_m^{h*})$, the statistical model developed using the 3D periodic sinusoidal model and Hertzian asperity model also show very good agreement (see Fig. 5.20(a) and Fig. 5.21(b)). All the statistical models developed using the axisymmetric sinusoidal asperity model always under predict the contact area of the statistical models developed using 3D periodic sinusoidal asperity model from the small deformation region to the intermediate region/ near the complete contact. However, from the intermediate region/ near the complete contact to the complete contact region, these models generally over predict the contact area compared to the statistical models developed using the 3D sinusoidal model. The reasons have described when analyzing the effect of asperity models on the generated surface contact (see Section 5.2.2.4). Fig. 5.19-5.21 are showing the effect of asperity models on the real rough surface contact when the PDF is Gaussian, $PDF = f\left(\xi^{h*}, k_g^{h*}\right)$), and $PDF = f(\xi^{h*}, k_m^{h*}))$, respectively.

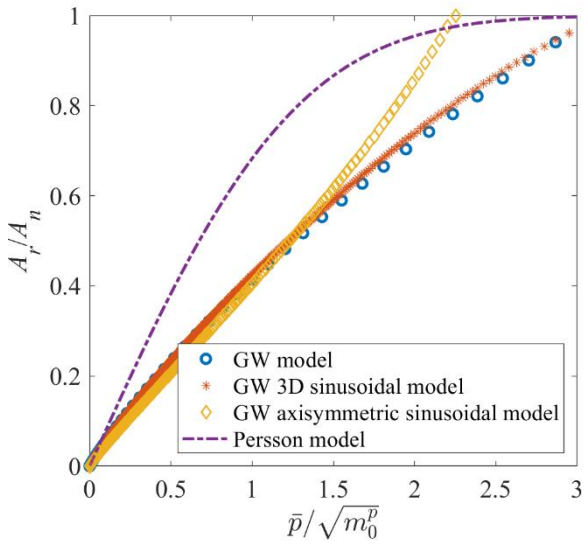

(a)

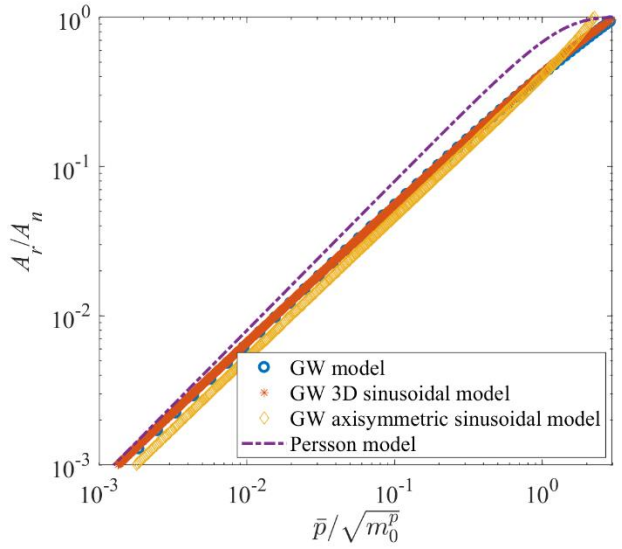

(b)

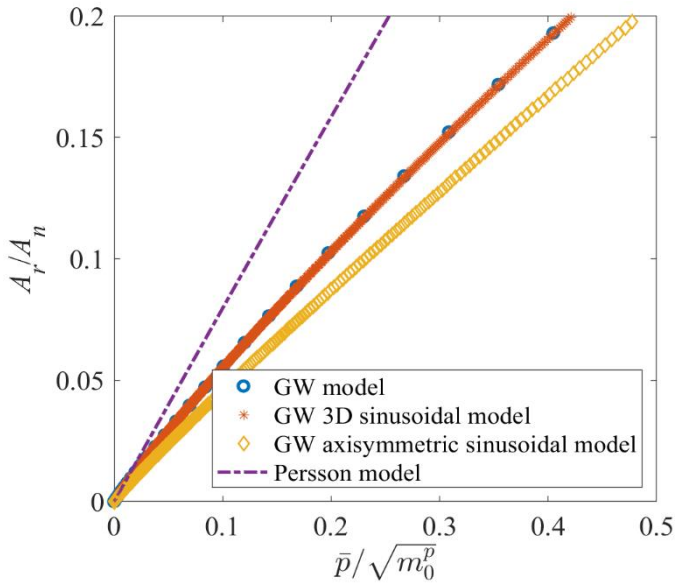

(c)

Fig. 5.19 (a) Comparison among GW model, GW 3D sinusoidal, GW axisymmetric sinusoidal and Persson's model, (a) full-scale plot (b) log-log plot (c) small deformation region.

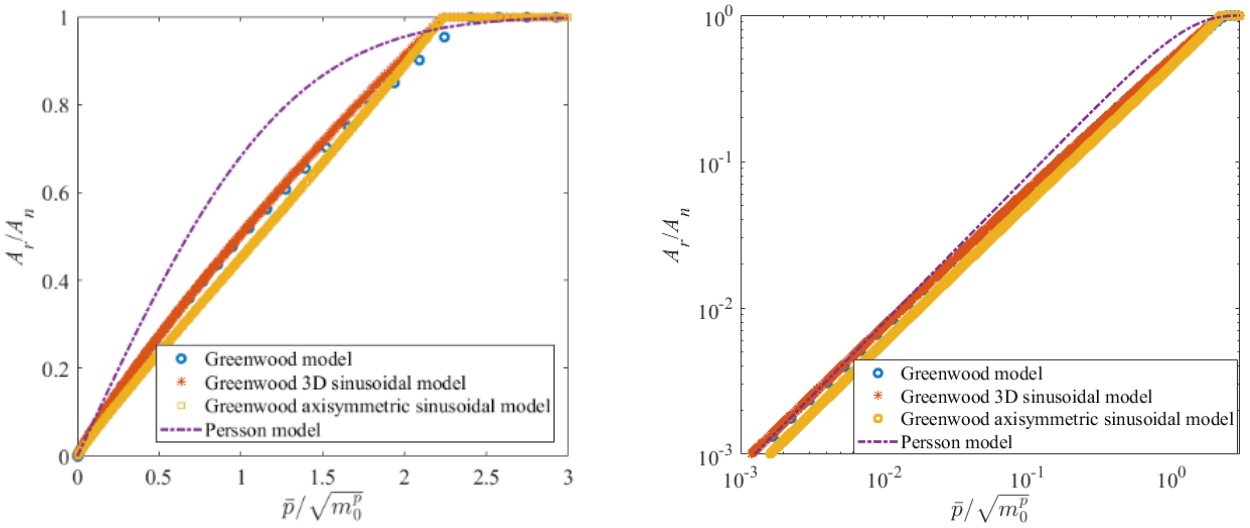

(a) (b)

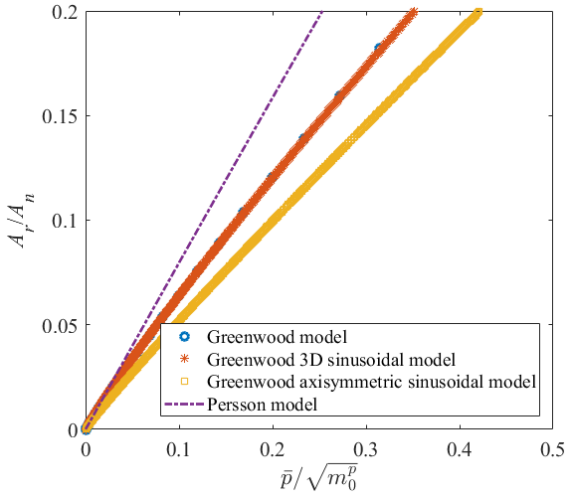

(c)

Fig. 5.20 (a) Comparison among Greenwood model, Greenwood 3D sinusoidal, Greenwood axisymmetric sinusoidal and Persson's model, (a) full-scale plot (b) log-log plot (c) small deformation region.

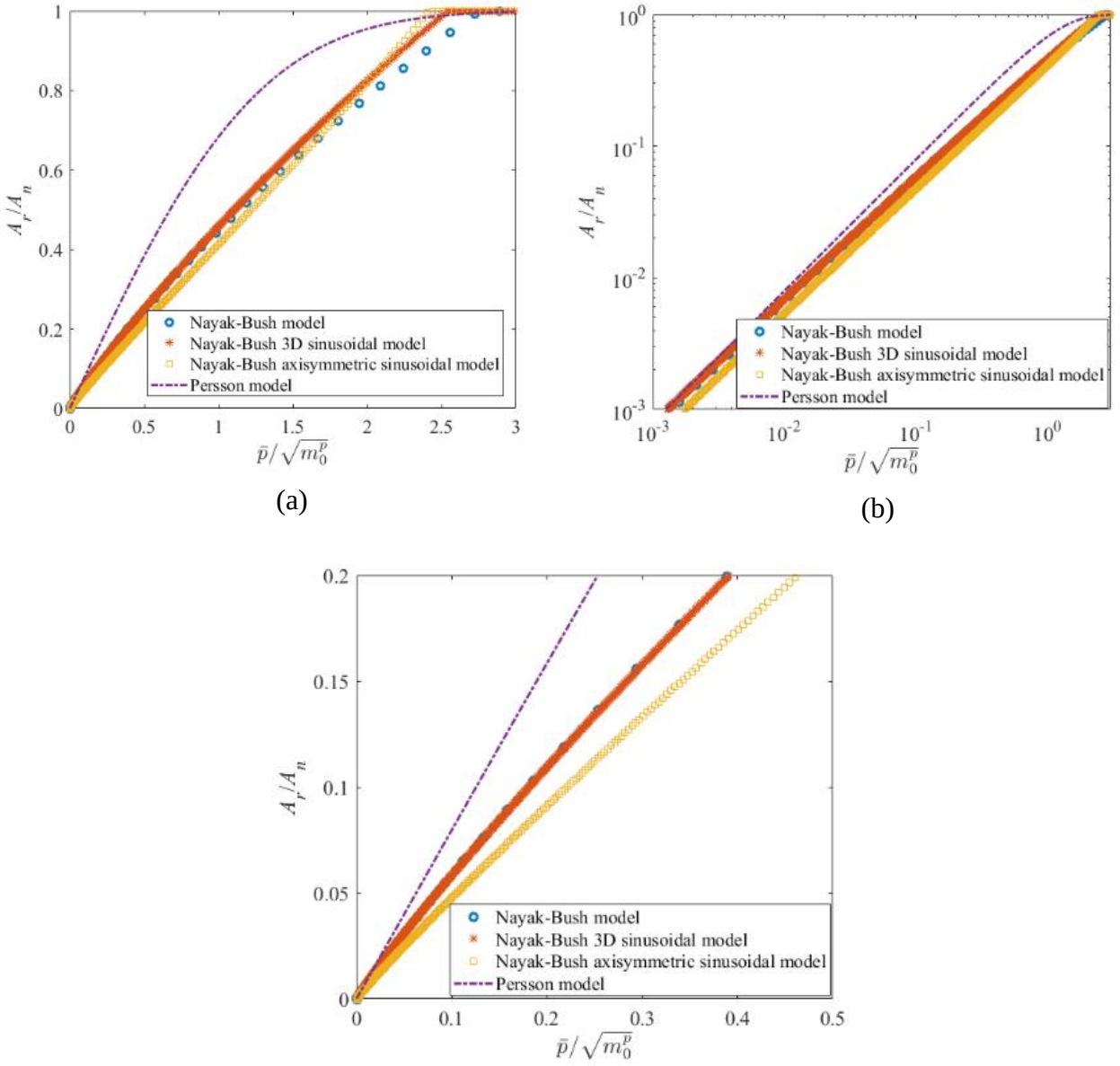

Fig. 5.21 (a) Comparison among Nayak-Bush model, Nayak-Bush 3D sinusoidal, Nayak-Bush axisymmetric sinusoidal and Persson's model, (a) full-scale plot (b) log-log plot (c) small deformation region.

5.3.1.5 Comparison of the Newly Developed Statistical Models with the Nearly Complete Contact Statistical Models

Fig. 5.22 is showing the comparison of the statistical models developed using the 3D periodic sinusoidal asperity models with the nearly complete contact statistical models for the real surface. During the validation of the generated surface, it has been found that the Greenwood 3D sinusoidal model in conjunction with the Greenwood crack model can predict the whole range of contact and show good agreement with the BEM. Therefore, it appears better to employ the statistical models developed for early to complete contact (Greenwood 3D sinusoidal model) with the statistical models for the nearly complete contact (Greenwood crack model) to make sure that statistical models developed for early to complete contact are well predicting near the complete contact. For the generated surface the Greenwood 3D sinusoidal model could predict from 0.1% to more than 80% of the total area and the rest of the range has been predicted by the nearly complete contact statistical model. However, for the real surface the Greenwood 3D sinusoidal model can predict almost the whole range of contact.

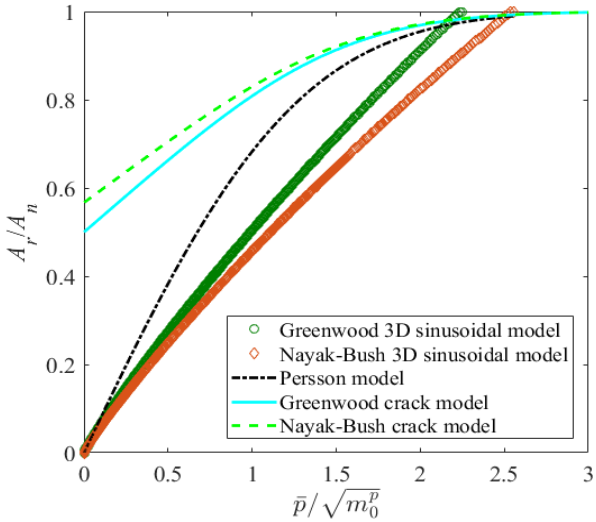

Fig. 5.22 Comparison among the statistical models developed using 3D periodic sinusoidal asperity models and nearly complete contact statistical models.

5.3.1.6 Comparison of the Newly Developed Statistical Models with the Multiscale Models

Figure 5.23 is showing the comparison of the multiscale models with the statistical models for the real surface. The real surface shows a very similar behavior as the generated surface. All the multiscale models developed using 3D periodic sinusoidal asperity model (Eq. (2.46), (2.47), and (2.48)), axisymmetric sinusoidal asperity model (Eq. (3.5), and (3.9)) and Hertz spherical asperity model (Eq. (2.17) and (2.18)) over predict the contact area compared to the statistical models. Among the three multiscale models, the multiscale model developed using the axisymmetric sinusoidal asperity predict the largest contact area, followed by the multiscale model developed using the 3D periodic sinusoidal asperity and then the multiscale model developed using the Hertz asperity.

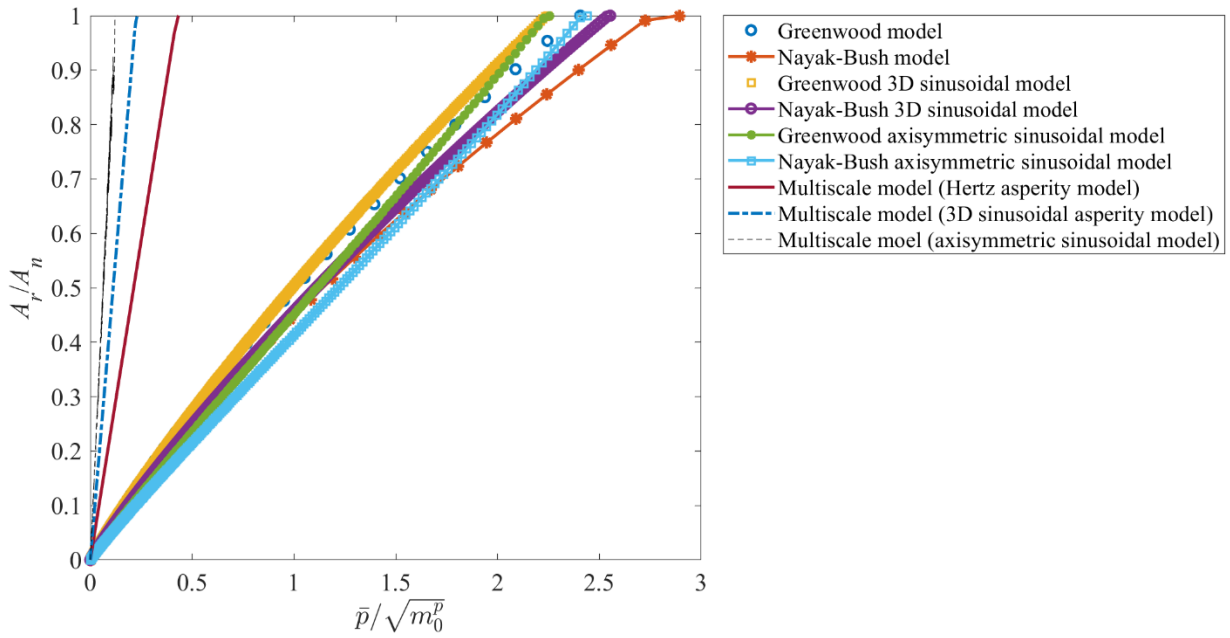

Fig. 5.23 Comparison among different statistical and multiscale elastic contact models.

5.4 Development and Validation of the Elastic-Plastic Rough Surface Contact

From the analysis in the previous sections, it has been found that when employing the statistical model to predict the contact behavior proper choice of the asperity model and PDF are important. Although the Gaussian PDF is widely used for rough surface contact analysis, it is more reliable to use the PDFs, which consider the change in both the asperity height and radius of curvature. Research work has been done on the elastic-plastic statistical models using Jackson-Green (JG) spherical asperity models (see Section 4.3.2.1), and 3D periodic elastic-plastic sinusoidal asperity models [12]. However, these statistical models did not consider the statistical distribution of asperity radius of curvature with asperity height, and employed the Gaussian distribution as the PDF irrespective of the surface nature. In this section, several elastic-plastic statistical rough surface contact models have been developed using spherical and sinusoidal asperity models and different PDFs. Change in the radius of curvature with the asperity heights have been considered both in the asperity models and PDFs. The newly developed statistical models have also been compared with the multiscale models. Then electrical contact resistance has been determined using these rough surface contact models. Unlike the elastic rough surface contact analysis, for the elastic-plastic rough surface contact models no numerical solution is available to validate the developed models. That is why an experiment has been performed using a four-wire resistance measurement method, and has been compared with the elastic-plastic rough surface contact models. The same aluminum surface that was used for the elastic rough surface contact analysis has been used for the elastic-plastic rough surface contact analysis. The methods to calculate surface properties for this surface have been described while analyzing the elastic rough surface contact analysis in Section 5.2.

5.4.1 Methodology

5.4.1.1 Statistical Model (Spherical Asperity Models + Different PDFs)

Greenwood Distribution and Jackson-Green Elastic-plastic Model (Greenwood Distribution and JG Elastic-plastic Model)

This statistical model has been developed using Jackson-Green spherical asperity model (Eqs. (2.64-2.67, and 2.70) and PDF that varies as a function of surface asperity height and geometric curvature, $PDF = f\left(\xi^{h*}, k_g^{h*}\right)$ (Eq. (4.31)). When employed this asperity model in the statistical model, instead of constant radius of curvature, varying radius of geometric curvature $\left(\text{i. e. } R = \frac{1}{k_g}\right)$ has been used. The value of geometric curvature in the asperity model and in the PDF will vary over the integration limit of the statistical model. To predict the rough surface contact area and contact force, Eqs. (5.5) and (5.6) have been used. The Jackson-Green single asperity model has been developed such that, when normalized interference (Eqs. (2.61) and (2.64)) for the single asperity is less than 1.9, the contact is effectively elastic, and Eqs. (2.64) and (2.65) have been used to calculate the single asperity contact area and force. When the normalized interference is greater than 1.9, the contact is elastic-plastic, and Eqs. (2.64, 2.66-2.67, and 2.70) have been used to predict the contact area and force. Then from these single asperity models, rough surface contact area and contact force have been calculated. For this statistical model, interference, ω or $\delta = \xi^h - d.\,\eta^h$ and $\emptyset(\xi^{h*})$ have been calculated using Eqs. (4.22) and (4.31), respectively.

Nayak-Bush Distribution and Jackson-Green Elastic-plastic Model (Nayak-Bush Distribution and JG Elastic-plastic Model)

This rough surface contact model has been developed using the same methodology as Greenwood distribution and JG elastic-plastic model. However, there are very few differences between these

two rough surface contact models. For this statistical model, the rough surface contact area and force have been determined from Eqs. (5.7) and (5.8). Instead of the radius of geometric curvature, the radius of mean curvature $\left(\text{i. e. } R = \frac{1}{k_m}\right)$ has been used in the asperity model. When employed, the asperity model and $PDF = f(\xi^{h*}, k_m^{h*})$ in the statistical model, the integral defines the value of mean curvature. For the PDF, Eq. (4.24) has been used.

5.4.1.2 Statistical Model (3D Periodic Sinusoidal Asperity Models + Different PDFs) Greenwood Distribution and 3D Sinusoidal Elastic-plastic Model (Greenwood 3D Sinusoidal Elastic-plastic Model)

This statistical model has been developed using 3D periodic elastic and elastic-plastic sinusoidal asperity model (Eqs. (2.43), (2.46-2.48), (2.90-2.99)) and $PDF = f\left(\xi^{h*}, k_g^{h*}\right)$ (Eq. (4.31). The rough surface contact area and contact force have been calculated employing Eqs. (5.5) and (5.6). Instead of using a constant radius of curvature in the asperity model and PDF, a varying radius of geometric curvature $\left(\text{i. e. } R = \frac{1}{k_g}\right)$ has been used. For this statistical model, $\Delta = \xi^h$, λ is calculated from $R = 1/k_g^h = \frac{\lambda^2}{4\pi^2\Delta} => \lambda = \sqrt{\frac{1}{k_g^h} \times 4\pi^2\Delta}$ (see Eq. (5.4)) and interference is, $\delta = \xi^h - d$. In the rough surface contact model, the integral defines the value of geometric curvature. Eq. (2.93) has been used to determine whether the surface will deform elastically or elasto-plastically. This equation gives the value of critical amplitude, Δ_c. If the value of Δ is less than Δ_c, the contact will deform elastically and the same method that has been used for the Greenwood 3D sinusoidal elastic model (see Section 5.2.1.2) has been applied. When the value of Δ is greater than Δ_c, contact will deform elasto-plastically. For the elastic-plastic contact, contact force has been determined using Eq. (2.94) and Eq. (2.99). Eq. (2.99) is the equation for surface separation (i.e. gap), which is a function of normalized pressure. For the elastic case, it was easy to simplify the equation of contact

gap. However, for the elastic-plastic case, normalized pressure cannot be determined from Eq. (2.99) algebraically. Therefore, the Bisection method has been used to numerically solve that equation and to calculate $\frac{\bar{p}}{p_{ep}^*}$ ($\bar{p}$ is the nominal pressure and $p_{ep}^*$is the pressure required to completely flatten the sinusoidal asperity when it deforms elastic-plastically). The surface separation for Eq. (2.99) can be calculated using $G = \frac{d}{\xi^h}$, where d is the separation between the mean of the contacting rough surface or separation between the mean of the composite surface and rigid flat. Once the value of $\frac{\bar{p}}{p_{ep}^*}$ is known, contact area for the single asperity is calculated using Eqs. (2.95-2.98). η^h and $\emptyset\left(\xi^{h*}, k_g^{h*}\right)$ have been calculated using Eq. (4.22) and (4.31), respectively.

Nayak-Bush Distribution and 3D Sinusoidal Elastic-plastic Model (Nayak-Bush 3D Sinusoidal Elastic-plastic Model)

This rough surface contact model has been developed using the same methodology as the Greenwood 3D sinusoidal elastic-plastic model. However, for this statistical model, rough surface contact area and force can be determined from Eqs. (5.7) and (5.8). Instead of the radius of geometric curvature in the asperity model and PDF, the radius of mean curvature $\left(\text{i. e. } R = \frac{1}{k_m}\right)$ has been used. The PDF has been calculated using Eq. (4.24), which is a function of asperity height and mean curvature. λ is calculated from $R = 1/k_m^h = \frac{\lambda^2}{4\pi^2\Delta} => \lambda = \sqrt{\frac{1}{k_m^h} \times 4\pi^2\Delta}$.

5.4.1.3 Statistical Model (Axisymmetric Sinusoidal Asperity Models + Different PDFs)

Greenwood Distribution and Axisymmetric Sinusoidal Elastic-plastic Model (Greenwood Axisymmetric Sinusoidal Elastic-plastic Model)

This statistical model has been developed using the axisymmetric sinusoidal asperity model (Eqs. (3.5, 3.9, (3.13-3.17)) and the Greenwood PDF that is a function of asperity height and geometric curvature, $PDF = f\left(\xi^{h*}, k_g^{h*}\right)$. Contact area and force for this rough surface contact model has been determined using Eqs. (5.5) and (5.6). These two equations are a function of single asperity models for contact area and contact force respectively. To implement the model, it is important to determine whether for a particular displacement, $\delta = \xi^h - d$, the contact is in the elastic or in the elastic-plastic range. For this purpose, the critical value of amplitude, Δ_c has been determined from Eq. (3.11). For this rough surface contact model, $\Delta = \xi^h$, surface separation, $G = \frac{d}{\xi^h}$ and λ is calculated from, $R = 1/k_g^h = \frac{\lambda^2}{4\pi^2\Delta} => \lambda = \sqrt{\frac{1}{k_g^h} \times 4\pi^2\Delta}$. If the value of $\frac{\Delta}{\Delta_c}$ is less than 1, the contact is elastic, if greater than 1, the contact is elastic-plastic. For $\frac{\Delta}{\Delta_c} < 1$, $1 \leq \frac{\Delta}{\Delta_c} \leq 12.2$, $12.2 \leq \frac{\Delta}{\Delta_c} \leq 48.8$, and $48.8 \leq \frac{\Delta}{\Delta_c} \leq 243.96$, Eqs. (3.9), (3.15), (3.16) and (3.17) have been applied respectively, to determine the contact force for the single asperity (see Section 3.3.1.3, and 3.3.2.3 for detail equations). p_e^* and p_{ep}^* have been determined using Eq. (3.4) and Eq. (3.12), respectively. From the single asperity contact force, using Eq. (5.6), contact force for the rough surface has been determined. Once the value of normalized pressure is known, for $\frac{\Delta}{\Delta_c} < 1$, $1 \leq \frac{\Delta}{\Delta_c} \leq 12.2$, and $12.2 \leq \frac{\Delta}{\Delta_c} \leq 243.96$, Eqs. (3.5), (3.13), and (3.14) have been employed, respectively, to determine the contact area for the single asperity (see Section 3.3.1.2 and 3.3.2.2 for detail

equations). Then from the single asperity contact area, contact area for the rough surface has been determined using Eq. (5.5).

Nayak-Bush Distribution and Axisymmetric Sinusoidal Elastic-plastic Model (Nayak-Bush Axisymmetric Sinusoidal Elastic-plastic Model)

The method to develop this rough surface contact model is similar to the Greenwood axisymmetric sinusoidal elastic-plastic model. However, contact area and contact force for the rough surface contact model have been determined using Eq. (5.7) and (5.8). In the asperity model and PDF, varying radius of mean curvature $\left(\text{i. e. } R = \frac{1}{k_m}\right)$ has been used and the integral defines the value of mean curvature. The PDF $\emptyset(\xi^{h*}, k_m^{h*})$, is determined using Eq. (4.24). λ for the asperity model is determined from, $R = 1/k_m^h = \frac{\lambda^2}{4\pi^2\Delta} => \lambda = \sqrt{\frac{1}{k_m^h} \times 4\pi^2\Delta}$.

5.4.1.4 Elastic-plastic Contact Analysis Using the Multiscale Method

Multiscale Jackson and Green Elastic-plastic Model (Multiscale JG Elastic-plastic Model)

Jackson and Streator have developed this multiscale model (see Section 4.3.1.4). However, in their model it has been assumed that there are two asperities in the nominal area of the asperity and nominal area of the asperity is λ^2. In this dissertation, it has been assumed that when employing Jackson-Green model in the multiscale model, there is only one asperity in the nominal area of the asperity and the nominal area for the asperity is $\pi\left(\frac{\lambda_i}{2}\right)^2$, where λ_i is the wavelength at a particular scale. This is done to match the methodology of the axisymmetric sinusoidal asperity model. The flow chart for multiscale modeling is given in Fig. 5.1. Using the method described in the flow chart, after calculating the force on each asperity, F_{asp}, if, $F_{asp} < F_c$, then Eq. (2.65) has been used

to calculate single asperity contact area. If $F_{asp} > F_c$ then Eqs. (2.66-67, 2.70) have been used to calculate the contact area. When using Eq. (2.67), the normalized interference cannot be determined algebraically, which is necessary to calculate asperity contact area. Therefore, Eq. (2.67) is numerically solved using the Bisection method. F_c has been calculated using Eq. (2.63). Eq. (4.73) is used to calculate total contact area at each scale, *i*.

Multiscale Axisymmetric Sinusoidal Elastic-plastic Model

This multiscale model has been developed using the axisymmetric sinusoidal asperity model. The methodology is the same as described in the flow chart (Fig. 5.1). After calculating the contact force on each asperity, the nominal pressure on each asperity will be, $\bar{p} = \frac{F_{asp}}{\pi\left(\frac{\lambda_i}{2}\right)^2}$. From this nominal pressure, normalized pressure for the elastic contact, $\frac{\bar{p}}{p_e^*}$ (see Eq. (3.4) for p_e^*) and for the elastic-plastic contact, $\frac{\bar{p}}{p_{ep}^*}$ (see Eq. (3.12) for p_{ep}^*) have been calculated which is necessary to calculate contact area.

- When $\frac{\Delta}{\Delta_c}$ is less than 1, the contact is elastic and the multiscale modeling method using elastic axisymmetric sinusoidal asperity model described in Section 5.2.1.5 has been used.
- When $1 \leq \frac{\Delta}{\Delta_c} \leq 12.2$, the contact is elastic-plastic. If $\frac{\bar{p}}{p_{ep}^*} < 0.0005$, then previously described multiscale model using the Jackson-Green asperity model. Otherwise, Eq. (3.13) has been used to calculate the contact area and if $\frac{\bar{p}}{p_{ep}^*} > 1$, it has been set to 1.
- When $12.2 \leq \frac{\Delta}{\Delta_c}$, if $\frac{\bar{p}}{p_{ep}^*} < 0.001$, then the previously described multiscale model using the Jackson-Green asperity model. Otherwise, Eq. (3.14) has been used to calculate the contact

area and if $\frac{\bar{p}}{p_{ep}^*} > 1$, it has been set to 1. (see Section 3.3.1.2 and 3.3.2.2 for details why to use different ranges for calculating contact area).

5.4.2 Results and Discussions for the Elastic-plastic Rough Surface contact Modeling

Fig. 5.24 shows the contact behavior for different elastic-plastic statistical models. The figure shows that, the PDF using either the mean or the geometric curvature do not significantly affect the results. All the contact pressure-area curves found from different statistical models qualitatively show almost the same behavior; however quantitatively there is large difference (see Fig. 5.24).

Fig. 5.25 shows the comparison of the statistical models (plotted in Fig. 5.24) with the multiscale model. Fig. 5.25(a) and (b) show that, the multiscale-axisymmetric sinusoidal elastic-plastic model almost coincides with the Greenwood distribution and JG elastic-plastic model and Nayak-Bush distribution and JG elastic-plastic model. At the very low load region, as shown in Fig. 5.25(c), these three models almost coincide with each other. A linear contact pressure-area relationship has been observed for all the multiscale models except the multiscale axisymmetric sinusoidal model. Apparently, from Fig. 5.25(a)-(b) it seems that the contact pressure-area relationship for the multiscale axisymmetric sinusoidal model is a straight line. When the curve has been plotted separately in Fig. 5.26(a), with the increase of the contact pressure, zigzag behavior has been observed in the curve. The possible reasons of this phenomenon will be described now. According to Chapter 3, $\frac{\Delta}{\Delta_c}$ is one of the important parameters, which controls the elastic-plastic contact behavior.

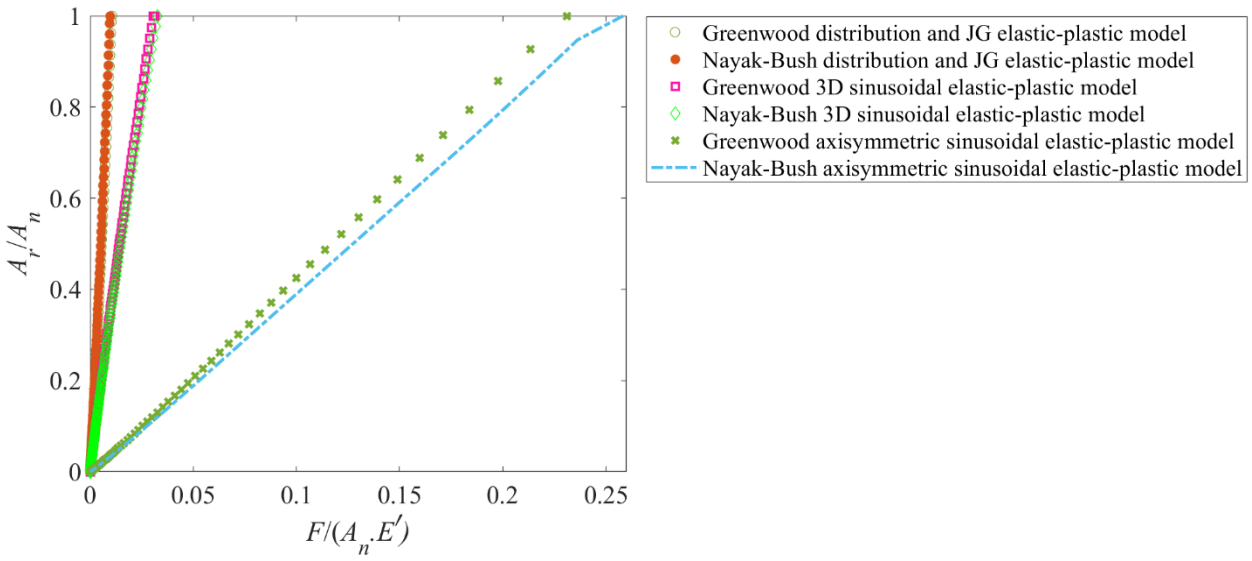

(a)

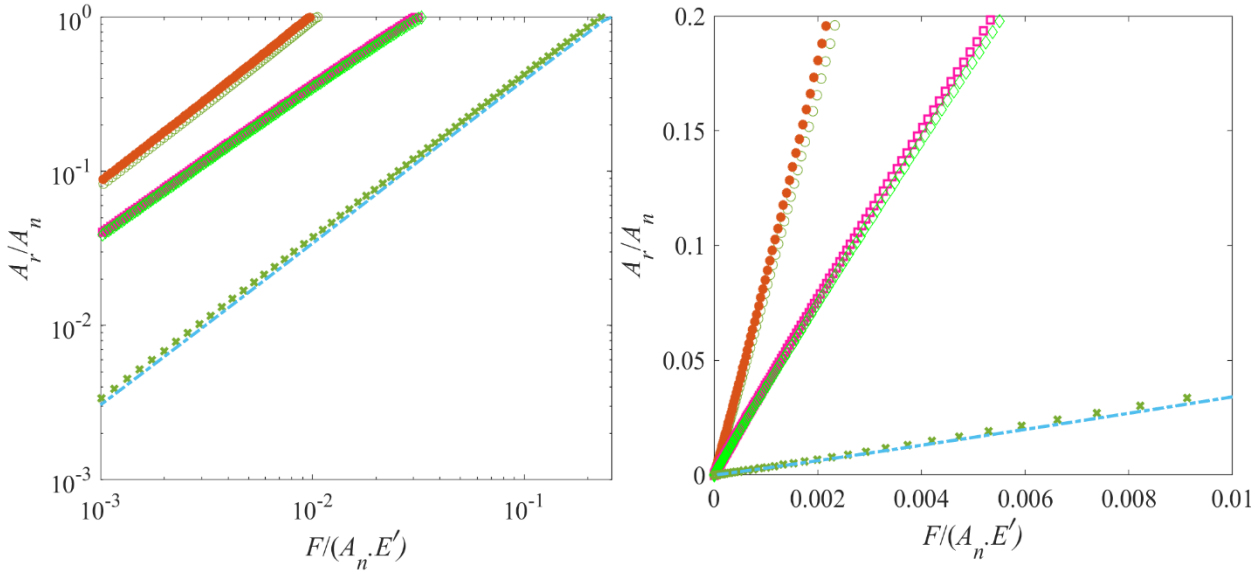

(b)

(c)

Fig. 5.24 Comparison among different elastic-plastic statistical models (a) full-scale plot (b) log-log plot (c) magnified view of Fig. 5.24(a).

Fig. 3.17(a) clearly shows that how the change in $\frac{\Delta}{\Delta_c}$ values change the shape of the contact pressure-area relation for the single asperity. When the $\frac{\Delta}{\Delta_c}$value is small, the contact behavior is more like elastic and the shape of the curve is concave upward. With the increase of this value, gradually the contact pressure-area curve becomes linear and with further increase of $\frac{\Delta}{\Delta_c}$, the shape of the curve gradually becomes convex upward. This change in shape of the contact pressure-area relation for the single asperity has an important effect when this asperity model has been employed into the multiscale model. A small numerical experiment has been performed to investigate the zigzag behavior. The contact area equations (Eqs. (3.5), (3.13-3.14)) of the axisymmetric involve lot of details. That is why to investigate the probable reason of zigzag, a very simple relationship has been assumed, $A = P^a$, where P is the normalized pressure ($\frac{\bar{p}}{p_e^*}$ for the elastic case and $\frac{\bar{p}}{p_{ep}^*}$for the elastic-plastic case) and a is the parameter which is defining the shape of the curve. This equation can express approximate similar shape as the contact pressure-area relationship for the axisymmetric sinusoidal asperity model. When $a < 1$, the shape of the curve is convex upward, when $a = 1$, the shape of the curve is linear and when $a > 1$, the shape of the curve is concave upward. Then this simple equation has been employed in the multiscale axisymmetric sinusoidal elastic-plastic model (see Section 5.4.1.4). Everything else has been kept same in this rough surface contact model. Fig. 5.26(b) shows the multiscale rough surface model plots for different values of a in the equation, $A = P^a$. The plot shows the effect of a i.e. the shape of the single asperity contact area equation on the contact pressure-area relation of the rough surface contact. For both Hertz and 3D periodic sinusoidal asperity model the contact pressure-area curve for single asperity is convex upward i.e. in the simplified equation, $A = P^a$, $a < 1$. That is why when these two models have been employed in the multiscale model no zigzag have been observed in the

multiscale rough surface contact model. From Fig. 5.15(d), the $\frac{\Delta}{\lambda}$ ratio for this rough surface varies from approximately 10^{-3} to 7×10^{-3}. Therefore for the properties mentioned in Table-5.4; the $\frac{\Delta}{\Delta_c}$ value will vary from 0.61 to 4.26 approximately. From Fig. 5.26(b), for these values of $\frac{\Delta}{\Delta_c}$, the shape of the curve is concave upward, i.e. $a > 1$. That is why in the multiscale axisymmetric sinusoidal model zigzag has been observed.

Like elastic rough surface contact model, for the elastic-plastic rough surface contact there is no results available for validation (deterministic elastic-plastic rough surface contact modeling can work as a validation tool, Section 4.3.2.3). It is therefore difficult to determine which model is better predicting the elastic-plastic contact behavior. That is why an experiment has been performed to determine the electrical contact resistance. Electrical contact resistance has also been determined using the developed statistical and multiscale elastic-plastic contact models. Then experimental and numerical models have been compared to predict which elastic-plastic rough surface contact model can better predict the elastic-plastic contact behavior.

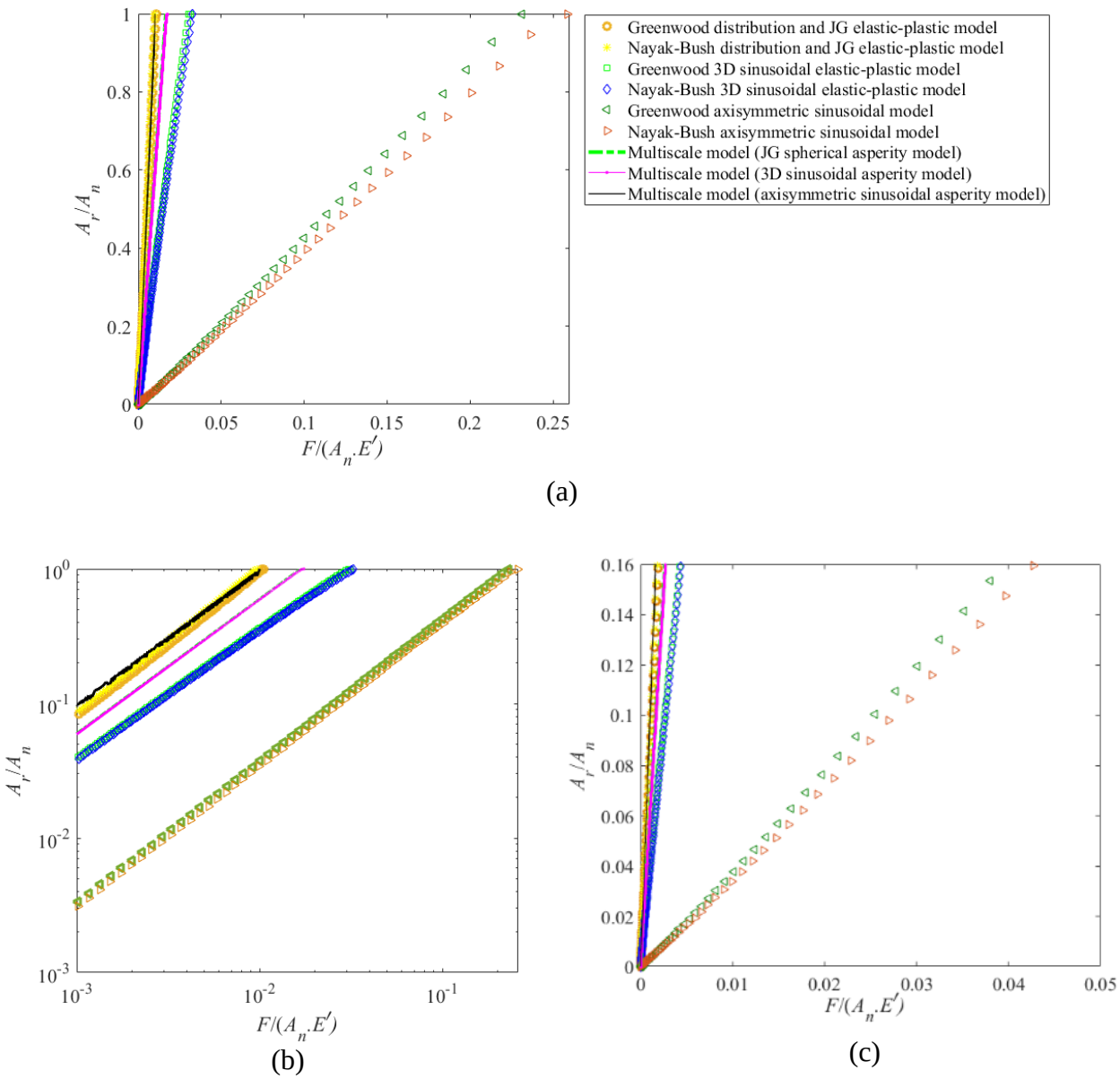

Fig. 5.25 Comparison among different elastic-plastic statistical and multiscale models (a) full-scale plot (b) log-log plot, (c) magnified view at the low load region.

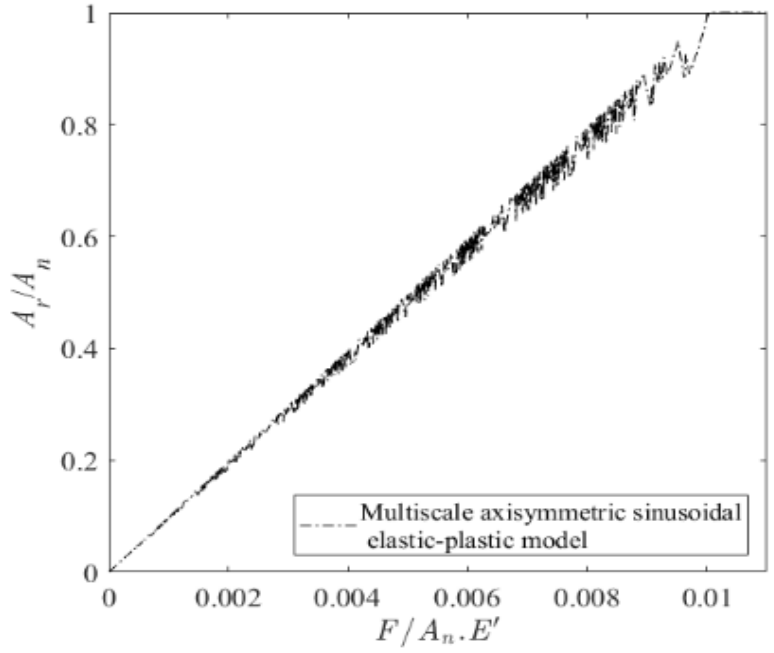

(a)

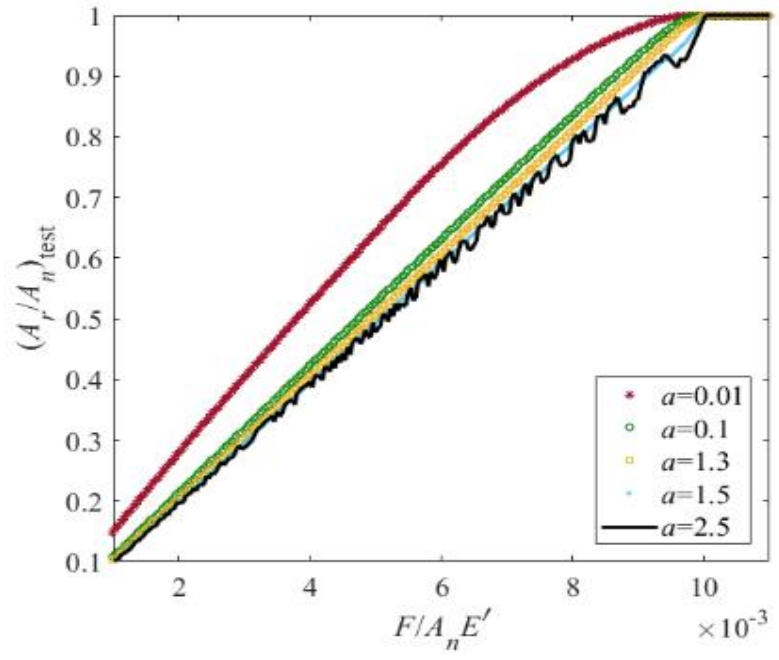

(b)

Fig. 5.26 (a) Contact pressure area curve using multiscale axisymmetric sinusoidal elastic-plastic model (b) Numerical experiment of the shape of the contact area equation, $A = P^a$, on the multiscale model.

5.5 Determination of the Electrical Contact Resistance and Comparison with the Experiment

5.5.1 Determination of Electrical Contact Resistance Using Numerical Models

Determination of Electrical Contact Resistance Using Statistical Method

The electrical contact resistance at the interface of the two mating parts can be determined using both statistical and multiscale models. The original GW model was developed to determine the electrical contact resistance (Eq. (4.96)). However, the model does not consider the statistical distribution of the asperity radius of curvature with the surface asperity height and used Gaussian height distribution in the statistical model. Electrical contact resistance is a function of contact radius. Therefore, similar to the statistical models developed to determine the contact area, the statistical model to determine the contact resistance, i.e. Eq. (4.96) can be modified to the following:

$$\frac{1}{E_{cr}} = \frac{A_n \eta^h}{\psi \sqrt{m_0^h m_4^h}} \int_d^\infty \int_0^\infty \frac{2a(\xi^h, k_g^h)}{\rho} \varphi\left(\xi^{h*}, k_g^{h*}\right) dk_g^h \, d\xi^h \tag{5.11}$$

$$\frac{1}{E_{cr}} = \frac{A_n \eta^h}{\psi \sqrt{m_0^h m_4^h}} \int_d^\infty \int_0^\infty \frac{2a(\xi^h, k_m^h)}{\rho} \varphi(\xi^{h*}, k_m^{h*}) dk_m^h \, d\xi^h \tag{5.12}$$

The above two equations are valid if the mating parts are made of the same material. ρ is the resistivity of the contacting rough surfaces. However, if the mating parts are made of different materials, then $\frac{2a(\xi^h, k_g^h)}{\rho}$ in Eq. (5.11) has to be replaced with $\frac{4a(\xi^h, k_g^h)}{\rho_1 + \rho_2}$, and $\frac{2a(\xi^h, k_m^h)}{\rho}$ in Eq. (5.12) has to be replaced with $\frac{4a(\xi^h, k_m^h)}{\rho_1 + \rho_2}$. ρ_1 and ρ_2 are the resistivity of the mating parts. For the experiment, the contact between two aluminum surfaces have been measured, so $\frac{2a}{\rho}$ has been used. In Eq. (5.11) and (5.12), E_{cr} is the total contact resistance, A_n is the nominal area. The areal

asperity density, η^h and allevation factor, ψ can be calculated using Eq. (4.22) and (4.97) respectively. When using the equation of allevation factor, A_r is the real rough surface contact area for a particular surface separation, *d*. $\varphi\left(\xi^{h*}, k_g^{h*}\right)$ and $\varphi(\xi^{h*}, k_m^{h*})$ have been calculated employing Eq. (4.31) and (4.24) respectively. *a* is the contact radius for a single asperity. Using the similar methodology as described for the statistical models to calculate contact area, the following steps have been performed to calculate asperity contact radius:

- For JG single asperity model, when employing in either Eq. (5.11) or (5.12), the contact resistance for a single asperity is, $\frac{1}{E_{asp}} = \frac{2\sqrt{\left(\frac{area_{asp}}{\pi}\right)}}{\rho}$. E_{asp} is the contact resistance for the single asperity and $area_{asp}$is the area of the single asperity. The nominal area for this asperity is, $\pi\left(\frac{\lambda}{2}\right)^2$. There is only one asperity in $\pi\left(\frac{\lambda}{2}\right)^2$. The method to calculate the single asperity contact area using the Jackson Green model is described in Section 5.4.1.1. Then using the single asperity contact resistance, the total contact resistance at the interface of the mating surfaces has been calculated employing Eq. (5.11) or (5.12) at a particular surface separation, *d*.
- When the 3D periodic sinusoidal elastic-plastic asperity model has been used, whether employing in Eq. (5.11) or (5.12), the contact resistance for the asperity is, $\frac{1}{E_{asp}} = \frac{2\sqrt{\left(\frac{area_{asp}}{2\pi}\right)}}{\rho}$. The nominal area for this asperity is λ^2 and there are two asperities in the nominal area. After calculating the asperity contact resistance (see Section 5.4.1.2), the total contact resistance has been calculated using Eq. (5.11) or (5.12) at a particular surface separation, *d*.

- For the axisymmetric sinusoidal elastic-plastic asperity model, the method to calculate total contact resistance at the interface of two contacting surfaces is the same as the JG single asperity model. Only the equation to calculate $area_{asp}$ is different and has been calculated using the method described in Section 5.4.1.3.

Determination of Electrical Contact Resistance Using Multiscale Method

To calculate the contact resistance at the interface of the two mating parts using the multiscale method, the following steps have been performed:

- When employing the JG single asperity model, after calculating the total contact area for each scale, *i*, from Eq. (4.73) and Eq. (4.74) (see the flow chart in Fig. 5.1), the contact radius, a_i for each of the asperities at scale, *i*, will be, $\frac{A_i}{A_{i-1}} = \frac{N_i \cdot \pi {a_i}^2}{N_i \cdot \pi \left(\frac{\lambda_i}{2}\right)^2} \Rightarrow\gg a_i = \sqrt{\left(\frac{\lambda_i}{2}\right)^2 . \frac{A_i}{A_{i-1}}}$. Here, A_i and $A_{i-1}$are the total real contact area at scale, *i* and *i*-1 respectively. The real contact area for scale, *i*-1 is the nominal contact area for scale, *i*. In addition, it has been assumed that all the asperities at a particular scale are identical. The method to calculate the total real contact area for each scale, A_i has described in Section 5.4.1.4. Now summing over all the considered scales (found from spectral analysis), the total resistance for the entire surface in contact has been calculated using, $E_{cr} = \sum_{i=1}^{i_{max}} \frac{\rho}{2a_i} \frac{1}{N_i} \psi_i$, where, i_{max} is the maximum number of scales found from the spectral analysis, N_i is the number of asperities at each scale and can be calculated using, $N_i = \eta A_{i-1} = \frac{1}{\pi \left(\frac{\lambda_i}{2}\right)^2} A_{i-1} . \psi_i$ has been calculated using Eq. (4.105).

- ❖ Determination of the contact resistance using the multiscale model developed employing the 3D periodic sinusoidal asperity model has been described in detail in Section 4.3.2.2.
- ❖ For the axisymmetric sinusoidal elastic-plastic asperity model, the method to calculate the total contact resistance at the interface is the same as the JG single asperity model. Only the equation to calculate the total real contact area for each scale, A_i is different and has been calculated using the method described in Section 5.4.1.4**.**

5.5.2 Experimental determination of the Electrical Contact Resistance

An experimental study has been performed to measure the contact resistance between two aluminum surfaces (aluminum alloy (6061-T6511B)). The material properties of the aluminum surface has been given in Table-5.4. The experimental results later will be compared with the electrical contact resistance for the same sample contact found from the numerical methods. To perform the experiment, two aluminum cylinders (1.75-inch diameter and 3-inch length) of the same sizes have been chosen. The surfaces of the samples have been machined such that, the surfaces are flat and even everywhere. They are polished so that surface roughness is relatively isotropic. The sample surfaces have been made flat to avoid the effect of surface curvature on the contact resistance value as much as possible, i.e. the surfaces are considered to be nominally flat. Fig. 5.27 is showing the spectral analysis of the rough surfaces. Table 5.7 and Table 5.8 are showing the average RMS surface roughness at different locations of the surfaces of the samples. From the spectral analysis and the tables, it is clear that both of the surfaces are almost identical. According to the spectral analysis of the surface, the maximum $\frac{\Delta}{\lambda}$ value for the rough surface is less than 0.003. From the analysis of Chapter-3, to mitigate the effect of sample thickness on the contact behavior, the substrate length has to be at least 1.2 mm when the $\frac{\Delta}{\lambda}$ value is 0.005 (see

Section 4.2.4 to see the methodology to calculate $\frac{\Delta}{\lambda}$). Besides that, the wires are connected to the sample using bolts. To avoid the effect of the stress generated by bolt on the contact, the final length of both of the samples have been chosen as 3 inches. The main objective of this experiment is to observe the change in the contact resistance value with the change in applied force.

To measure the contact resistance, a high precision digital multimeter-Keithley 2001 has been used, shown in Fig. 5.28. The resolution of the multimeter is 1μΩ for resistance measurement, i.e. the smallest change the multimeter can detect is 1μΩ. Fig. 5.29(a) is showing the schematic of the sample set-up to the multimeter. The four-wire resistance method has been used to measure the contact resistance between the aluminum surfaces. If very small resistances or small changes in resistance measurement are required, this method is used. Fig. 5.29 (b) is showing how the multimeter connects the sample internally, if the sample is connected to the multimeter according to the schematic of Fig. 5.29(a). To measure the contact resistance, multimeter passes a very small amount of current through the circuit. However, for small currents the voltage drop at the wires and connections can be significant with respect to the desired contact resistance value. In the Four-wire resistance method, two wires are used to create one path and another two wires to create another path. One of the paths where contact resistance will be measured, the multimeter connects to the voltmeter with high internal resistance. As current always chooses the path which has less resistance, the current will not go through the wire that is connected to the internal voltmeter. Therefore, there will be little voltage drop across that path. All the voltage drop will be in the path through which current is passing. Then, from the known current value and the voltage drop across the sample contact, the multimeter measures the contact resistance and it is more accurate. The bulk resistance of the aluminum sample is in the range of μΩ (from hand calculation, $R = \rho \frac{L}{A}$ where ρ is the resistivity of the material, L is the length and A is the nominal cross-sectional area

of the sample) and the measured contact resistance is in the range of mΩ, which is why bulk resistance has been neglected during the calculation of the contact resistance.

The mechanical load has been applied on the sample using a UMT (Universal Material Tester) machine, shown in Fig. 5.30. This machine can perform a wide range of tests. However, for this experiment it has only been used to control the applied force very precisely according to the pre-programmed routine. This routine can be written and modified according to the user requirement. The load sensor that has been used to apply the force on the sample, can measure force from 0.2 to 20N with 1 mN resolution. The following steps are performed to measure the contact resistance:

- At the beginning of the experiment, both of the samples have been cleaned using methanol first and then acetone.
- Then the UMT machine has been centered so that during the experiment, it applies the force evenly on the sample.
- One of the samples is connected to the pin-holder of the UMT-machine using a fixture, shown in Fig. 5.30 and another sample is set on the fixed lower stage of the machine. Then the sample is connected to the multimeter as shown in the Fig. 5.29(a).
- To apply force using the UMT machine, the program is set such that, at the beginning of the experiment, the UMT machine will bring the two samples in contact and then gradually the force will be increased. Five different forces, 12N, 14N, 16N, 18N and 20N have been applied using the machine. To get a stable measurement for the contact resistance, each of the forces has been kept constant for 10 minutes and before another load step begins, contact resistance has been measured.
- The whole process has been repeated twice and an average of the two measurement is calculated to determine the resistance between the aluminum surfaces.

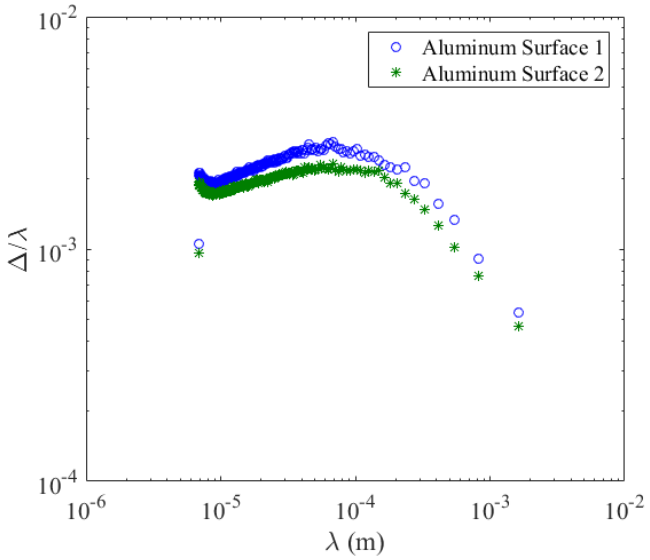

Fig. 5.27 Average spectral analysis of Aluminum surfaces.

Table-5.7 Average RMS surface roughness (R_q) of Aluminum surface-1 at different locations

R_q(µm) East	R_q(µm) North	R_q(µm) Origin	R_q(µm) South	R_q(µm) West
1.47	1.43	1.72	1.71	2.2

Table-5.8 Average RMS surface roughness (R_q) of Aluminum surface-2 at different locations

R_q(µm) East	R_q(µm) North	R_q(µm) Origin	R_q(µm) South	R_q(µm) West
1.47	1.25	1.43	1.36	1.63

Fig. 5.28 High precision Keithley-2001 digital multimeter.

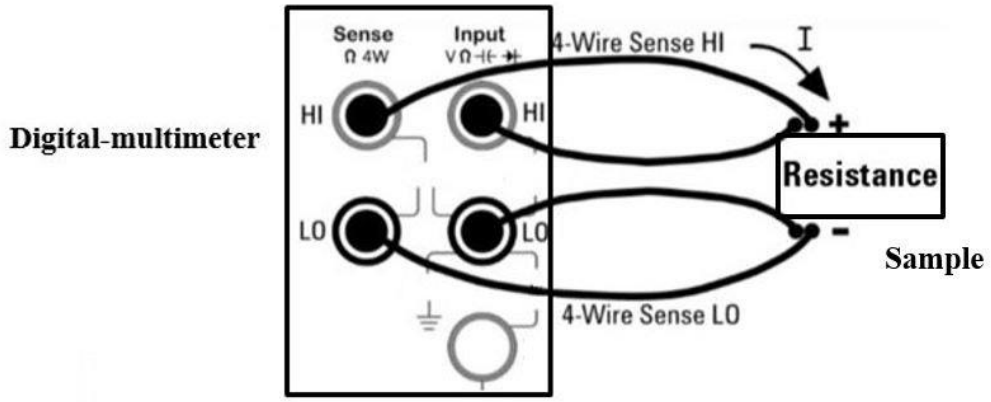

(a)

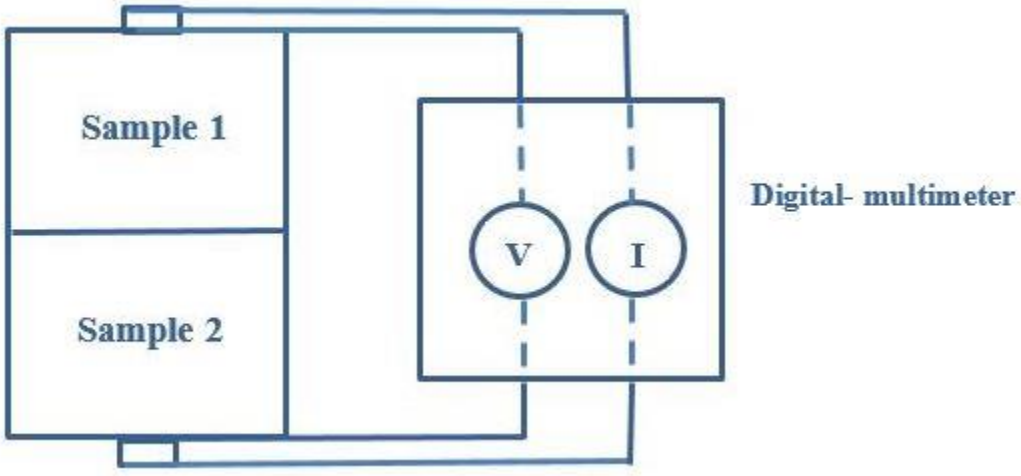

(b)

Fig. 5.29(a) Schematic set-up of the sample to the multimeter, (b) Set-up inside the multimeter.

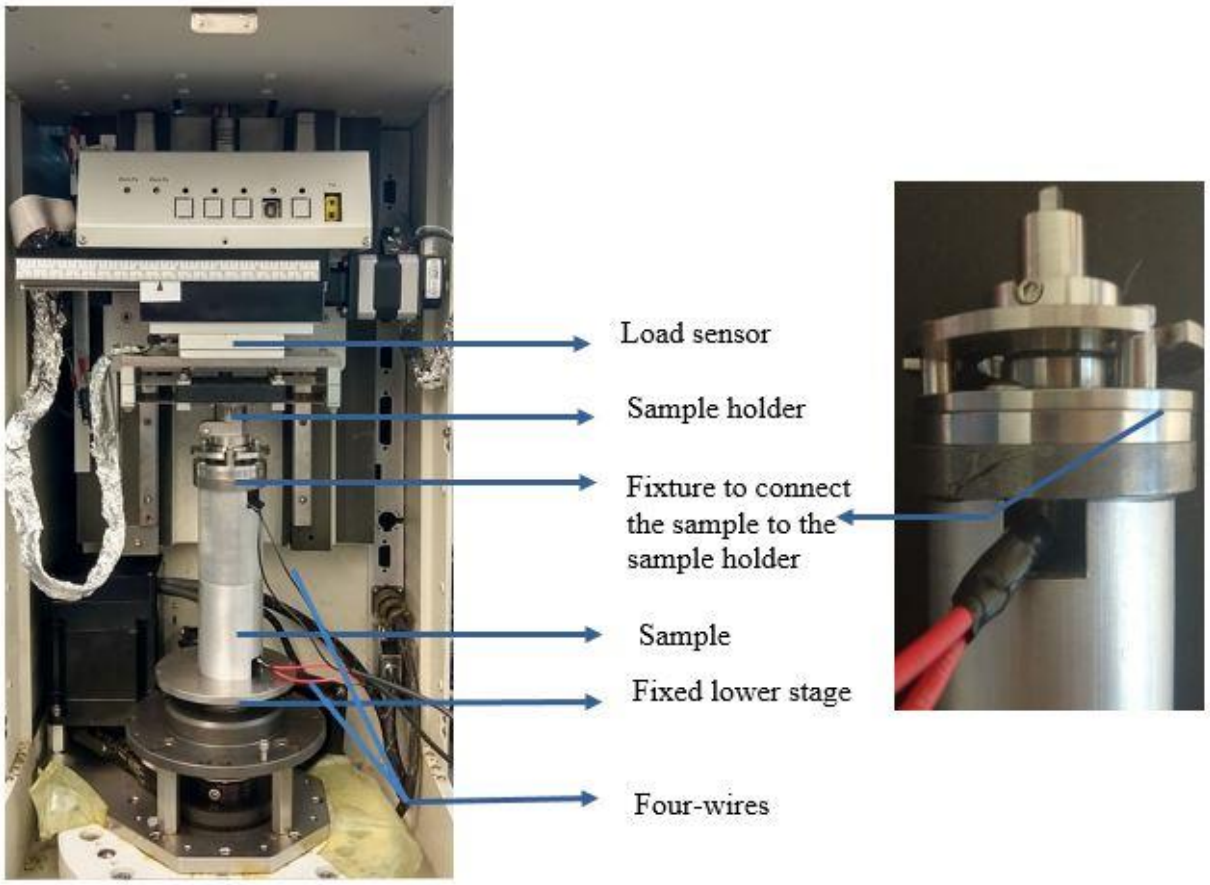

Fig. 5.30 Sample set-up in the UMT machine.

5.6 Results and Discussion of the Contact Resistance Values Measured Using Numerical Method and Experiment

Fig. 5.31 is showing the comparison of the electrical contact resistance (ECR) values found from the experiment (Section 5.5.2) and the numerical models (Section 5.5.1). The comparison shows that like the contact area (Fig. (5.24) and (5.25)), for the ECR also when geometric/mean curvature have been varied in the asperity model and PDF, the statistical models developed using geometric and mean curvature show very similar rough surface contact predictions. The Greenwood axisymmetric sinusoidal elastic-plastic model and Nayak-Bush axisymmetric sinusoidal elastic-

plastic model show the best agreement with the experimental results. The experimental measurements and numerical results found from these two statistical models are in the same order of magnitude and the amount of error varies from 0% to 25%. All the other statistical models show more than one order of magnitude difference with the experimental results. With the increase of normalized force, ECR found from the statistical models continuously decreases as expected. There are several possible reasons that are causing the difference among the developed analytical models and experiment. One of the reasons is, for the developed models the material properties are assumed exact, however, material properties are not constant and continuously changing with scale. Jackson et al. [16] has performed a detail investigation to observe the effect of scale dependent properties on the electrical contact resistance. Another possible reason is the formation of oxides when measuring the contact resistance between the aluminum surfaces. Although precaution has been taken before performing the experiment, generally oxides form very easily on the metal electrical contact. From previous research works it has been found that in many cases, oxide formation may increase the electrical contact resistance significantly.

Like the statistical model, with the increase of the normalized pressure, the ECR found from the multiscale model also continuously decreases up to the complete contact. The Multiscale JG elastic-plastic model show closer agreement with the experimental results than the statistical models developed using JG and 3D periodic sinusoidal elastic-plastic asperity model and the multiscale model developed using 3D periodic sinusoidal asperity model and axisymmetric sinusoidal elastic-plastic model. However, it still show several orders of magnitude difference with the experimental results and the statistical models that show good agreement with the experiment. A zigzag behavior has been observed in the ECR values found from the multiscale axisymmetric sinusoidal elastic-plastic model. The reason is the same as described for the zigzag behavior

observed in the contact pressure-area relation (see Section 5.4.2). Multiscale models developed using 3D periodic sinusoidal asperity model and axisymmetric sinusoidal asperity model coincide with each other at the small deformation region, however with the increase of pressure gradually diverge from each other.

For the numerical models of the rough surface contact, electrical contact resistance has been determined for a wide range of forces. However, the experiment has been performed for a small range of forces (10N to 20N). If force is lower than 10 N, it is difficult to establish proper contact between the samples and as a result, it is difficult to obtain a stable result. For the higher value of forces, contact resistance values decrease. To measure very small values of resistance the experiment needs to be designed in a different way. One of the ways can be by passing high current through the circuit. However high current will cause high temperature at the contact and will enhance the probability of oxide formation. Therefore, contact resistance measurement for a wider range of forces requires the consideration of different factors and complicated experimental design, which has not been performed here. Few examples of small ECR determination using experimental methods have been described briefly in the Chapter 1. Although an extensive experiment has not been performed in this dissertation, the performed experiment gives an idea about which model better predicts the elastic-plastic contact. However, further experimental or deterministic modeling of the elastic-plastic rough surface contact is necessary to confirm which model is better and if any modifications are necessary in the developed models to consider the whole range of contact. Jackson and his research group [17-19] have performed a detail investigation on the deterministic elastic-plastic rough surface contact modeling. Although in none of these two works mesh convergence has been obtained, these works show the path of further development of the

deterministic models which could help to validate these elastic-plastic models for a wide range of deformation.

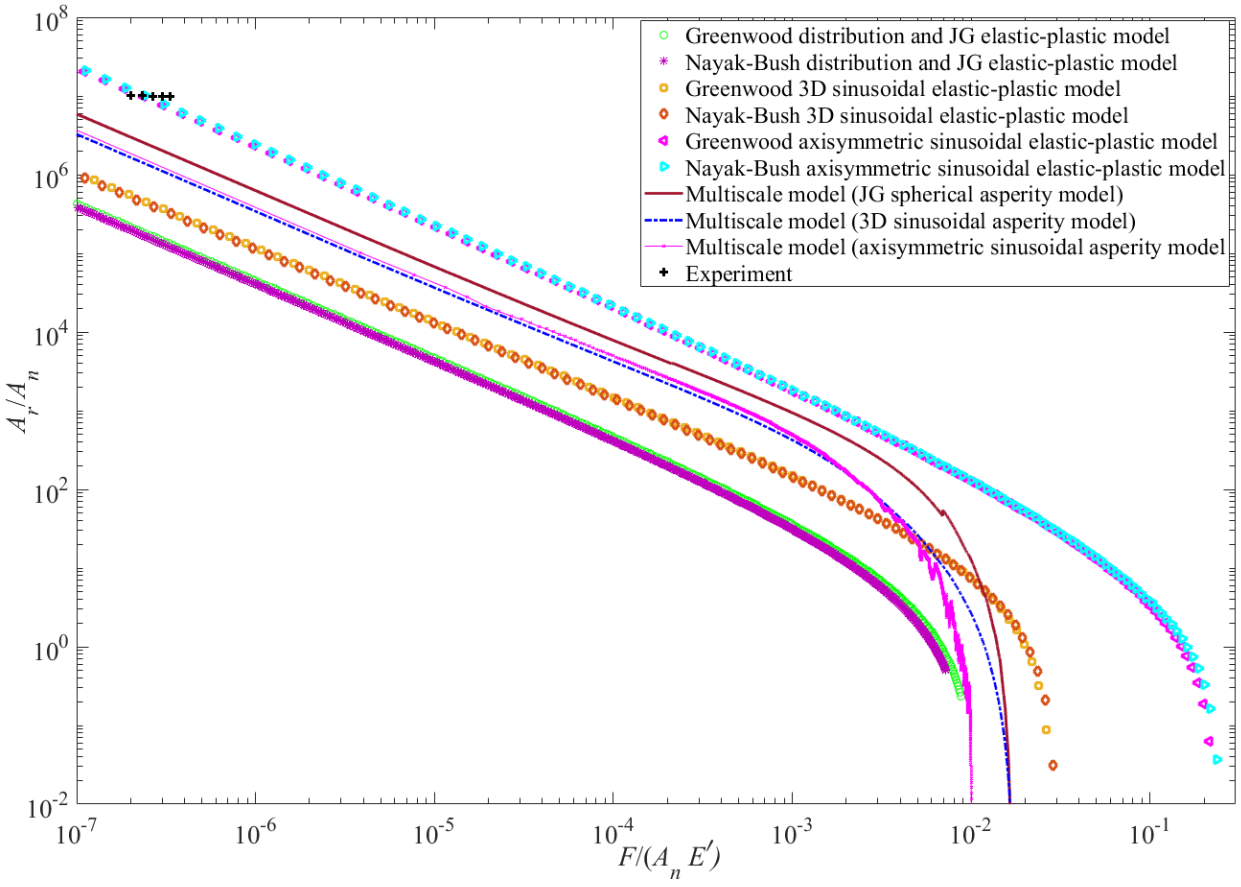

Fig. 5.31 Comparison of the contact resistance values (ECR) found from the numerical analysis of the rough surface interface and experiment.

5.7 Summary

This chapter focuses on the development and validation of the elastic and elastic-perfectly plastic rough surface contact models and determination of the electrical contact resistance (ECR) employing the developed numerical models. By analyzing the developed models the following conclusions can be drawn:

- The probability distribution function (PDF) of the asperities of the rough surface has a significant effect on the rough surface contact prediction. The Gaussian distribution is very popular to use in the rough surface contact models irrespective of the surface nature. However, the analysis in this chapter shows that it is more reliable to use the PDFs that consider the change in the asperity mean or geometric curvature to predict the contact behavior whether the surface is self-affine fractal or Gaussian or both.
- One of the important assumptions in contact mechanics modeling is that, spherical/ elliptical/ mildly elliptical asperity models can predict the contact behavior well at the small deformation region and when the asperity interaction becomes important due to the large deformation, a sinusoidal asperity model needs to be employed in the rough surface contact models. This chapter shows that in several cases statistical models developed using spherical/ mildly elliptical model show very close agreement with the statistical models developed using 3D periodic sinusoidal asperity. Therefore, the assumption is not completely true. However, for the large deformation it is more reliable to use the statistical models developed using a sinusoidal asperity model.
- Several new elastic rough surface contact models have been developed by modifying the previous statistical and multiscale models. For the purpose of validation, these models have been compared with the BEM results and Persson's model. The comparison with the BEM result shows that Greenwood 3D sinusoidal elastic model in conjunction with the Greenwood crack model (developed for the nearly complete contact by Xu and Jackson based on fracture mechanics) can predict the whole range of contact.
- The Greenwood axisymmetric sinusoidal model and Nayak-Bush 3D sinusoidal model show good agreement with the Persson model. The comparison between Greenwood

axisymmetric model and Persson's model shows that Greenwood axisymmetric sinusoidal model can predict from very small deformation region to the heavy deformation region (0.1-70% of the total area for the analysis shown in this chapter). Nayak-Bush 3D sinusoidal model both qualitatively and quantitatively shows very good agreement with the Persson model from small area to near the complete contact. For the analysis shown in this chapter, when the real contact area is ~12-90% of the total area, the difference between the Nayak-Bush 3D sinusoidal and the Persson model is less than %10. Persson's model is derived assuming the self-affine fractal rough surface. However, the Greenwood axisymmetric sinusoidal model and the Nayak-Bush 3D sinusoidal model can be applied for both the self-affine rough surfaces and real surface contact predictions.

- Several new elastic-plastic rough surface contact models have been suggested by modifying the previous statistical and multiscale models.
- Electrical contact resistance has been predicted using these newly developed models and compared with experimental results. The comparison suggests that, Greenwood axisymmetric sinusoidal elastic-plastic model and Nayak-Bush axisymmetric sinusoidal elastic-plastic model can better predict the elastic-plastic rough surface contact behavior. However, further validation of the elastic-plastic rough surface contact models is important to ensure that these two models can predict the whole range of contact.

References

1. Xu, Y. (2017). Statistical Models of Nominally Flat Rough Surface Contact. PhD Dissertation, Auburn University.
2. Xu, Y., & Jackson, R. L. (2017). Statistical models of nearly complete elastic rough surface contact-comparison with numerical solutions. Tribology International, 105, 274-291.
3. Yu, N., & Polycarpou, A. A. (2002). Contact of rough surfaces with asymmetric distribution of asperity heights. J. Trib., 124(2), 367-376.B
4. Yu, N., & Polycarpou, A. A. (2004). Combining and contacting of two rough surfaces with asymmetric distribution of asperity heights. J. Trib., 126(2), 225-232.
5. Yu, N., & Polycarpou, A. A. (2004). Extracting summit roughness parameters from random Gaussian surfaces accounting for asymmetry of the summit heights. J. Trib., 126(4), 761-766.
6. Tayebi, N., & Polycarpou, A. A. (2004). Modeling the effect of skewness and kurtosis on the static friction coefficient of rough surfaces. Tribology international, 37(6), 491-505.
7. Lee, C. H., Eriten, M., & Polycarpou, A. A. (2010). Erratum:" Application of Elastic-Plastic Static Friction Models to Rough Surfaces With Asymmetric Asperity Distribution"[Journal of Tribology, 2010, 132 (3), p. 031602]. Journal of Tribology, 132(4), 047001.
8. Hu, S., Huang, W., Shi, X., Peng, Z., & Liu, X. (2019). Mechanism of bi-Gaussian surface topographies on generating acoustic emissions under a sliding friction. Tribology International, 131, 64-72.
9. Chu, N. (2018). The Effect of Asperity Geometry on Elastic-plastic Statistical and Multi-scale rough Surface Contact Models. Masters Thesis, Auburn University.

10. Wilson, W. E., Angadi, S. V., & Jackson, R. L. (2010). Surface separation and contact resistance considering sinusoidal elastic–plastic multi-scale rough surface contact. Wear, 268(1-2), 190-201.
11. Greenwood, J. A. (2006). A simplified elliptic model of rough surface contact. Wear, 261(2), 191-200.
12. Saha, S., & Jackson, R. L. (2020). Elastic and elastic-perfectly plastic analysis of an axisymmetric sinusoidal surface asperity contact. Tribology-Materials, Surfaces & Interfaces, 14(1), 1-21.
13. Jackson, R. L., & Streator, J. L. (2006). A multi-scale model for contact between rough surfaces. Wear, 261(11-12), 1337-1347.
14. Greenwood, J. A. (2015). On the almost-complete contact of elastic rough surfaces: The removal of tensile patches. International Journal of Solids and Structures, 56, 258-264.
15. Johnson, K. L., Greenwood, J. A., & Higginson, J. G. (1985). The contact of elastic regular wavy surfaces. International journal of mechanical sciences, 27(6), 383-396.
16. Jackson, R. L., Crandall, E. R., & Bozack, M. J. (2015). Rough surface electrical contact resistance considering scale dependent properties and quantum effects. Journal of Applied Physics, 117(19), 195101.
17. Wang, X., Xu, Y., & Jackson, R. L. (2018). Theoretical and finite element analysis of static friction between multi-scale rough surfaces. Tribology Letters, 66(4), 146.
18. Wang, X., An, B., Xu, Y., & Jackson, R. L. (2020). The effect of resolution on the deterministic finite element elastic-plastic rough surface contact under combined normal and tangential loading. Tribology International, 144, 106141.

19. An, B., Wang, X., Xu, Y., & Jackson, R. L. (2019). Deterministic elastic-plastic modelling of rough surface contact including spectral interpolation and comparison to theoretical models. Tribology International, 135, 246-258.

Chapter 6

Literature Review on Electrical Contact Resistance at the High temperature Conditions of the Interface

6.1 Introduction

Electrical contact resistance (ECR) models in Chapter 5 have been developed using the Holm [1] and Cooper et al. [2] equations. The Holm equation for contact resistance works well when the electrical current through the asperity or "a-spot" is sufficiently small so that effect of heat generation due to electrical transport does not have a considerable effect on the ECR [3]. However, for the cases, when high density current passes through the "a-spots" at the interface, significant Joule-heating occurs due to current constriction and as a result a thermal gradient develops across the constriction. Holm's ECR equation does not hold for such cases as the high thermal gradient across the constriction complicates the relationship among contact voltage, current, and size of the "a-spots". In this chapter, the previous research works that have been done to analyze the electrical contact for high temperature cases are discussed.

6.2 Analytical, Numerical Models and Experimental Investigation

Surface roughness exists over a wide range of scales. Therefore, for the same current conditions, the current density at different scales of asperities are different. As a result, heat generation due to the current constriction may soften or even melt some of the asperities and can cause significant damage to the contact. Most of the analytical models developed to consider electrical contact behavior for such cases assume that the outer surfaces of the conductors are thermally insulated from the external environment [3-4]. Because the phenomena of softening and melting are highly

localized and happens so quickly, the heat transfer due to convection and radiation can be simply neglected [3-4].Under such circumstances, the electric and thermal current flow lines follow the same path. That is why electrical and thermal contact resistance (ECR and TCR) problems are very similar. Kohlarausch [3-6] derived the following equation to relate the voltage drop and maximum temperature at the contact interface:

$$V = \left\{2\int_{T_1}^{T_m} \lambda_1 \rho_1 dT\right\}^{1/2} + \left\{2\int_{T_2}^{T_m} \lambda_2 \rho_2 dT\right\}^{1/2} \tag{6.1}$$

In the above equation, T_1 and T_2 are the bulk temperatures, λ and ρ are thermal conductivity and electrical resistivity of the conductors. The subscripts 1 and 2 refers to the conductor materials that are in contact. $V$is the contact voltage and T_m is the maximum temperature. If the contacting parts are made of same materials, the above equation becomes [3]:

$$V = 2\left\{2\int_{T_1}^{T_m} \lambda \rho dT\right\}^{1/2} \tag{6.2}$$

Both Eq. (6.1) and (6.2) consider the change in electrical resistivity and thermal conductivity with temperature. However, these two equations work well if resistivity and thermal conductivity change linearly with temperature. If the change in these two properties with the temperature is very small, Eq. (6.2) reduces to the following voltage-temperature relation [3]:

$$V = \{8\lambda\rho(T_m - T_1)\}^{1/2} \tag{6.3}$$

where, $(T_m - T_1)$ is defined as the super temperature. The amount by which the temperature at any point in the region of constricted flow exceeds that of the bulk metal is called the super temperature [3-4]. In general, connectors are designed such that super temperature does not exceed 1℃-3℃ under extreme operating conditions [3].

Wiedemann and Franz [3] provided a law, which states that with temperature the variations of the thermal conductivity, λ and electrical resistivity, ρ of metals are related by the following expression:

$$\lambda\rho = LT \tag{6.4}$$

where L is the Lorentz constant ($2.45 \times 10^{-8}\, V^2K^{-2}$) and T is the absolute temperature. Now using Eq. (6.4), Eq. (6.2) can be modified to the following relation [3, 7]:

$$V^2 = 4L(T_m^2 - T_1^2) \tag{6.5}$$

Although the Wiedemann and Franz law is applicable for a wide range of metals and conditions, the law is not true universally [3, 8-10].

Greenwood and Williamson [11] performed an extensive experimental investigation to observe the influence of current on the contact between solids. The experiment was performed between clean surfaces of gold and for different periods, magnitudes and shapes of current pulses. According to the experimental analysis, for a given conductor and current value there is a certain critical degree of constriction through which it will just pass without causing any permanent change in the contact region. However, if the contact resistance is greater than this critical contact resistance, a change will occur and the resistance of the constriction will be lowered until it becomes equal to the critical value associated with the current. Results also show that the shape and duration of the current pulse (10 μs to 10 ms) does not have any effect on the electrical contact behavior. Generally, temperature generated due to current flow at the interface reaches thermal equilibrium within a very short period (a few μs or less) [4, 12]. However, if sufficiently high current passes through the contact within a short period of time, mechanical collapse may occur. Experimental results were also compared with the mathematical formulation provided by

Kohlarausch for the voltage drop at the interface and maximum temperature of the conductor (Eq. (6.1)). Comparison with the Kohlarausch equation shows that, melting or collapse of the gold interface will occur below the melting temperature of gold at 950°C and 0.38 V, although there is no evidence of any sudden change in the physical properties of gold near this temperature. However, the experiment shows clear evidence that some of the gold had reached the melting point, 1063°C at that voltage. As the Kohlarausch law cannot describe the contact behavior adequately at high temperatures, Greenwood and Williamson [4] later explained this phenomenon and provided an analytical solution for the maximum temperature and the total current passing through the contact. According to Greenwood and Williamson, it is more revealing to describe the temperature as a function of "cold resistance", R_c of the conductor and the total current, I than the contact voltage and maximum temperature. "Cold resistance" is the resistance presented to a current small enough not to cause any appreciable rise in the temperature at any point. According to [4], the maximum contact temperature, T_m and the current, I are related by the following expression [3-4]:

$$R_c I = \rho_{1,0} \int_{T_1}^{T_m} \left\{ 2 \int_{T}^{T_m} \lambda_1 \rho_1 dT \right\}^{-1/2} \lambda_1 dT + \rho_{2,0} \int_{T_2}^{T_m} \left\{ 2 \int_{T}^{T_m} \lambda_2 \rho_2 dT \right\}^{-1/2} \lambda_2 dT \qquad (6.6)$$

In the above equation, $\rho_{1,0}$ and $\rho_{2,0}$ are the "cold" resistivities or resistivities at the bulk temperature. Temperature dependent thermal conductivity and electrical resistivity can be expressed using $\rho = \rho_{1,0}(1 + \alpha T)$ and $\lambda = \lambda_{1,0}(1 - \beta T)$. β and α are temperature co-efficients of thermal conductivity and electrical resistivity respectively. According to the analysis, if both α and β are positive there is an upper limit of the product $R_c I$, if the value of $R_c I$ is less than the upper limit, then whatever value of current passes through the contact there will be no permanent change of the contact and thermal equilibrium or a steady state condition will be achieved after

current passes through the contact. However, if R_cI is greater than the upper limit of the product ($\overline{R_cI}$) then no thermal equilibrium is possible anymore and with the increase of current, the temperature will continuously rise until the melting and collapse of the interface. The upper limit of the R_cI is given by the following equation [4]:

$$\overline{R_cI} = 2\left[\frac{\lambda_0\rho_0}{\alpha}\right]^{1/2}\left[\left(1+\frac{\beta}{\alpha}\right)sec^{-1}\left(1+\frac{\alpha}{\beta}\right)^{1/2}-\left(\frac{\beta}{\alpha}\right)^{1/2}\right] \tag{6.7}$$

When the contact reaches the upper limit, the maximum temperature and voltage at the contact will be [4]:

$$\overline{\theta_m} = \frac{1}{\alpha}\left[\left(1+\frac{\alpha}{\beta}\right)^{1/2}-1\right] \tag{6.8}$$

$$\overline{U} = 2\left[\frac{\lambda_0\rho_0}{\beta}\right]^{1/2} \tag{6.9}$$

According to Greenwood and Williamson's explanation, instead of a melting voltage as assumed in the Kohlarausch equation, the collapse ought to have been correlated with the creation of potential differences greater than the value, $\overline{U}$. The Kohlarausch melting voltage cannot explain the experimental phenomena, but $\overline{U}$ can as no thermal equilibrium is possible above the voltage , $\overline{U}$.

Employing $\rho = \rho_{1,0}(1+\alpha T)$ and $\lambda = \lambda_{1,0}(1-\beta T)$ where β is sufficiently smaller than α, Slade [3] simplified the equation provided by Greenwood and Williamson [4] and obtained the following approximated form of the integral in Eq. (6.6):

$$\int_{T_1}^{T_m}\left\{2\int_{T}^{T_m}\lambda\rho dT\right\}^{-1/2}\lambda dT' = \left(\frac{\lambda_0}{\{\alpha-\beta\}\rho_0}\right)^{1/2}\left\{\frac{\alpha}{\alpha-\beta}\right\}cos^{-1}\left(\frac{1+\{\alpha-\beta\}T_1}{1+\{\alpha-\beta\}T_m}\right)$$

Using the above integration approximation for the monometallic contact and Holm equation for the cold contact resistance, $R_c = \frac{\rho}{2a}$, Eq. (6.6) has been further simplified to the following [3]:

$$I = 4a\left(\frac{\lambda_0}{\{\alpha-\beta\}\rho_0}\right)^{1/2}\left\{\frac{\alpha}{\alpha-\beta}\right\}cos^{-1}\left(\frac{1+\{\alpha-\beta\}T_1}{1+\{\alpha-\beta\}T_m}\right) \tag{6.10}$$

where, a is the contact radius of the "a-spot".

If the thermal conductivity and resistivity do not change with temperature much, then Eq. (6.6) for total current can be modified to the following [4]:

$$I = 2\frac{\rho_0}{R_0}[2(T_m - T_{Bulk})\lambda_0/\rho_0]^{1/2} \tag{6.11}$$

In the above equation, λ_0 and ρ_0 are the thermal conductivity and electrical resistivity at bulk temperature. R_0 is the "cold resistance" and can be calculated as shown previously using the Holm equation. Previously described R_c and R_0 are the same resistance.

Bansal and Streator [12] performed an experiment to investigate the behavior of electrical contact resistance for copper against copper and aluminum against aluminum sphere on flat contacts as a function of the current through the interface. According to the experimental results [12], when the current passing through the contact is small, voltage gradually increases with the increase of current. Due to the increase in voltage, temperature also increases, which increases the resistivity of the contact material. However, because of thermal induced softening, the contact area increases and as a result the contact resistance decreases. In this way, with the increase of current, the contact resistance decreases and contact voltage gradually increases until the voltage saturation zone is reached. At the voltage saturation zone, with the increase of current, contact voltage does not increase anymore and stays almost constant. During the experiment, the contact force was kept

constant. According to the discussion in the paper, the change in temperature at the voltage saturation zone was small; therefore, due to temperature the change in hardness was negligible. Although the voltage, load and hardness were almost constant at the voltage saturation zone, with the increase in current, the contact resistance was continuously decreasing in the experiment. Viscoplastic creep has been declared as being responsible for the voltage saturation phenomenon and a continuous decrease in the contact resistance in the voltage saturation zone. No quantitative model has been developed in the work; however, a semi-quantitative analysis of viscoplastic creep has been performed to explain the result at the voltage saturation zone. The semi-quantitative analysis shows that once the temperature reaches a sufficiently high value, the strain rate becomes exceedingly rapid. Therefore, a small increase in temperature can cause large increases in contact area, which reduces contact resistance such that contact voltage does not increase further. The contact voltage becomes almost constant because at this temperature, the rate of decrease of contact resistance becomes sufficient to overcome the effects of increasing the current [12].

Gatzsche et al. [13] performed an FEA to investigate the electro-thermal performance of high power electrical connector contact elements. The contact points in these high power connectors are heated up rapidly when current pulses pass through the contact and thus soften and contact resistance drops instantly. The results show that for an accurate measurement of the contact temperature and contact resistance drop, a more complex multi-physics model is necessary. Later Israel et al. [13] extended the work considering the effect of temperature dependent hardness and observed the influence of contact temperature, contact hardness and contact force on the contact resistance. However, for the temperature dependent hardening modeling the conventional way to model material has not been used. In the work [13], hardness has been expressed as a function of contact resistance, contact force and electromagnetic force. Contact resistance has been measured

experimentally as a function of current. Electromagnetic force has been calculated analytically for different values of current. Later, employing the electromagnetic force, applied contact force and experimentally measured contact resistance, temperature dependent hardness has been determined. Although, the FEM predicted results were close to the experimental results, however, this method of temperature dependent hardening modeling needs further validation to determine the accuracy and applicability.

Bottauscio [14] explored heat generation and thermal diffusion in an electrical contact under short circuit condition by solving thermal, electrical and mechanical couple-field contact problem using Finite Difference Method (FDM). Temperature dependent resistivity and stress-strain behavior were considered in the numerical modeling. Experimentally determined and numerically predicted contact voltage were compared and showed good agreement with each other. Monnier et al. [7] solved a very similar problem later using FEM. For the analysis of the electrical contact of Cu and Ag, temperature dependent Young's modulus, hardness, electrical and thermal conductivities, specific heat, and coefficient of thermal expansion were considered during FE modeling and all the multi-physics phenomena were coupled. The influence of the current intensity, the contact force, and the duration of the current flow on the potential distribution have been studied in the work and comparison of the FEA showed good agreement with experimental results. However, this study did not provide any generalize results of the model for use in other applications.

Hennessy [15] employed the finite element approach to model the coupled thermo-electro-mechanical contact between an elastic hemisphere pressed against an elastic half-space. Several different materials- Au, Pt, Rh, Ru, Ti and OFHC Cu have been investigated in the work to observe the effect of electric potential or current values on the contact area. However, plasticity and temperature dependent material properties have not been considered during FE modeling. The

results show a distinct difference in contact behavior between force-controlled and displacement-controlled modeling in the presence of an applied electrical potential. For the force-controlled contact, the contact area does not increase significantly and shows good agreement with the Hertz model. For the displacement-controlled contact, contact area increases more rapidly and a new relationship is provided to accurately predict the behavior of the contact. As the model does not consider the temperature dependent material properties, the contact voltage-temperature relationship matched well with Eq. (6.3).

Ghaednia et al. [16] performed a very similar multi-physics analysis as Hennessy [15] between a spherical asperity and cylindrical block, however, the plasticity effect has been considered in the model and both the materials in contact are deformable in nature. The analysis shows that the plasticity and thermal expansion significantly effect on the contact area, temperature and contact resistance and must be considered for an accurate estimation of the contact behavior. The effect of thermal expansion co-efficient at different values of interference have also been analyzed and it has been found that at small interferences, the effect of the thermal expansion is significant. Therefore, at small interferences, if high current passes through the contact it may cause softening and even melting of the contact. However, with the increase of interference the effect of thermal expansion gradually decreases. A non-dimensional parameter has been provided in the work which predicts whether thermal expansion is important or not for a given spherical electrical contact.

6.3 Summary

- When small current passes through the contact and heat generation due to current is small, the Holm equation for contact resistance, $\frac{\rho}{2a}$ is applicable and voltage drop across the contact will be $\frac{\rho}{2a}I$. However, when high current passes through the interface, contact

voltage drop, temperature and resistance need to be determined in a different way. This chapter discussed the theories and numerical models available to analyze the contact behavior for high temperature cases.

- The Kohlarausch law for contact voltage and maximum temperature cannot explain the phenomena for high temperature cases. Greenwood and Williamson elucidated the phenomena and provided an analytical solution for total current and maximum temperature at the interface.
- Kohlarausch defined the contact voltage at maximum temperature as the melting voltage. From the experiment and theoretical analysis, Greenwood and Williamson showed that it is not the melting voltage as defined by Kohlarausch but critical voltage after which any increase in current will cause the damage of the surface. For any conductor and particular value of current, there is a critical voltage. When current passes through the interface, if the generated voltage across the contact is less than the critical voltage there will be no permanent change in the contact. However, if the voltage across the contact crosses the critical voltage no thermal equilibrium is possible and with the increase of current, the contact may collapse.
- For high temperature electrical contact cases, it is important to consider temperature dependent electrical and material properties as electrical and material properties change continuously with temperature.

References

1. Holm, R. (1958). Elektrische Kontakte/Electric Contacts Handbook. Springer, Berlin Heidelberg, Berlin, Heidelberg.
2. Cooper, M. G., Mikic, B. B., & Yovanovich, M. M. (1969). Thermal contact conductance. International Journal of heat and mass transfer, 12(3), 279-300.
3. Slade, P. G. (Ed.). (2017). Electrical contacts: principles and applications. CRC press.
4. Greenwood, J. A., & Williamson, J. B. P. (1958). Electrical conduction in solids II. Theory of temperature-dependent conductors. Proceedings of the Royal Society of London. Series A. Mathematical and Physical Sciences, 246(1244), 13-31.
5. Greenwood, J. A., & Williamson, J. P. (1966). Contact of nominally flat surfaces. Proceedings of the royal society of London. Series A. Mathematical and physical sciences, 295(1442), 300-319.
6. Holm, R. (2000). Electric Contacts, Theory and Applications. Springer-Verlag Berlin Heidelberg Germany.
7. Monnier, A., Froidurot, B., Jarrige, C., Meyer, R., & Testé, P. (2005). A mechanical, electrical, thermal coupled-field simulation of a sphere-plane electrical contact. In Proceedings of the Fifty-First IEEE Holm Conference on Electrical Contacts, 2005, 224-231. IEEE.
8. Craven, G. T., & Nitzan, A. (2020). Wiedemann–Franz Law for Molecular Hopping Transport. Nano Letters, 20(2), 989-993.
9. Gloos, K., Mitschka, C., Pobell, F., & Smeibidl, P. (1990). Thermal conductivity of normal and superconducting metals. Cryogenics, 30(1), 14-18.

10. Lee, S., Hippalgaonkar, K., Yang, F., Hong, J., Ko, C., Suh, J., ... & Dames, C. (2017). Anomalously low electronic thermal conductivity in metallic vanadium dioxide. Science, 355(6323), 371-374.
11. Bowden, F. P., & Williamson, J. B. P. (1958). Electrical conduction in solids I. Influence of the passage of current on the contact between solids. Proceedings of the Royal Society of London. Series A. Mathematical and Physical Sciences, 246(1244), 1-12.
12. Bansal, D. G., & Streator, J. L. (2011). Voltage saturation in electrical contacts via viscoplastic creep. Acta materialia, 59(2), 726-737.
13. Israel, T., Schlegel, S., Großmann, S., Kufner, T., & Freudiger, G. (2019, September). Modelling of Transient Heating and Softening Behaviour of Contact Points During Current Pulses and Short Circuits. In 2019 IEEE Holm Conference on Electrical Contacts (pp. 9-18). IEEE.
14. Bottauscio, O., Crotti, G., & Farina, G. (1993). Numerical analysis of heating transient of electric contacts under short-circuit conditions. IEEE transactions on components, hybrids, and manufacturing technology, 16(5), 563-570.
15. Hennessy, R. P. (2014). Exploration of hot switching damage and damage mechanisms in MEMS switch contacts. Doctoral dissertation, Northeastern University Boston.
16. Ghaednia, H., Rostami, A., & Jackson, R. L. (2012). The influence of thermal expansion and plastic deformation on a thermo-electro mechanical spherical asperity contact. In 2012 IEEE 58th Holm Conference on Electrical Contacts (Holm), 1-7. IEEE.

Chapter 7

Coupled Electrical-thermal-mechanical Analysis of the Electrical Contact Considering the Temperature Dependent Material Properties

7.1 Introduction

Closed form solutions are available to analyze the electrical contact behavior for high temperature cases. However, most of these analytical solutions consider only the change in the electrical resistivity and thermal conductivity with temperature. Very few works have been done on the multi-physics modeling of the electrical contact considering temperature dependent plasticity of the material. This chapter will focus on the coupled electro-thermo-mechanical analysis of electrical contact considering temperature dependent yield strength, thermal conductivity, and resistivity of the material from room temperature to the melting temperature. Coupled electro-thermo-mechanical analysis means the mechanical, electrical and thermal phenomena are coupled during the modeling, as a result, all phenomena will be affected by temperature variations and every phenomenon has an effect on all others. Young's modulus generally does not change much with temperature [1] that is why a constant value of Young's modulus has been used in the multiphysics modeling. The thermal expansion coefficient has also been considered during modeling. The objectives of this chapter are the following:

- To analyze the effect of temperature dependent material properties on the contact behavior separately and to compare with the case when all the properties vary with temperature at the same time. This comparison will help to evaluate which temperature dependent properties are controlling the contact behavior and should be considered during the electrical contact behavior analysis.

- To validate the developed FEM comparing with the available theories and experimental studies.
- To observe the effect of voltage or current on the contact area, resistance and temperature.
- To discern the change in contact behavior when contact is frictionless and perfectly bonded in nature. Frictionless and perfectly bonded contact are the two limiting traction cases. In many of the practical cases, contact either behaves very close to the frictionless case or perfectly bonded case and in some cases, contact behavior may fall in between these two ideal conditions. That is why both of these cases have analyzed in this Chapter.

7.2 Methodology

7.2.1 Finite Element Modeling (FEM) of the Multi-physics Model

For the multi-physics contact modeling, the contact between two axisymmetric sinusoidal asperities with an amplitude equal to 0.004 mm and a wavelength equal to 1 mm has been developed and analyzed. Commercial finite element software ANSYS has been used for the modeling. According to the analysis of Chapter 3, when the amplitude to wavelength ratio equals 0.004, if the substrate length at the base of the asperity is 1.2 mm then there will be no effect of substrate length on the contact stress distribution and the developed model can be considered as a semi-infinite solid. That is why for the electro-thermo-mechanical contact analysis, a substrate length of 1.2 mm has been considered at the base of both of the asperity models. Fig. 7.1 is showing the schematic diagram of the contact between two sinusoidal asperity models. For meshing the entire sinusoidal surface and its substrate, PLANE 223, an 8 node axisymmetric element with mid-nodes, is used. CONTA 172, a 3-node contact element with a mid-node and TARGE 169, a 2-node target element are used to model the contact between the asperities.

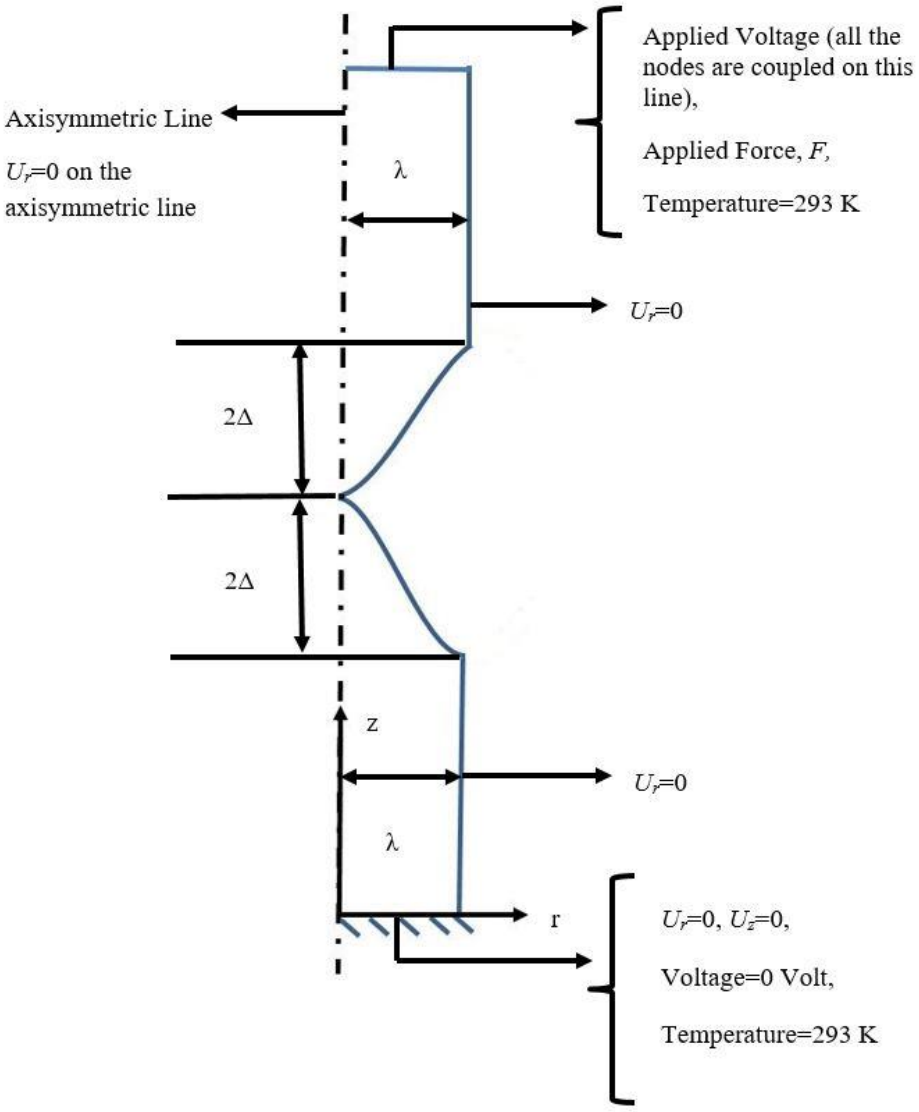

Fig. 7.1 Schematic diagram and boundary conditions applied on the coupled multi-physics model.

The asperity models have identical geometries, mesh and material properties; and therefore the surface of either of them can be chosen as “contact” surface and “target” surface. For the contact modeling, the Augmented Lagrangian contact algorithm has been used.

Numerical experiments have been performed to determine the suitable values of contact stiffness and penetration tolerance for the frictionless and perfectly bonded cases. From the simulation results, it has been found that an ANSYS contact stiffness factor equal to 5.0 and a penetration tolerance factor equal to 0.1 are adequate to make the solution independent of contact element stiffness and to enforce almost zero penetration at the contact for the frictionless cases modeled in this work. For the perfectly bonded cases, a stiffness factor equal to 100.0 and penetration tolerance equal to 0.1 have been used. Besides that, for both the frictionless and perfectly bonded cases, contacts have been modeled such that contact stiffness will be updated during each iteration based on the current mean stress of the underlying elements. For the thermal contact conductance (TCC), all the models use a value equal to $10^7 \frac{W}{m^2K}$, as further increase in the TCC value showed negligible difference in the contact behavior. It has been assumed during modeling that, all the dissipated electric energy will convert into Joule heating and the heat will be equally distributed between the two contacting surfaces. The boundary conditions that are considered during modeling are:

- The temperature at the base of the substrate of the asperities is $293°K$ i.e. 20℃.
- Zero voltage has been applied at the base of the substrate of the bottom asperity. The nodes at the base of the substrate of the top asperity have been coupled and voltage has been gradually changed at these nodes at different load steps to observe the effect of voltage on the contact behavior.
- The nodes at the base of the substrate ($z = 0$) of the bottom asperity are fixed in all directions.
- Force, F has been applied at the coupled nodes of the base of the substrate of the top asperity.

- The axisymmetric boundary condition is applied at the axis of symmetry, which is U_r (0, z) =0. Boundary conditions that consider interaction with adjacent asperities are applied to the displacement in the radial direction along the side surfaces, such that U_r (0, z) =U_r (λ/2, z) =0 and to the value of shear stress which is zero at x=λ/2, (σ_{rz} (λ/2, z) = 0). This is very similar to a periodic boundary condition. However, the model is not perfectly periodic. Details about periodicity of the axisymmetric model has been described in Chapter 3.

7.2.2 Governing Equations for Material, Electrical and Thermal Modeling

For the material modeling, the Johnson-Cook material model has been used. According to the Johnson-Cook model, the von Mises flow stress as a function of temperature i.e. thermal softening can be calculated using the following expression [1]:

$$\sigma = [A + B\epsilon^n][1 + Cln\,\dot{\epsilon}^*][1 - T^{*m}] \tag{7.1}$$

where, ϵ is the equivalent plastic strain, $\dot{\epsilon}^* = \frac{\dot{\epsilon}}{\dot{\epsilon_0}}$ is the dimensionless plastic strain rate for $\dot{\epsilon_0}$= 1.0 s^{-1} and $T^*$is the homologous temperature. $T^* = \frac{T - T_{Room}}{T_{Melt} - T_{Room}}$, where T is the temperature at which von Mises stress will be calculated, T_{Melt} is the melting temperature of the material and T_{Room} is the room temperature. When $T = T_{Melt}$, the RHS of the Eq. (7.1) becomes zero, i.e. von Mises flow stress becomes zero. When $T^* = 0$ and $\dot{\epsilon}^* = 1$, Eq. (7.1) gives the stress as a function of strain at room temperature. The second and third sets of brackets represent the effects of strain rate and temperature, respectively. *A*, *B*, *n*, *C* and *m* are material constants and vary from material to material. For the analysis in the current chapter, it has been assumed that von Mises flow stress equals to yield stress.

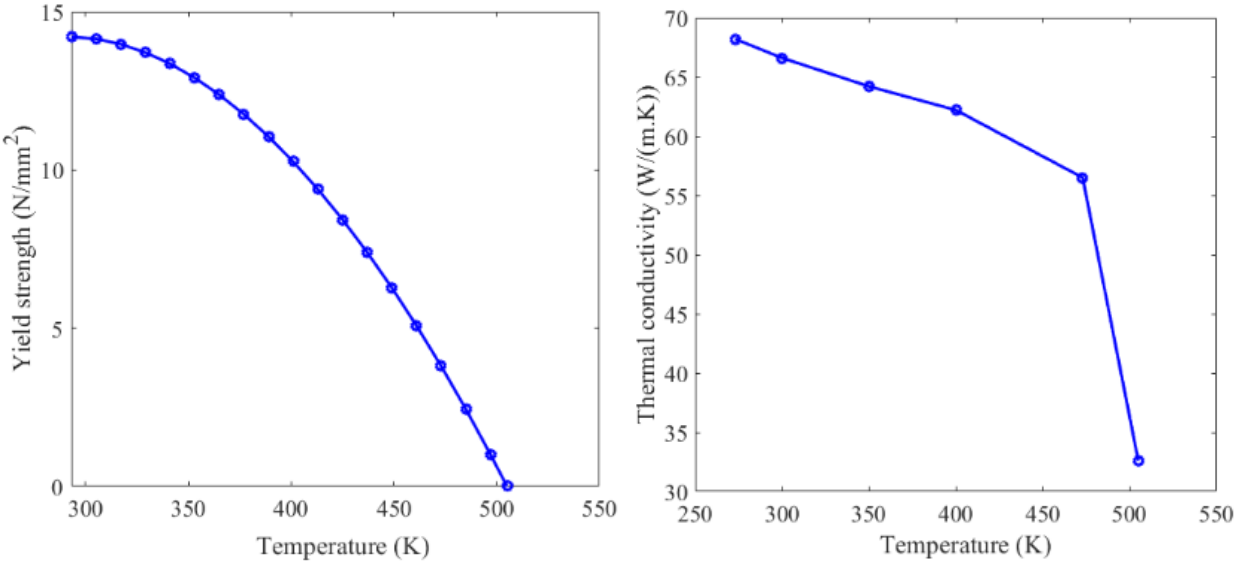

(a) (b)

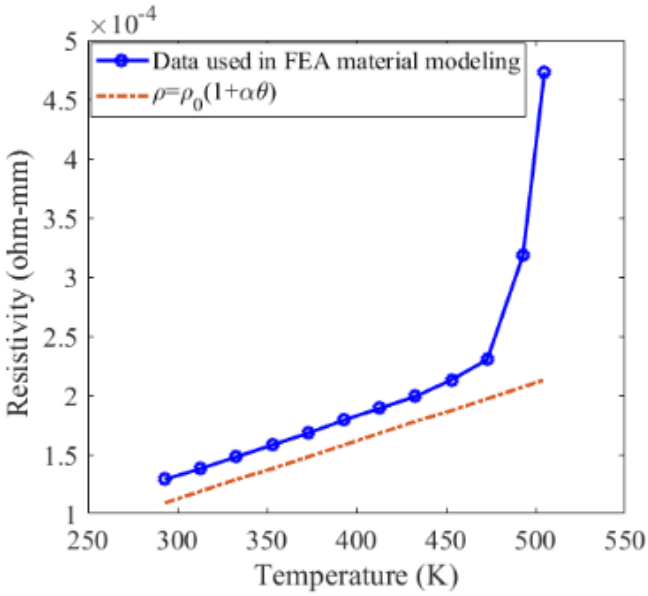

(c)

Fig. 7.2 Change in (a) yield strength, (b) thermal conductivity and (c) resistivity with temperature [2-3].

As in the current analysis, no hardening and transient effects have been considered and that is why the strain rate, $\dot{\epsilon}^* = 1.0\ s^{-1}$ and the strain-hardening exponent, n have been assumed zero in the Johnson-Cook material model. Tin is one of the most common materials used in the applications where electrical contact behavior is a major concern. The temperature dependent yield strength properties of Tin [2] have been curve fitted using the Johnson-Cook material model and the constants *A*, *B* and *m* are determined, which are $(A+B)$=14.2 $\frac{N}{(mm)^2}$ and *m*=1.9 when the temperature is in ℃. Fig. 7.2(a) is showing the change in the yield strength properties of Tin with temperature. Fig. 7.2 (b)-(c) are showing the change in thermal conductivity and resistivity properties of Tin with temperature that are used in the material modeling [2]. Fig. 7.2(c) is also showing the comparison of the experimental resistivity properties that are used in the material modeling with the case when resistivity varies linearly with temperature, $\rho = \rho_0(1 + \alpha(T - T_{Bulk}))$, where ρ_0 is the resistivity at room temperature and α is the temperature coefficient of the resistivity. For ρ_0 and α, $1.09 \times 10^{-4} \Omega mm$ and 0.0045 k^{-1}have been used, respectively [3]. Young's modulus, Poisson's ratio and the thermal expansion coefficient have been kept constant with temperature and $41.6 \times 10^3 \frac{N}{mm^2}$, $0.33\ and\ 2.38 \times 10^{-5} K^{-1}$have been used, respectively [2].

The developed multi-physics model does not consider the transient heat effect. For the steady state conditions, the rate of heat production inside the conductor must equal the rate at which heat is dissipated from its surafce. Therefore [4],

$$\frac{1}{\rho}(\nabla\varphi)^2 = -div(\lambda\nabla\theta) \tag{7.2}$$

where, $\emptyset$ is the potential and θ is the temperature.

Besides that, for the electrical contact the amount of current entering must has to be equal to the amount of current leaving, that is Kirchhoff's law has to be maintained at every node. The thermal field is governed by the following equation [5]:

$$\frac{\partial}{\partial x}\left(\lambda\frac{\partial\theta}{\partial x}\right)+\frac{\partial}{\partial y}\left(\lambda\frac{\partial\theta}{\partial y}\right)+\frac{\partial}{\partial z}\left(\lambda\frac{\partial\theta}{\partial z}\right)+\rho J^2=c\frac{\partial\theta}{\partial t} \tag{7.3}$$

Where, J is the current density and c is the specific heat. For the steady state condition, $\frac{\partial\theta}{\partial t}=0$. So, Eq. (7.3) reduces to the following:

$$\frac{\partial}{\partial x}\left(\lambda\frac{\partial\theta}{\partial x}\right)+\frac{\partial}{\partial y}\left(\lambda\frac{\partial\theta}{\partial y}\right)+\frac{\partial}{\partial z}\left(\lambda\frac{\partial\theta}{\partial z}\right)+\rho J^2=0 \tag{7.4}$$

7.2.3 Cases Analyzed and Solving Procedure

As mentioned in the previous section, for the material modeling Young's modulus, Poisson's ratio, thermal expansion coefficient, thermal conductivity, resistivity and yield strength have been considered. To observe the effect of applied voltage on the contact area, temperature and resistance the following cases are analyzed:

- FEM has been developed and analyzed applying a constant force rather than a constant displacement as most of the electrical contact in practical applications behave as a constant force case rather than a constant displacement case. Two different values of constant force, 1mN and 0.25N have been analyzed. For each of the forces, the following seven cases are analyzed:
    1. **Frictionless-all properties vary:** The contact has been modeled as a frictionless contact. Temperature dependent yield strength, thermal conductivity and resistivity have been considered. All other material properties have been kept constant with temperature.

2. **Perfectly bonded-all properties vary:** This contact modeling is same as the frictionless case. However, contact has been modeled as perfectly bonded instead of frictionless.
3. **Perfectly bonded-elastic:** The contact has been modeled as perfectly bonded. All the mechanical and electrical properties have been kept constant with temperature. No plasticity has been considered in the model.
4. **Perfectly bonded-elastic plastic:** Same as perfectly boned-elastic case; however, plasticity has been considered in the model. Yield strength has not been varied with temperature and kept constant at room temperature, 293K.
5. **Perfectly bonded-yield strength vary:** The contact has been modeled as perfectly bonded. Yield strength has been varied with temperature. However, all the other thermal, mechanical and electrical properties have been kept constant at room temperature, i.e. 293 K.
6. **Perfectly bonded-electrical resistivity vary:** The contact has been modeled as perfectly bonded. Resistivity has been varied with temperature. All the other properties have been kept constant.
7. **Perfectly bonded-thermal conductivity vary:** The contact has been modeled as perfectly bonded. Thermal conductivity has been varied with temperature. All the other properties have been kept constant.

For 0.25N force, perfectly bonded-elastic case has not been analyzed. For all the cases analyzed, the total simulation has been divided into several load steps. At the first load step, only force has been applied (either 1 mN or 0.25N). Temperature has been kept constant at room temperature and no voltage has been applied. Once the contact has been established between the asperities, from

the second load step the force has been kept constant at 1mN or 0.25 N and gradually voltage has been increased at each subsequent load step. The large deflection effect has been considered since the beginning of the analysis, i.e. the effect of geometric non-linearity (the NLGEOM command in ANSYS). The implicit solver (Newton Raphson technique) has been used for solving the FEM. In non-linear implicit analysis, solution of each step requires each iteration to establish equilibrium within a certain tolerance. There is another method-explicit solver to solve the FEM. However, in the explicit analysis, no iteration is required as the problem is solved directly (not iteratively) by taking inverse of the diagonal mass matrix times the net nodal force vector where net nodal force includes contributions from exterior sources. Explicit analysis handles contact and material nonlinearities with relative ease as compared to implicit analysis. The multiphysics simulation is computationally very expensive. Using a high performance super computer (128 GB RAM, 20 processor and single node), for the 1.0 mN force case, when the total number of element was 153,837 it took about 1.5 months to simulate a single case when voltage was increased from 0 to ~0.11 volt. When the number of element was 78,933 for the same case it took less than 1 month to simulate from 0 voltage to melting voltage, i.e. ~0.13 Volt.

7.3 Results and Discussions

7.3.1 Cases Analyzed for Force Equals to 1 mN

Contact Voltage-Maximum Temperature Relation

At the beginning of contact, the FEM requires a fine resolution to capture the contact behavior. That is why at the tip of the asperity the mesh resolution is very fine and then gradually the element size has been increased when away from the contact. Fig. 7.3(a) and (b) are showing the mesh near the contact area for 1.0 mN force case.

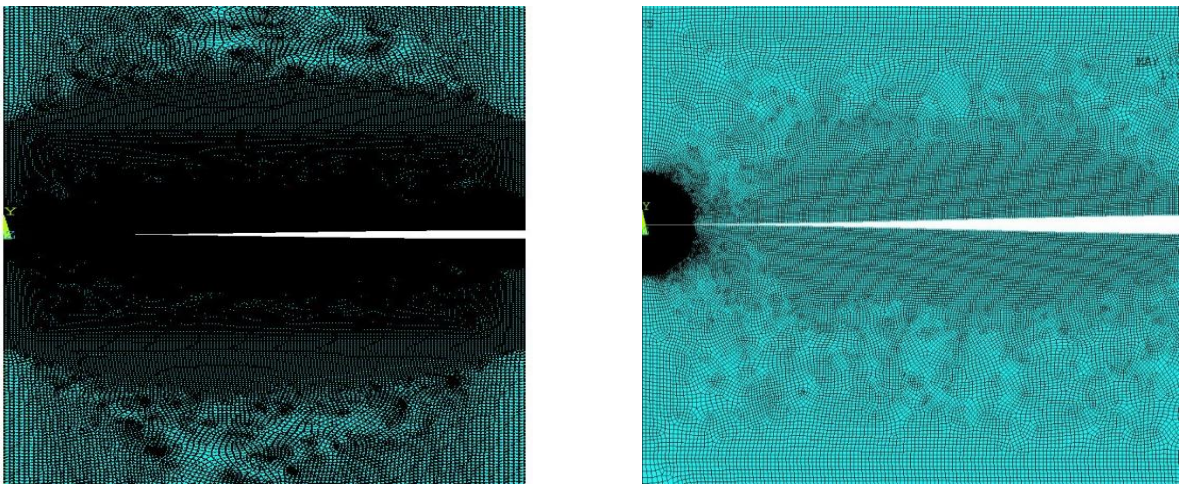

(a) (b)

Fig. 7.3 Finite element mesh near the contact region for 1.0 mN force when (a) total number of element is, 78,933 and (b) total number of element is 153,837.

Fig. 7.4 is showing the comparison of the contact voltage and maximum temperature relation for two different number of elements. As the plots have coincided with each other, the comparison manifests that a total number of 78,933 elements is enough to capture the contact voltage and maximum temperature relation. At the beginning of the contact, it requires a highly refined mesh to capture the contact behavior. As all the plots have coincided with each other from the beginning of the contact to about 0.11 Volt, that is why when the number of elements was 153,837, a simulation has not performed up to the melting voltage, i.e. 0.13 Volt.

From the literature review in Chapter 2 and according to Eq. (2.92), the value of force that will cause yielding in the tin asperity at room temperature is 9.8 mN. Therefore, the for the 1 mN force, at the first load step the deformation should be in the elastic region. However, as the thermal expansion is not zero at the room temperature in the current analysis, due to the combined effect of mechanical and thermal strain the contact deforms plastically even at 1 mN or 0.001 N force.

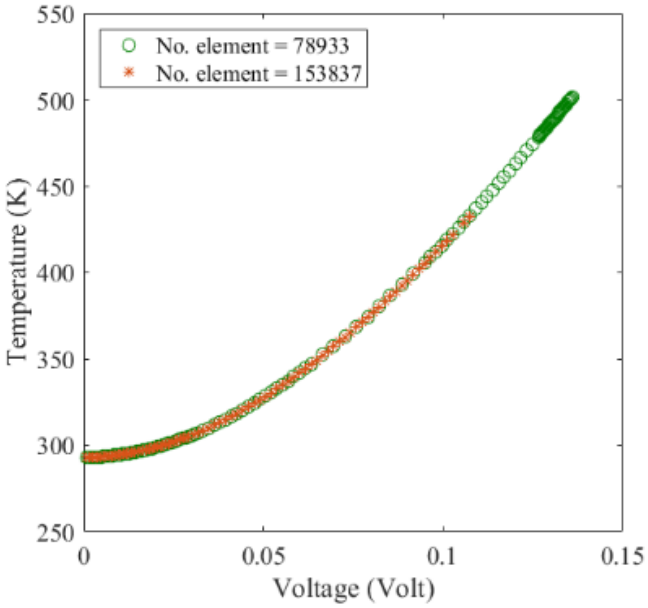

Fig. 7.4 Comparison of the contact voltage and maximum temperature for different element sizes and meshing methods.

Fig. 7.5 is showing the comparison of the contact voltage and maximum temperature relation at the low voltage region for all the cases analyzed when the force is 1mN. When the contact has been modeled as frictionless, the results match with all the other cases. However, the frictionless simulations did not converge when the contact voltage becomes greater than 0.043 Volt (see red circles in Fig. 7.5). Thankfully, for all the other cases when contact has been modeled as perfectly bonded, convergence has been obtained from zero voltage to the melting voltage (see Fig. 7.6). For the perfectly bonded cases, when the two surfaces are in contact, the stresses are exactly the same at the contacting nodes and they are unable to slide in relative motion. However, for the frictionless contact, when the two surfaces are in contact the shear stresses are nil at the contacting nodes and they can slide on each other. This is probably the reason that the simulation for the frictionless contact case did not converge. With the increase of voltage, current gradually increases. As a result, heat generates and temperature increases. Due to the increase of temperature,

resistivity also increases, which may cause more heat generation. However, at the same time heat softens the contact material and increase the contact area. If the increase in contact area is not high enough to mitigate the effect of the increase in resistivity, then contact temperature will continuously increase and eventually contact will collapse. Therefore, proper contact is important for the electrical interfaces. 1mN force is very small for an mm scale analysis. Besides that for frictionless contact, the contact is not as stable as perfectly bonded cases. That is why near the softening voltage region (0.07 V for Tin), the frictionless contact case did not converge. Several important facts have been found from Fig 7.6:

- From the beginning of the contact to the softening voltage of the Tin (0.07 Volt for Tin), curves for all the cases have coincided with each other (see also Fig. 7.5). However, after the softening voltage, the cases show deviation from each other.
- Contact voltage-maximum temperature relation for the perfectly bonded-yield vary, perfectly bonded-elastic plastic, and perfectly bonded-elastic have coincided with each other from zero voltage to near the melting voltage (0.13 Volt for Tin). However, these three cases show deviation from the perfectly bonded-all properties vary, perfectly bonded-thermal conductivity vary and perfectly bonded-electrical resistivity vary cases, especially after the saturation voltage (the voltage after which the thermal softening effect becomes significant) and maximum near the melting voltage. This suggests that, temperature dependent yield strength does not have a significant effect on the contact behavior; rather temperature dependent thermal conductivity and resistivity have an effect that is more important for these limited cases. However, to check the validity of this statement further analysis is necessary at higher forces.

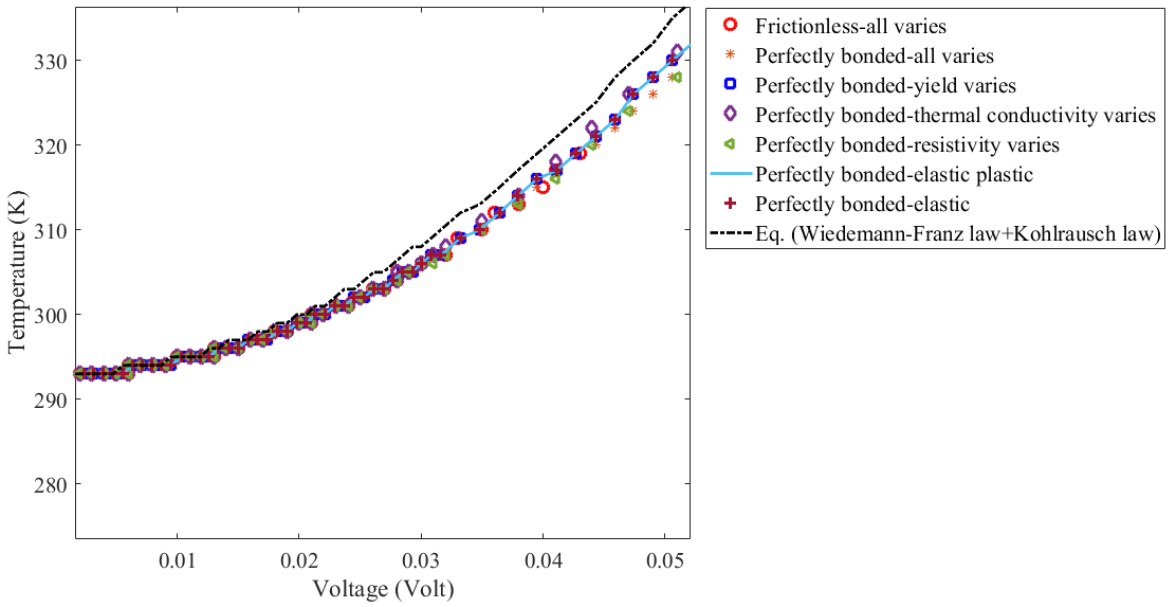

Fig. 7.5 Comparison of the contact voltage and maximum temperature for all the cases performed for 1mN force with Eq. (6.5) at the low voltage region

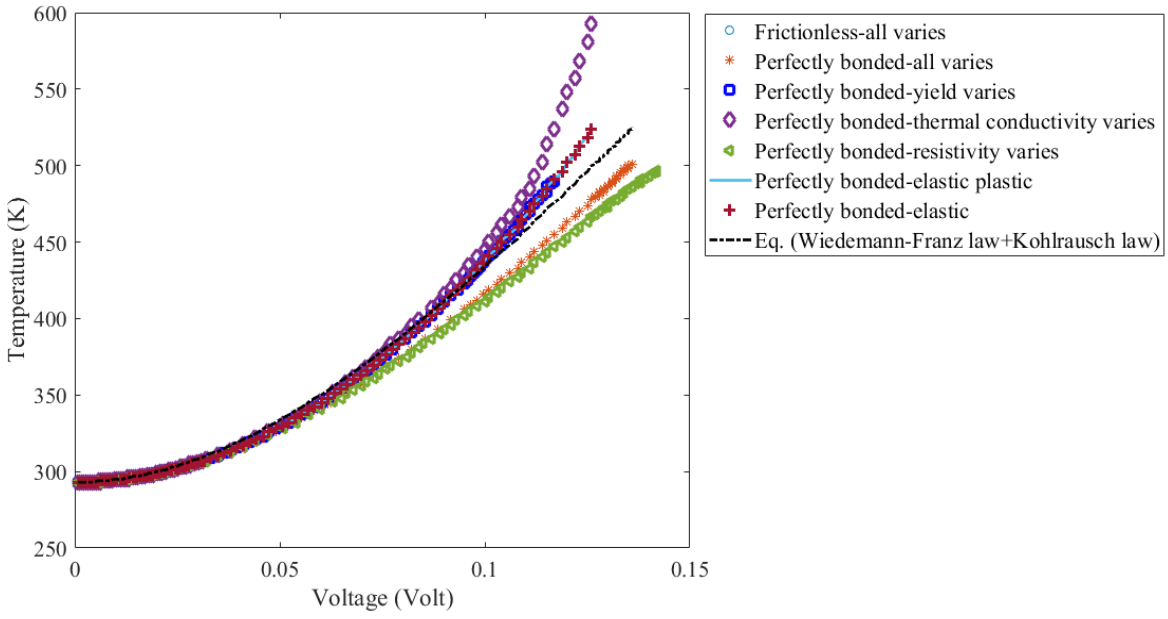

Fig. 7.6 Comparison of the contact voltage and maximum temperature for all the cases performed for 1mN force with Eq. (6.5) from low voltage to the melting voltage.

- Perfectly bonded-all properties vary and perfectly bonded-electrical resistivity vary almost coincided with each other up to 0.1 Volt. After that start to show deviation from each other, although the maximum deviation between these two cases is less than 2.6% for the 1mN force case. From Fig. 7.2(b), when temperature is greater than 450K (i.e. voltage is about 0.1 V from Fig. 7.6), thermal conductivity drops sharply up to the melting point. This is the reason for the difference between the perfectly bonded-all properties vary and perfectly bonded-electrical resistivity vary case. Therefore, it can be said that it is the temperature dependent resistivity and thermal conductivity, which are controlling the electrical contact behavior most for the cases considered in this work.
- The contact voltage and maximum temperature relation for the monometallic contact that has been obtained by combining the Kohlrausch law and Wiedemann-Franz law i.e. Eq. (6.5) show good agreement with almost all the cases up to 0.1 Volt. However, shows the best agreement with the perfectly bonded-yield varies, perfectly bonded-elastic plastic, and the perfectly bonded-elastic cases from low voltage up to near the melting point. The difference that Eq. (6.5) shows with the perfectly bonded-all properties vary case and perfectly bonded-electrical resistivity vary case are shown is Fig. 7.7. When compared with the perfectly bonded-all properties vary case, Eq. (6.5) shows a maximum of 4.65% error and with perfectly bonded-electrical resistivity vary case shows a maximum of 8.97% error. Therefore, for the contact voltage-maximum temperature prediction Eq. (6.5) can be used.

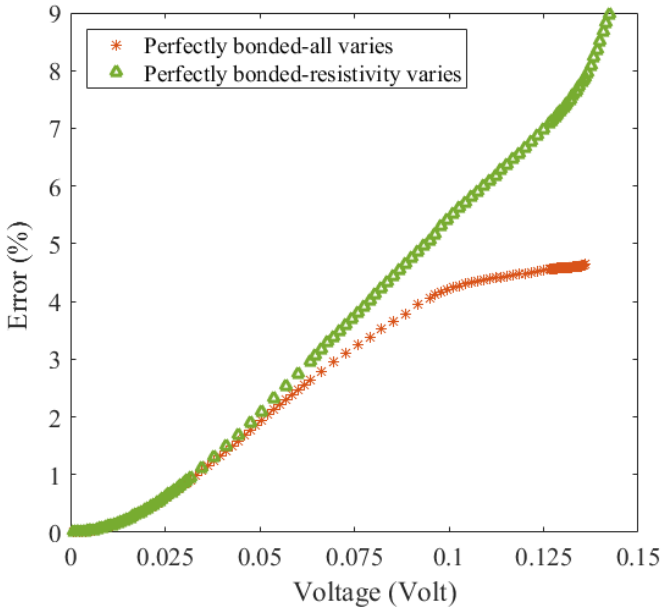

Fig. 7.7 Percentage of error that Eq. (6.5) shows with perfectly bonded-all varies and perfectly bonded-resistivity varies.

Change in Contact Area, Contact Resistance and Total Current with Voltage

The changes in the contact area, resistance and total current have not been analyzed in detail for the 1mN force case. Because, at the first load step, a contact has been established between the two tin asperities applying 1mN force. However, the temperature is kept constant at room temperature and the voltage difference across the contact is zero. From the second load step, when force has been kept constant and voltage is gradually increased, the change in contact area was negligible approximately up to the softening voltage. After the softening voltage, the effect of increase in voltage has been observed on the contact area and resistance. In addition, although 78,933 elements were enough to capture the contact voltage and maximum temperature relation, even 153,837 elements were not enough to capture the change in contact area, resistance and current properly. As the change in contact area is very small up to the softening voltage for the 1.0 mN force that is

why, to observe the effect of temperature dependent material properties separately, a higher value of force is applied which has been discussed later.

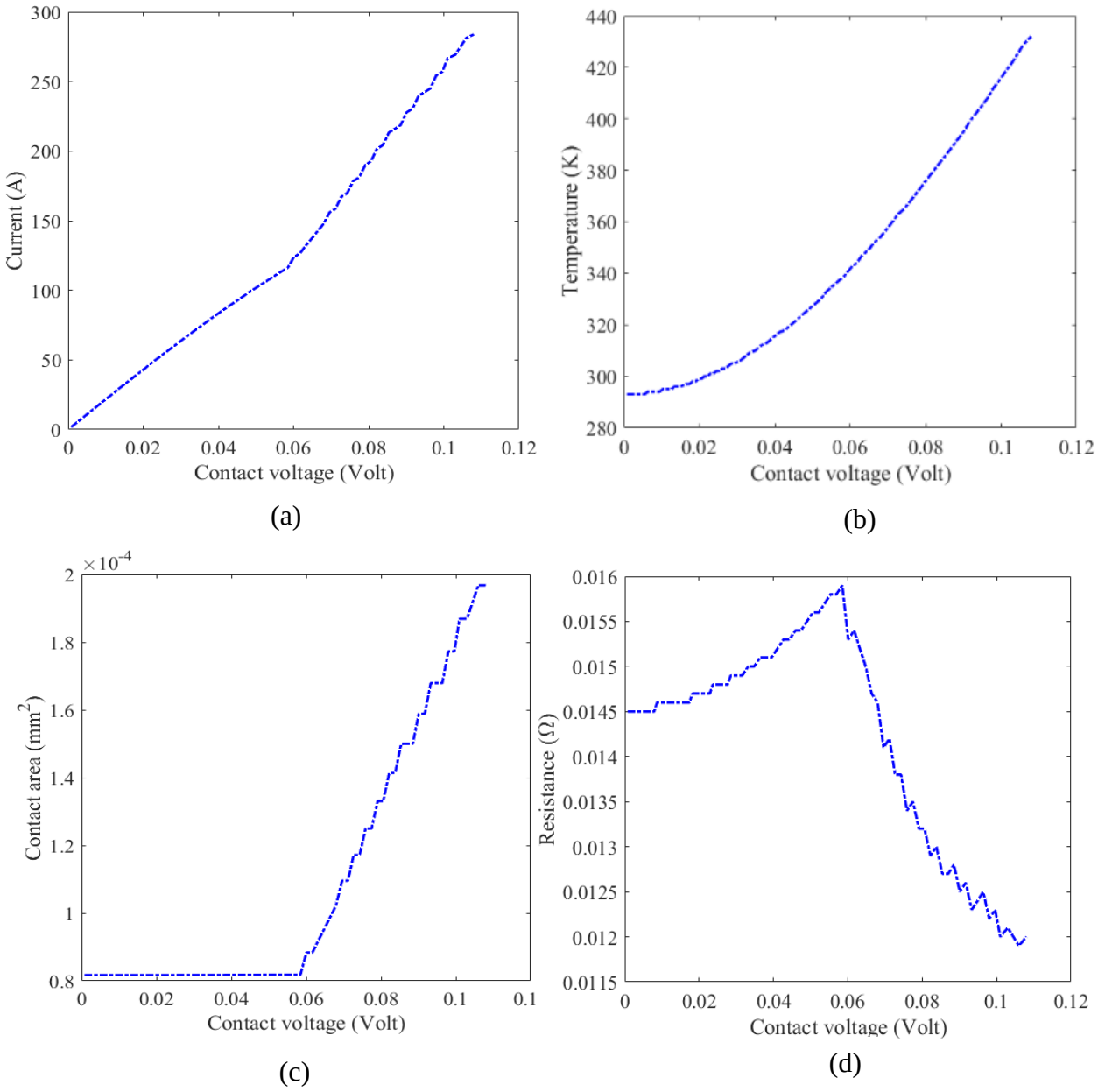

Fig. 7.8 Change in (a) total current, (b) contact temperature, (c) contact area, and (d) contact resistance with voltage for a mesh with 153,837 elements.

Although for the 1.0 mN force case, the change in contact area is negligible before the softening voltage (~0.07 Volt for tin), the simulation results give a clear idea about how the temperature dependent properties are affecting the overall contact phenomena. Fig. 7.8 is showing that, with the increase in the contact voltage, total current through the conductor is increasing. As a result, temperature also increases. With the increase in temperature, contact resistivity also increases. However, as the contact area is nearly constant up to the softening voltage (~0.07 Volt), with the increase in contact voltage, contact resistance continuously increases. After the softening voltage ($\sim 0.07\ V$), when the thermal softening is significant, contact area continuously increases with the increase in voltage. As a result, contact resistance decreases.

7.3.2 Cases Analyzed for Force Equals to 0.25 N

For the 0.25 N case, from the mesh convergence test it has been found that 225,854 elements are enough to capture the change in contact current, resistance, area and maximum temperature with the change in voltage. Fig. 7.9 is showing the mesh that has been used for this force.

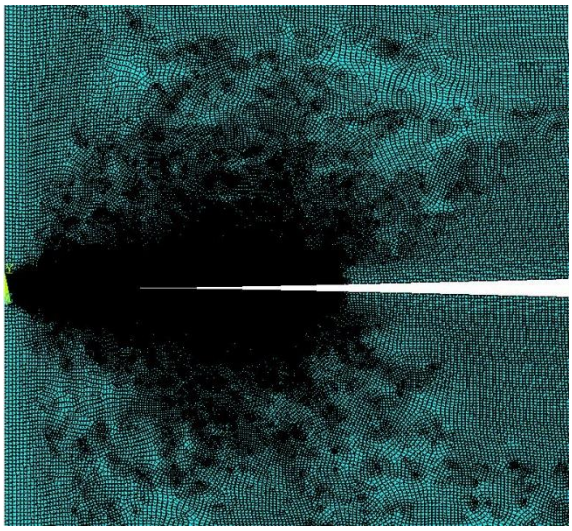

Fig. 7.9 Finite element mesh for 0.25N force.

Fig. 7.10(a-d) are showing the change in total current, maximum temperature, contact area and contact resistance value with the increase in voltage when the force is 0.25N. All the analyzed cases show a similar trend with the change in voltage. When the contact voltage across the interface increases, the total current through the conductor gradually increases (Fig. 7.10(a)). With the increase in current, the temperature continuously rises (Fig. 7.10(b)). Due to the increase in temperature, the electrical resistivity increases and thermal conductivity decreases. As thermal conductivity decreases, the generated heat gets trapped and softens the interface. As a result, contact area increases (Fig. 7.10(c)). For the applied voltage range, the amount of increase in contact area is large enough to counter the effect of the increase in resistivity with temperature. Therefore, contact resistance continuously decreases with the increase in voltage (Fig. 7.10(d)).

Similar to the 1.0 mN force case, for 0.25N, the perfectly bonded-all properties vary and perfectly bonded- electrical resistivity vary cases coincide with each other. The frictionless-all properties vary case also coincides with these two cases. With the increase in force (about 250 times), contact area for all the cases have increased several orders of magnitude compared to the 1.0 mN force, and that is why the frictionless-all properties vary case has reached a higher temperature for the 0.25N force. Although contact area has increased with the increase in force, the contact area is still very small (see Fig. 7.10(c)). That is why almost no difference has been found between the frictionless-all properties vary and perfectly bonded-all properties vary cases. However, as the perfectly bonded-electrical resistivity vary case concide with the perfectly bonded-all properties vary case, it again confirms that the interaction between the temperature dependent resistivity and plasticity is adequate enough to predict the contact behavior if the temperature dependent yield strength is not available. This finding could be very benificial for the multiphysics analysis as the

temperature dependent yield strength measurement is not trivial and also not readily available for all materials.

For the 0.25N case, no convergence has been found, when the voltage across the interface reaches the softening voltage or close to the softening voltage (0.07 Volt). The von Mises stress distribution shown in Fig. 7.11 (a-c) describes the probable reason. As the force is constant in the developed multiphysics model, the contact stess or pressure is very high at the center of the axisymmetric model. When the contact voltage is about 0.07 Volt, contact stress near the axisymmetric line and where the force has been applied becomes very high and reaches the yield strength value. That is why the simulation did not converge with the further increase in voltage. Fig. 7.11(a) shows that for the 1mN force, even when the voltage across the interface is close to the melting voltage, the von Mises stress near the center of the axisymmetric line is not high as the force was low. For the constant dispacement model, this wouldn't be a problem as the model will allow the contact force to rise continuously and contact area will grow along the radial direction of the interface.

7.3.3 Comparison of the Multiphysics Contact Resistance with the Analytical Models

Closed form solutions are available for voltage and current as a function of maximum temperature of contacting conductor (see Chapter 6). When high current passes through the conductors, the temperature distribution in the conductors is not uniform. Greenwood and Williamson showed that resistance at the equipotential surfaces are different and expressed the equation for total current (Eq. (6.6)) as a function of equipotential distance and contact area (area at the "cold resistance" condition) [4, 7] (see Eq. (13) and (14) in Ref. [4] and Eq. (1.44) in Ref. [7]).

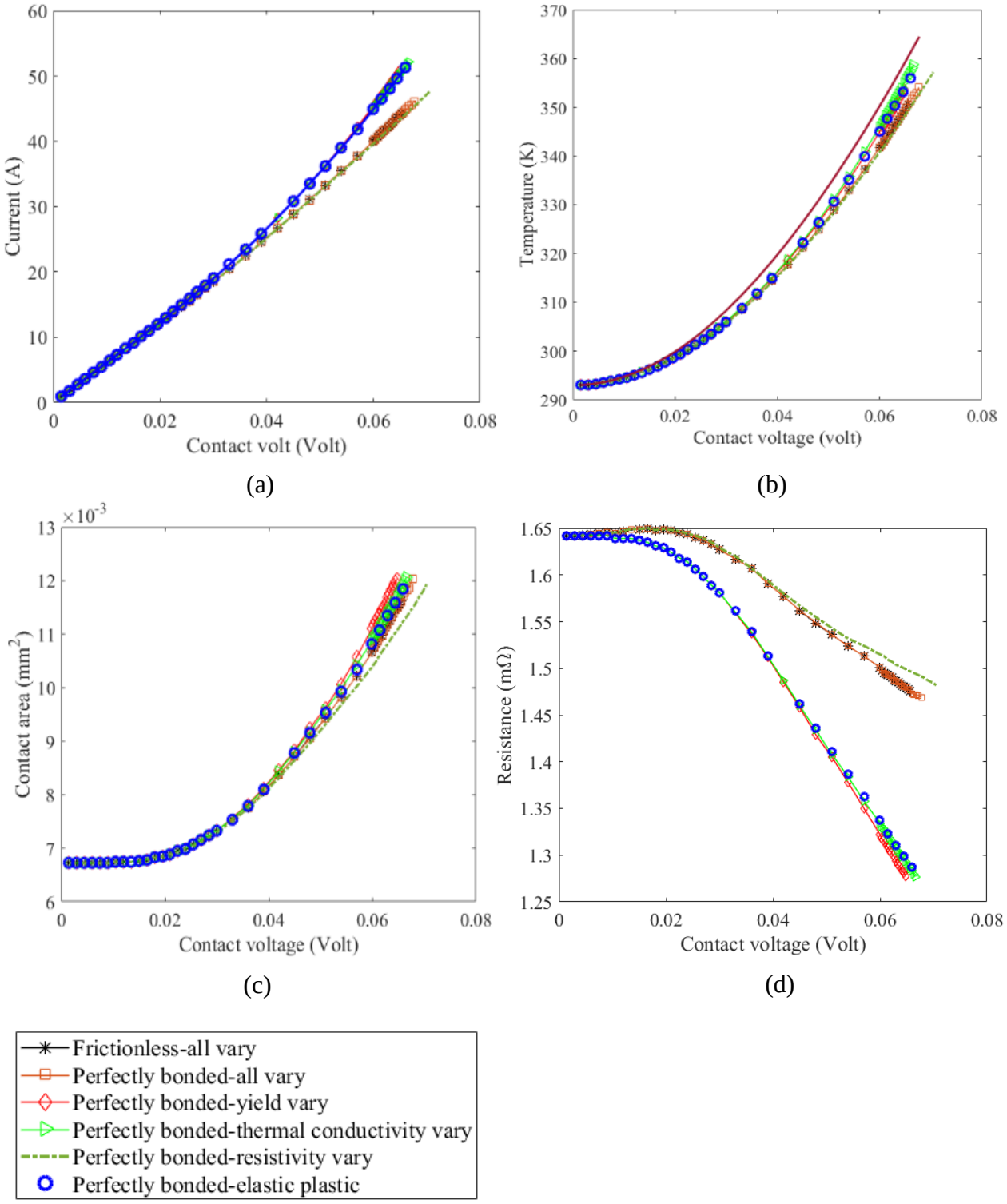

Fig. 7.10 Change in (a) total current (b) maximum temperature (c) contact area and (d) contact resistance with the change in voltage when the force is 0.25N.

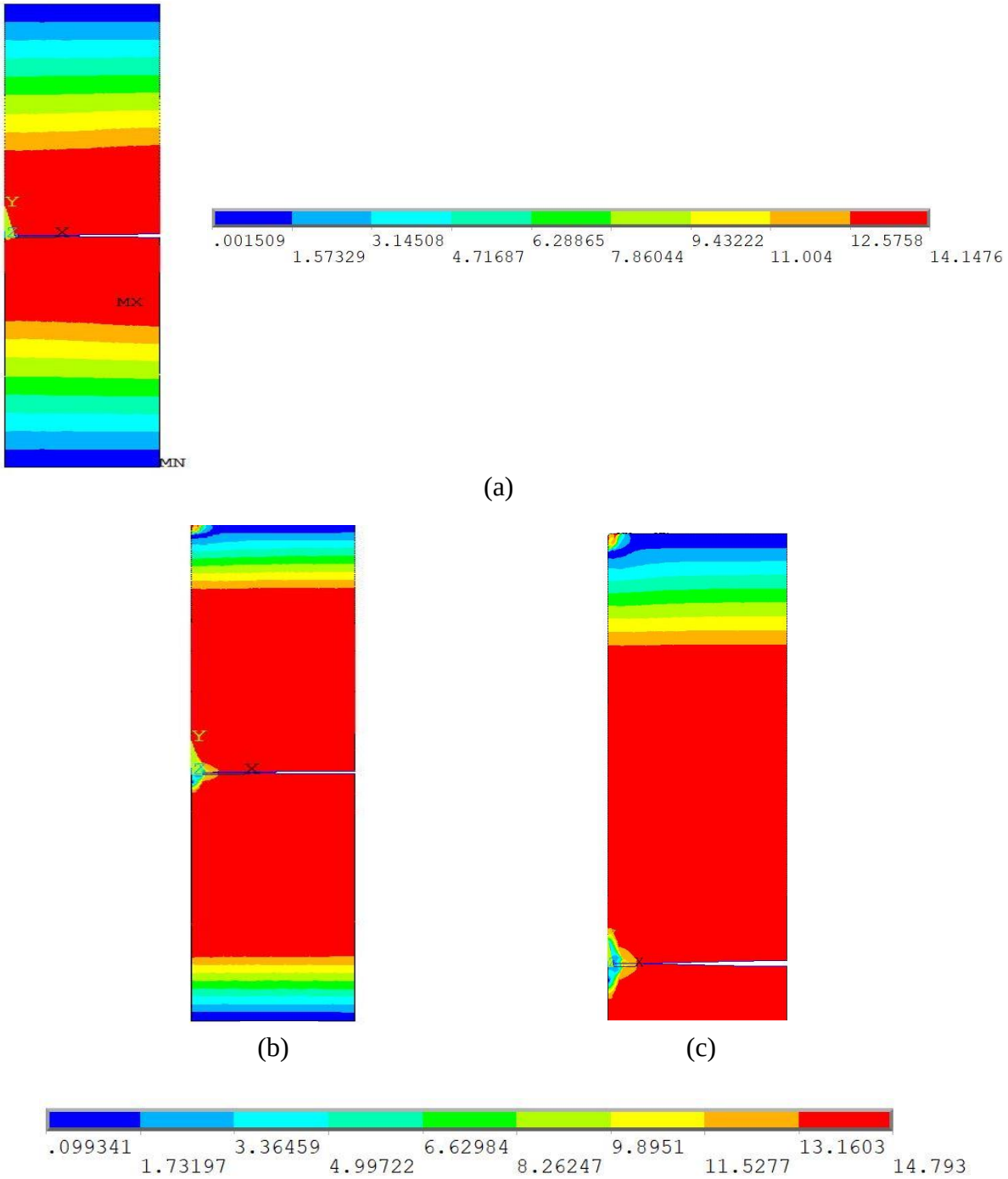

Fig. 7.11 Von Misses stress distribution (units in MPa) for 1mN force when voltage is about 0.13 Volt, (b) von Misses stress distribution for 1mN force when voltage is about 0.07 Volt, (c) magnified view of Fig. 7.11(b).

The total current equation provided by Greenwood and Williamson (Eq. (6.11)) which is a function of "cold resistance", electrical resistivity and thermal conductivity at room temperature is:

$$I = 2\frac{\rho_0}{R_0}[2(T_m - T_{Bulk})\lambda_0/\rho_0]^{1/2}$$

In the above equation, according to [4], R_0 is the "cold resistance" and therefore can be determined using the Holm equation, $\frac{\rho_0}{2a_0}$. a_0 is the contact area at the "cold resistance" condition, i.e. when the current passing through the interface causes negligible temperature rise. In this section, instead of using contact area at the "cold resistance" condition, a variable contact area has been used in the above equation to determine the total current. The advantage of the above equation is that it is not a function of the equipotential distance. Then from the total current and using Eq. (6.5) for the voltage, the contact resistance has been determined. Therefore, the contact resistance equation is:

$$ECR = \frac{V}{I} = \frac{\left(4L(T_m^2 - T_{Bulk}^2)\right)^{0.5}}{4a_{variable}[2(T_m - T_{Bulk})\lambda_0/\rho_0]^{1/2}} \quad (7.5)$$

where, $a_{variable}$ will change with the change in voltage and has been calculated based on the model prediction.

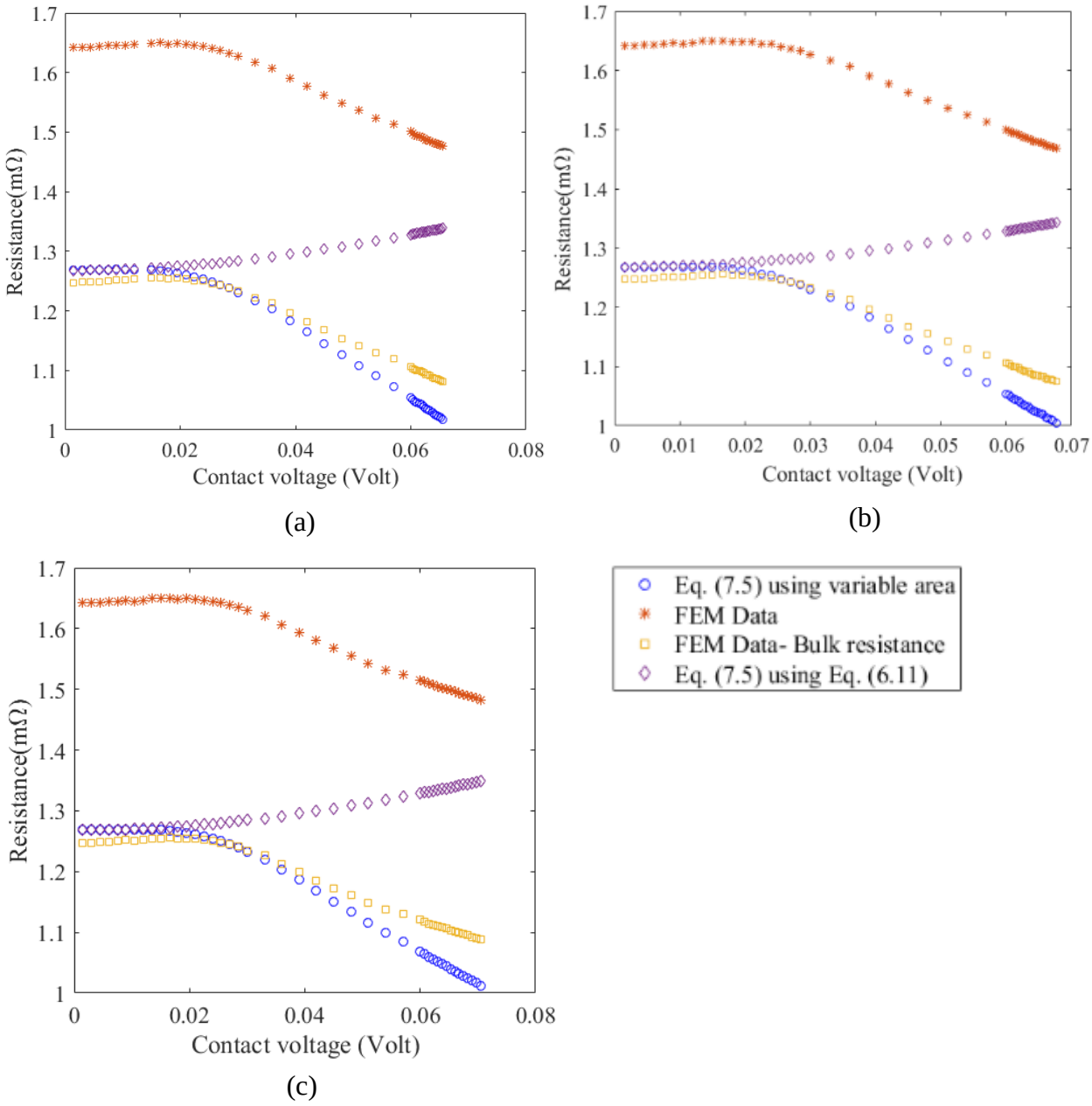

Fig. 7.12 Comparison of contact resistance determined from the newly suggested Eq. (7.5), Eq. (7.5) using "cold resistance" contact area, i.e. Eq. (6.11) and (a) FEA result for the frictionless-all varies, (b) perfectly bonded-all varies and (c) perfectly bonded-resistivity varies.

Fig. 7.12 (a), (b) and (c) show the comparison of Eq. (7.5) with the multiphysics FEA results for the frictionless-all properties vary, perfectly bonded-all properties vary and perfectly bonded-electrical resistivity vary. The various cases comparison manifests that Eq. (7.5) can predict the contact resistance reasonably well from low voltage to the saturation voltage. The maximum error that Eq. (7.5) shows with perfectly bonded-all properties vary, perfectly bonded-resistivity vary and frictionless contact-all properties vary are 6.05%, 6.42% and 6.08% respectively. In this Chapter, $a_{variable}$ in Eq. (7.5) has been determined from the FEA. However, $a_{variable}$ can be determined from the axisymmetric single asperity model developed in Chapter 3. Further analysis is necessary for that to relate temperature with the yield strength of the axisymmetric model. Fig. 7.12 also shows that if instead of variable area, contact area at the "cold resistance" condition is employed in Eq. (7.5); the equation cannot predict the electrical contact resistance values.

7.4 Summary

- Thermal softening is a major concern in many of the electrical contact applications. Research works have been done to analyze the effect of temperature dependent yield strength on the thermal softening. However, it is not clear which electrical, thermal, or mechanical properties contributing most on the electrical contact behavior. This chapter has performed a detail investigation by varying one parameter at a time with the temperature while other properties are constant at room temperature. Then all the analyzed cases are compared with the case when all properties are varying with temperature.
- The investigation shows that, resistivity and thermal conductivity are the most important parameters that are controlling the contact behavior. For the cases considered, consideration of the interaction between plasticity and the temperature dependent resistivity are enough to capture the contact behavior up to the softening voltage. After

that, the decrease in thermal conductivity effect becomes important as heat gets trapped at the interface and softens the interface. However, if the temperature dependent thermal conductivity property is not available, then temperature dependent resistivity can be used with other properties (at room temperature), as perfectly bonded-resistivity varies case show reasonably good agreement with the perfectly bonded- all properties varies and frictionless- all properties varies cases for both of the force.

- The voltage temperature relation provided by Kohlrausch in combination with Wiedemann-Franz law show good agreement with the perfectly bonded-all varies case. For 1mN force, the maximum difference was less than 4.5% from the low voltage to the melting voltage region.
- Electrical contact applications that behave more likely to the perfectly bonded contact provide better contact support than the cases where contact behaves more close to the frictionless contact. At low forces the difference is especially prominent. If the contact force is high, as thermal softening and melting are highly localized phenomena, much difference has not been observed between these two cases.
- Contact voltage and total current equations are available as a function of maximum temperature. In this chapter, the total current equation provided by Greenwood and Williamson has been modified so that it can be applied to predict the electrical contact resistance from low voltage to the softening voltage.

References

1. Johnson, G. R., & Cook, W. H. (1983, April). A constitutive model and data for metals subjected to large strains, high strain rates and high temperatures. In Proceedings of the 7th International Symposium on Ballistics (Vol. 21, No. 1, pp. 541-547).

2. MatWeb Material Property Data. http://www.matweb.com/search/datasheet.aspx?matguid=64d7cf04332e428dbca9f755f4624a6c&ckck=1

3. Wikipedia. https://en.wikipedia.org/wiki/Electrical_resistivity_and_conductivity

4. Greenwood, J. A., & Williamson, J. B. P. (1958). Electrical conduction in solids II. Theory of temperature-dependent conductors. Proceedings of the Royal Society of London. Series A. Mathematical and Physical Sciences, 246(1244), 13-31.

5. Bottauscio, O., Crotti, G., & Farina, G. (1993). Numerical analysis of heating transient of electric contacts under short-circuit conditions. IEEE transactions on components, hybrids, and manufacturing technology, 16(5), 563-570.

6. Bowden, F. P., & Williamson, J. B. P. (1958). Electrical conduction in solids I. Influence of the passage of current on the contact between solids. Proceedings of the Royal Society of London. Series A. Mathematical and Physical Sciences, 246(1244), 1-12.

7. Slade, P. G. (Ed.). (2017). Electrical contacts: principles and applications. CRC press.

Chapter 8

Closure

8.1 Conclusions

Electrical contact resistance (ECR) is one of the important factors that affect the reliability of the electrical contact in different applications. Contact mechanics models are widely used to analyze the electrical contact behavior. Analytical and semi-empirical solutions are available to model the elastic and elastic-plastic contact behavior. However, to develop a more realistic model and to reduce the computational expense, an axisymmetric sinusoidal asperity model has been developed both for the elastic and elastic-perfectly plastic material. The developed model is not perfectly periodic, however it considers the effect of interaction with adjacent asperities because of the boundary conditions. The non-contact area for this asperity model is ring-shaped. As a result, for the rough surface models developed using this asperity model, the contact pressure distribution will be a non-periodic wavy shape, which seems more realistic for the fractal or real multiscale random surfaces. The formulated empirical equations for the single asperity model are a function of surface roughness and material properties. Therefore, if the surface roughness and temperature dependent material properties are known, the formulated equations can be used to determine the ECR.

Significant improvement has been made on the rough surface contact models. Employing the axisymmetric sinusoidal asperity and other asperity models available in the framework of the statistical and multiscale rough surface contact models, several new rough surface contact models have been proposed both for the elastic and elastic-plastic material. The newly suggested elastic models are compared with Boundary Element Method (BEM) predictions and Persson's model.

The comparison shows that the multiscale model does not exhibit close behavior with the BEM or the Persson model, however the statistical models do. When employing the statistical model to predict contact behavior, results show that the probability distribution function (PDF) of the asperity of the rough surface and asperity model have an important effect on the contact behavior prediction. Whether the surface asperity distribution is Gaussian in nature or show an asymmetric distribution with different skewness and kurtosis, it is more reliable to consider both the statistical distribution of the surface asperity height and radius of curvature in the statistical asperity model and PDF. When compared the BEM result with the developed statistical models, the comparison shows that Greenwood 3D sinusoidal elastic model in conjunction with the Greenwood crack model (modified Greenwood model) can predict the whole range of contact with less than 12% error when contact area is greater than 0.1% of the total area. The Nayak-Bush 3D sinusoidal elastic model and Greenwood axisymmetric sinusoidal elastic model show good agreement with the Persson's model. Greenwood axisymmetric sinusoidal model matches with the Persson model from 0.1-70% of the total area with less than 10% error. Nayak-Bush 3D sinusoidal show good qualitative and quantitative agreement with the Persson model. The difference between the Persson model and Nayak-Bush model is less than 10% when the real contact area is 12-90% of the total area. Although in contact mechanics, it is a common assumption that spherical/ mildly elliptical model can predict only the small deformation region. Analysis in this dissertation shows that this statement is not always true. It depends on the technique used to develop the statistical model and also on the surface nature. Therefore, it is always better to consider sinusoidal asperity model to predict large deformation. The objective to develop these rough surface contact models are to reduce the computation expense of the BEM/ FEM and Persson model is derived by assuming self-

affine rough surfaces, however the newly developed models are applicable for both self-affine fractal and multiscale random surfaces.

For the validation of the elastic-plastic rough surface contact models, an experiment has been performed to determine the ECR between two rough surfaces. Comparison shows that the Nayak-Bush axisymmetric sinusoidal and Greenwood axisymmetric sinusoidal elastic-plastic model show close agreement with the experimental result. The experiment was performed for a small range of forces. To validate the newly developed statistical models from small to the heavy deformation region further investigation is necessary.

Surface roughness varies over a wide range of scales and as a result, for the same amount of current, the current density is not the same everywhere at the interface. When current density is high, heat generates, temperature rises, which may cause eventual softening and melting at the interface. Generally, the phenomena of softening and melting are highly localized. In this dissertation, two methods of electrical contact resistance determination between two rough surfaces have been suggested. As the phenomena of softening and melting are highly localized, when the heat/ current flows through the interface, electrical and thermal contact resistance behave in a very similar way. That is why based on the newly developed statistical models, Holm ECR equation for single asperities and the Cooper et al. thermal contact resistance model, several new electrical contact resistance models have been suggested to determine the contact resistance between the rough surfaces.

An electro-thermo-mechanical analysis has also been performed considering the temperature dependent material properties (i.e. a fully coupled multi-physics model of a single asperity electrical contact). The objective of this analysis is to observe which temperature dependent

properties are affecting the electrical contact behavior most. For the cases considered, which are dominated by elastic deformation, show that for the analyzed cases, it is the temperature dependent thermal conductivity and resistivity that govern the contact behavior. Other properties and temperature dependent yield strength do not have a noticeable effect on the electrical contact behavior. However, this finding is limited to the cases considered in this work. Analyzing the results, an electrical contact resistance equation for single asperity has been suggested which is applicable from low voltage to the softening voltage of the material. The developed ECR equation for the asperity is a function of contact radius, which can be determined from the developed axisymmetric sinusoidal asperity model.

8.2 Future Work

- Comparison of the newly developed statistical models show that there is a model which shows good agreement with the BEM and there are also models which show good match with the Persson model. That is why finite element analysis of the deterministic elastic rough surface contact model can be performed to gain more confidence in the validation of the developed elastic statistical contact models as FEM is a versatile numerical method.
- The developed elastic-plastic contact models have been compared with the experimental results. However, the experiment was performed for a small range of forces. To validate the developed elastic-plastic statistical models for a wide range of deformation, a finite element analysis of the deterministic elastic-plastic rough surface contact model can be performed.
- Electro-thermo-mechanical analysis has been performed only for tin material properties. The multi-physics analysis should be extended for higher value of forces to observe whether temperature dependent yield strength has any effect for the higher force cases

when plastic deformation is more dominant. The analysis should also be extended for other materials that are common in electrical contact applications such as-Ag and Au to observe whether the same ECR equation and conclusions that have been drawn for the tin material are also applicable for other materials or not.

- The suggested ECR equation for asperity contact from the multi-physics analysis is a function of contact radius, which changes with the change of voltage or temperature. An analysis can be performed to relate the developed axisymmetric sinusoidal model with temperature.